






Universitat Autònoma de Barcelona

## Solution-Processed Organic Field-Effect Transistors: from Fundamental Aspects to Applications

Inés Temiño Gutiérrez

**ADVERTIMENT.** L'accés als continguts d'aquesta tesi queda condicionat a l'acceptació de les condicions d'ús establertes per la següent llicència Creative Commons:  [http://cat.creativecommons.org/?page\\_id=184](http://cat.creativecommons.org/?page_id=184)

**ADVERTENCIA.** El acceso a los contenidos de esta tesis queda condicionado a la aceptación de las condiciones de uso establecidas por la siguiente licencia Creative Commons:  <http://es.creativecommons.org/blog/licencias/>

**WARNING.** The access to the contents of this doctoral thesis it is limited to the acceptance of the use conditions set by the following Creative Commons license:  <https://creativecommons.org/licenses/?lang=en>

# **Solution-Processed Organic Field-Effect Transistors: from Fundamental Aspects to Applications**

**Inés Temiño Gutiérrez**

Doctoral Thesis

PhD Programme in Materials Science

**DIRECTOR: Dr. Marta Mas Torrent**

**TUTOR: Prof. Jordi Sort Viñas**

Institut de Ciència de Materials de Barcelona (ICMAB-CSIC)

Physics Department / Science Faculty, Universitat Autònoma de  
Barcelona (UAB)

**September, 2019**



Memòria presentada per aspirar al Grau de Doctor per:

Inés Temiño Gutiérrez

Vist i plau:

Dra. Marta Mas Torrent

Prof. Jordi Sort Viñas

Bellaterra, 26 de Septiembre de 2019





**MARTA MAS TORRENT**, Research Scientist of the Spanish Council of Research (CSIC) at the Materials Science Institute of Barcelona (ICMAB), and **JORDI SORT VIÑAS**, Professor at the Autonomous University of Barcelona (UAB)

CERTIFY

That **Inés Temiño Gutiérrez** has performed, under their supervision, the research work entitled “**Solution-Processed Organic Field-Effect Transistors: from Fundamental Aspects to Applications**”. This work has been carried out under the framework of the Materials Science PhD programme of the Physics Department of the Autonomous University of Barcelona.

And in witness whereof this is signed by

Director:

Dr. Marta Mas-Torrent

Tutor:

Prof. Jordi Sort Viñas

September 26<sup>th</sup>, 2019



# Acknowledgements (Agradecimientos)

---

El desarrollo de esta tesis no puede resumirse tan sólo como 4 años y pico de trabajo, no sería justo. En cambio, prefiero verlo como un viaje lleno de experiencias y aprendizaje, de ideas y gente nueva, de evolución y, por supuesto, de curvas. Aunque mirando hacia atrás me doy cuenta de que el recorrido ha sido largo, la verdad es que se me ha pasado volando... Y eso, sin ninguna duda, ha sido gracias a toda la gente que ha sido parte activa de este trabajo y que me ha apoyado cuando más hacía falta.

Para comenzar me gustaría agradecer a la Dra. Marta Mas Torrent que confiara en mí, abriéndome las puertas al mundo de la investigación y dándome la oportunidad de hacer la tesis bajo su dirección. Si esta tesis ha sido un viaje, tu papel como copiloto ha sido fundamental. Gracias por la paciencia y los consejos cuando me escuchabas decir “esto no lo tengo claro” o “no sé por dónde empezar”, sobre todo al principio. Contigo he aprendido muchísimo de transistores orgánicos, pero también de todo lo demás que envuelve la ciencia. Gracias por creer en mí y hacerme ver mis puntos fuertes, porque eso me ha ayudado enormemente a crecer profesional y personalmente.

The work carried out in this thesis would not have been possible without the collaboration of other research groups. There is no doubt that cooperative and multidisciplinary work has enriched both my research experience and the results presented herein; thus, I would like to thank all the collaborators for their contribution.

Primero, me gustaría agradecer a la Dra. Ana Pérez, Dra. Esther Barrena y Dra. Carmen Ocal del ICMA B su implicación para llevar a cabo un tremendo trabajo de AFM con los films de C8-BTBT. Especialmente gracias a Ana por trabajar conmigo codo con codo, por ayudarme a entender las medidas y los resultados, y por estar siempre disponible para resolver todas mis dudas y contrastar ideas.

También me gustaría dar las gracias al Prof. Joaquim Puigdollers de la Universitat Politècnica de Catalunya (UPC) por permitirnos utilizar su laboratorio y ayudarnos en las primeras evaporaciones de contactos metálicos.

I would like to thank Prof. Annalisa Bonfiglio from the University of Cagliari and her group, Prof. Piero Cossedu and Dr. Stefano Lai, for their collaboration in the study employing flexible devices. Also thanks for hosting me for one week and letting me work in your lab.

Special thanks to Stefano, who showed me how to measure devices under strain and also helped me interpret the results.

I would also like to thank Prof. Beatrice Fraboni from the University of Bologna for hosting me during a 3 month stay and making it possible for me to step into the field of radiation detectors. Also thanks to all the collaborators from her group that were part of this and other studies, Dr. Laura Basiricò, Dr. Andrea Ciavatti, Dr. Tobias Cramer and Ilaria Fratelli. I learnt a lot working with all of you and from all the ideas arising during our meetings. Special thanks to Ilaria and Maria for all the shared moments, the coffee breaks and the long talks. It was really nice meeting you during this period away from home.

Finally, I would like to mention all the people from the OFET team, those that were there when I started working in the group and also those that arrived while I was doing my thesis. Thank you for all the time we spent together in the lab, talking about work and life. Your company made time pass by more easily, and all of you have contributed in some way or another to this thesis work. Special thanks to Dr. Sergi Galindo for showing me around during my first months in the group and Dr. Ajayakumar Murugan Rathamony for the synthesis of DT-TTF. Thanks to Dr. Antonio Campos and Dr. Qiaoming Zhang for always sharing your results and ideas with me and giving me a hand when I needed it, I learnt a lot from you both. Also thanks to Adrián Tamayo for helping me with the thin-film fabrication while I was doing my stay abroad, it was great working with you. And thanks to Simona Ricci for always cheering me up and making me believe I could do it, *grazie!*

Desde un punto de vista más personal que científico, tengo que reconocer que trabajar estos años en el grupo Nanomol ha sido como formar parte de una gran familia. A todos los jefes, técnicos y estudiantes, gracias por estar siempre dispuestos a ayudar y por generar un ambiente de trabajo tan positivo. Me gustaría mencionar especialmente a la gente del despacho, gracias por las charlas, la comida compartida, las distracciones tan necesarias y los ánimos en los peores momentos. Y en general, gracias a todos los que habéis hecho mi día a día más feliz, tanto dentro del ICMAB como en nuestros habituales planes: Paula, Guillem, Edu, Simona, Marc, Judit, Nathaly, David, Albert, Ángel, Jose... y a los que ya no están, como Silvia, Adriana, Francesc y María.

Por supuesto me gustaría agradecerle a Toni su apoyo y su paciencia. Me has enseñado y ayudado muchísimo, a pesar de que siempre te hacía las mismas preguntas. Además, aunque vivir dos tesis seguidas no ha sido fácil, siempre has estado ahí para escucharme y animarme. Contigo esta tesis ha pesado un poco menos, así que mil gracias por todo.

Por último, gracias a mi familia por su apoyo incondicional y por esforzarse siempre en entender de qué iba mi trabajo y para qué servía. Si aún tenéis dudas, espero que este libro las resuelva todas.

# Abstract

---

In this thesis we have studied several aspects related to organic field-effect transistors (OFETs) printed from solution, including their fabrication, their electrical characterisation, and further applications, especially in the field of physical sensing. Blends of different p-type small molecule organic semiconductors (OSCs) and insulating polymer binders have been employed in this research work. For the deposition of such blends as active layers for OFETs a scalable solution processing technique has been exploited, namely bar-assisted meniscus shearing (BAMS). The main purpose of the work carried out has been understanding the influence of the fabrication parameters of choice on the morphological and structural features of the resulting active layer and, thus, their impact on the electrical performance of the final devices. A detailed nanoscale study of OSC:insulating polymer thin films has been conducted, elucidating the vertical stratification of both components and its effect on the devices stability and performance. Further, aiming at improving the electrical characteristics of devices exhibiting high contact resistance values, different doping methodologies have been explored. In addition, the morphology-performance relationship has been studied for flexible OFET devices subjected to mechanical strain. Finally, OFETs exhibiting high sensitivity to X-ray radiation have been fabricated by optimising the processing parameters, rationalising how the morphological and transport properties of the active layer determine the sensing capability of such devices.



# List of abbreviations and symbols

---

## Abbreviations

<b>AFM</b>	Atomic force microscopy
<b>BAMS</b>	Bar-assisted meniscus shearing
<b>BGBC</b>	Bottom-gate bottom-contact
<b>BGTC</b>	Bottom-gate top-contact
<b>C8-BTBT</b>	2,7-dioctyl[1]benzothieno[3,2-b][1]benzothiophene
<b>CPD</b>	Contact potential difference
<b>CZT</b>	Cadmium zinc telluride
<b>diF-TES-ADT</b>	2,8-difluoro-5,11-bis(triethylsilylethynyl)anthradithiophene
<b>DT-TTF</b>	dithiophene-tetrathiafulvalene
<b>EGOFET</b>	Electrolyte-gated organic field-effect transistor
<b>F4-TCNQ</b>	2,3,5,6-tetrafluoro-7,7,8,8-tetracyanoquinodimethane
<b>FFM</b>	Friction force microscopy
<b>HOMO</b>	Highest occupied molecular orbital
<b>KPFM</b>	Kelvin probe force microscopy
<b>LUMO</b>	Lowest unoccupied molecular orbital
<b>MOSFET</b>	Metal-oxide-semiconductor field-effect transistor
<b><math>M_w</math></b>	Molecular weight
<b>OFET</b>	Organic field-effect transistor
<b>OSC</b>	Organic semiconductor
<b>PS</b>	Polystyrene
<b>PVD</b>	Physical vapour deposition
<b>R2R</b>	Roll-to-roll
<b>SAM</b>	Self-assembled monolayer
<b>TGBC</b>	Top-gate bottom-contact
<b>TGTC</b>	Top-gate top-contact
<b>TIPS-pentacene</b>	6,13-bis(triisopropylsilylethynyl)pentacene
<b>ToF-SIMS</b>	Time-of-flight secondary ion mass spectrometry
<b>XPS</b>	X-ray photoelectron spectroscopy



## Symbols

<b><math>C</math></b>	capacitance
<b><math>\epsilon</math></b>	strain
<b><math>E_F</math></b>	Fermi energy
<b><math>I_{off}</math></b>	off current
<b><math>I_{on}</math></b>	on current
<b><math>I_{SD}</math></b>	source-drain current
<b><math>I_{SG}</math></b>	source-gate current
<b><math>L</math></b>	channel length
<b><math>\mu_{FE}</math></b>	field-effect mobility
<b><math>N_T</math></b>	density of charge carrier traps
<b><math>on/off</math></b>	on/off current ratio ( $I_{on}/I_{off}$ )
<b><math>R_c</math></b>	contact resistance
<b><math>R_{ch}</math></b>	channel resistance
<b><math>SS</math></b>	subthreshold swing
<b><math>V_{on}</math></b>	switch-on voltage
<b><math>V_{SD}</math></b>	source-drain voltage
<b><math>V_{SG}</math></b>	source-gate voltage
<b><math>V_{th}</math></b>	threshold voltage
<b><math>W</math></b>	channel width

# Contents

---

<b>CHAPTER 1: Introduction and objectives .....</b>	<b>1</b>
1.1 Organic electronics .....	1
1.2 Organic semiconductors .....	4
1.3 Organic semiconductor processing techniques.....	10
1.4 Organic field-effect transistors .....	18
1.5 Organic field-effect transistors in sensing applications .....	30
1.6 Objectives .....	33
1.7 References .....	34
<b>CHAPTER 2: A unified experimental recipe to fabricate from solution state-of-the-art performance OFETs based on OSCs belonging to four different families.....</b>	<b>41</b>
2.1 Introduction and objectives.....	41
2.2 Device fabrication and optimisation of the experimental conditions.....	44
2.3 Thin-film characterisation.....	47
2.4 OFET electrical characterisation .....	53
2.5 Comparison with similar reported devices processed from solution .....	57
2.6 Development of devices for aqueous media operation.....	59
2.7 Summary.....	63
2.8 References .....	64
<b>CHAPTER 3: Role of the vertical phase separation on the performance and stability of OFETs fabricated from organic semiconductor:insulating polymer blends.....</b>	<b>69</b>
3.1 Introduction and objectives.....	69
3.2 Device fabrication and electrical characterisation .....	73
3.3 Morphological characterisation.....	74
3.4 Role of PS in the films shelf-stability .....	79

3.5 Kelvin probe force microscopy in operando OFETs .....	80
3.6 Summary .....	85
3.7 References.....	86
<b>CHAPTER 4: Doping methodologies for the optimisation of the performance of C8-BTBT based OFETs .....</b>	<b>91</b>
4.1 Introduction and objectives .....	91
4.2 Inserting a doping interlayer at the OSC/electrode interface .....	96
4.3 Doping the OSC film by solution-based methodologies .....	107
4.3.1 Adding the dopant molecule in the OSC ink solution .....	107
4.3.2 Superficial exposure of the OSC film to a dopant water solution.....	113
4.4 Summary .....	119
4.5 References.....	120
<b>CHAPTER 5: Mechanical stress response of bendable OFETs and relationship with the thin-film morphology .....</b>	<b>123</b>
5.1 Introduction and objectives .....	123
5.2 Device fabrication and thin-film characterisation .....	127
5.3 OFET electrical characterisation.....	130
5.4 Characterisation upon bending deformation .....	132
5.5 Morphological and local electrical characterisation .....	138
5.6 Summary .....	142
5.7 References.....	143
<b>CHAPTER 6: X-ray sensitivity of OFET based detectors tuned by controlling the processing parameters .....</b>	<b>147</b>
6.1 Introduction and objectives .....	147
6.2 TIPS-pentacene OFETs as X-ray detectors.....	152
6.3 Sensitivity vs. thin-film morphology: controlling the coating speed .....	155
6.4 Sensitivity vs. charge carrier mobility: controlling the TIPS-pentacene:PS ratio.....	158
6.5 Reliability and stability: towards real X-ray sensors .....	165
6.6 Summary .....	169
6.7 References.....	170

<b>CHAPTER 7: Materials and experimental methods</b> .....	175
7.1 Materials .....	175
7.2 OFET fabrication .....	177
7.3 Thin-film characterisation.....	182
7.4 Electrical characterisation .....	184
7.5 Characterisation upon physical inputs .....	186
7.5 References .....	188
<b>CHAPTER 8: Conclusions</b> .....	189
<b>List of publications</b> .....	191



# CHAPTER 1

---

## Introduction and objectives

### 1.1 ORGANIC ELECTRONICS

---

In 1947, the first germanium-based transistor was created by John Bardeen, Walter H. Brattain and William Shockley at Bell Laboratories, which was also home for the fabrication of the first operative silicon-based transistor by Morris Tannenbaum in 1954.<sup>1,2</sup> Since then, transistors have attracted great attention from both the academy and the industry, and its invention is recognised as the most important of the 20<sup>th</sup> century as transistors are considered the building blocks of all modern electronic devices. Indeed, electronic devices are present in almost every aspect of our lives, carrying out the most complex tasks thanks to the realisation of complex and reliable circuits. Although silicon technology dominates the market of modern electronics, not all applications require high-performance microprocessors. On the contrary, for some emerging applications other properties such as low production cost, low power consumption, light-weight or flexibility are more desired. For those applications, the use of organic materials has arisen as an interesting alternative for new electronic devices.

In general, organic materials are molecules and polymers based on carbon (C) and hydrogen (H) atoms in combination with other elements such as nitrogen (N), phosphorus (P), oxygen (O), sulphur (S) as well as halogens or metals. The mechanical, electrical and optical properties of organic materials are of great interest for numerous applications. In particular, their application as electrically active materials was demonstrated in the 1970's by the discovery of the first organic metal, tetrathiafulvalene-tetracyanoquinodimethane (TTF-TCNQ),<sup>3</sup> and the first highly conducting polymer, chemically doped polyacetylene.<sup>4</sup> These achievements led to a huge research interest and promoted the development of a new field called "organic electronics", which includes all the devices where the active component is based on an organic material. On top of the light-weight and flexibility that organic materials offer,<sup>5,6</sup> their compatibility with low-cost printing processes is key for their applicability (**Figure 1.1**).<sup>7-10</sup> The low temperature processability in comparison with

inorganic materials and the possibility of solution processing open the opportunity to fabricate devices on flexible plastic substrates and over large areas.

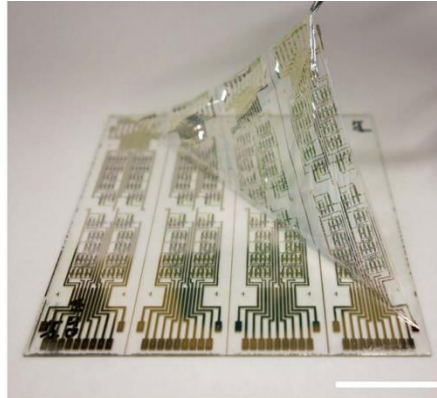


**Figure 1.1.** Photograph of an ultrathin organic CMOS logic circuit. Scale bar: 25 mm. Extracted from ref. 10.

Specifically, organic semiconductors (OSCs) have been implemented in devices for a wide range of potential applications, among which the most studied ones are organic light-emitting diodes, organic solar cells and organic field-effect transistors, which will be briefly discussed in the following.<sup>11</sup> Their basic architecture and operation principle are depicted in **Figure 1.2**.

► **Organic light-emitting diodes (OLEDs)**

OLEDs are, generally speaking, devices that convert current into visible light. Their structure consists of two organic films (one electron transporting layer and one hole transporting layer) sandwiched between two electrodes, so that light emission is stimulated by an electric current. The operation principle behind OLEDs is the emission of light caused by the recombination of the injected holes and electrons, forming excitons (i.e., electron-hole pairs) that decay through the emission of light. The first functional OLED was fabricated in 1987 by Tang et al.<sup>12</sup> and nowadays it is a consolidated technology with commercial products on the market such as RGB digital displays.<sup>13</sup>

► **Organic solar cells or photovoltaic devices (OPVs)**

Organic solar cells are devices devoted for the conversion of sunlight into electrical power. Their structure is similar to OLEDs, although in this case the organic semiconductors are responsible for the light absorption instead of the emission. However, for both technologies at least one of the electrodes must be transparent to visible light to allow light emission or transmission. The physics behind the operation of OPVs is the generation of excitons in the organic material layer which are then dissociated into a free electron and a free hole at the electron-donor/electron-acceptor interface, so that both charge carriers can diffuse to the electrodes generating an electric current. Although organic solar

cells exhibit an acceptable power conversion efficiency, reaching 17%,<sup>14</sup> the main factor currently limiting this technology is the relative low lifetime of these devices.<sup>15</sup>

### ► Organic field-effect transistors (OFETs)

Finally, OFETs can be used as switching or current modulating devices. In this case, the current flowing between two electrodes (source and drain) through an organic semiconductor is modulated by the strong electric field created by a third electrode (gate). More details regarding their operation principle can be found in section 1.4. The first OFET was reported in 1987 by Koezuka et al. employing a conjugated polymer, polythiophene, instead of the inorganic semiconductor traditionally used for field-effect transistors.<sup>16</sup> Nowadays, the performance of the best OFETs rivals that of amorphous silicon transistors (typically  $0.5\text{-}1\text{ cm}^2/\text{V}\cdot\text{s}$ ),<sup>17</sup> and, thus, their implementation in small integrated circuits,<sup>18</sup> radio frequency identification (RFID) tags<sup>19</sup> or chemical and physical sensing devices is being investigated.<sup>20</sup>

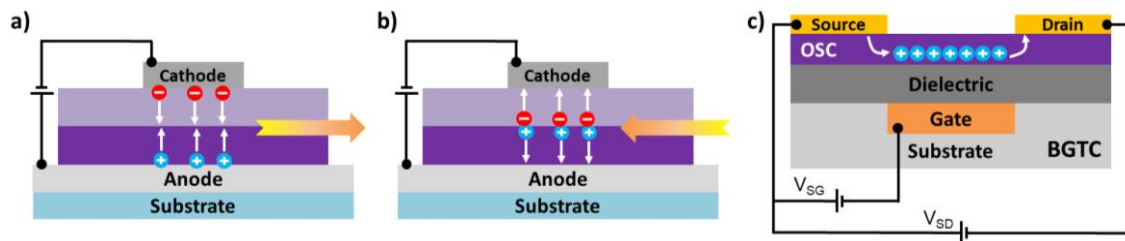


**Figure 1.2.** Schematic illustration of a typical (a) OLED, (b) OPV and (c) p-type OFET structure, including their operation principle.

Since the moment organic electronics was born over four decades ago, the research community invested an intensive effort to develop this new field in order to make possible to fabricate real devices using this technology. To do so, different strategies have been addressed: i) the design and synthesis of new organic semiconductors with improved electrical properties and solubility, ii) the development of new processing methodologies for organic semiconductors compatible with roll-to-roll (R2R) processes aiming at large scale manufacturing, and iii) the investigation of new geometries and structures to fully exploit these materials and overcome their drawbacks. Altogether has resulted in a remarkable improvement of the devices performance, but current research is still focused on understanding the relationship between the organic materials processing, the microstructure and the final performance, as well as the development of new applications.



## 1.2 ORGANIC SEMICONDUCTORS

---

### Organic vs. inorganic semiconductors

Inorganic materials can be classified, from an electrical point of view, as insulators, semiconductor or metals regarding their electrical resistivity ( $\rho$ ), which is an intrinsic property that quantifies how strongly a given material opposes to the flow of electric current. Insulators exhibit high resistivity values, about  $\rho > 10^{10} \Omega\cdot\text{m}$ , while for metals these values are typically below  $10^{-6} \Omega\cdot\text{m}$ . Between these two extreme cases, semiconductors cover a broad range of resistivity values with  $10^{-6} < \rho < 10^6 \Omega\cdot\text{m}$ . Microscopically, inorganic semiconductors consist of atoms such as Si or Ge covalently bonded forming a giant net of atoms, as depicted in **Figure 1.3 (a)**.<sup>21</sup> In this structure individual atomic orbitals fuse forming bands of electronic orbitals that extend along the whole material. These materials are characterised by the existence of a bandgap or energy gap ( $E_g$ ), a forbidden energy range in which allowed states cannot exist, and, thus, this is the energy necessary to promote an electron from the lower valence band to the upper conduction band. However, this bandgap is usually small enough (e.g.  $E_g = 1.12 \text{ eV}$  for Si at atmospheric conditions) to be overcome with thermal energy. Moreover, the bandgap of most inorganic semiconductors decreases with increasing temperature and, as a result of the bigger amount of free charges, macroscopically the electrical resistivity of the material decreases.<sup>22</sup> In addition, inorganic semiconductors can be turned into more efficient semiconductors by the introduction of electron-donor or electron-acceptor dopant atoms into their structure (i.e., extrinsic n- or p-type semiconductors), which also reduces the bandgap. Finally, the unique property that makes semiconductors so interesting is that their conductivity can be tuned upon the influence of an electric field.

Organic materials can also be classified as insulators, semiconductors or metals; however, due to their intrinsic properties, the conductivity values that they exhibit and the transport mechanisms differ strongly from inorganic materials. Organic semiconductors (OSCs) are carbon-based small molecules or polymers rich in  $\pi$ -electrons through which they interact with each other, i.e., van der Waals forces, depending on their supramolecular structure. An example of a molecular crystal based on pentacene is shown in **Figure 1.3 (b)**.<sup>23</sup> In the  $\pi$ -bonds, electrons are delocalised below and above the molecular plane inducing a lowering of the energy gap between the so called highest occupied molecular orbital (HOMO) and lowest unoccupied molecular orbital (LUMO). These can be assimilated with the valence and conduction bands of inorganic semiconductors in the sense that, in the ground state, all the energy levels below the HOMO are fully filled with electrons and all the energy levels above the LUMO are empty. Thus, electron and hole transport take place through the LUMO and HOMO, respectively. Moreover, their energies determine the opto-electronic properties of conjugated organic materials.<sup>11</sup>

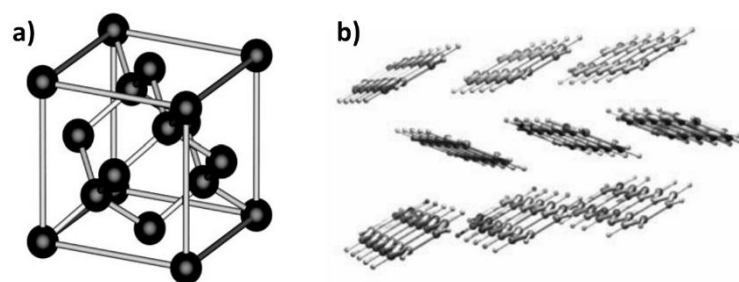


**Figure 1.3.** (a) Diamond crystal structure of silicon. Extracted from ref. 21 (b) Crystal structure of pentacene. Extracted from ref. 23.

As a result of their different nature, the bonding energy in organic materials, that is via van der Waals forces, is significantly lower compared to that of covalent interatomic bonds in inorganic semiconductors. For this reason, while the charge transport in inorganic semiconductors takes place via delocalised states following a band transport, the conductivity in organic materials is determined by the relative position of the  $\pi$ - $\pi$  orbitals and the overlap between them, resulting in lower speeds of electronic transport (i.e., mobility). For example, while high quality polycrystalline silicon displays an electron mobility of  $1450 \text{ cm}^2/\text{V}\cdot\text{s}$  and a hole mobility of  $500 \text{ cm}^2/\text{V}\cdot\text{s}$ ,<sup>22</sup> the best OFET mobility values obtained for benchmark organic semiconductors are in the order of  $10 \text{ cm}^2/\text{V}\cdot\text{s}$ .<sup>17</sup> However, it is important to keep in mind that the goal of organic electronics is not to substitute inorganic electronics in the fabrication of high-performance microprocessors. On the contrary, organic electronics is a field willing to open a path towards new applications that involve the use of plastics and that take advantage of the intrinsic properties of organic materials such as flexibility, low-cost and light-weight.

### Charge transport mechanisms in organic semiconductors

As previously mentioned, charge carrier mobilities found in organic materials are significantly lower compared to their inorganic counterparts. The reason for this is related to the different mechanisms dominating the charge transport. Several different transport mechanisms depending on the degree of charge carrier localisation have been proposed for organic materials ranging from single crystals to amorphous and polycrystalline thin films. However, a theory to fully understand charge transport is still lacking, and so it is difficult to associate a specific mechanism to an OSC system. The most widely used transport models will be described in the following.<sup>11,24,25</sup>

### ► Band transport

In the case of high quality organic crystals, a classic band-like transport is expected due to the strong delocalisation of charge carriers that can travel in extended Bloch-waves through the periodic lattice structure. In band transport, an increase of mobility is expected upon decreasing temperature due to charge scattering processes caused by lattice phonons. Indeed, a highly periodical structure and strong enough intermolecular interactions are required for the band model to be applied. This, however, is not the general case in organic crystalline materials, which include a significant number of structural and chemical defects plus strong lattice vibrations.

### ► Hopping transport

Hopping transport is the most common charge transport mechanism associated to amorphous or highly disordered OSCs. In hopping transport, a high localisation of charge carriers is assumed; thus, a charge carrier would hop from an occupied localised site to an adjacent unoccupied localised site. This mechanism is sometimes explained employing the model introduced by Marcus in 1956, which described the oxidation-reduction reaction between a charged and a neutral molecule in solution.<sup>26</sup> In molecular crystals, however, the charge carrier strongly interacts with the carrying molecule, forming a polaron. As the charged molecule couples to the surrounding ones, inter-molecular displacements and polarisation effects arise, altering the crystalline structure. Thus, transport occurs via inter-site polaron hopping and is controlled by two parameters: i) the electronic coupling or transfer integral ( $J$ ), which indicates the interaction between the HOMOs or LUMOs of two adjacent molecules, and ii) the reorganisation energy ( $\lambda$ ), which takes into account the conformational changes that the molecules suffer due to the acceptance or release of a charge. A potential energy diagram of the charge carrier transfer is shown in **Figure 1.4**.

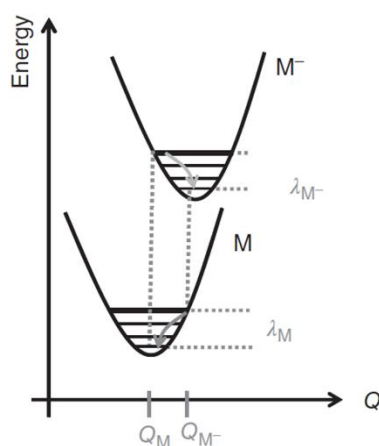


**Figure 1.4.** Schematic of the potential energy curves for a neutral molecule (M) and negatively charged molecule ( $M^-$ ) showing the reorganisation energy associated to the relaxation from the charged to the neutral state ( $\lambda_M$ ), and vice versa ( $\lambda_{M^-}$ ). Extracted from ref. 11.

The mobility of charge carriers in an OSC is proportional to the transfer integral and inversely proportional to the reorganisation energy; thus, it is correlated to the distance and orientation between molecules and to the molecular structure of the OSC. Moreover, the temperature dependence of mobility differs from that of band transport. In this case, the lattice vibrations enhance the movement of the charge carriers by providing the energy necessary to overcome the energetic barrier; hence, hopping charge transport is a phonon-assisted mechanism that can be thermally activated.

#### ► Multiple trapping and release model

In the case of polycrystalline OSCs, in which the crystallites are separated by grain boundaries, the multiple trapping and release model has been proposed. It is based on the assumption that charge carriers travel in narrow, delocalised bands but their motion is disturbed by the high concentration of traps (i.e., localised states within the energy gap) present in the material. These traps may come from chemical impurities, defects of the crystal structure, grain boundaries, etc. As a result, the intrinsic mobility of the perfectly pure and ordered material is hindered by the trapping and release mechanisms, which is also in agreement with the thermally activated behaviour observed in most OSCs. Moreover, the often observed gate voltage dependence of the charge carrier mobility can be described with this model.

#### Organic semiconductor materials

As mentioned, in general, organic semiconductors are electroactive small conjugated molecules or polymers with a strongly  $\pi$ -conjugated system where electrons are delocalised over the whole structure. OSCs can be classified according to their polarity as p-type, n-type and ambipolar OSCs. Firstly, p-type OSCs are electron donor molecules that can be easily oxidised and consequently their HOMO (highest occupied molecular orbital) energy is high, usually around -5.0 eV. On the other hand, n-type OSCs are electron acceptor molecules that can be easily reduced and display low LUMO (lowest unoccupied molecular orbital) energy, around -4.0 eV. In these materials, the majority of charge carriers are holes and electrons, respectively. Finally, in ambipolar OSCs, charge transport of both holes and electrons can take place depending on the electric field applied.

It is worth noting that the HOMO and LUMO energies determine the stability of the semiconductor in ambient conditions, i.e., the resistance to water, oxygen and other harmful agents. The lower intrinsic stability of n-type OSCs and the difficulty of synthesising molecules with such a low LUMO energy are the main factors limiting the progress of n-channel devices; on the contrary, p-type OSCs have been widely studied and

have displayed the best performances.<sup>17,27</sup> The work presented in this thesis is focused on p-type organic semiconductors.

Another distinction can be made regarding the nature of the OSCs: conjugated polymers and small conjugated molecules. In both cases, the conductivity is mainly determined by the relative position of the  $\pi$ - $\pi$  orbitals, and thus the molecular ordering is very important to achieve OFETs with high performance.

Polymer OSCs can be defined as long chains of interconnected electroactive and aromatic groups. These materials cannot be evaporated due to their high molecular weight, however, they are highly compatible with solution processing techniques due to their good solubility in organic solvents and film-forming properties. This is often counter-balanced by a low degree of crystallinity in polymeric films, which in most cases are organised in microcrystalline structures embedded in an amorphous polymer matrix. Probably, the most studied polymer for OFETs has been poly(3-hexylthiophene) (P3HT), shown in **Figure 1.5**, exhibiting a mobility of  $0.1 \text{ cm}^2/\text{V}\cdot\text{s}$ .<sup>28</sup> Since high disorder is the main factor limiting charge transport, molecular design strategies have been exploited in order to increase the structural order of thin films and the resulting performance. For example, OFETs based on the liquid crystal poly(2,5-bis(3-alkylthiophene-2-yl)thieno [3,2-b] thiophene) (PBTTT) (**Figure 1.5**) have led to mobilities as high as  $0.72 \text{ cm}^2/\text{V}\cdot\text{s}$  thanks to the improved crystallinity of the film caused by the better side-chain packing.<sup>29</sup> Another strategy to obtain higher molecular order has been the use of copolymers based on electron-acceptor units combined with electron-donor units, resulting in a significant increase of the performance. An example of a high mobility donor-acceptor copolymer is cyclopentadithiophene-benzothiadiazole (CDT-BTZ) (**Figure 1.5**), which has exhibited mobilities up to  $3.3 \text{ cm}^2/\text{V}\cdot\text{s}$ .<sup>30</sup>

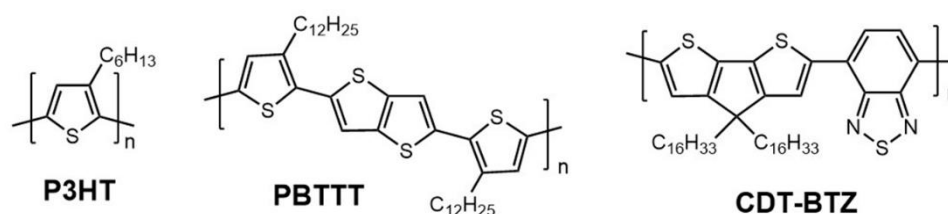


**Figure 1.5.** Chemical structures of conjugated polymer OSCs.

On the other hand, small molecule OSCs can be either thermally evaporated or deposited using solution-based techniques, although they generally show poor solubility.<sup>27</sup> This issue has been mainly addressed by the addition of side groups to the conjugated rigid cores, improving the solubility without compromising the transport properties of the material. Small molecule semiconductors display a higher structural order than polymer OSCs,

forming polycrystalline thin films or single crystals resulting in high field-effect mobilities around  $10 \text{ cm}^2/\text{V}\cdot\text{s}$ .<sup>17</sup> Although higher performances can be achieved in single crystals, they are generally not suitable for large scale manufacturing. In this sense, many advances have been achieved in the solution-processing of high quality thin films based on small molecule OSCs.<sup>7,8,31</sup> Moreover, focus is being placed in understanding the structure-performance relationship. Currently, some of the most widely investigated small molecules are 6,13-bis(triisopropylsilylethynyl) pentacene (TIPS-pentacene), 5,6,11,12-tetraphenyltetracene (rubrene), 2,8-difluoro-5,11-bis(triethylsilylethynyl) anthradithiophene (diF-TES-ADT), 2,9-alkyl-dinaphtho[2,3-b:2',3'-f]thieno[3,2-b]thiophene (C10-DNTT), dibenzo-tetrathiafulvalene (DB-TTF), and 2,7-dioctyl[1]benzothieno [3,2-b][1]benzothiophene (C8-BTBT), shown in **Figure 1.6**.

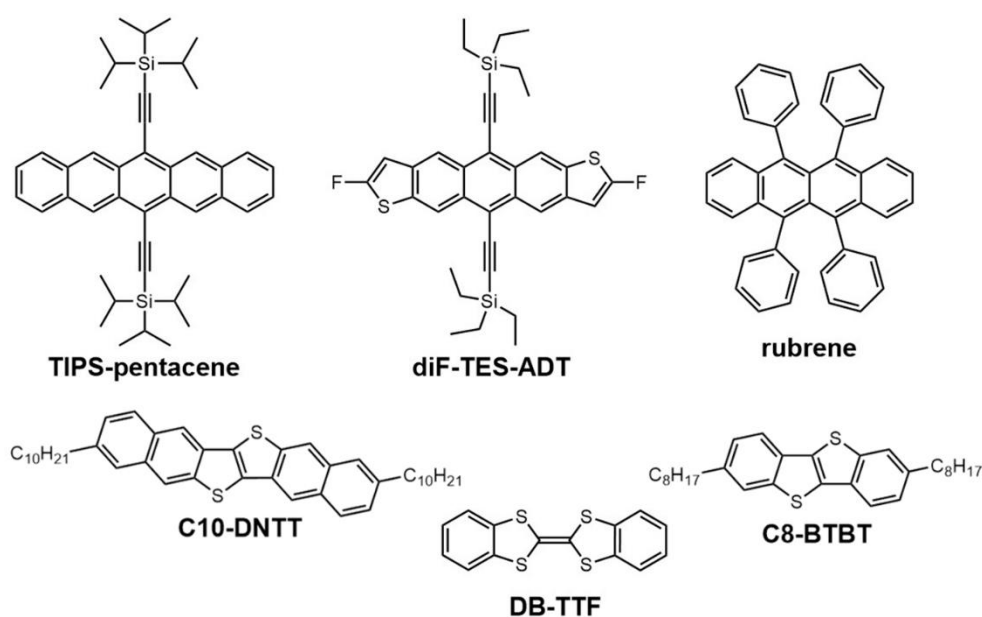


**Figure 1.6.** Molecular structures of small molecule p-type OSCs.

However, achieving uniform thin films using solution processing techniques can be challenging due to the low viscosity of small molecule OSC solutions. A promising strategy to overcome this problem consists in blending the small semiconducting molecule with an insulating polymer binder to improve the material processability. The use of organic semiconductor:insulating polymer blends gives rise to thin films with an increased uniformity and reproducibility, which in turn results in an enhancement of the electrical properties. This approach is key in the work developed in this thesis, and so it will be further discussed in section 1.3.

## 1.3 ORGANIC SEMICONDUCTOR PROCESSING TECHNIQUES

The deposition of the OSC is a fundamental step in the fabrication of organic electronic devices. The processing techniques can be subdivided into two main categories: vapour-phase deposition techniques and solution-based deposition techniques.

### Vapour-phase deposition techniques

Physical vapour deposition or PVD consists in the thermal evaporation of the organic material in high vacuum. In this kind of deposition, the material is typically placed on an alumina boat (highly resistant to the temperature) inside a vacuum chamber with a pressure ranging from  $10^{-6}$  to  $10^{-8}$  mbar.<sup>32</sup> A schematic representation of an evaporation chamber is depicted in **Figure 1.7**. Once the vapour pressure of the heated semiconductor, which increases with the temperature, exceeds the pressure in the chamber, the material starts to evaporate and condense on the target substrate, to which the opening of the boat is directed. In this system, a shutter can be opened and closed to control the amount of material that is deposited, while the rate of deposition is monitored by a quartz microbalance.

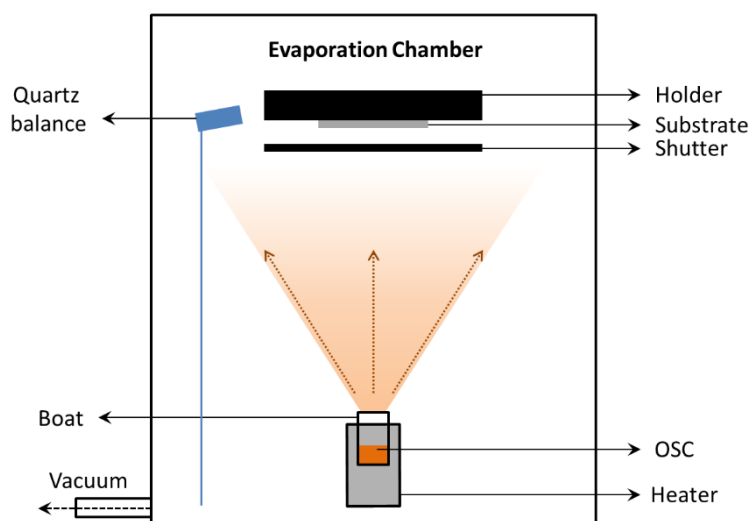


**Figure 1.7.** Schematic representation of a thermal evaporation system.

This process generally results in high quality organic semiconductor films with high control and reproducibility in terms of film thickness. Further, controlling the substrate temperature can have an impact on the final film morphology and crystallinity. In addition,

this method offers the possibility of multilayer deposition and co-deposition of different materials. However, it normally requires expensive equipment and, importantly, it is not suitable for large-area low-cost fabrication.

### Solution-based deposition techniques

Solution processing techniques are generally preferred for the deposition of organic semiconductor thin films due to the cost-effectiveness and their suitability for large-area fabrication.<sup>7,8</sup> In this kind of approach, the OSC material is firstly dissolved into an appropriate organic solvent and then processed on a target substrate. The most common solution-based deposition techniques are drop-casting, spin-coating, dip coating, spray coating, zone casting, blade coating and bar-assisted meniscus shearing, which will be briefly described in the following.

#### ► Drop-casting

Drop-casting is probably the simplest technique for the deposition of organic semiconductors. It consists in depositing a drop of the OSC solution on the substrate and allowing the solvent to evaporate.<sup>33</sup> A schematic representation of drop casting is shown in **Figure 1.8**. In order to completely dry the material, and also to improve the crystallinity, this process is commonly followed by a thermal annealing. Drop-casting is traditionally used to obtain single crystals of organic semiconductors but its potential is limited due to the lack of control and reproducibility, and the impossibility of being applied in large scale.

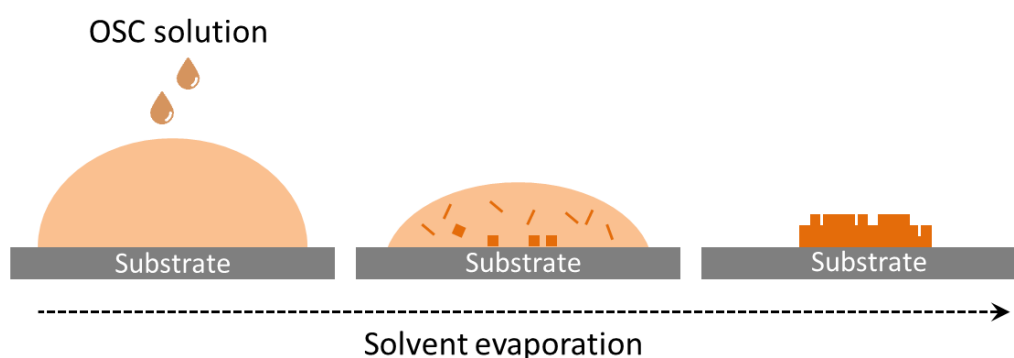


**Figure 1.8.** Schematic representation of the drop-casting technique.



### ► Spin-coating

Spin-coating is one of the most commonly used techniques for the deposition of organic semiconductor thin films at laboratory scale, since it is simple and quick and does not require complex equipment.<sup>34</sup> The procedure consists in dropping an OSC solution on the substrate and subsequently spinning the sample at high speed, as depicted in **Figure 1.9**. In this method, the rotation spreads the solution ejecting the excess and also drying the thin film, giving uniform coverage. The thickness of the resulting film is known to be dependent on the solution employed (i.e., concentration and viscosity) and also on the working parameters of the spin-coater (mainly the angular speed). Although this technique is widely used for research purposes, it cannot be up-scaled and therefore is not suitable for large-area applications.

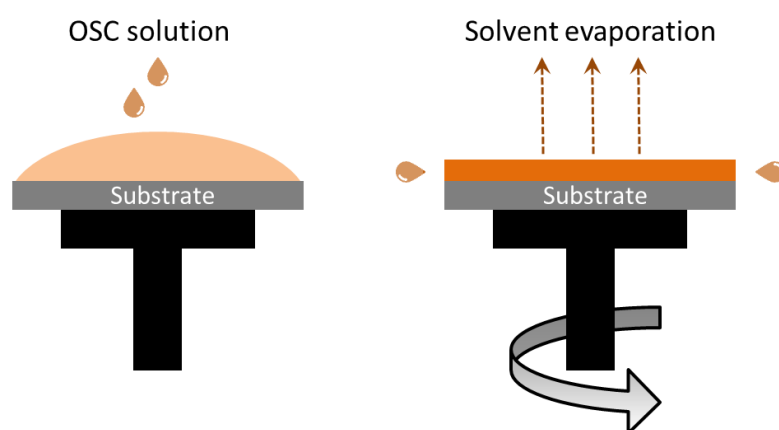


**Figure 1.9.** Schematic representation of the spin-coating technique.

### ► Dip coating

Dip coating is another laboratory scale technique that consists in the immersion of a substrate in a OSC solution followed by its controlled vertical withdrawal at low speed, as shown in **Figure 1.10**. This method results in uniform thin organic layers with a thickness determined by the speed at which the substrate is removed from the solution and the properties of the solution (i.e., its boiling point and concentration). Dip coating is suitable for covering large areas and can be easily up-scaled; however, one of its drawbacks is the need of large volumes of solution, increasing the cost of production.<sup>35</sup>

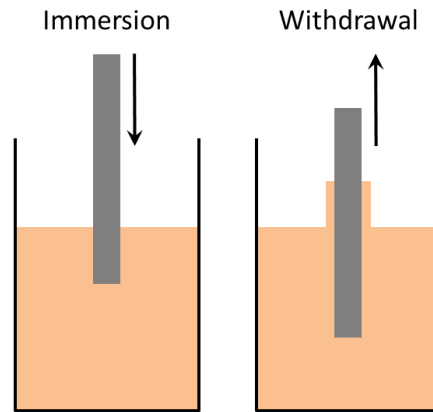


**Figure 1.10.** Schematic representation of the dip coating technique.

### ► Spray coating

Spray coating is based on the vaporisation of an OSC solution due to the high pressure of a gas carrier, usually  $N_2$ , and the deposition of these small droplets on a target substrate, as depicted in **Figure 1.11**. In this technique there are many parameters that can be controlled and that have an impact on the film thickness and morphology, such as the gas carrier pressure, the choice of solvent, the solution viscosity, the nozzle geometry, the nozzle-substrate distance and the substrate temperature.<sup>36</sup> This technique is widely employed at industrial scale since it can be used to cover large areas and it is versatile in terms of target materials (i.e., glass, metal and plastic substrates). However, the resulting films show higher roughness compared to other solution-based techniques.

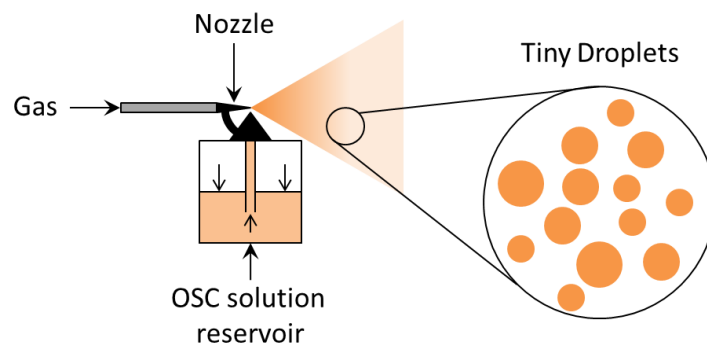


**Figure 1.11.** Schematic representation of the spray coating technique.

### ► Zone casting

Zone casting consists in the continuous deposition of an OSC solution by a flat nozzle on a moving substrate, as shown in **Figure 1.12**.<sup>37</sup> The solvent evaporation from the meniscus zone can be controlled by adjusting the temperature of the substrate, while the final thickness and crystalline quality of the film are determined by the supply rate of the solution, its concentration and the speed of the substrate. Although this technique is suitable for large scale manufacturing, it has some disadvantages such as the slow deposition speed ( $< 1$  mm/s) and that it leads to highly anisotropic films.

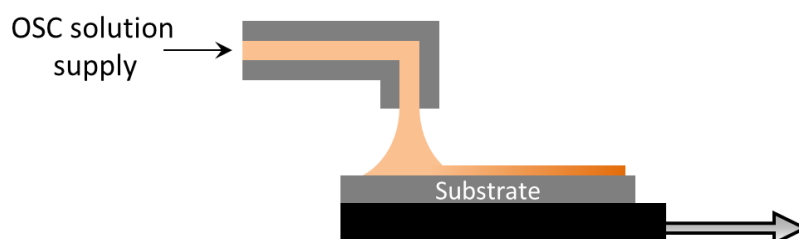


**Figure 1.12.** Schematic representation of the zone casting technique.

### ► Blade coating

Blade coating consists in the controlled spreading of an OSC solution, previously deposited onto a substrate, by a blade (**Figure 1.13**). The horizontal movement of either the substrate or the blade leaves a uniform wet film, and the evaporation of the solvent can be assisted by heating the substrate. Importantly, the distance between the substrate and the blade determines the amount of solution that remains on the substrate and therefore, together with the solution concentration, it controls the film thickness. This technique can be used in a similar manner if the blade is changed for a wired bar in direct contact with the substrate (known as wire coating). Some important advantages of blade coating are that the coating speed can be potentially very high, reaching values of tens of cm/s, and that it can be adapted to roll-to-roll deposition processes, which is of high interest for large scale production.<sup>38</sup>

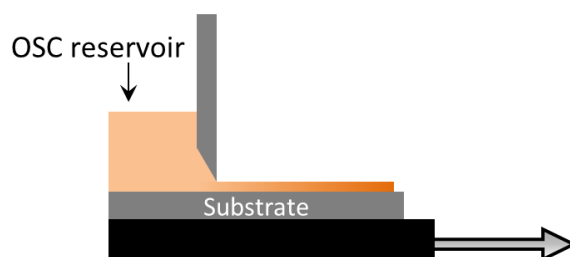


**Figure 1.13.** Schematic representation of the blade coating technique.

### ► Bar-assisted meniscus shearing

Bar-assisted meniscus shearing (BAMS) is a variant of the traditional blade coating, and differs from it mainly because it is based on the formation of a liquid meniscus between the substrate and a rounded bar. It consists in pouring an OSC solution in the gap between a substrate placed on a hot plate and a metallic bar forming a confined meniscus; this meniscus is subsequently dragged due to the horizontal movement of the bar (or the substrate) at a constant speed, leaving a dry uniform thin film behind.<sup>39</sup> This process is schematically depicted in **Figure 1.14**. BAMS can be classified among the meniscus-guided techniques, which have demonstrated to be able to deposit high quality OSC thin films at speeds compatible with roll-to-roll processes.<sup>40</sup> It has been developed in our research group and was firstly optimised to process from solution the small semiconducting molecule dibenzo-tetrathiafulvalene (DB-TTF) blended with polystyrene (PS), which resulted in highly crystalline films as shown in the inset in **Figure 1.14**. BAMS will be widely exploited in this thesis for the deposition of organic semiconducting thin films.

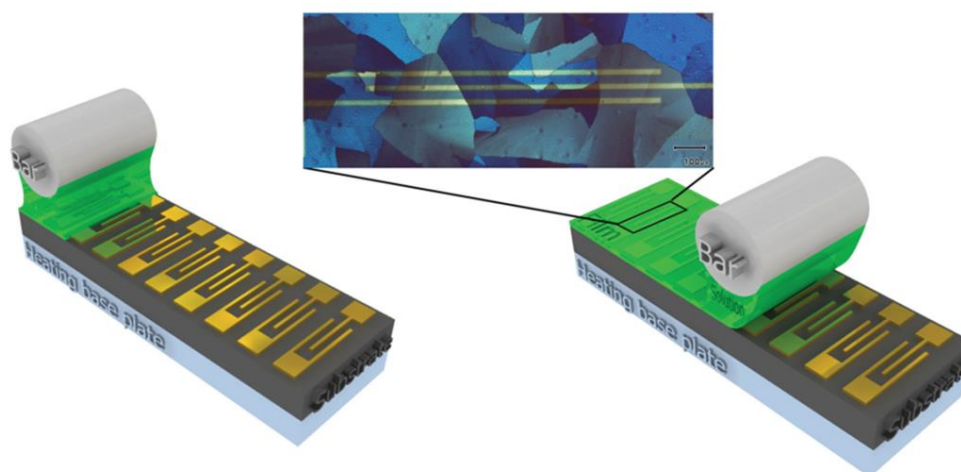


**Figure 1.14.** Schematic representation of the BAMS technique. Extracted from ref. 39.

In this technique, the thickness of the resulting organic layer depends on the viscosity of the solution, its surface tension, the surface energy of the substrate, and the speed of the bar/substrate movement, among others. Moreover, the temperature of the substrate, which can be adjusted according to the solvent employed in order to ensure its immediate evaporation, also plays a role on the film formation. The crystallisation of the organic semiconductor is thus controlled by the concentration of the OSC solution, the solvent evaporation rate and the substrate surface that can act as a nucleation agent.<sup>41</sup> All these parameters can be finely tuned to adapt the deposition process to different organic semiconductor materials and substrates. Furthermore, the simplicity of BAMS coating technique and the lack of any post-coating treatments make it really attractive for processing OSC thin films of high crystallinity and on large areas.

## Deposition of organic semiconductor:insulating polymer blends

Small molecule organic semiconductor thin films deposited by solution processing techniques often exhibit poor uniformity. To overcome this problem, the strategy of blending small semiconducting molecules with insulating polymers is commonly employed as it facilitates tuning the material processability and the thin-film properties.<sup>42,43</sup> This approach also provides additional advantages such as a lower manufacturing cost (by reducing the amount of semiconductor), a higher reproducibility and an improved crystallisation. Indeed, mixing both components in the ink solution can lead to structural and morphological changes. On one hand, the addition of the binding polymer increases the solution viscosity, resulting in thin films displaying more homogeneous morphologies with larger crystal domains. On the other hand, it has been demonstrated for various benchmark OSCs such as diF-TES-ADT, C8-BTBT or DB-TTF blended with polystyrene (PS) that in this kind of thin films a vertical phase separation driven by the crystallisation of the OSC takes place; thus, a crystalline semiconducting layer is formed on top of a polymer layer (see **Figure 1.15 (a-b)**).<sup>34,44–46</sup> This underlying polymeric layer confers stability to the OSC and improves the performance of the final device by reducing the direct contact of the OSC with the substrate, which usually consist in a dielectric such as SiO<sub>2</sub>.<sup>47</sup> The passivation of the polar surface prevents the dewetting of the organic film and reduces the density of interfacial charge carrier traps.

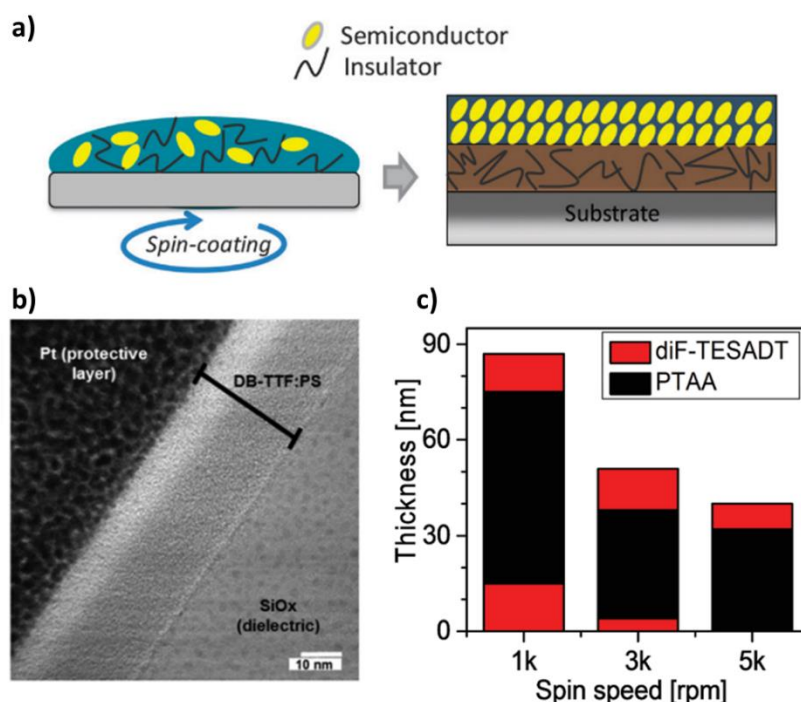


**Figure 1.15.** (a) Schematic representation of the phase separation observed in small molecule OSC:insulating polymer blends. Extracted from ref. 34. (b) Energy-filtered transmission electron microscopy image of a DB-TTF:polystyrene thin-film cross section. Extracted from ref. 46. (c) Thickness and vertical stratification of diF-TES-ADT and PTAA components in thin films spin-coated at different speeds. Extracted from ref. 49.

In addition to blend systems of OSCs and insulating polymers, which show excellent film formation characteristics, blends employing semiconducting polymers have also been reported with remarkable electrical results. For example, Anthopoulos et al. have reported thin films based on diF-TES-ADT and the conjugated polymer PTAA with morphology independent hole transport properties attributed to the formation of highly conductive grain boundaries, as they confirmed by conductive atomic force microscopy measurements.<sup>48</sup>

Of course, there are several parameters that have a strong impact on the crystallisation of the small molecule OSC when it is deposited from organic semiconductor:polymer blends such as the solvent choice, the weight ratio, the molecular weight and nature of the polymer, and the deposition technique, among others. Moreover, the deposition parameters can also affect the vertical stratification as demonstrated for diF-TES-ADT based blends spin-coated at different speeds (**Figure 1.15 (c)**).<sup>49</sup>

## 1.4 ORGANIC FIELD-EFFECT TRANSISTORS

An organic field-effect transistor (OFET) is a three terminal device in which the charge carrier density in the organic semiconductor layer, and thus the current flowing from the source to the drain electrodes, can be tuned by the application of a voltage at the gate electrode (see **Figure 1.2 (c)**). The gate electrode is isolated from the OSC by a dielectric arranged in a metal/insulator/semiconductor architecture so that an accumulation of charge carriers at the OSC/dielectric interface is induced by the generated electric field, creating a conductive channel.<sup>32</sup> It is important to note that in these devices only the first few monolayers of organic semiconductor are turned conductive allowing charge transport to take place.<sup>50</sup>

### Device geometries

OFETs can be assembled into four different geometries, as depicted in **Figure 1.16**. These architectures are called (a) bottom-gate bottom-contact (BGBC), (b) bottom-gate top-contact (BGTC), (c) top-gate bottom-contact (TGBC) and (d) top-gate top-contact (TGTC) depending on the position of the source/drain contacts and the gate electrode with respect to the OSC layer.<sup>51</sup>

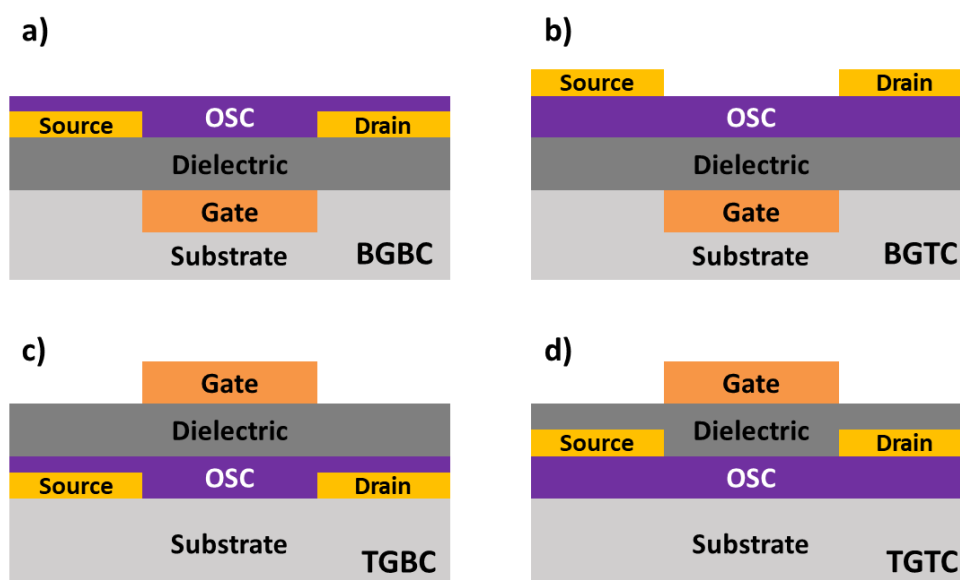


**Figure 1.16.** (a) Bottom-gate bottom-contact (BGBC), (b) bottom-gate top-contact (BGTC), (c) top-gate bottom-contact (TGBC) and (d) top-gate top-contact (TGTC) OFET geometries.

There are some differences in the effect the device architecture has on the OFET performance. Firstly, it is expected that BGBC and TGTC devices display higher contact resistance due to the limited contact area between the channel of the organic semiconductor and the source injecting electrode. On the other hand, in TC configurations metal electrodes are commonly evaporated through a shadow mask as a final step; in this case, the penetration of metal atoms into the OSC layer upon this process usually reduces the contact resistance as the total metal/OSC interface is increased, resulting in a better charge injection. Furthermore, TG configurations encapsulate the device, improving the stability of the organic semiconductor towards harmful agents present in air.<sup>52,53</sup>

The employed OFET geometry also determines the order of the processing or deposition steps; hence, their advantages and disadvantages must be considered prior to OFET fabrication. For example, BGBC architecture is the common choice when an easy and fast processing is required, since the deposition of the semiconducting thin film is the last fabrication step. This allows testing novel OSC materials or optimising the deposition of organic layers in a time-effective way by employing a fixed platform. In addition, bottom electrodes are also amenable to work-function modification by self-assembled monolayers (SAMs), which help mitigate charge injection issues. However, it should be taken into account that if the crystallisation of the organic material is sensitive to the different surfaces of the underlying structure (i.e., the electrodes, the dielectric, or their chemically modified surface), the deposition process can result in different OSC morphologies on the different areas of the device. Moreover, height steps have also to be considered, since a good connectivity between crystals is required to achieve good electrical performance. In contrast, when a BGTC configuration is employed, the OSC is deposited on top of the dielectric layer and source/drain deposition is performed afterwards. In this configuration the thin organic layer is more homogenous and smooth, which is usually beneficial for the 2D conduction at the OSC/dielectric interface; however, in this case the sensitive OSC layer is exposed to potential damage from top contact evaporation.

Among all the previously mentioned architectures, the most used ones in this thesis have been the BGBC and BGTC.

### Operation principle and main device characteristics

The operation principle of an organic field-effect transistor is based on the ability to modulate the conductivity of the organic semiconductor by the application of a gate voltage. To explain this effect a simplified electronic energy level diagram is shown in **Figure 1.17 (a)**, which reflects the HOMO and LUMO of an organic semiconductor relative to the Fermi levels of the source/drain electrodes (determined by the work-function of



the metal).<sup>51</sup> Here, since no source-gate voltage ( $V_{SG}$ ) is applied, there are no mobile charges, and in an ideal device there will be no charge transport upon applying a source-drain voltage ( $V_{SD}$ ). Considering a p-type semiconductor, the majority charge carriers (i.e., holes) can be accumulated in the OSC/dielectric interface by applying a negative  $V_{SG}$  (**Figure 1.17 (b)**). Due to the negative  $V_{SG}$  the HOMO and LUMO energies shift upwards, so that the HOMO becomes closer to the Fermi energy ( $E_F$ ) of the source electrode. Indeed, if the gate electric field is large enough, the HOMO becomes resonant with the  $E_F$  of the electrode allowing the injection of holes and a current flow from source to drain ( $I_{SD}$ ) upon applying a negative  $V_{SD}$  (**Figure 1.17 (c)**). In the case of an n-type semiconductor, the situation is reversed: electrons are the majority charge carriers, injection and conduction are related to the LUMO, and to achieve charge accumulation and current flow positive voltages ( $V_{SG}$  and  $V_{SD}$ ) must be applied (**Figure 1.17 (d-e)**).

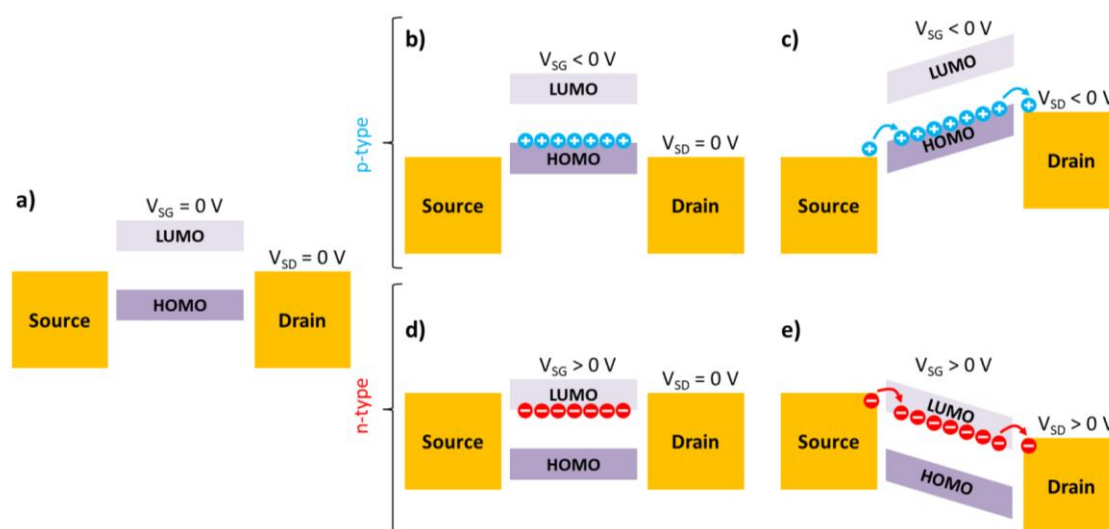


**Figure 1.17.** Schematic illustration of the working principle of an OFET. (a) Ideal device in off-state, when no  $V_{SD}$  and  $V_{SG}$  are applied. (b) Shift of the HOMO/LUMO, due to negative  $V_{SG}$  and accumulation of holes near the OSC/insulator interface. (c) Hole transport upon applying a negative  $V_{SD}$ . (d) Shift of HOMO/LUMO due to positive  $V_{SG}$  and accumulation of electrons near the OSC/insulator interface. (e) Electron transport due to positive  $V_{SD}$ .

It can be easily observed that the alignment of the  $E_F$  of the metal electrodes with the HOMO or the LUMO energies of the p-type or n-type OSC, respectively, is a key factor to achieve an efficient charge injection in the material and, thus, to obtain high performing devices. However, the above description of an OFET operation and the charge transport mechanisms is rather simplified. To study real devices in a quantitative way this model is too simple and other effects should be taken into account. Charge trapping, for example, can be caused by chemical or structural defects in the OSC or at the OSC/dielectric interface, and significantly affects the OFET performance. Contact resistance, on the other

hand, arises due to a mismatch between the metal and the semiconductor energy levels, and can also limit the device performance.

To describe the current-voltage characteristics of an OFET mathematically, Horowitz et al. developed a simple comprehensive model based on the metal-oxide-semiconductor field-effect transistors (MOSFETs) theory of traditional inorganic electronics.<sup>54</sup> This model is based on three assumptions that are not strictly correct for most OFETs and hence should be applied with caution: i) the charge carrier mobility ( $\mu$ ) is assumed to be constant within the range of operation; ii) the parasitic contact resistance between the electrodes and the organic semiconductor are not considered; iii) the electric field perpendicular to the channel (created by the gate electrode) is significantly stronger than the one parallel to the channel (caused by the source and drain electrodes), known as the gradual channel approximation.

In this model the OFET operates in two distinct regimes, according to the flow of charge carriers dependency with the potential difference in the three electrodes. The so-called linear regime can be defined as the regime where  $|V_{SD}| \ll |V_{SG} - V_{th}|$ . In this regime the source-drain current ( $I_{SD}$ ) increases linearly with  $V_{SD}$  as described by the following equation:

$$I_{SD,lin} = \mu_{FE,lin} \cdot \frac{W \cdot C}{L} \cdot \left[ (V_{SG} - V_{th}) \cdot V_{SD} - \frac{V_{SD}^2}{2} \right] \quad (1.1)$$

where  $I_{SD,lin}$  is the source-drain current in the linear regime,  $\mu_{FE,lin}$  is the field-effect mobility in the linear regime,  $C$  is the dielectric capacitance per unit area,  $W$  and  $L$  are the channel width and length, respectively, and  $V_{th}$  is the threshold voltage.

The other regime is called saturation regime and can be defined as the regime where  $|V_{SD}| \gg |V_{SG} - V_{th}|$ . In this regime  $I_{SD}$  reaches a value independent on  $V_{SD}$  (i.e., current saturates) as described by the following equation:

$$I_{SD,sat} = \mu_{FE,sat} \cdot \frac{W \cdot C}{2 \cdot L} \cdot (V_{SG} - V_{th})^2 \quad (1.2)$$

where  $I_{SD,sat}$  and  $\mu_{FE,sat}$  are the source-drain current and the field-effect mobility in the saturation regime, respectively.

In an OFET basically two different device characteristics are measured. On one hand, the output characteristics are obtained when the  $I_{SD}$  is measured sweeping the source-drain voltage ( $V_{SD}$ ) at constant gate voltages ( $V_{SG}$ ), as depicted in **Figure 1.18 (a)**. On the other hand, the transfer characteristics are obtained by measuring  $I_{SD}$  as a function of  $V_{SG}$  at constant  $V_{SD}$ , as shown in **Figure 1.18 (b)**. Transfer characteristics are commonly plotted

in semilogarithmic scale, since the OFET current can vary over several orders of magnitude (**Figure 1.18 (c)**).

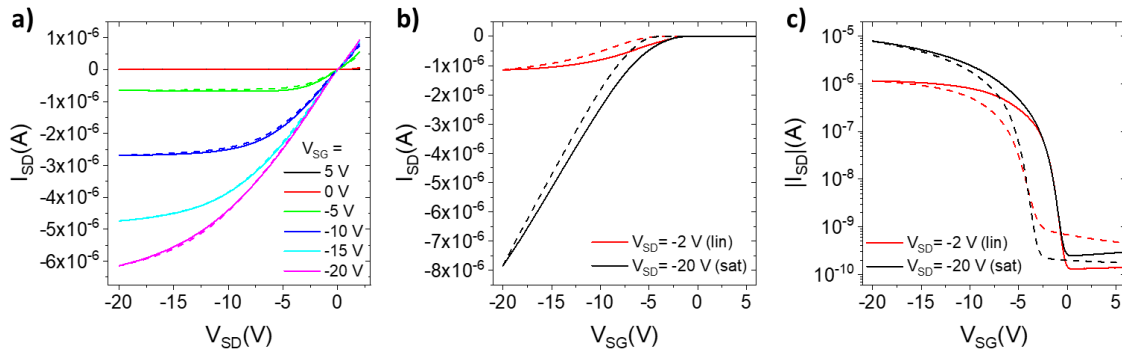


**Figure 1.18.** Typical current voltage characteristics of a p-type OFET. (a) Output characteristics. Transfer characteristics in (b) lin-lin scale and (c) log-lin scale. Straight and dashed lines correspond to forward and reverse sweeps, respectively, for both output and transfer characteristics.

### OFET parameters

The electrical performance of OFETs can be characterised by many parameters that are normally extracted in order to evaluate, and compare, device quality and performance. In the following, the most important OFET parameters, as well as their extraction, will be described.<sup>55</sup>

#### ► Field-effect mobility

The mobility of a material ( $\mu$ ) quantifies the ease with which charge carriers move inside the material when an electric field is applied. At low electric fields,  $E$ , the average drift velocity of the charge carriers,  $v$ , is linearly dependent on the field magnitude and so the material mobility is given by:

$$\mu = \frac{|v|}{|E|} \tag{1.3}$$

From this equation it can be derived that the units for mobility are  $\text{cm}^2/\text{V}\cdot\text{s}$ . However, it should be noted that at high electric fields this linear relationship is no longer valid.

The key parameter in OFET devices is the field-effect mobility ( $\mu_{FE}$ ). In an ideal case, the field-effect mobility extracted from the OFET characteristics and the intrinsic material mobility would be the same; however, real devices usually display lower mobility values due to the presence of defects, contact resistance and traps. This value is, thus, a device

parameter rather than a material intrinsic property. In fact, different  $\mu_{FE}$  values can be extracted for devices based on the same OSC but processed differently or employing different device configurations. Although comparisons between devices are not straightforward, the field-effect mobility is the most important figure of merit in order to evaluate the performance of OFETs. It can be calculated in the linear regime and in the saturation regime from the corresponding transfer characteristics.

In the linear regime,  $\mu_{FE}$  can be extracted using the following equation:

$$\mu_{FE,lin} = \frac{L}{W \cdot C \cdot |V_{SD}|} \cdot \left( \frac{\partial I_{SD,lin}}{\partial V_{SG}} \right)_{V_{SD}=const} \quad (1.4)$$

By plotting  $I_{SD,lin}$  vs.  $V_{SG}$ , calculating the slope of the curve through a linear fit, and subsequently introducing such slope in **Equation 1.4** a mean value for the device mobility in linear regime can be obtained. Another strategy consists in calculating the derivative of  $I_{SD,lin}$  vs.  $V_{SG}$  to obtain  $\mu_{FE,lin}$  vs.  $V_{SG}$ , which provides some additional information of the gate voltage dependence of the mobility. In an ideal case, the mobility should be independent of the gate voltage.

In the saturation regime,  $\mu_{FE}$  can be extracted using the following equation:

$$\mu_{FE,sat} = \frac{2 \cdot L}{W \cdot C} \cdot \left( \frac{\partial \sqrt{|I_{SD,sat}|}}{\partial V_{SG}} \right)_{V_{SD}=const}^2 \quad (1.5)$$

By plotting the square root of the absolute value of  $I_{SD,sat}$  vs.  $V_{SG}$ , extracting the slope of the curve through a linear fit and then introducing this slope in **Equation 1.5** a mean value for the device mobility in saturation regime can be obtained. Such parameter extraction is shown in **Figure 1.19**. Again, the dependence of the mobility with respect to the gate voltage,  $\mu_{FE,sat}$  vs.  $V_{SG}$ , can be evaluated calculating the derivative instead of the slope.

#### ► Threshold voltage and switch-on voltage

In conventional MOSFETs the threshold voltage ( $V_{th}$ ) is an important parameter needed for circuit design, and is defined as the onset of strong inversion. Although, most OFETs operate in the accumulation regime and no source-drain current is observed in the inversion regime, the term threshold voltage is generally used for OFETs to quantify the gate voltage at which current begins to flow (i.e., the onset of charge carrier accumulation). A widely used method to extract the  $V_{th}$  in the saturation regime consists in plotting the square root of the absolute value of  $I_{SD,sat}$  vs.  $V_{SG}$ . For an ideal device, a straight line will be obtained in this plot, whose intercept point with the  $V_{SG}$  axis is the

threshold voltage (see **Figure 1.19**). However, in real devices  $|I_{SD,sat}|^{1/2}$  vs.  $V_{SG}$  commonly deviates from linearity mostly due to the gate voltage dependence of the mobility. As a result, this method depends strongly on the range used to perform the linear fit and is purely empirical.

The switch-on voltage ( $V_{on}$ ) is another parameter that can be used to determine when a transistor turns on. In other words, this parameter defines when the accumulation channel starts to form, which can be clearly seen when the absolute value of the source-drain current,  $|I_{SD,sat}|$ , is plotted versus  $V_{SG}$  in semilogarithmic scale (see **Figure 1.19**). In this plot, the switch-on voltage can be extracted as the voltage at which the current starts to increase with the gate voltage. In an ideal OFET, there should be no difference between the threshold voltage and the switch-on voltage and both should be zero.

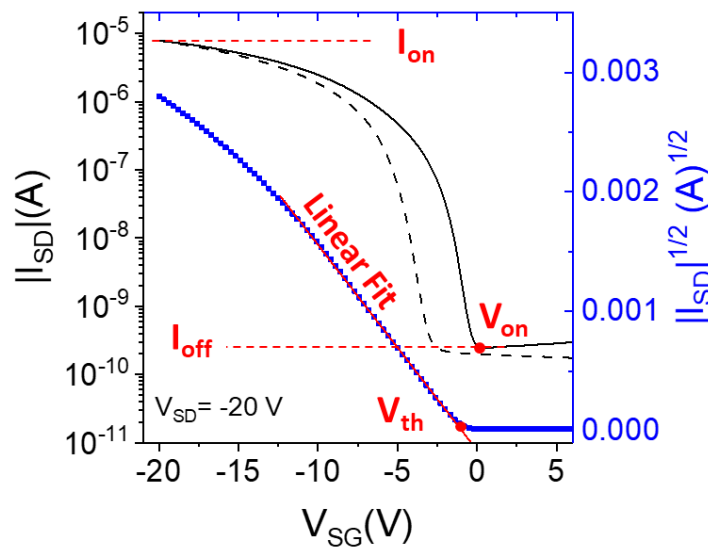


**Figure 1.19.** OFET parameters extraction shown in a typical transfer curve measured in the saturation regime.

#### ► On/off current ratio

The on current ( $I_{on}$ ), seen as the maximum source-drain current measured for an OFET in on state, should be as high as possible for high performing devices. This parameter depends strongly on the device geometry, the OSC mobility and the dielectric capacitance. The off current ( $I_{off}$ ), on the other hand, should be as low as possible since it reflects the quality and the purity of the active material. Thus, the *on/off* ratio is another important device parameter which provides information about the switching efficiency and current amplification capability of OFETs. Strictly speaking, only *on/off* values extracted at the same  $V_{SG}$  and  $V_{SD}$  should be compared. In **Figure 1.19** these parameters are evidenced.

### ► Subthreshold swing

The subthreshold region is the region in the transfer characteristics where the gate voltage is below the threshold voltage ( $V_{SG} < V_{th}$ ). This region is important since it provides information on the effectiveness of the charge accumulation process upon the application of a gate voltage. The subthreshold swing ( $SS$ ) is a parameter that quantifies how sharply an OFET turns on, and it is defined as the voltage necessary to increase the source-drain current one order of magnitude.

$$SS = \left( \frac{\partial \log|I_{SD}|}{\partial V_{SG}} \right)^{-1} \quad (1.6)$$

Thus, the subthreshold swing is usually expressed in V/dec.

It should be noted that a small value of  $SS$  indicates that it is possible to switch on the device within a small voltage, reducing the power consumption of the final device. Moreover, a small subthreshold swing also points towards a low density of charge carrier traps ( $N_T$ ) and, thus, it is a good indicator of the OSC/dielectric interface quality.<sup>44,56,57</sup> Indeed, the following equation correlates both parameters:

$$N_T \approx \frac{C}{q^2} \cdot \left[ \frac{q \cdot SS}{k_B \cdot T \cdot \ln(10)} - 1 \right] \quad (1.7)$$

where  $q$  is the electron charge,  $k_B$  is the Boltzmann constant, and  $T$  is the temperature.

### Detrimental effects of the device performance

The device performance, regarding all the previously described parameters, is usually optimised taking care of the OSC crystallisation, the choice of the dielectric and the electrodes material, and their interface with the semiconductor layer. However, when this optimisation is not completely accomplished, some undesirable effects can be observed in the OFET characteristics, which are mainly related to charge trapping and charge injection issues.

### ► Trapping of charge carriers and hysteresis effects

Hysteresis is a memory effect that can be observed in the OFET characteristics as a looping in the source-drain current between forward and reverse  $V_{SG}$  sweeps and is commonly caused by charge trapping, reducing the overall performance of the transistor. As it was mentioned before, even the purest organic single crystals have a certain number of structural defects and chemical impurities. In addition, in order to obtain high

performance devices, it is important to fabricate transistors with well-formed OSC/dielectric and OSC/electrode interfaces to avoid defects at those interfaces that can lead to traps sites where charge carriers will be highly localised.

Further, organic materials are often not stable under ambient conditions, where moisture and oxygen act as dopants increasing the number of charges within the active material. This also results in a hysteresis effect in the  $I_{SD}$  curves, although in this case it is generally also accompanied by a general degradation in time (i.e., current and threshold voltage variations).

All in all, it should be taken into account that extraction of OFET parameters, such as mobility or threshold voltage, in the presence of hysteresis is a sensitive matter.

### ► Contact resistance

The contact resistance is the electrical resistance given by the electrodes/OSC interface, a factor that can considerably limit charge injection and, hence, the overall OFET performance.<sup>58</sup> Indeed, the lowest width-normalised contact resistance ( $R_C \cdot W$ ) values reported for OFETs with solution-processed semiconductors is around  $\sim 1\text{-}10 \text{ k}\Omega \cdot \text{cm}$ , which is several orders of magnitude higher than that of Si MOSFETs ( $\sim 0.1 \text{ }\Omega \cdot \text{cm}$ ).<sup>59</sup> As it was already mentioned, to have an efficient charge injection the HOMO/LUMO energies of the semiconductor must be aligned with the work-function of the metal electrodes. If these levels are not aligned an energy barrier will be formed, preventing the correct injection of charges into the channel.

The total resistance of a transistor ( $R$ ) can be described as the sum of the channel resistance ( $R_{ch}$ ) and the contact resistance ( $R_C$ ):

$$R = R_{ch} + R_C \quad (1.8)$$

For the contact resistance, both the injecting and the extracting electrodes, that is source ( $R_{C,source}$ ) and drain ( $R_{C,drain}$ ), must be considered. Moreover, contact resistance not only depends on the charge injection/extraction processes taking place at electrodes/OSC interface ( $R_{int}$ ), but also on the transport through an OSC bulk region with low conductivity towards the accumulation channel ( $R_{bulk}$ ). Thus, in staggered devices (i.e., with BGTC or TGBC architectures) the semiconductor layer thickness should be carefully chosen. A very simple scheme of contact and channel resistances in a BGTC OFET is shown in **Figure 1.20**.

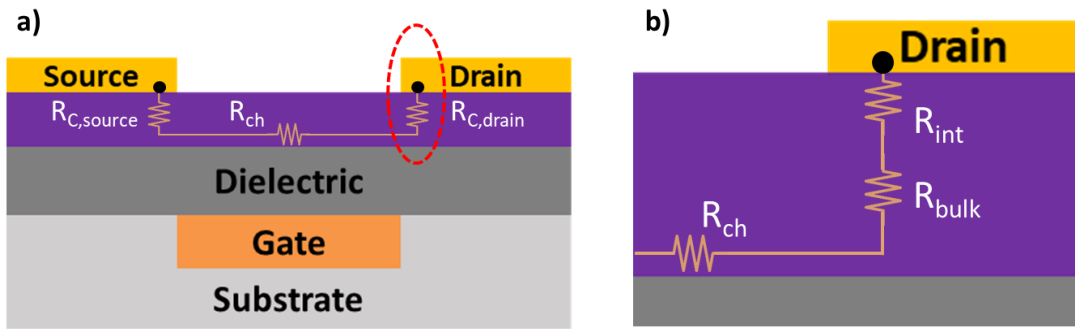


**Figure 1.20.** (a) Scheme of contact and channel resistances in a bottom-gate top-contact OFET. (b) Closer look showing the contribution of the interface and bulk resistance.

To obtain OFETs with an ideal performance it is important that the contact resistance is not significant compared to the channel resistance, which is usually referred to as ohmic contacts. In fact, since  $R_{ch}$  scales with channel length but  $R_C$  is independent of  $L$ , in short channel devices the contact resistance starts to dominate and the performance can be strongly degraded. For example, when the contact resistance is non-linear with the drain voltage, output characteristics typically show low linearity at all low  $V_{SD}$ . Moreover, the improvement of the conducting properties of OSCs has opened the discussion about the high importance of the contact resistance in OFETs, since gate voltage dependency can lead to the overestimation of field-effect mobility values.<sup>31,60,61</sup>

Different methods can be employed in order to extract the contact resistance by electrically measuring one or several OFETs, among which the most common ones are the Y-function method, the transfer-length method (TLM) and the four-point probe method (summarised in **Figure 1.21**). In addition, Kelvin probe force microscopy (KPFM) can also be employed to evaluate contact resistance from top-contact devices (**Figure 1.22**). All these methodologies will be briefly described in the following:<sup>55,58</sup>

- The Y-function method allows the extraction of  $R_C$  from the transfer characteristics recorded in the linear regime, through the calculation of the transconductance ( $g$ ) and the Y-function ( $Y$ ). A clear advantage of this simple method is that single devices can be independently characterised; however, it cannot ascertain the dependence of the contact resistance with  $V_{SG}$ .
- The TLM method consists in measuring similar OFETs with different channel lengths in the linear regime. Then, assuming that increasing  $L$  only  $R_{ch}$  is increased, by plotting the total resistance of the devices at a certain  $V_{SG}$  vs. their channel length,  $R_C$  can be extracted from the y-intercept of the linear fit of these points. The device resistance can be extracted from the linear fit of  $I_{SD}$  at low drain



voltages in the output characteristics. Although with this method the dependence of the contact resistance with the gate voltage can be ascertained, it requires the fabrication of sufficiently homogeneous devices, which cannot be taken for granted.

- The four-point probe method requires patterning two additional electrodes in the transistor channel in order to measure the potential drop. In this method a constant decay of the potential over the channel is assumed, so that any additional drops in electrostatic potential occurring at the contacts (due to contact resistance) can be estimated. The advantage over the other two-terminal methods is that the resistance of the source and the drain electrodes can be obtained separately; however, non-uniformities in the channel can strongly affect the extrapolated values from this method.

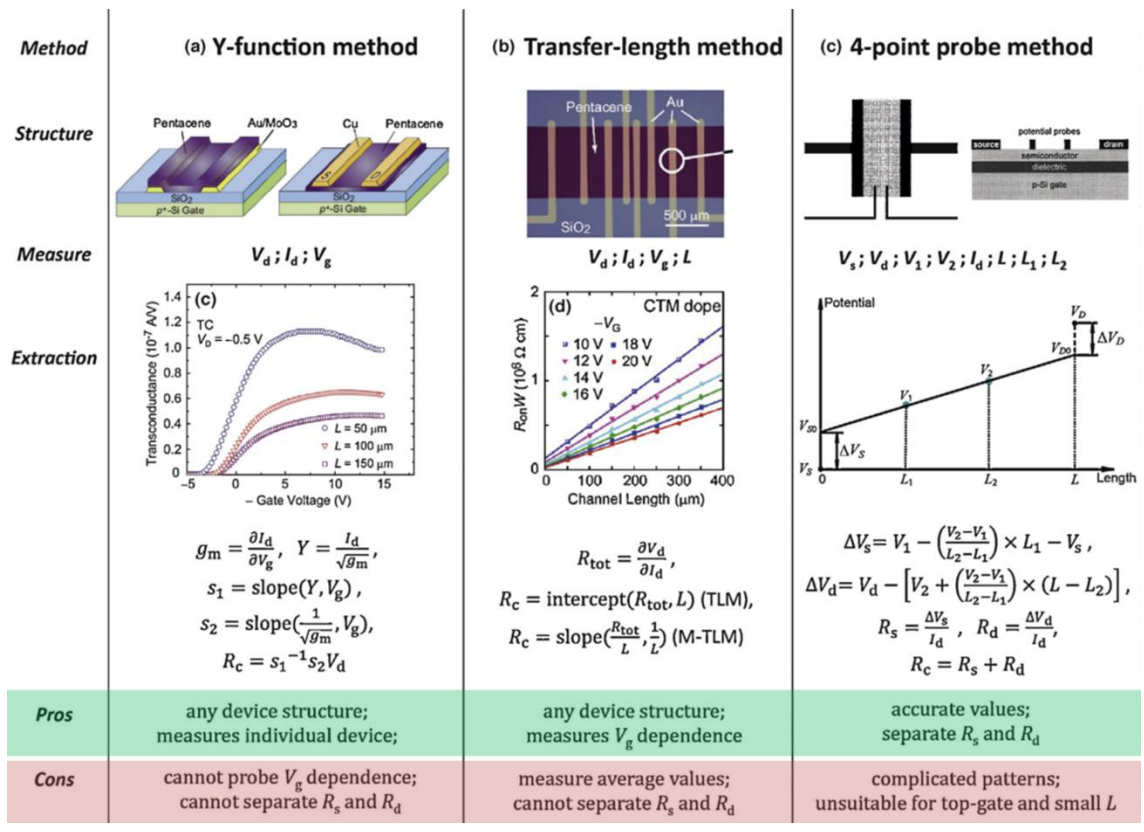


**Figure 1.21.** Summary of the most common methods used to extract the contact resistance in OFETs, showing their equations, the advantages and disadvantages. Extracted from ref. 58.

- The potential maps obtained by KPFM can provide valuable information regarding the contact resistance of OFETs. In fact, this technique allows evaluating the independent contribution of source and drain electrodes from the measurement of abrupt potential drops ( $\Delta V_S$  and  $\Delta V_D$ ) at the electrostatic potential maps (see **Figure 1.22**). For the source electrode, for example, the following equation can be employed:<sup>62</sup>

$$R_{C,source} = W \cdot \frac{\Delta V_S}{I_{SD}} \quad (1.9)$$

The same equation can be derived for the drain electrode.

A clear advantage of this method over the four-point probe technique is that the entire channel potential profile can be measured experimentally; this way, other bottlenecks to charge transport such as grain boundaries in the channel can also be visualised.

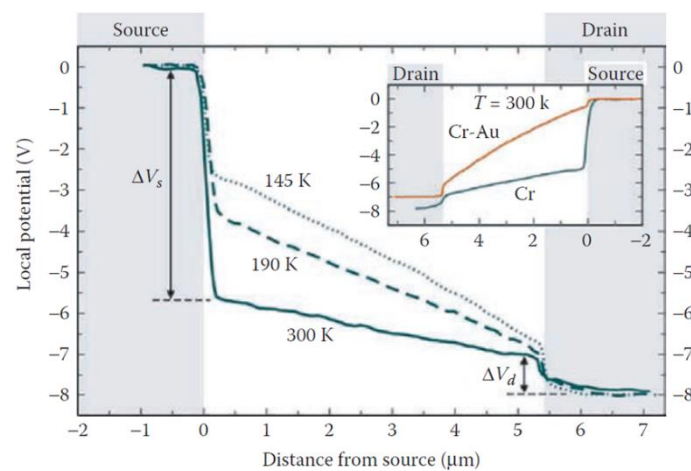


**Figure 1.22.** Electrostatic potential profiles obtained by Kelvin probe force microscopy from a P3HT transistor with Cr electrodes and channel length of 5.5  $\mu\text{m}$ , showing the potential drops at source and drain. Extracted from ref. 55.

## 1.5 ORGANIC FIELD-EFFECT TRANSISTORS IN SENSING APPLICATIONS

---

As it has been previously mentioned, the processing characteristics of organic semiconductors (i.e., low temperature and compatibility with solution-based techniques) make them potentially useful for electronic applications where low-cost, light-weight, large area coverage and structural flexibility are desired. In particular, organic field-effect transistors are being intensely investigated for their implementation in new chemical and physical sensing devices.<sup>20</sup> Firstly, organic semiconductors are susceptible to non-covalent interactions, trapping, doping, photoexcitation, dimensional deformations, and other mild (and often reversible) transformations. Moreover, their multi-parametric electrical characteristics make them interesting platforms to detect chemical/physical inputs that alter the conductivity properties of the active layer, that is, the density of charge carriers or their transport.

### ► Chemical and bio-chemical sensing

The detection of analytes at low concentrations with sufficient stability, reproducibility and selectivity is of great interest for applications in food processing and packaging, environmental analysis and medical diagnostics. Organic semiconductors can interact with different analytes at the OSC surface, between the crystallites that make up a polycrystalline film and at the OSC/dielectric or OSC/electrode interfaces; then, the OFET current-voltage characteristics can be employed to transduce the chemical information into measurable electronic information.

Most OFET based chemical sensors consist in measuring the device response in presence of certain gases or chemical vapours (**Figure 1.23 (a)**).<sup>63,64</sup> Also, devices with biological recognition capabilities are being developed mainly by functionalising or integrating bio-systems such as DNA strains, antibodies or enzymes in their structure.<sup>65–67</sup> For this latter application, the possibility of aqueous media operation, such as water or electrolyte-gated OFETs, has attracted plenty of attention.<sup>68</sup> As shown in **Figure 1.23 (b)**, upon the recognition event the electrical properties of the device, such as the capacitance, are modified.

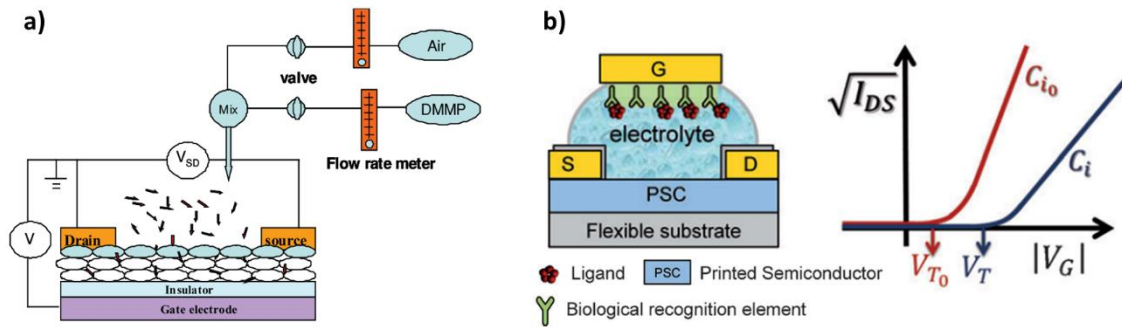


**Figure 1.23.** (a) Scheme of an analyte delivery system for dimethyl methylphosphonate gas. Extracted from ref. 20. (b) Schematic illustration of an electrolyte-gated thin-film transistor with a bio-functionalised gate in which the recognition event modulates the device capacitance. Extracted from ref. 66.

### ► Physical sensing

OFETs also play an important role in realising new sensors of physical phenomena, and can be categorised in two different functions: mechanical force detection and electromagnetic energy detection.

The most investigated mechanical-sensing devices are pressure sensors,<sup>69–71</sup> which can be used in a variety of innovative applications such as electronic artificial skin, rollable displays and wearable health-care devices. In these devices, the application of pressure can induce changes in the active layer structure or in the dielectric capacitance, which in turn results in current variations (**Figure 1.24 (a-b)**).<sup>69</sup> The exhibited sensitivity depends on the semiconductor and the layer microstructure, among other factors. Moreover, sensors based on the detection of acoustic waves are being investigated for the development of real-time and low-cost 3D imaging ultrasonic systems.<sup>72</sup>

On the other hand, electromagnetic signal detection, ranging from visible light to X-rays, is appealing for applications in the fields of biomedical imaging/sensing and optical communications.<sup>73,74</sup> In phototransistors the photogenerated charges (i.e., electron-hole pairs) are transported through the conduction channel and collected at the source/drain electrodes (**Figure 1.24 (c)**). Thus, the current characteristics of the transistor are modulated by the intensity of radiation exposure, as shown in the example in **Figure 1.24 (d)**.

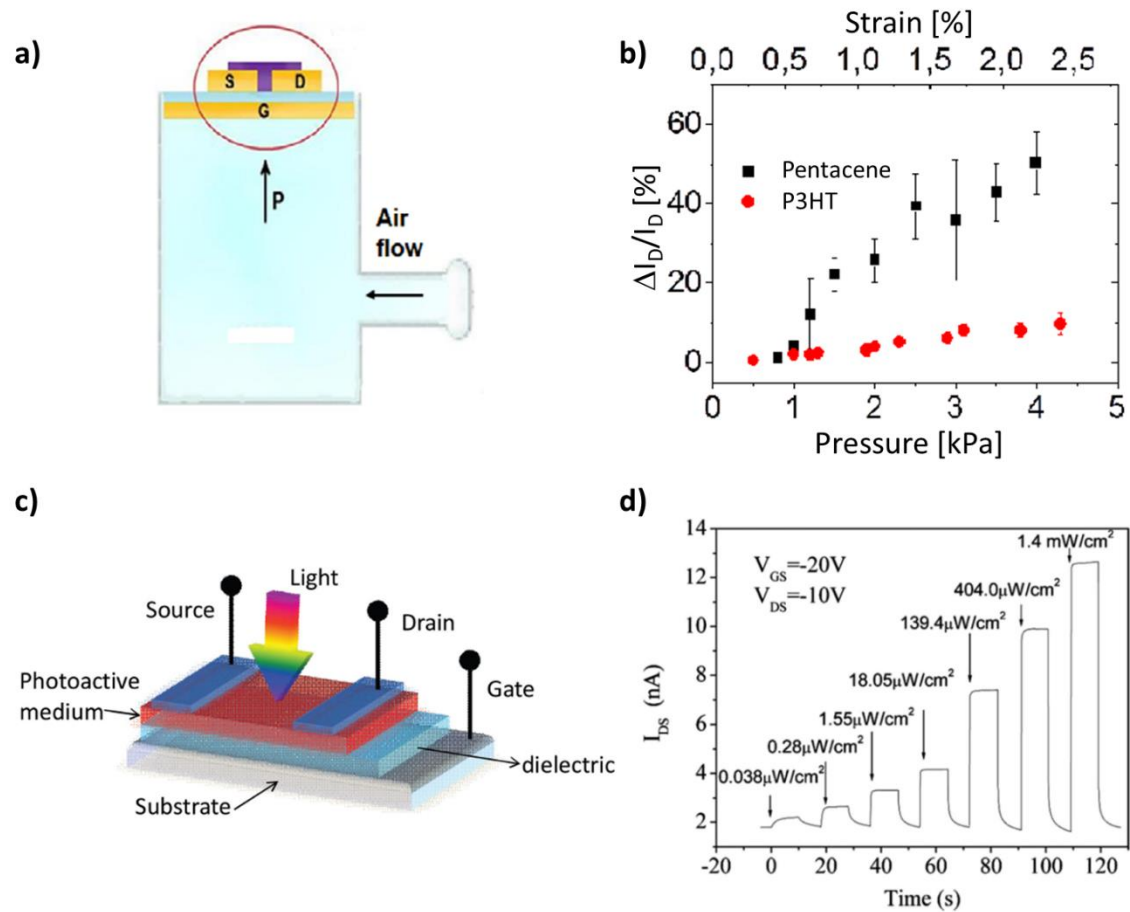


**Figure 1.24.** (a) Schematic representation of a setup employed for the electromechanical characterisation of single OFETs. (b) Electrical response to mechanical deformation of pentacene and P3HT based transistors. Extracted from ref. 69. (c) Schematic illustration of the typical structure of an organic phototransistor (bottom-gate bottom-contact with top-light illumination). (d) Source-drain current variation of an organic phototransistor based on a composite of P3HT and  $\text{TiO}_2$  nanoparticles measured under UV-light illumination with different intensities. Extracted from ref. 73.

## 1.6 OBJECTIVES

---

This thesis is focused on the fabrication of high performance organic field-effect transistors (OFETs) based on blends of p-type small molecule organic semiconductors (OSCs) and insulating polymer binders processed by a solution-based deposition technique, namely bar-assisted meniscus shearing (BAMS). The main purpose of the work developed herein is to understand how all the different parameters involved in the fabrication of such devices influence the morphological and structural features of the active layer and, thus, the electrical performance of the final devices. More specifically, the objectives of this thesis are the following:

- i. Extend the use of BAMS as processing technique for organic active layers based on different small molecule organic semiconductors, to show that such a fast and simple technique can be easily adapted to different types of materials. Study the morphology and structure of the thin films, and statistically analyse the OFET performance to test reproducibility.
- ii. Investigate the vertical structure at the nanoscale of OSC:insulating polymer thin films, in order to understand the superior performance generally achieved by employing such blends and the role played by the binding polymer. Correlate the use of different ink formulations (as regards OSC:polymer weight ratio) with the electrical characteristics macroscopically measured in OFET devices.
- iii. Study the performance limitations of OFETs with high contact resistance (i.e., high injection barrier) and explore simple doping methodologies aiming to improve the electrical characteristics of such devices at low cost. Optimise the doping dose and investigate the stability of the devices with doped OSC.
- iv. Explore the possibility to implement low-cost solution-processed OSC:polymer thin films in new applications, including flexible electronics and sensing of physical inputs, such as mechanical strain and high-energy radiation. Investigate the morphology-performance relationship in order to optimise the devices response.

These issues are addressed in five different experimental chapters (from Chapter 2 to 6), and in Chapter 7 the experimental details are described.

1.7 REFERENCES

---

- (1) Bardeen, J.; Brattain, W. H. The Transistor, A Semi-Conductor Triode. *Phys. Rev.* **1948**, *74*, 230.
- (2) Tanenbaum, M.; Valdes, L. B.; Buehler, E.; Hannay, N. B. Silicon N-p-n Grown Junction Transistors. *J. Appl. Phys.* **1955**, *26*, 686–692.
- (3) Anderson, P. W.; Lee, P. A.; Saitoh, M. Remarks on Giant Conductivity in TTF-TCNQ. *Solid State Commun.* **1973**, *13*, 595–598.
- (4) Shirakawa, H.; Louis, E.; MacDiarmid, A.; Chiang, C.; Heeger, J. Synthesis of Electrically Conducting Organic Polymers: Halogen Derivatives of Polyacetylene, (CH)<sub>x</sub>. *J.C.S Chem. Comm* **1977**, *16*, 578–580.
- (5) Choi, M. C.; Kim, Y.; Ha, C. S. Polymers for Flexible Displays: From Material Selection to Device Applications. *Prog. Polym. Sci.* **2008**, *33*, 581–630.
- (6) Zhan, Y.; Mei, Y.; Zheng, L. Materials Capability and Device Performance in Flexible Electronics for the Internet of Things. *J. Mater. Chem. C* **2014**, *2*, 1220–1232.
- (7) Diao, Y.; Shaw, L.; Mannsfeld, S. C. B. Morphology Control Strategies for Solution-Processed Organic Semiconductor Thin Films. *Energy Environ. Sci.* **2014**, *7*, 2145–2159.
- (8) Xu, Y.; Liu, C.; Khim, D.; Noh, Y.-Y. Development of High-Performance Printed Organic Field-Effect Transistors and Integrated Circuits. *Phys. Chem. Chem. Phys.* **2015**, *17*, 26553–26574.
- (9) Grau, G.; Cen, J.; Kang, H.; Kitsomboonloha, R.; Scheideler, W. J.; Subramanian, V. Gravure-Printed Electronics: Recent Progress in Tooling Development, Understanding of Printing Physics, and Realization of Printed Devices. *Flex. Print. Electron.* **2016**, *1*, 023002.
- (10) Takeda, Y.; Hayasaka, K.; Shiwaku, R.; Yokosawa, K.; Shiba, T.; Mamada, M.; Kumaki, D.; Fukuda, K.; Tokito, S. Fabrication of Ultra-Thin Printed Organic TFT CMOS Logic Circuits Optimized for Low-Voltage Wearable Sensor Applications. *Sci. Rep.* **2016**, *6*, 25714.
- (11) Köhler, A.; Bässler, H. *Electronic Processes in Organic Semiconductors: An Introduction*; Wiley-VCH, 2015.
- (12) Tang, C. W.; Vanslyke, S. A. Organic Electroluminescent Diodes. *Appl. Phys. Lett.* **1987**, *51*, 913–915.
- (13) Geffroy, B.; le Roy, P.; Prat, C. Organic Light-Emitting Diode (OLED) Technology:

- Materials, Devices and Display Technologies. *Polym. Int.* **2006**, *55*, 572–582.
- (14) Meng, L.; Zhang, Y.; Wan, X.; Li, C.; Zhang, X.; Wang, Y.; Ke, X.; Xiao, Z.; Ding, L.; Xia, R.; et al. Organic and Solution-Processed Tandem Solar Cells with 17.3% Efficiency. *Science* **2018**, *361*, 1094–1098.
- (15) Abdulrazzaq, O. A.; Saini, V.; Bourdo, S.; Dervishi, E.; Biris, A. S. Organic Solar Cells: A Review of Materials, Limitations, and Possibilities for Improvement. *Part. Sci. Technol.* **2013**, *31*, 427–442.
- (16) Koezuka, H.; Tsumura, A.; Ando, T. Field-Effect Transistor with Polythiophene Thin Film. *Synth. Met.* **1987**, *18*, 699–704.
- (17) Sirringhaus, H. 25th Anniversary Article: Organic Field-Effect Transistors: The Path beyond Amorphous Silicon. *Adv. Mater.* **2014**, *26*, 1319–1335.
- (18) Dodabalapur, A.; Laquindanum, J.; Katz, H. E.; Bao, Z. Complementary Circuits with Organic Transistors. *Appl. Phys. Lett.* **1996**, *69*, 4227–4229.
- (19) Baude, P. F.; Ender, D. A.; Haase, M. A.; Kelley, T. W.; Muyres, D. V.; Theiss, S. D. Pentacene-Based Radio-Frequency Identification Circuitry. *Appl. Phys. Lett.* **2003**, *82*, 3964–3966.
- (20) Someya, T.; Dodabalapur, A.; Huang, J.; See, K. C.; Katz, H. E. Chemical and Physical Sensing by Organic Field-Effect Transistors and Related Devices. *Adv. Mater.* **2010**, *22*, 3799–3811.
- (21) Grundmann, M. *Physics of Semiconductors*; Springer, 2010.
- (22) Sze, S. M.; Ng, K. K. *Physics of Semiconductor Devices*; Wiley-Interscience, 2006.
- (23) MacGillivray, L. R. On Substituents, Steering, and Stacking to Control Properties of the Organic Solid State. *CrystEngComm* **2004**, *6*, 77.
- (24) Coropceanu, V.; Cornil, J.; da Silva Filho, D. A.; Olivier, Y.; Silbey, R.; Brédas, J.-L. Charge Transport in Organic Semiconductors. *Chem. Rev.* **2007**, *107*, 926–952.
- (25) Liu, C.; Huang, K.; Park, W.-T. T.; Li, M. M.; Yang, T.; Liu, X.; Liang, L.; Minari, T.; Noh, Y.-Y. A Unified Understanding of Charge Transport in Organic Semiconductors: The Importance of Attenuated Delocalization for the Carriers. *Mater. Horiz.* **2017**, *4*, 608–618.
- (26) Marcus, R. A. On the Theory of Oxidation-Reduction Reactions Involving Electron Transfer. I. *J. Chem. Phys.* **1956**, *24*, 966–978.
- (27) Mas-Torrent, M.; Rovira, C. Novel Small Molecules for Organic Field-Effect Transistors: Towards Processability and High Performance. *Chem. Soc. Rev.* **2008**,



37, 827–838.

- (28) Sirringhaus, H.; Brown, P. J.; Friend, R. H.; Nielsen, M. M.; Bechgaard, K.; Langeveld-Voss, B. M. W.; Spiering, A. J. H.; Janssen, R. A. J.; Meijer, E. W.; Herwig, P.; et al. Two-Dimensional Charge Transport in Self-Organized, High-Mobility Conjugated Polymers. *Nature* **1999**, *401*, 685–688.
- (29) McCulloch, I.; Heeney, M.; Bailey, C.; Genevicius, K.; MacDonald, I.; Shkunov, M.; Sparrowe, D.; Tierney, S.; Wagner, R.; Zhang, W.; et al. Liquid-Crystalline Semiconducting Polymers with High Charge-Carrier Mobility. *Nat. Mater.* **2006**, *5*, 328–333.
- (30) Tsao, H. N.; Cho, D. M.; Park, I.; Hansen, M. R.; Mavrinskiy, A.; Yoon, D. Y.; Graf, R.; Pisula, W.; Spiess, H. W.; Müllen, K. Ultrahigh Mobility in Polymer Field-Effect Transistors by Design. *J. Am. Chem. Soc.* **2011**, *133*, 2605–2612.
- (31) Paterson, A. F.; Singh, S.; Fallon, K. J.; Hodsden, T.; Han, Y.; Schroeder, B. C.; Bronstein, H.; Heeney, M.; McCulloch, I.; Anthopoulos, T. D. Recent Progress in High-Mobility Organic Transistors: A Reality Check. *Adv. Mater.* **2018**, *30*, 1801079.
- (32) Kymissis, I. *Organic Field Effect Transistors: Theory, Fabrication and Characterization*; Springer, 2008.
- (33) Li, H.; Tee, B. C.-K.; Giri, G.; Chung, J. W.; Lee, S. Y.; Bao, Z. High-Performance Transistors and Complementary Inverters Based on Solution-Grown Aligned Organic Single-Crystals. *Adv. Mater.* **2012**, *24*, 2588–2591.
- (34) Liu, C.; Li, Y.; Lee, M. V.; Kumatani, A.; Tsukagoshi, K. Self-Assembly of Semiconductor/Insulator Interfaces in One-Step Spin-Coating: A Versatile Approach for Organic Field-Effect Transistors. *Phys. Chem. Chem. Phys.* **2013**, *15*, 7917–7933.
- (35) Coan, T.; Barroso, G. S.; Motz, G.; Bolzán, A.; Machado, R. A. F. Preparation of PMMA/HBN Composite Coatings for Metal Surface Protection. *Mater. Res.* **2013**, *16* (6), 1366–1372.
- (36) Reale, A.; LaNotte, L.; Salamandra, L.; Polino, G.; Susanna, G.; Brown, T. M.; Brunetti, F.; DiCarlo, A. Spray Coating for Polymer Solar Cells: An Up-to-Date Overview. *Energy Technol.* **2015**, *3*, 385–406.
- (37) Tracz, A.; Pakula, T.; Jeszka, J. K. Zone Casting - a Universal Method of Preparing Oriented Anisotropic Layers of Organic Materials. *Mater. Sci.* **2004**, *22* (4), 415–421.
- (38) Chang, Y. H.; Tseng, S. R.; Chen, C. Y.; Meng, H. F.; Chen, E. C.; Horng, S. F.; Hsu, C. S. Polymer Solar Cell by Blade Coating. *Org. Electron.* **2009**, *10*, 741–746.
- (39) del Pozo, F. G.; Fabiano, S.; Pfattner, R.; Georgakopoulos, S.; Galindo, S.; Liu, X.; Braun, S.; Fahlman, M.; Veciana, J.; Rovira, C.; et al. Single Crystal-Like Performance

- in Solution-Coated Thin-Film Organic Field-Effect Transistors. *Adv. Funct. Mater.* **2016**, *26*, 2379–2386.
- (40) Gu, X.; Shaw, L.; Gu, K.; Toney, M. F.; Bao, Z. The Meniscus-Guided Deposition of Semiconducting Polymers. *Nat. Commun.* **2018**, *9*, 534.
- (41) Niazi, M. R.; Li, R.; Abdelsamie, M.; Zhao, K.; Anjum, D. H.; Payne, M. M.; Anthony, J.; Smilgies, D.-M.; Amassian, A. Contact-Induced Nucleation in High-Performance Bottom-Contact Organic Thin Film Transistors Manufactured by Large-Area Compatible Solution Processing. *Adv. Funct. Mater.* **2016**, *26*, 2371–2378.
- (42) Hamilton, R.; Smith, J.; Ogier, S.; Heeney, M.; Anthony, J. E.; McCulloch, I.; Veres, J.; Bradley, D. D. C.; Anthopoulos, T. D. High-Performance Polymer-Small Molecule Blend Organic Transistors. *Adv. Mater.* **2009**, *21*, 1166–1171.
- (43) Riera-Galindo, S.; Leonardi, F.; Pfattner, R.; Mas-Torrent, M. Organic Semiconductor/Polymer Blend Films for Organic Field-Effect Transistors. *Adv. Mater. Technol.* **2019**, 1900104.
- (44) Niazi, M. R.; Li, R.; Qiang Li, E.; Kirmani, A. R.; Abdelsamie, M.; Wang, Q.; Pan, W.; Payne, M. M.; Anthony, J. E.; Smilgies, D.-M.; et al. Solution-Printed Organic Semiconductor Blends Exhibiting Transport Properties on Par with Single Crystals. *Nat. Commun.* **2015**, *6*, 8598.
- (45) Yuan, Y.; Giri, G.; Ayzner, A. L.; Zoombelt, A. P.; Mannsfeld, S. C. B.; Chen, J.; Nordlund, D.; Toney, M. F.; Huang, J.; Bao, Z. Ultra-High Mobility Transparent Organic Thin Film Transistors Grown by an off-Centre Spin-Coating Method. *Nat. Commun.* **2014**, *5*, 3005.
- (46) Leonardi, F.; Casalini, S.; Zhang, Q.; Galindo, S.; Gutiérrez, D.; Mas-Torrent, M. Electrolyte-Gated Organic Field-Effect Transistor Based on a Solution Sheared Organic Semiconductor Blend. *Adv. Mater.* **2016**, *28*, 10311–10316.
- (47) Bobbert, P. a.; Sharma, A.; Mathijssen, S. G. J.; Kemerink, M.; De Leeuw, D. M. Operational Stability of Organic Field-Effect Transistors. *Adv. Mater.* **2012**, *24*, 1146–1158.
- (48) Hunter, S.; Anthopoulos, T. D. Observation of Unusual, Highly Conductive Grain Boundaries in High-Mobility Phase Separated Organic Semiconducting Blend Films Probed by Lateral-Transport Conductive-AFM. *Adv. Mater.* **2013**, *25*, 4320–4326.
- (49) Zhao, K.; Wodo, O.; Ren, D.; Khan, H. U.; Niazi, M. R.; Hu, H.; Abdelsamie, M.; Li, R.; Li, E. Q.; Yu, L.; et al. Vertical Phase Separation in Small Molecule:Polymer Blend Organic Thin Film Transistors Can Be Dynamically Controlled. *Adv. Funct. Mater.* **2016**, *26*, 1737–1746.
- (50) Shehu, A.; Quiroga, S. D.; D'Angelo, P.; Albonetti, C.; Borgatti, F.; Murgia, M.;

- Scorzoni, A.; Stoliar, P.; Biscarini, F. Layered Distribution of Charge Carriers in Organic Thin Film Transistors. *Phys. Rev. Lett.* **2010**, *104*, 246602.
- (51) Klauk, H. Organic Thin-Film Transistors. *Chem. Soc. Rev.* **2010**, *39*, 2643–2666.
- (52) Hwang, D. K.; Fuentes-Hernandez, C.; Kim, J.; Potscavage, W. J.; Kim, S. J.; Kippelen, B. Top-Gate Organic Field-Effect Transistors with High Environmental and Operational Stability. *Adv. Mater.* **2011**, *23*, 1293–1298.
- (53) Ahmed, R.; Kadashchuk, A.; Simbrunner, C.; Schwabegger, G.; Baig, M. A.; Sitter, H. Geometrical Structure and Interface Dependence of Bias Stress Induced Threshold Voltage Shift in C60-Based OFETs. *ACS Appl. Mater. Interfaces* **2014**, *6*, 15148–15153.
- (54) Horowitz, G. Organic Field-Effect Transistors. *Adv. Mater.* **1998**, *10*, 365–377.
- (55) *Organic Field-Effect Transistors*; Bao, Z., Locklin, J., Eds.; CRC Press, 2007.
- (56) McDowell, M.; Hill, I. G.; McDermott, J. E.; Bernasek, S. L.; Schwartz, J. Improved Organic Thin-Film Transistor Performance Using Novel Self-Assembled Monolayers. *Appl. Phys. Lett.* **2006**, *88*, 073505.
- (57) Yoon, M. H.; Kim, C.; Facchetti, A.; Marks, T. J. Gate Dielectric Chemical Structure–Organic Field-Effect Transistor Performance Correlations for Electron, Hole, and Ambipolar Organic Semiconductors. *J. Am. Chem. Soc.* **2006**, *128*, 12851–12869.
- (58) Liu, C.; Xu, Y.; Noh, Y. Y. Contact Engineering in Organic Field-Effect Transistors. *Mater. Today* **2015**, *18*, 79–96.
- (59) Natali, D.; Caironi, M. Charge Injection in Solution-Processed Organic Field-Effect Transistors: Physics, Models and Characterization Methods. *Adv. Mater.* **2012**, *24*, 1357–1387.
- (60) Bittle, E. G.; Basham, J. I.; Jackson, T. N.; Jurchescu, O. D.; Gundlach, D. J. Mobility Overestimation Due to Gated Contacts in Organic Field-Effect Transistors. *Nat. Commun.* **2015**, *7*, 10908.
- (61) Choi, H. H.; Cho, K.; Frisbie, C. D.; Sirringhaus, H.; Podzorov, V. Critical Assessment of Charge Mobility Extraction in FETs. *Nat. Mater.* **2018**, *17*, 2–7.
- (62) Bürgi, L.; Richards, T. J.; Friend, R. H.; Sirringhaus, H. Close Look at Charge Carrier Injection in Polymer Field-Effect Transistors. *J. Appl. Phys.* **2003**, *94*, 6129.
- (63) Pacher, P.; Lex, A.; Proschek, V.; Etschmaier, H.; Tchernychova, E.; Sezen, M.; Scherf, U.; Grogger, W.; Trimmel, G.; Slugovc, C.; et al. Chemical Control of Local Doping in Organic Thin-Film Transistors: From Depletion to Enhancement. *Adv. Mater.* **2008**, *20*, 3143–3148.

- (64) Zhang, C.; Chen, P.; Hu, W. Organic Field-Effect Transistor-Based Gas Sensors. *Chem. Soc. Rev.* **2015**, *44*, 2087–2107.
- (65) Stoliar, P.; Bystrenova, E.; Quiroga, S. D.; Annibale, P.; Facchini, M.; Spijkman, M.; Setayesh, S.; de Leeuw, D.; Biscarini, F. DNA Adsorption Measured with Ultra-Thin Film Organic Field Effect Transistors. *Biosens. Bioelectron.* **2009**, *24*, 2935–2938.
- (66) Manoli, K.; Magliulo, M.; Mulla, M. Y.; Singh, M.; Sabbatini, L.; Palazzo, G.; Torsi, L. Printable Bioelectronics to Investigate Functional Biological Interfaces. *Angew. Chemie - Int. Ed.* **2015**, *54*, 12562–12576.
- (67) Torsi, L.; Magliulo, M.; Manoli, K.; Palazzo, G. Organic Field-Effect Transistor Sensors: A Tutorial Review. *Chem. Soc. Rev.* **2013**, *42*, 8612–8628.
- (68) Cramer, T.; Campana, A.; Leonardi, F.; Casalini, S.; Kyndiah, A.; Murgia, M.; Biscarini, F. Water-Gated Organic Field Effect Transistors-Opportunities for Biochemical Sensing and Extracellular Signal Transduction. *J. Mater. Chem. B* **2013**, *1*, 3728–3741.
- (69) Loi, A.; Basirico, L.; Cosseddu, P.; Lai, S.; Barbaro, M.; Bonfiglio, A.; Maiolino, P.; Baglini, E.; Denei, S.; Mastrogiovanni, F.; et al. Organic Bendable and Stretchable Field Effect Devices for Sensing Applications. *IEEE Sens. J.* **2013**, *13*, 4764–4772.
- (70) Lai, S.; Cosseddu, P.; Bonfiglio, A.; Barbaro, M. Ultralow Voltage Pressure Sensors Based on Organic FETs and Compressible Capacitors. *IEEE Electron Device Lett.* **2013**, *34*, 801–803.
- (71) Zhang, Q.; Leonardi, F.; Pfattner, R.; Mas-Torrent, M. A Solid-State Aqueous Electrolyte-Gated Field-Effect Transistor as a Low-Voltage Operation Pressure-Sensitive Platform. *Adv. Mater. Interfaces* **2019**, 1900719.
- (72) Smith, S. W.; Chu, K.; Idriss, S. F.; Ivancevich, N. M.; Light, E. D.; Wolf, P. D. Feasibility Study: Real-Time 3-D Ultrasound Imaging of the Brain. *Ultrasound Med. Biol.* **2004**, *30*, 1365–1371.
- (73) Baeg, K. J.; Binda, M.; Natali, D.; Caironi, M.; Noh, Y. Y. Organic Light Detectors: Photodiodes and Phototransistors. *Adv. Mater.* **2013**, *25*, 4267–4295.
- (74) Fraboni, B.; Ciavatti, A.; Merlo, F.; Pasquini, L.; Cavallini, A.; Quaranta, A.; Bonfiglio, A.; Fraleoni-Morgera, A. Organic Semiconducting Single Crystals as next Generation of Low-Cost, Room-Temperature Electrical X-Ray Detectors. *Adv. Mater.* **2012**, *24*, 2289–2293.



## CHAPTER 2

---

# A unified experimental recipe to fabricate from solution state-of-the-art performance OFETs based on OSCs belonging to four different families\*

### 2.1 INTRODUCTION AND OBJECTIVES

---

From the first report of an organic field-effect transistor (OFET) based on a small conjugated molecule in 1989,<sup>1</sup> several fundamental investigations were carried out employing evaporation processes. However, it was soon realised that in order to exploit these devices in real applications great efforts should be made regarding two essential aspects: the design and synthesis of stable and soluble organic semiconducting molecules and the development of low-cost solution processing techniques. Thanks to this shifting perspective, nowadays there is a vast library of known materials that can be employed as active components in OFETs<sup>2-4</sup> and also plenty available processing techniques that give rise to highly crystalline and homogenous films resulting in high mobility devices.<sup>5,6</sup>

In order to make organic electronics competitive with their inorganic counterparts, such solution-based techniques must be simple, cheap, and compatible with up-scaling and high throughput processes such as roll-to-roll. Yet, not all these techniques are scalable and some of them require of additional time-consuming post-treatment steps (such as crystallisation via vapour or temperature annealing). For instance, spin-coating is an interesting technique for achieving homogeneous thin films in the lab scale, but it is not compatible with high throughput processes. In contrast, techniques based on solution-

---

\* This work has been published in: (i) Temiño, I.; Del Pozo, F. G.; Ajayakumar, M. R.; Galindo, S.; Puigdollers, J.; Mas-Torrent, M. A Rapid, Low-Cost, and Scalable Technique for Printing State-of-the-Art Organic Field-Effect Transistors. *Adv. Mater. Technol.* **2016**, *1*, 1600090. (ii) Zhang, Q.; Leonardi, F.; Casalini, S.; Temiño, I.; Mas-Torrent, M. High Performing Solution-Coated Electrolyte-Gated Organic Field-Effect Transistors for Aqueous Media Operation. *Sci. Rep.* **2016**, *6*, 39623.

shearing, such as zone casting or blade coating, have demonstrated to be highly appealing to be included in up-scaled processes. Among the solution-shearing techniques, as mentioned in the introduction chapter, our group has developed one in which a meniscus formed between a bar and a heated substrate is sheared, and so it is named bar-assisted meniscus shearing (BAMS).<sup>7</sup> This process is typically realised at a high output speed of 10 mm/s, pointing out its potential for applications. Interestingly, BAMS demonstrated its full potential when the organic semiconductor (OSC) was mixed with an insulating polymer binder, such as polystyrene (PS). Indeed, the use of solution inks based on blends of OSCs and inert polymers has shown to be an efficient way to facilitate material processability as well as to enhance film homogeneity and reproducibility,<sup>8-10</sup> while it is still possible to take advantage of the high carrier mobility of the crystalline component.

Using this technology, in 2015 it was reported for the first time the deposition by BAMS of an organic thin film (~30 nm thick) based on the small semiconducting molecule dibenzo-tetrathiafulvalene (DB-TTF), which resulted in a highly crystalline film and ideal OFET characteristics.<sup>7,11</sup> Moreover, by employing this strategy an enhancement of the device environmental stability was achieved.<sup>7</sup>

Since most processing techniques are often adapted for a particular organic semiconductor, the main question raised at this point was if the BAMS technique could be applied to other OSC:polymer systems. To approach this issue, four small molecules belonging to different families of organic semiconductors were chosen:

- 6,13-bis(triisopropylsilylethynyl)pentacene (TIPS-pentacene)
- 2,8-difluoro-5,11-bis(triethylsilylethynyl)anthradithiophene (diF-TES-ADT)
- 2,7-dioctyl[1]benzothieno[3,2-b][1]benzothiophene (C8-BTBT)
- dithiophene-tetrathiafulvalene (DT-TTF)

As polymer binder, PS was chosen given the promising results previously obtained with DB-TTF.<sup>7</sup> The chemical structures of all the selected OSCs and PS are shown in **Figure 2.1**. It is worth pointing out that these four OSCs are well-known materials for the fabrication of OFET devices with high performance<sup>12-14</sup> and, hence, it is desirable to find methods to process them at low cost and at high speed.

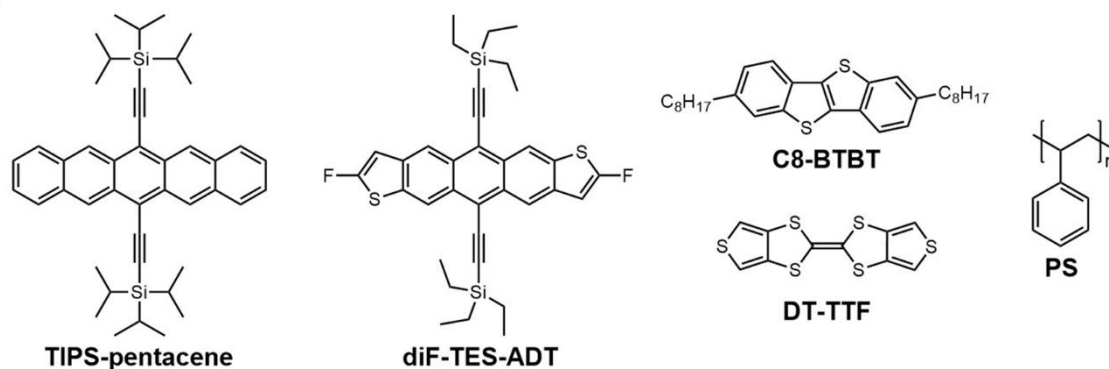


**Figure 2.1.** Molecular structures of the organic semiconductors TIPS-pentacene, diF-TES-ADT, C8-BTBT and DT-TTF, and polystyrene.

## Objectives

Thus, the objective of this thesis chapter is to extend the use of BAMS processing technique to deposit thin films based on small molecule OSCs blended with an insulating polymer in order to fabricate high performing OFETs by a fast and simple methodology. To do so, materials belonging to different families of OSCs were chosen to blend with PS: TIPS-pentacene, diF-TES-ADT, C8-BTBT and DT-TTF, all of which have been reported to be excellent candidates for OFETs. First, we proceeded to optimise a unified experimental recipe to process all the considered molecules under the same conditions. Then, the resulting films were fully characterised and, subsequently, applied as active materials in OFETs, which were electrically measured and statistically analysed. Finally, TIPS-pentacene and diF-TES-ADT thin films were applied for the development of devices operating in aqueous media.



## 2.2 DEVICE FABRICATION AND OPTIMISATION OF THE EXPERIMENTAL CONDITIONS

---

Films processed by BAMS based on the four chosen organic semiconductors, TIPS-pentacene, diF-TES-ADT, DT-TTF and C8-BTBT, were tested by screening several experimental parameters mainly regarding the ink formulation, such as the molecular weight of PS, the OSC:PS blend ratio or the solvent, but also regarding the OFET structure, like the use of bottom or top source/drain (S/D) electrodes and their functionalisation. First, films based on TIPS-pentacene and diF-TES-ADT were deposited, and then, the employed conditions were adapted for the other OSCs. Focus was set at improving the overall results and achieving a unified experimental recipe that gave rise to both highly crystalline films and high performance OFETs. For this reason, during the optimisation process, the film morphology and crystallinity were checked by polarised optical microscopy and the electrical performance was also carefully tested and compared. It should be highlighted that the complete experimental procedure was carried out under ambient conditions. The details about the main screening tests are displayed in **Table 2.1**.

In a first stage, TIPS-pentacene and diF-TES-ADT based thin films were deposited using different ratios of OSC:PS and PS of different molecular weights (1, 10 and 100 kg/mol, namely PS1k, PS10k and PS100k). Chlorobenzene (CB) and toluene (Tol) solutions were prepared in a 2% and 1% weight concentration, respectively. Likewise, the temperature was adjusted at 105 and 90 °C, respectively, to guarantee the immediate evaporation of the solvent. Bottom-gate bottom-contact devices consisting of Si/SiO<sub>2</sub> substrates with patterned interdigitated Cr/Au electrodes were employed. The channel lengths varied from  $L = 25$  to  $100 \mu\text{m}$  while the width/length ratio was set to  $W/L = 100$ . The electrical measurements indicated that the best performance is obtained when employing PS10k at a blending ratio of 4:1. It is noteworthy that the field-effect mobility ( $\mu_{FE}$ ) decreased by one or two orders of magnitude when no PS was included in the ink formulation. In addition, electrodes were treated with a self-assembled monolayer (SAM) of pentafluorobenzenethiol (PFBT), which has previously shown to assist the crystallisation of these OSCs in spin-coated films and also improve charge injection and the overall OFET performance.<sup>12,15-17</sup> Although previous works reported that PFBT SAMs disrupted the formation of spherulitic crystalline films fabricated by plate-shearing,<sup>12</sup> in this work we found that they lead to more homogenous and interconnected crystallites, which in turn results in higher mobility OFET devices. This discrepancy can be attributed to two different factors: the higher speed of our process (10 mm/s instead of 1.5 mm/s, i.e., one order of magnitude faster) and the less confinement of the solution when a bar is used instead of a plate.

**Table 2.1.** Summary of the most relevant experiments carried out for the optimisation of TIPS-pentacene, diF-TES-ADT, C8-BTBT and DT-TTF based OFETs processed by BAMS at 10 mm/s. \* Indicates the best experimental conditions for each OSC.

OSC	Polymer	Ratio	Solvent (wt%)	S/D electrodes	$\mu_{FE}$ (cm <sup>2</sup> /V·s)	$V_{th}$ (V)
TIPS-pentacene	-	-	CB (2%)	Au/PFBT	0.007	-17.3
diF-TES-ADT	-	-	CB (2%)	Au/PFBT	0.17	7.7
TIPS-pentacene	PS10k	1:2	CB (2%)	Au/PFBT	0.84	-1.2
diF-TES-ADT	PS10k	1:2	CB (2%)	Au/PFBT	0.79	-0.06
* TIPS-pentacene	PS10k	4:1	CB (2%)	<b>Au/PFBT</b>	1.05	-0.27
* diF-TES-ADT	PS10k	4:1	CB (2%)	<b>Au/PFBT</b>	1.11	-1.1
TIPS-pentacene	PS1k	4:1	Tol (1%)	Au/PFBT	0.02	4.1
TIPS-pentacene	<b>PS10k</b>	4:1	Tol (1%)	Au/PFBT	0.35	0.57
TIPS-pentacene	PS100k	4:1	Tol (1%)	Au/PFBT	0.37	2.4
diF-TES-ADT	PS1k	4:1	Tol (1%)	Au/PFBT	x	x
diF-TES-ADT	<b>PS10k</b>	4:1	Tol (1%)	Au/PFBT	0.48	4.1
diF-TES-ADT	PS100k	4:1	Tol (1%)	Au/PFBT	0.39	6.6
DT-TTF	PS10k	4:1	Tol (1%)	Au/PFBT	x	x
DT-TTF	PS10k	4:1	CB (2%)	Au/PFBT	0.03	2.1
* DT-TTF	PS10k	4:1	<b>CB (2%)</b>	<b>Au</b>	0.11	2.9
TIPS-pentacene	PS10k	4:1	CB (2%)	Au	0.01	-6.1
diF	PS10k	4:1	CB (2%)	Au	0.001	0.89
C8-BTBT	PS10k	4:1	CB (2%)	Au/PFBT	x	x
* C8-BTBT	PS10k	4:1	CB (2%)	<b>MoO<sub>3</sub>/Au (TC)</b>	0.21	-22.8

When processing DT-TTF, we found that it could not be sufficiently dissolved in toluene. Hence, although it is a non-chlorinated and less toxic solvent and it allows processing at a lower temperature, all the following experiments were performed with CB. Regarding the functionalisation of the contacts, it was found that the crystallisation of DT-TTF films is not

influenced by the PFBT treatment. In fact, the resulting OFETs show a degraded performance in comparison with the use of bare electrodes.

Finally, for C8-BTBT the same printing procedure was followed. In spite of the crystallinity of the films, transistors showed bad characteristics due to injection issues related with the very low lying highest occupied molecular orbital (HOMO) level of this molecule (ca. -5.7 eV)<sup>18</sup> and its misalignment with the Au work-function ( $\sim$ -5.1 eV). In order to ensure efficient charge injection into the material, top MoO<sub>3</sub>/Au contacts were evaporated through a shadow mask giving devices with channel lengths from  $L = 30$  to  $100 \mu\text{m}$  and fixed channel width of  $W = 4 \text{ mm}$ .

After this optimisation process, we concluded that the best experimental conditions to process thin films based on the four chosen OSCs are the following (indicated with an asterisk in **Table 2.1**):

### Ink formulation

- Polymer: PS10k
- OSC:PS ratio: 4:1
- Solvent: chlorobenzene (concentration 2 wt%)

### Deposition parameters

- Speed: 10 mm/s
- Temperature: 105 °C

### Device parameters

- S/D electrodes: PFBT-functionalised electrodes for TIPS-pentacene and diF-TES-ADT devices, bare Au electrodes for DT-TTF and MoO<sub>3</sub>/Au top electrodes for C8-BTBT devices

Additional tests employing different binding polymers, as poly(methyl methacrylate) (PMMA), and also solvents, such as anisole or decalin, were performed. However, none of these improved the performance of the fabricated devices.

## 2.3 THIN-FILM CHARACTERISATION

---

Once the optimisation of the experimental conditions was completed and a unified processing recipe for the four chosen semiconductors was achieved, we proceeded to perform a more in-depth study of the OSC:PS thin films.

The optical microscope and crossed-polarised optical microscope images of the prepared thin films are shown in **Figure 2.2**. Here, uniform crystalline domains can be clearly observed. While TIPS-pentacene, diF-TES-ADT and C8-BTBT grow isotropically, forming films with no preferential orientation relative to the shearing direction, DT-TTF domains grow along the shearing direction, reaching several millimetres of length. Atomic force microscopy (AFM) topography images shown in **Figure 2.3 (a-d)** were obtained in order to further characterize the thin-films morphology. The surface roughness, quantified with the root mean square roughness (*rms*), was estimated to be 3.3, 1.2, 6.0 and 11.3 nm for TIPS-pentacene, diF-TES-ADT, C8-BTBT and DT-TTF films, respectively. This result points out the smoothness and homogeneity of the blended films. In addition, the total thickness of the films was estimated from the height profiles shown in **Figure 2.3 (e-h)**. TIPS-pentacene and diF-TES-ADT were found to be around 20 nm thick, while C8-BTBT and DT-TTF films were estimated to be 43 and 13 nm, respectively.

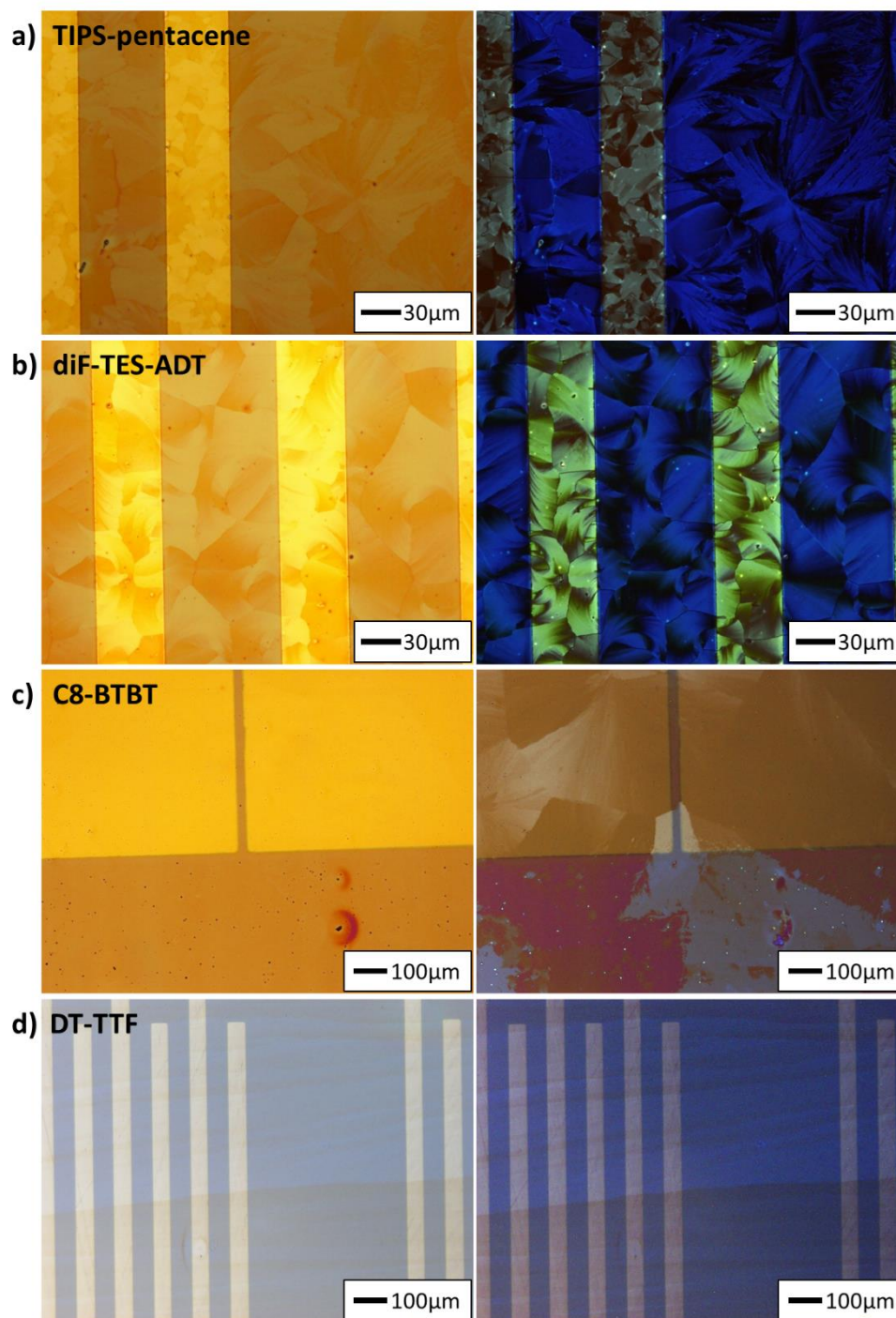


**Figure 2.2.** Optical microscope (left) and crossed-polarised optical microscope (right) images of thin films based on (a) TIPS-pentacene, (b) diF-TES-ADT, (c) C8-BTBT and (d) DT-TTF blended with PS.



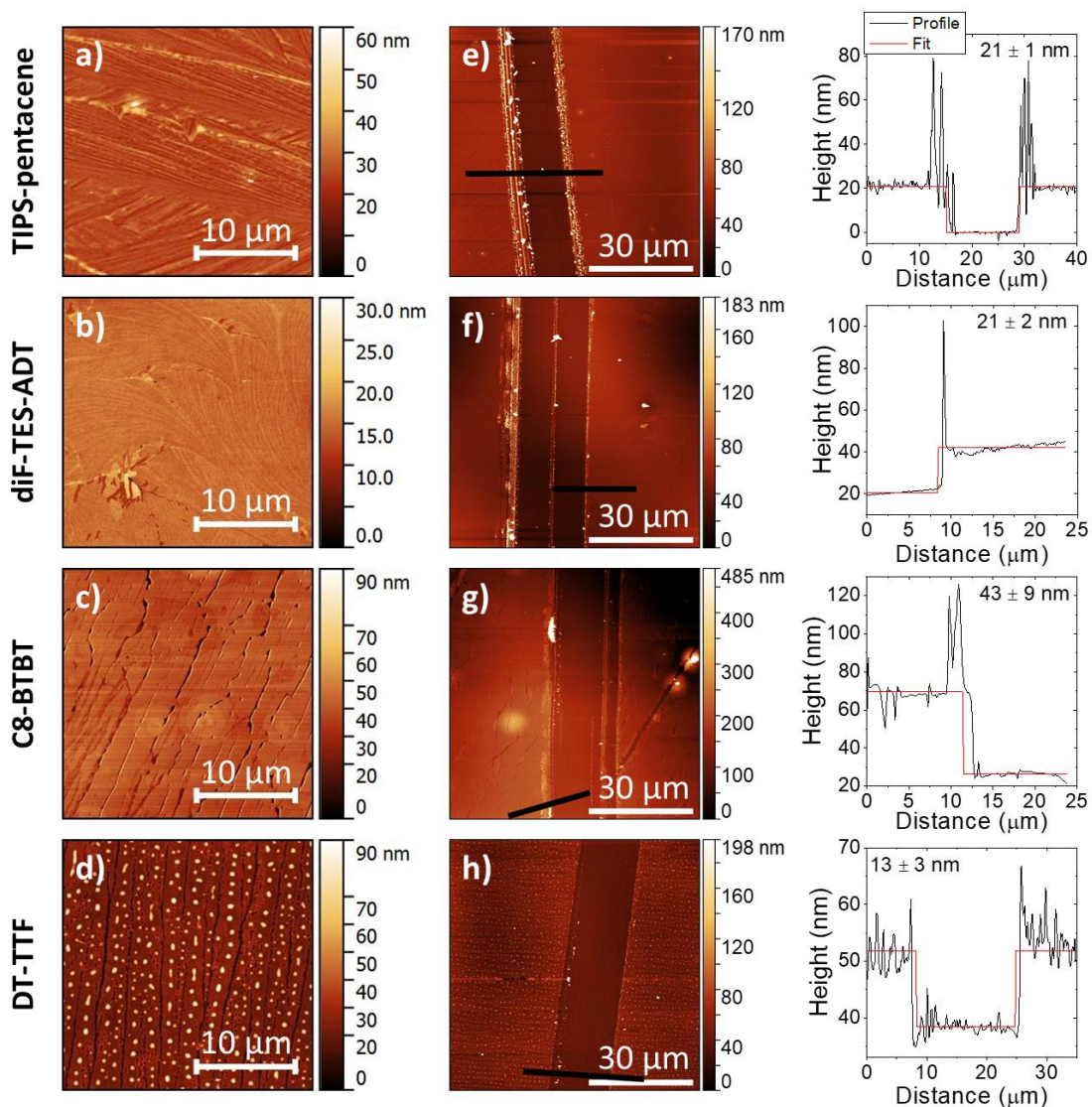


**Figure 2.3.** (a-d) AFM topography images and (e-h) height step for thickness estimation of thin films based on TIPS-pentacene, diF-TES-ADT, C8-BTBT and DT-TTF blends. The black bar indicates the path in which the height profile has been obtained.

The high degree of crystallinity of the films was confirmed by X-ray powder diffraction (**Figure 2.4**). The diffraction patterns of TIPS-pentacene and diF-TES-ADT are in agreement with the triclinic phases previously reported for both materials, where the molecules present a brick wall-like face-to-face arrangement resulting in a 2D  $\pi$ -stack.<sup>19–22</sup> On the other hand, the crystal phase of C8-BTBT and DT-TTF correspond to their known monoclinic crystal structures, in which molecules arrange in a herringbone configuration.<sup>14,23</sup> In particular, DT-TTF crystallizes in its already known  $\beta$ -phase. It is interesting to note that only  $(00l)$  type reflections were observed for all the studied OSCs, indicating that the crystallites in the thin films are highly oriented with the  $ab$  plane parallel to the substrate. This is the most favourable scenario for charge transport since corresponds to the plane where intermolecular electronic interactions exist.

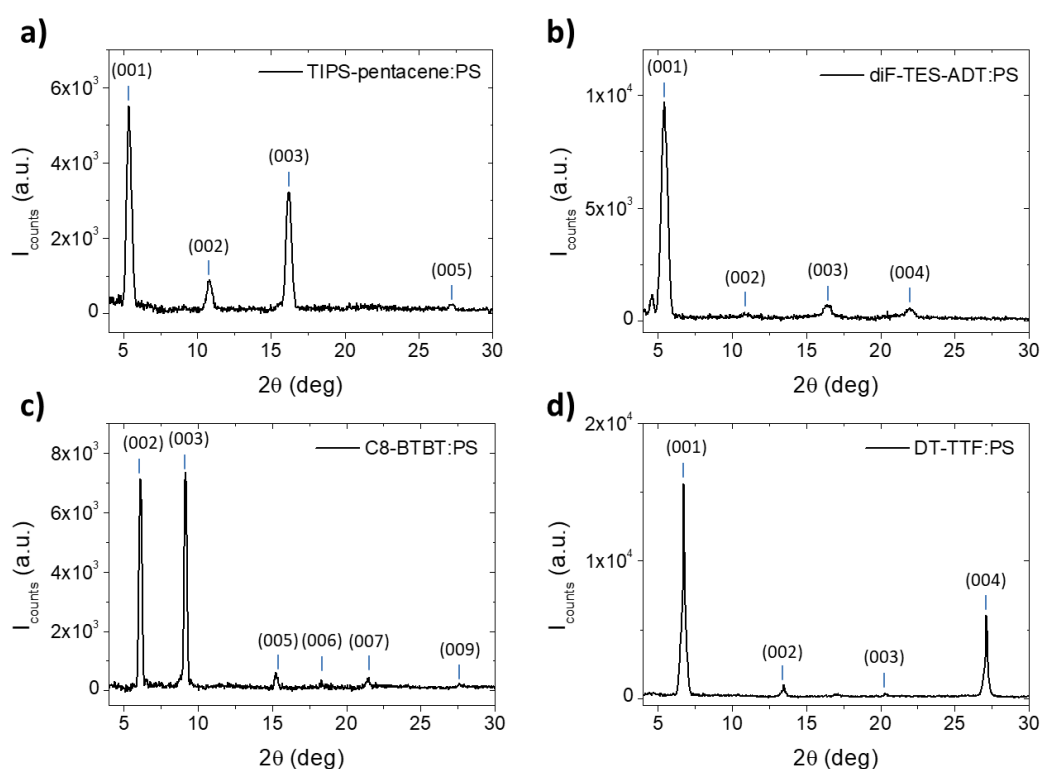


**Figure 2.4.** X-ray diffractograms of thin films based on (a) TIPS-pentacene, (b) diF-TES-ADT, (c) C8-BTBT and (d) DT-TTF blended with PS.

X-ray photoelectron spectroscopy (XPS) measurements were performed to analyse the chemical composition at the thin-films surface. In **Figure 2.5** the C1s, Si2p and S2p core level lines, measured at different incidence angles between 0° (normal to the surface) and 60° (grazing incidence), are shown. The observation of the Si (for TIPS-pentacene) or S (for diF-TES-ADT, C8-BTBT and DT-TTF) signals at grazing incidence, i.e., when the studied depth is minimised, suggests the presence of the OSCs at the top film surface.

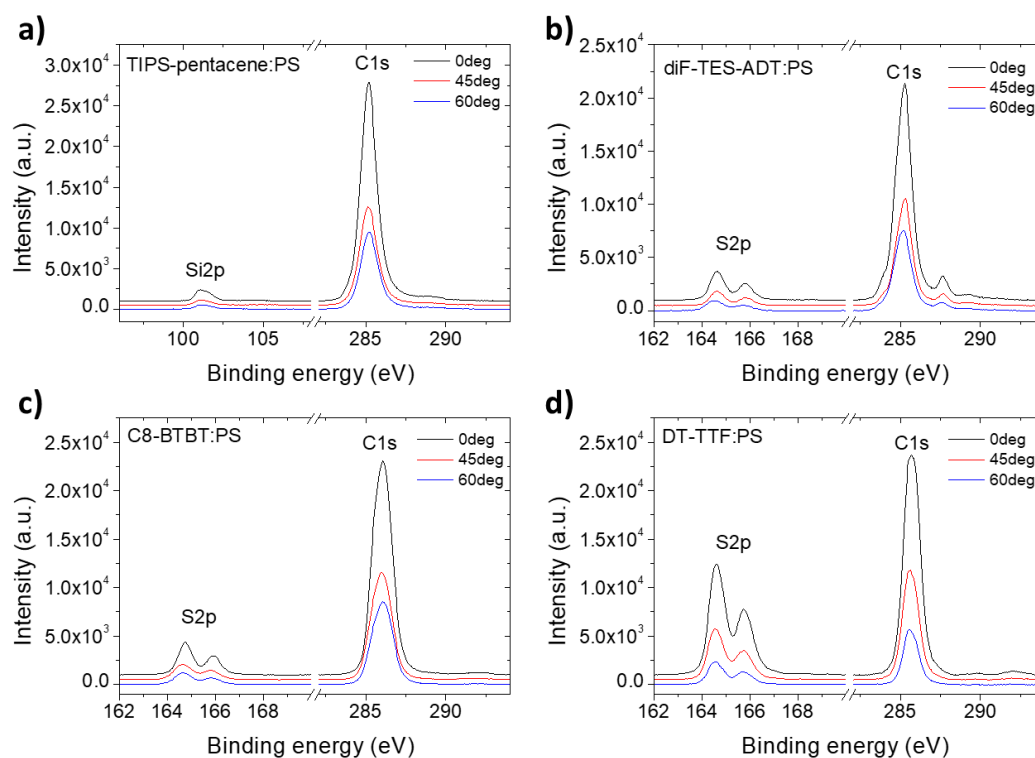


**Figure 2.5.** XPS spectra of the C1s, Si2p and S2p of thin films based on (a) TIPS-pentacene, (b) diF-TES-ADT, (c) C8-BTBT and (d) DT-TTF blended with PS for different incidence angles.



The distribution of these elements at different film depths was analysed using time-of-flight secondary ion mass spectrometry (ToF-SIMS) (**Figure 2.6**). The content profiles suggest that there is a vertical phase separation where the OSC layer is formed on top of a PS layer. Such stratification during the OSC crystallisation has been commonly observed in other blends.<sup>9,24</sup> In particular, diF-TES-ADT and C8-BTBT profiles indicate a major content of S (and F, for diF-TES-ADT) on the top part of the film, while the C signal remains almost constant until the interface with the Si/SiO<sub>2</sub> substrate is reached. On the other hand, for the TIPS-pentacene film the Si signal from the OSC and from the substrate cannot be distinguished. Even employing the SiC energy instead, information on the stratification of this blended film is not so accurate. Finally, the S and C signals in the DT-TTF profile drop almost at the same depth. However, their intensity slightly varies within the film thickness. Along with this result, from the ToF-SIMS data the thickness of the organic films could also be roughly estimated to be around 27, 19, 41, and 15 nm for TIPS-pentacene, diF-TES-ADT, C8-BTBT and DT-TTF, respectively. It should be noticed that these values are also in agreement with the previous AFM studies.

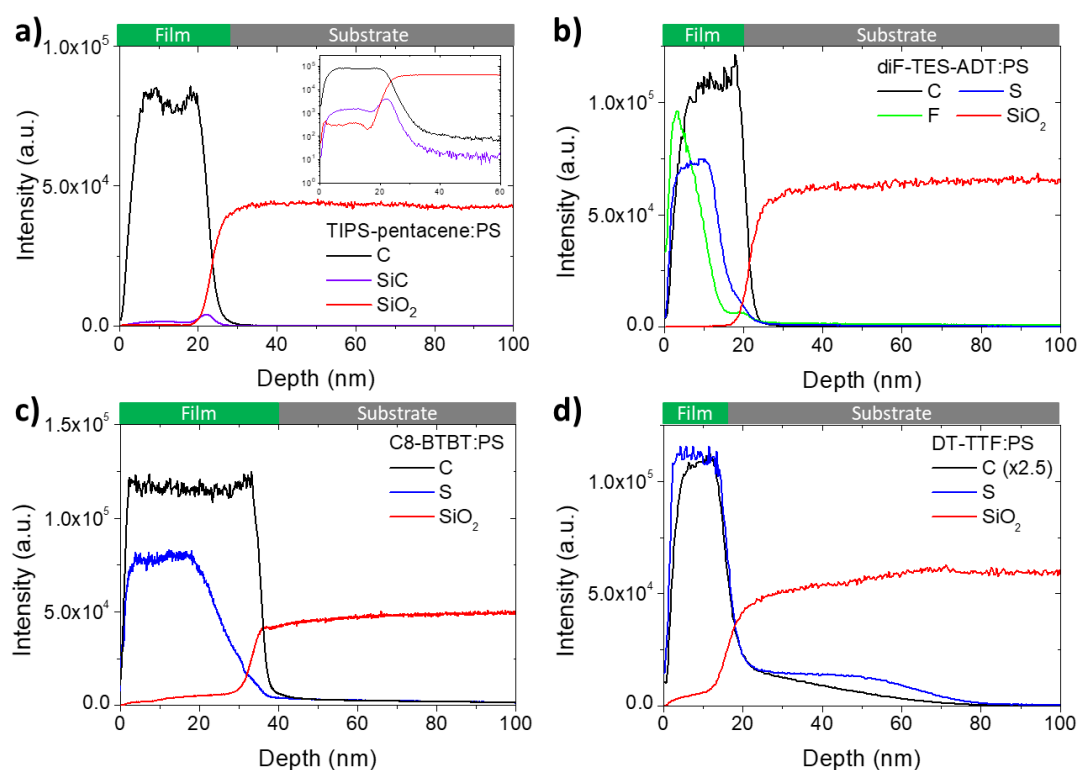


**Figure 2.6.** ToF-SIMS depth profiles of C, SiC, S, F, and SiO<sub>2</sub> of thin films based on (a) TIPS-pentacene, (b) diF-TES-ADT, (c) C8-BTBT and (d) DT-TTF blended with PS, starting from the surface and reaching the Si/SiO<sub>2</sub> substrate.

## 2.4 OFET ELECTRICAL CHARACTERISATION

---

OFET devices based on the four investigated blends, TIPS-pentacene, diF-TES-ADT, C8-BTBT and DT-TTF with PS, were electrically measured under ambient conditions. A statistical analysis was performed using several devices prepared on different areas of one film but also on different substrates, to ensure film homogeneity and device-to-device reproducibility.

Typical saturation transfer characteristics and mobility profiles of devices based on TIPS-pentacene, diF-TES-ADT, C8-BTBT and DT-TTF are shown in **Figure 2.7 (a-d)** and **Figure 2.7 (e-h)**, respectively, and the corresponding output curves are collected in **Figure 2.7 (i-l)**. The main parameters of the measured OFETs, including average and standard deviation values, are summarised in **Table 2.2**. For TIPS-pentacene, the transfer (and the output) characteristics showed a very small hysteresis between the forward and reverse  $V_{SG}$  (and  $V_{SD}$ ) sweeps, which indicates a pristine semiconductor/dielectric interface. Furthermore, the measured devices exhibited a high average ( $\mu_{FE,av}$ ) and maximum ( $\mu_{FE,max}$ ) field-effect mobility of  $1.6 \text{ cm}^2/\text{V}\cdot\text{s}$  and  $2.1 \text{ cm}^2/\text{V}\cdot\text{s}$ , respectively, which were extracted in the saturation regime. Also, a low average threshold voltage of about  $V_{th} = -0.9 \text{ V}$  was extracted. A similar picture is found for diF-TES-ADT based devices, for which the field-effect mobility was found to be  $\mu_{FE,av} = 1.3 \text{ cm}^2/\text{V}\cdot\text{s}$  and  $\mu_{FE,max} = 1.9 \text{ cm}^2/\text{V}\cdot\text{s}$ , while the average threshold voltage extracted is  $V_{th} = +0.8 \text{ V}$ . It is worth noting that devices based on both TIPS-pentacene and diF-TES-ADT semiconductors turn on at a source-gate voltage near to  $0 \text{ V}$  and afterwards the current is enhanced by 7 orders of magnitude, giving an *on/off* ratio of  $10^7$ . Also, in both cases no significant injection problems are observed in the output characteristics. In the case of C8-BTBT based OFETs, an average and maximum field-effect mobility of  $\mu_{FE,av} = 0.3 \text{ cm}^2/\text{V}\cdot\text{s}$  and  $\mu_{FE,max} = 0.7 \text{ cm}^2/\text{V}\cdot\text{s}$  were extracted in the saturation regime. On the other hand, an average threshold voltage of  $V_{th} = -29 \text{ V}$  was found. This high negative value is in agreement with previous studies employing this organic semiconductor and other BTBT derivatives, and is related with the high injection barrier that holes must overcome due to the mismatch between the HOMO and the work-function of the gold electrode.<sup>25-27</sup> This issue has also an impact on the contact resistance of the devices, which gives rise to the low linearity observed at low source-drain voltage in the output characteristics. Finally, the average and maximum field-effect mobility shown by DT-TTF based devices were  $\mu_{FE,av} = 0.10 \text{ cm}^2/\text{V}\cdot\text{s}$  and  $\mu_{FE,max} = 0.13 \text{ cm}^2/\text{V}\cdot\text{s}$ , respectively, as well as an average threshold voltage of  $V_{th} = +3.9 \text{ V}$ . These mobility values are as high as the ones previously reported for single crystals of the DT-TTF  $\beta$ -phase.<sup>14</sup> Devices based on both C8-BTBT and DT-TTF semiconductors showed a slightly smaller *on/off* ratio, on the order of  $10^6$ - $10^7$ . It is also worth mentioning that the mobility dependence with the source-gate voltage is

quite small, indicative of the high crystalline quality of all the deposited semiconducting films.

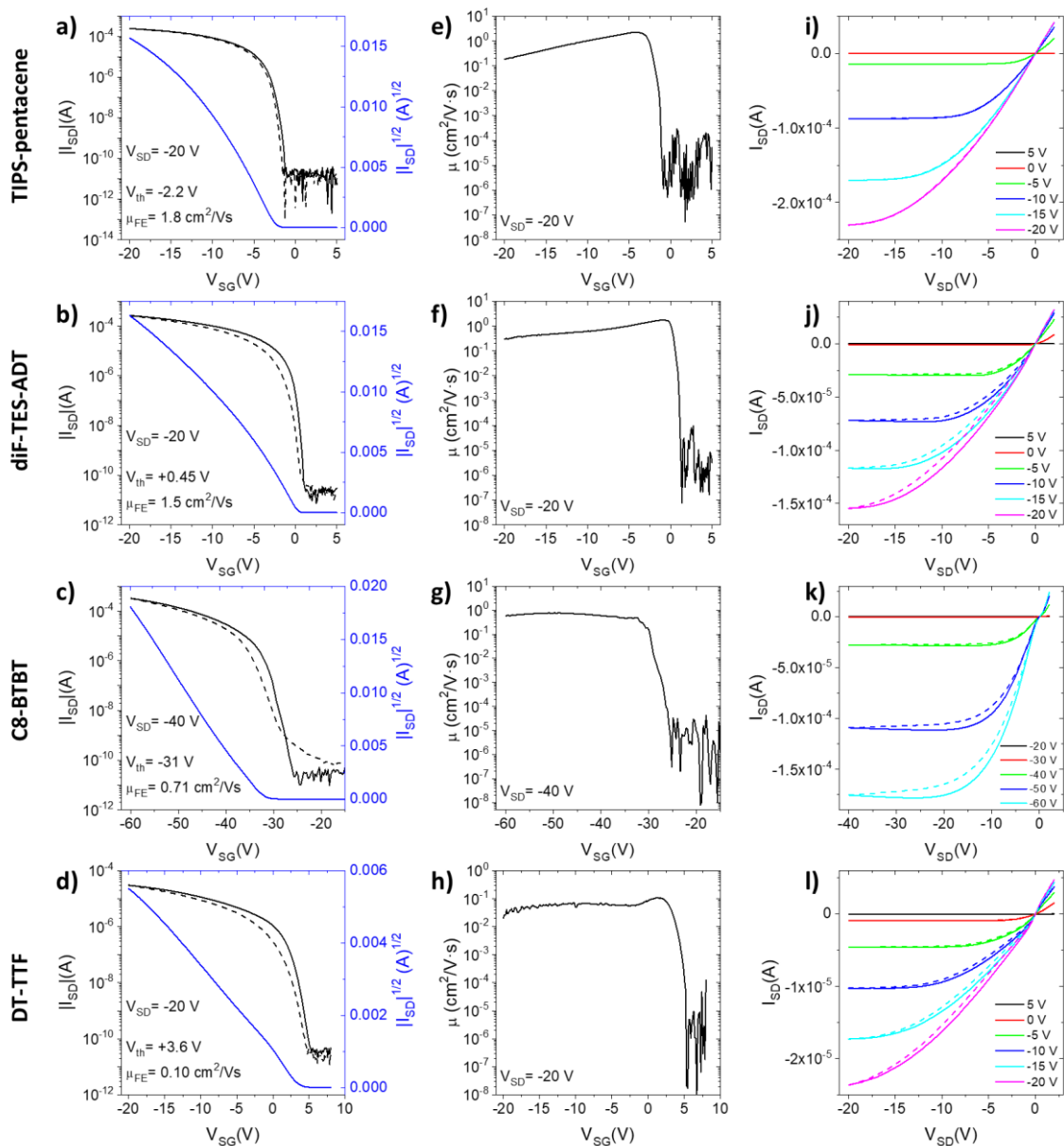


**Figure 2.7.** Electrical characteristics of typical OFET devices based on blends of TIPS-pentacene, diF-TES-ADT, C8-BTBT and DT-TTF. (a-d) Transfer characteristics in the saturation regime and square root of the absolute value of the source-drain current vs. source-gate voltage for the extraction of field-effect mobility and threshold voltage. (e-h) Mobility profiles in saturation regime. (i-l) Output characteristics. Straight and dashed lines correspond to forward and reverse sweeps, respectively, for both transfer and output characteristics.

**Table 2.2.** Main OFET parameters of the studied OSC:PS blends for a statistical amount of devices ( $n_{\text{OFETs}}$ ). The on-current, mobility and threshold voltage were extracted in the saturation regime. \*Indicates the high mobility achieved by some C8-BTBT devices, considered as outliers for the statistical analysis.

OSC	$on/off$	$\mu_{FE,av}$ ( $\text{cm}^2/\text{V}\cdot\text{s}$ )	$\mu_{FE,max}$ ( $\text{cm}^2/\text{V}\cdot\text{s}$ )	$V_{th}$ (V)	$n_{\text{OFETs}}$
TIPS-pentacene	$10^7$	$1.6 \pm 0.2$	2.1	$-0.9 \pm 1.1$	36
diF-TES-ADT	$10^7$	$1.3 \pm 0.2$	1.9	$+0.8 \pm 0.5$	34
C8-BTBT	$10^6$ - $10^7$	$0.26 \pm 0.16$	0.71 (*1.6)	$-29 \pm 5$	13
DT-TTF (  )	$10^6$ - $10^7$	$0.10 \pm 0.01$	0.13	$+3.9 \pm 0.9$	14
DT-TTF ( $\perp$ )	$10^5$ - $10^6$	$0.022 \pm 0.011$	0.032	$+1.4 \pm 0.9$	15

As could be expected from the morphological anisotropy shown by DT-TTF films, whose domains grow along the shearing direction (see **Figure 2.8 (a)**), OFET devices showed electrical anisotropy too. The measured field-effect mobility was around one order of magnitude higher when the device channel length was parallel to the shearing direction than when it was perpendicular to it (**Table 2.2**). For comparison, the transfer characteristics of a typical device processed perpendicularly to the channel length is depicted in **Figure 2.8 (b)**. The observed difference can be ascribed to the orientation of the molecular stacking axis along the shearing direction, resulting in the presence of less grain boundaries and a more favourable charge transport when it is parallel to the transistor channel length; hence, better performing OFETs are obtained. On the other hand, the rest of the materials were fully isotropic.

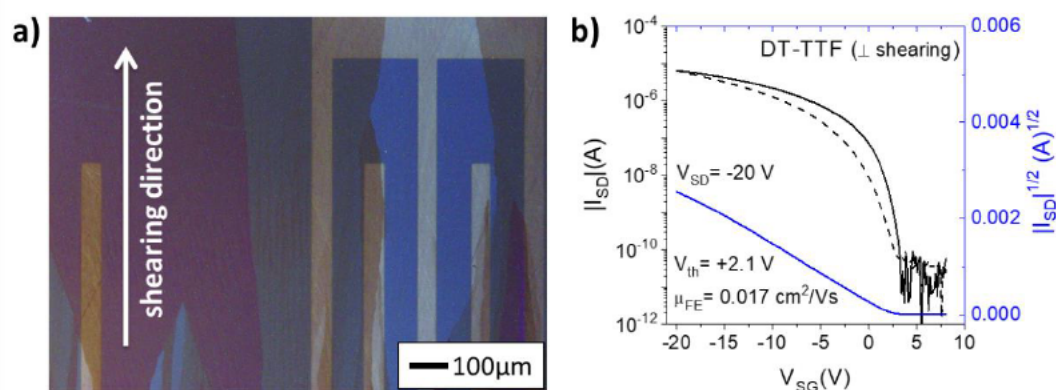


**Figure 2.8.** Typical DT-TTF:PS device prepared with the shearing direction perpendicular to the device channel length. (a) Crossed-polarised optical microscope image. (b) Transfer characteristics in the saturation regime and square root of the absolute value of the source-drain current vs. source-gate voltage for the extraction of field-effect mobility and threshold voltage. Straight and dashed lines correspond to forward and reverse sweeps of source-gate voltage, respectively.

The box-plot of **Figure 2.9** collects the mobility values of all the TIPS-pentacene, diF-TES-ADT, C8-BTBT, and DT-TTF devices that were measured for this statistical study. Note that only the best performing DT-TTF (II) devices, that is, the ones processed with the shearing direction parallel to the channel length, have been considered. In this kind of plot, all the data between the first and the third quartile is gathered inside the box, and the mean, the maximum and the minimum values are also clearly indicated. It can be observed that there is not a large dispersion between the mobility values exhibited by each semiconductor, which indicates that there is a low device-to-device variation thanks to the high uniformity of the films obtained with the BAMS processing technique.

It should be highlighted that the broader dispersion shown by C8-BTBT based devices arises from the less reproducible top electrodes, since the gold evaporation and posterior penetration into the organic thin film can determine the final performance exhibited by the devices. Indeed, a couple of devices based on C8-BTBT showed an outstanding mobility ( $\mu_{FE}$  up to  $1.6 \text{ cm}^2/\text{V}\cdot\text{s}$ ). However, they were considered as outliers and thus they were not included in the data set for statistical calculations, see the blue stars in **Figure 2.9**. This result is in fact a clear indicator of the high quality of the crystalline C8-BTBT thin film and the lack of a proper contact optimisation for this kind of devices.

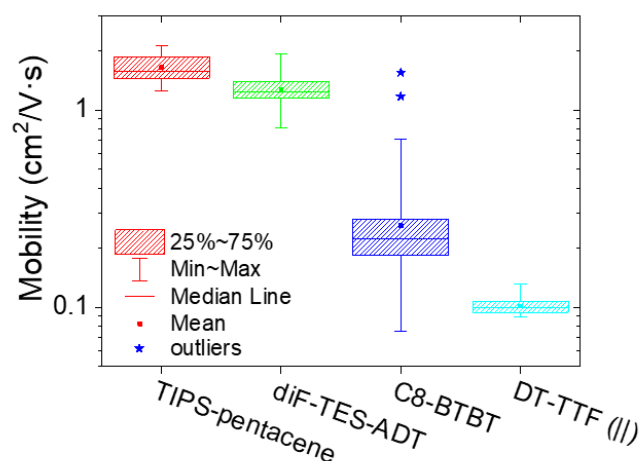


**Figure 2.9.** Box-plot for field-effect mobility values for TIPS-pentacene, diF-TES-ADT, C8-BTBT, and DT-TTF (II) based devices extracted in the saturation regime. For each data set, the box includes all the data between the first and the third quartile, and the line inside each box is the second quartile or the median. The square represents the mean value and the extremes are the maxima and minima data found.

## 2.5 COMPARISON WITH SIMILAR REPORTED DEVICES PROCESSED FROM SOLUTION

---

The mobility values achieved by the OFET devices based on TIPS-pentacene, diF-TES-ADT, C8-BTBT and DT-TTF processed by BAMS have been carefully compared with other recent works employing solution techniques compatible with roll-to-roll. **Table 2.3** collects the experimental conditions, including the velocity of the coating process, the use of post-treatments or a polymeric binder, as well as the OFET mobility reached (either the average or the maximum value).

Most of the efforts on engineering high-performing OFET devices have been placed on TIPS-pentacene and diF-TES-ADT. Both materials have been carefully investigated by Bao and coworkers, who developed a shearing technique consisting in the confinement of the semiconducting ink between a heated phenyltrichlorosilane (PTS) SiO<sub>2</sub> modified substrate and a top silicon wafer plate functionalised with a monolayer of octadecyltrichlorosilane (OTS).<sup>28</sup> Then, the shearing plate drags the solution across the substrate keeping the bulk of the solution between the plate and the substrate, with only the evaporation front exposed. This methodology resulted in mobility values of up to 4.6 and 6.7 cm<sup>2</sup>/V·s for TIPS-pentacene and diF-TES-ADT, respectively.<sup>12,29</sup> For TIPS-pentacene, mobilities up to 11 cm<sup>2</sup>/V·s were also reported when plates with patterned micropillars were used, although in that case the resulting films were very anisotropic.<sup>30</sup> However, it should be noted that in all these blade coating experiments the speed is typically one order of magnitude smaller than the one used by BAMS. Only in two cases these materials have been printed at a comparable speed, but not only the mobility values achieved were lower but also either a long post-treatment step was required<sup>31</sup> or a semiconducting polymer was used as binder.<sup>32</sup>

Similarly, C8-BTBT semiconductor has been extensively studied employing processing techniques such as drop-casting<sup>33,34</sup> or spin-coating<sup>13,27,35</sup> followed by additional crystallisation steps; however, both are far from being scalable. Working in this direction, blade coating or zone casting have also been utilized for the deposition of C8-BTBT. In particular, a mobility of 9.2 cm<sup>2</sup>/V·s was reported from thin films processed by the previously mentioned plate-shearing technology.<sup>36</sup> However, the slow shearing speed employed (0.05 mm/s) resulted in anisotropic films and poor substrate coverage ranging from 65 to 80% of the total channel area. Indeed, the mobility value was compensated for the covered channel width. Without this correction, the device effective mobility was between 6 and 7.4 cm<sup>2</sup>/V·s. In a latter work, a similar ribbon like morphology was obtained but, in this case, the addition of a polymer binder permitted increasing the deposition speed to 0.25 mm/s while boosting the device mobility up to 12 cm<sup>2</sup>/V·s.<sup>37</sup> Finally, high mobility films of DT-TTF have been previously fabricated by zone-casting.<sup>38</sup> Nevertheless, this is a far too slow processing technique for industrial applications. Considering all the



above results, the mobility exhibited by the OFETs fabricated by BAMS can be regarded as state-of-the-art, especially taking into account the high speed of this processing technique.

**Table 2.3.** Comparison of reported results of TIPS-pentacene, diF-TES-ADT, C8-BTBT and DT-TTF based OFETs processed from solution-based techniques compatible with roll-to-roll, highlighting some of the experimental details as the coating speed ( $v$ ), the use of post-treatments, the binder used (if any), and the maximum ( $\mu_{FE,max}$ ) and average ( $\mu_{FE,av}$ ) mobility values achieved. nr stands for not reported. Binders: P $\alpha$ MS (poly( $\alpha$ -methylstyrene)), PS (polystyrene), PTAA (poly[bis(4-phenyl)-(2,4,6-trimethylphenyl)amine]).

OSC	Experimental method details	$v$ (mm/s)	Binder	$\mu_{FE,av}$ (cm <sup>2</sup> /V·s)	$\mu_{FE,max}$ (cm <sup>2</sup> /V·s)	Ref.
TIPS-pentacene	Horizontal dipping, post-treatment at 100 °C for 60 min	15	P $\alpha$ MS	0.15	0.22	(31)
	Shearing plate 8° tilt, substrate and plate chemically modified, 70 °C	≈1	P $\alpha$ MS	nr	4.6	(12)
	Shearing plate 8° tilt, substrate and plate chemically modified, plate with patterned micropillars, 135 °C	0.6	--	8.1	11	(30)
	<b>BAMS</b>	<b>10</b>	<b>PS</b>	<b>1.6</b>	<b>2.1</b>	
diF-TES-ADT	Doctor Blade coating in a glovebox, drying, and post-treatment at 100 °C for 10 min and cooling to 65 °C	10-20	PTAA	0.68	1.6	(32)
	Shearing plate 8° tilt, substrate and plate chemically modified, 70 °C	≈1	P $\alpha$ MS	nr	3.6	(12)
	Shearing plate 8° tilt, substrate and plate chemically modified, dual solvent, 100 °C	0.5	PS	nr	6.7	(29)
	<b>BAMS</b>	<b>10</b>	<b>PS</b>	<b>1.3</b>	<b>1.9</b>	
C8-BTBT	Shearing plate 8° tilt, substrate and plate chemically modified, stage at 50 °C	0.05	--	6-7.4	nr	(36)
	Shearing plate 8° tilt, PTS modified substrate, stage at 30 °C, annealing at 50 °C for 70 h	0.25	PS	12	nr	(37)
	<b>BAMS</b>	<b>10</b>	<b>PS</b>	<b>0.26</b>	<b>1.6</b>	
DT-TTF	Zone-casting at 60 °C	0.03	--	nr	0.17	(38)
	<b>BAMS</b>	<b>10</b>	<b>PS</b>	<b>0.10</b>	<b>0.13</b>	

## 2.6 DEVELOPMENT OF DEVICES FOR AQUEOUS MEDIA OPERATION

The excellent performance shown by the previously studied TIPS-pentacene and diF-TES-ADT based OFETs lead us to pursue a more ambitious objective: the development of organic electronic devices for aqueous media operation. A huge interest lies on this kind of devices since they are considered a promising sensing platform for new applications, especially in the field of bioelectronics. In particular, the configuration of electrolyte-gated organic field-effect transistors (EGOFETs) consists of a top electrode (gate) immersed in an electrolytic solution that is in direct contact with the semiconducting film and acts as the effective gate dielectric, as depicted in **Figure 2.10**. Interestingly, the two electrical double layers (EDLs) established at the top gate/electrolyte and electrolyte/OSC interfaces bear a capacitance in the order of  $\mu\text{F}/\text{cm}^2$ , instead of  $\text{nF}/\text{cm}^2$  as for standard dielectrics. As a result, the operational voltages are drastically lowered.

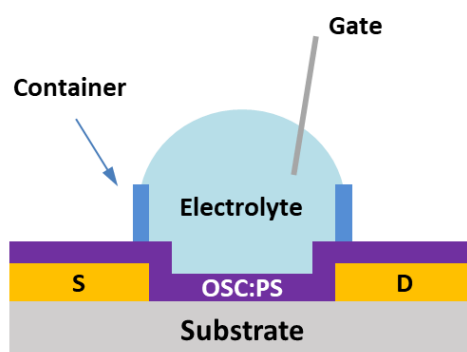


**Figure 2.10.** Schematic representation of the EGOFET configuration.

The extended homogeneity and crystallinity of the semiconducting thin films deposited by BAMS are two of the desirable features for EGOFETs operability. Further, the addition of a binding polymer (PS) has already demonstrated to be an efficient strategy to improve the stability of EGOFET devices against water or strong ionic aqueous solutions thanks to the encapsulation of the moisture sensitive OSC by a thin polymer layer.<sup>24</sup> Thus, we decided to test the TIPS-pentacene and diF-TES-ADT blended thin films as active materials in EGOFETs. Although a full electrical characterisation was performed in our group by Q. Zhang et al.<sup>39</sup>, only the main results will be presented herein.



## EGOFET electrical characterisation

A Pt wire was employed as top gate electrode, while MilliQ water was chosen as electrolyte media to study the transistor operation. As expected, the transfer characteristics of TIPS-pentacene:PS and diF-TES-ADT:PS based EGOFETs, shown in **Figure 2.11 (a-b)**, exhibit p-type behaviour in a  $V_{SG}$  window ranging from 300 mV to -500 mV. The corresponding output characteristics are displayed in **Figure 2.11 (c-d)**. In order to obtain more information about the role that the presence of PS plays in the electrical performance, devices without PS were also fabricated as a cross-check (shown in red in **Figure 2.11**). The transfer characteristics of both OSC:PS blends do not show hysteresis and the devices have excellent amplification capability (namely both have an *on/off* ratio close to  $10^4$ , as shown in **Table 2.4**). On the contrary, when PS is not present in the active layer, the current dramatically decreases by one or two orders of magnitude, which is related to the smaller crystal size obtained and the absence of the stabilising effect of PS. This demonstrates, as it was previously observed in OFET configuration, the beneficial effects derived from the addition of the binder polymer as regards device performance. Considering this, the following characterisation studies have been carried out only on OSC:PS blended devices.

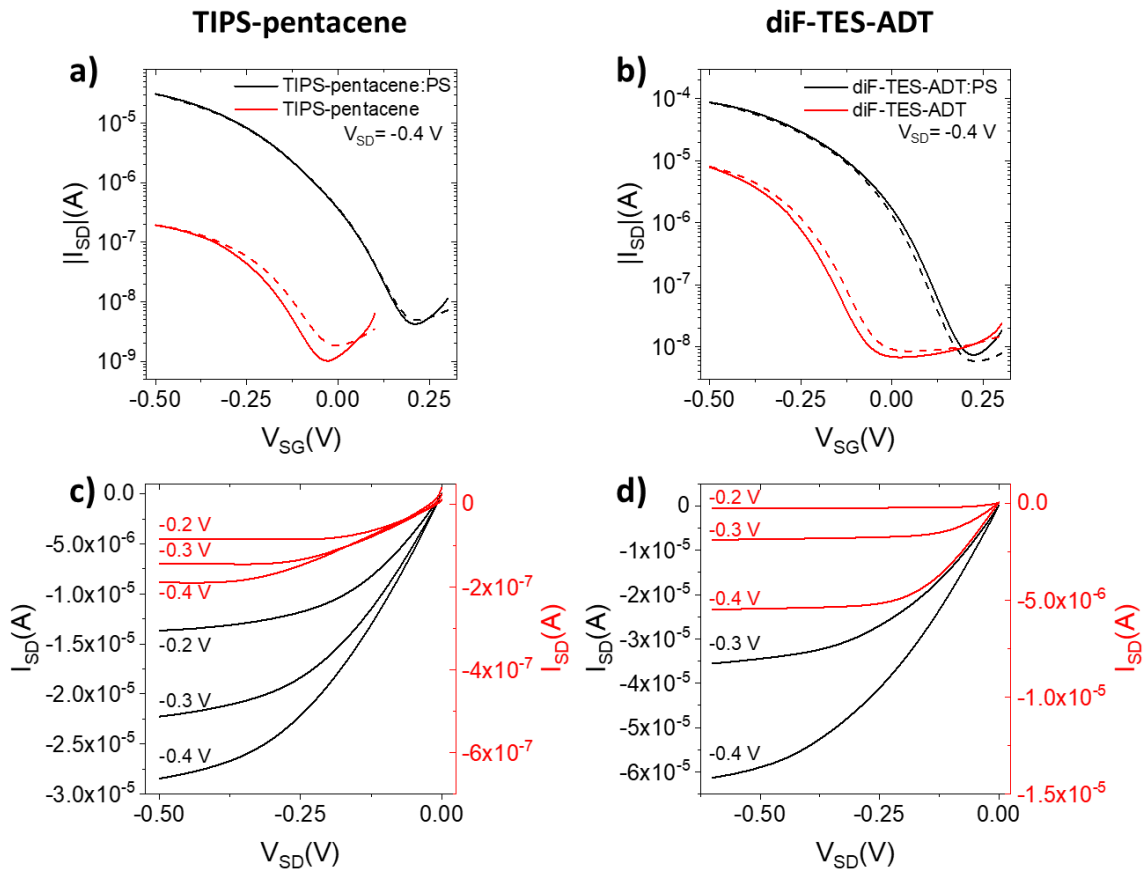


**Figure 2.11.** Electrical characteristics in MilliQ water of EGOFET devices based on TIPS-pentacene and diF-TES-ADT blended or not with PS. (a-b) Transfer characteristics in the saturation regime. (c-d) Output characteristics. Straight and dashed lines correspond to forward and reverse sweeps, respectively.

In order to calculate the EGOFET mobility ( $\mu_{EGOFET}$ ) in saturation regime of PS containing devices, the dielectric capacitance was first extracted through electrochemical impedance spectroscopy measurements by short-circuiting S/D electrodes and applying different values of gate bias while scanning the frequency. A capacitance of  $2.9 \mu\text{F}/\text{cm}^2$  and  $5.3 \mu\text{F}/\text{cm}^2$  was found for TIPS-pentacene and diF-TES-ADT based devices in MilliQ water, respectively, at a reference frequency of 10 Hz and  $V_{SG} = -0.4 \text{ V}$ .<sup>39</sup> These values are comparable to others reported for thin films based on different semiconductors, such as pentacene or poly(3-hexylthiophene) (P3HT).<sup>40,41</sup> The corresponding mobility ( $\mu_{EGOFET}$ ) and threshold voltage ( $V_{th}$ ) values extracted for the prepared EGOFETs are summarised in **Table 2.4**. The data shown here include the average values together with the standard deviations extracted for at least 10 devices of each type.

**Table 2.4.** Main EGOFET parameters in the saturation regime for TIPS-pentacene:PS and diF-TES-ADT:PS devices measured in MilliQ water. \*These values are affected by an error ranging from 2% to 20%.

OSC	<i>on/off</i>	$\mu_{EGOFET}$ ( $\text{cm}^2/\text{V}\cdot\text{s}$ )*	$V_{th}$ (mV)	<i>max P.S.</i> ( $\mu\text{V}$ )	$\tau_{on}$ (ms)	$\tau_{off}$ (ms)
TIPS-pentacene	$7.3 \cdot 10^3$	0.12	$12 \pm 2$	100	0.45	0.25
diF-TES-ADT	$1.5 \cdot 10^4$	0.18	$49 \pm 1$	200	0.65	0.31

### Potentiometric sensitivity and switching speed

If EGOFETs are to be used as sensing platforms, it is important to study their ability to transduce a chemical or biological signal into a measurable electric current. One interesting figure of merit is the potentiometric sensitivity (*P.S.*), which is the lowest voltage shift that can be detected by the system. For both TIPS-pentacene and diF-TES-ADT based EGOFETs, square pulses of source-gate voltage ( $\Delta V_{SG}$ ) ranging from 50 mV to 100  $\mu\text{V}$  were applied to the devices and the corresponding output current was recorded, as shown in **Figure 2.12 (a-b)**. The former devices turned out to be more sensitive reaching sensitivities down to 100  $\mu\text{V}$ , whereas the latter ones were capable to detect  $\Delta V_{SG}$  equal to 200  $\mu\text{V}$ , as displayed in **Table 2.4**. In both cases, the signal to noise ratio was equal to 50.

Also important is the speed of the response, that would permit to detect punctual fluctuations of the input signal. To obtain the EGOFETs switching speed ( $\tau$ ), a  $V_{SG}$  pulse from 0 V to -500 mV and vice versa was applied while the corresponding output current

was monitored as a function of time (**Figure 2.12 (c-d)**). The two potential changes, which correspond to the channel formation and disruption, have been exponentially fitted ( $I_{SD} \propto e^{\pm t/\tau}$ ) in order to extract the characteristic time response, i.e.,  $\tau_{on}$  and  $\tau_{off}$ . The  $\tau$  values listed in **Table 2.4** show a slight asymmetry between switch-on and switch-off, as already published for other EGOFETs.<sup>41</sup> It is important to highlight that our devices are at least one order of magnitude faster than previously reported EGOFETs, for which  $\tau$  was found to be 4.6 ms and 50 ms for devices based on a pentacene evaporated film and a spin-coated P3HT film, respectively.<sup>40,41</sup> Indeed, the  $\tau$  values here reported are lower than 1 ms, indicating that the devices can work at frequencies higher than 1 kHz.

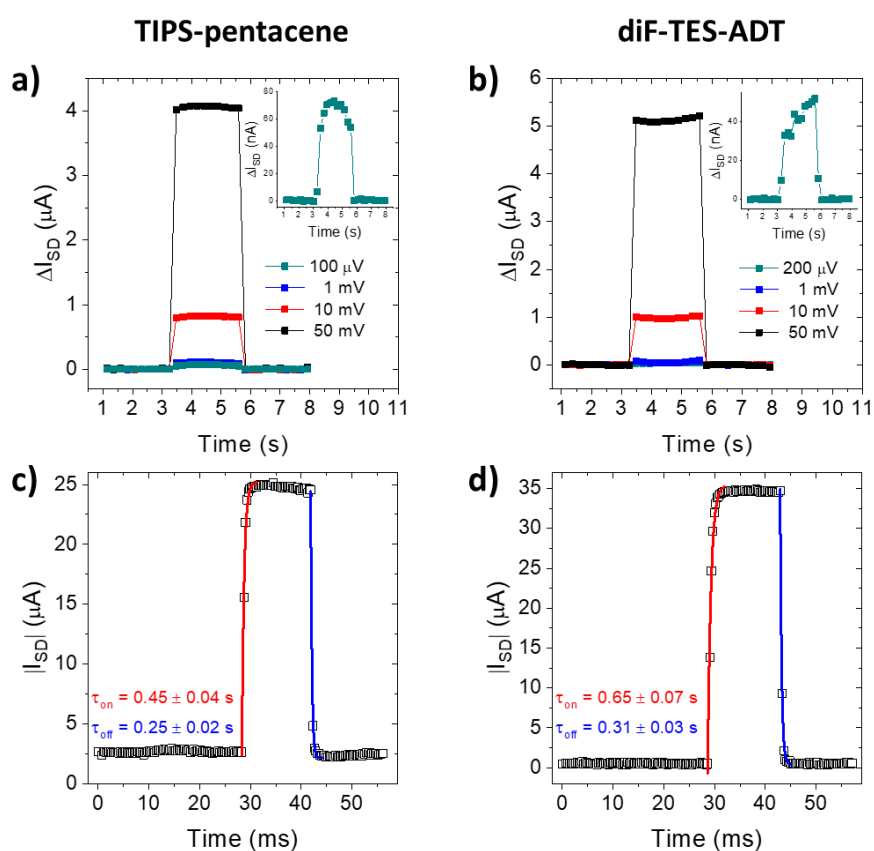


**Figure 2.12.** (a-b) Potentiometric sensitivity for different step potentials ( $\Delta V_{SG}$ ) and (c-d) switching speed measurements with the exponential fit used to obtain the switch-on (in red) and switch-off time (in blue) of TIPS-pentacene:PS and diF-TES-ADT:PS EGOFETs in MilliQ water. All measurements were recorded in saturation regime ( $V_{SD} = -0.4$  V).

Thus, our approach of combining OSC:PS blends with BAMS as solution processing technique allowed to achieve highly crystalline and homogeneous thin films suitable for measurements in liquid environments, exhibiting remarkable EGOFET performance with respect to the state-of-the-art.

## 2.7 SUMMARY

---

In summary, four well-known organic semiconductors, namely TIPS-pentacene, diF-TES-ADT, C8-BTBT and DT-TTF, have been successfully deposited by BAMS employing a unified recipe for the ink formulation and thin-film processing. As confirmed by several characterisation techniques, thin films exhibit high homogeneity and crystallinity, thanks to the processability enhancement provided by the polymer binder. The resulting devices show high and reproducible performance with state-of-the-art mobilities, especially considering the high coating speed employed (i.e., 10 mm/s) and the lack of post-treatments. Importantly, these results demonstrate the versatility and applicability of BAMS and support the use of OSC:PS blends as a promising route for the fabrication of large-area uniform films. Finally, TIPS-pentacene and diF-TES-ADT blends were exploited as active layers in EGOFET devices, leading to robust behaviour in MilliQ water.

2.8 REFERENCES

---

- (1) Horowitz, G.; Fichou, D.; Peng, X.; Xu, Z.; Garnier, F. A Field-Effect Transistor Based on Conjugated Alpha-Sexithienyl. *Solid State Commun.* **1989**, *72* (4), 381–384.
- (2) Mas-Torrent, M.; Rovira, C. Novel Small Molecules for Organic Field-Effect Transistors: Towards Processability and High Performance. *Chem. Soc. Rev.* **2008**, *37*, 827–838.
- (3) Paterson, A. F.; Singh, S.; Fallon, K. J.; Hodsden, T.; Han, Y.; Schroeder, B. C.; Bronstein, H.; Heeney, M.; McCulloch, I.; Anthopoulos, T. D. Recent Progress in High-Mobility Organic Transistors: A Reality Check. *Adv. Mater.* **2018**, *30*, 1801079.
- (4) Lamport, Z. A.; Haneef, H. F.; Anand, S.; Waldrip, M.; Jurchescu, O. D. Tutorial: Organic Field-Effect Transistors: Materials, Structure and Operation. *J. Appl. Phys.* **2018**, *124*, 071101.
- (5) Xu, Y.; Liu, C.; Khim, D.; Noh, Y.-Y. Development of High-Performance Printed Organic Field-Effect Transistors and Integrated Circuits. *Phys. Chem. Chem. Phys.* **2015**, *17*, 26553–26574.
- (6) Diao, Y.; Shaw, L.; Mannsfeld, S. C. B. Morphology Control Strategies for Solution-Processed Organic Semiconductor Thin Films. *Energy Environ. Sci.* **2014**, *7*, 2145–2159.
- (7) del Pozo, F. G.; Fabiano, S.; Pfattner, R.; Georgakopoulos, S.; Galindo, S.; Liu, X.; Braun, S.; Fahlman, M.; Veciana, J.; Rovira, C.; et al. Single Crystal-Like Performance in Solution-Coated Thin-Film Organic Field-Effect Transistors. *Adv. Funct. Mater.* **2016**, *26*, 2379–2386.
- (8) Hamilton, R.; Smith, J.; Ogier, S.; Heeney, M.; Anthony, J. E.; McCulloch, I.; Veres, J.; Bradley, D. D. C.; Anthopoulos, T. D. High-Performance Polymer-Small Molecule Blend Organic Transistors. *Adv. Mater.* **2009**, *21*, 1166–1171.
- (9) Zhao, K.; Wodo, O.; Ren, D.; Khan, H. U.; Niazi, M. R.; Hu, H.; Abdelsamie, M.; Li, R.; Li, E. Q.; Yu, L.; et al. Vertical Phase Separation in Small Molecule:Polymer Blend Organic Thin Film Transistors Can Be Dynamically Controlled. *Adv. Funct. Mater.* **2016**, *26*, 1737–1746.
- (10) Riera-Galindo, S.; Leonardi, F.; Pfattner, R.; Mas-Torrent, M. Organic Semiconductor/Polymer Blend Films for Organic Field-Effect Transistors. *Adv. Mater. Technol.* **2019**, 1900104.
- (11) Georgakopoulos, S.; del Pozo, F. G.; Mas-Torrent, M. Flexible Organic Transistors Based on a Solution-Sheared PVDF Insulator. *J. Mater. Chem. C* **2015**, *3*, 12199–12202.

- (12) Niazi, M. R.; Li, R.; Abdelsamie, M.; Zhao, K.; Anjum, D. H.; Payne, M. M.; Anthony, J.; Smilgies, D.-M.; Amassian, A. Contact-Induced Nucleation in High-Performance Bottom-Contact Organic Thin Film Transistors Manufactured by Large-Area Compatible Solution Processing. *Adv. Funct. Mater.* **2016**, *26*, 2371–2378.
- (13) Yuan, Y.; Giri, G.; Ayzner, A. L.; Zoombelt, A. P.; Mannsfeld, S. C. B.; Chen, J.; Nordlund, D.; Toney, M. F.; Huang, J.; Bao, Z. Ultra-High Mobility Transparent Organic Thin Film Transistors Grown by an off-Centre Spin-Coating Method. *Nat. Commun.* **2014**, *5*, 3005.
- (14) Pfattner, R.; Mas-Torrent, M.; Bilotti, I.; Brillante, A.; Milita, S.; Liscio, F.; Biscarini, F.; Marszalek, T.; Ulanski, J.; Nosal, A.; et al. High-Performance Single Crystal Organic Field-Effect Transistors Based on Two Dithiophene-Tetrathiafulvalene (DT-TTF) Polymorphs. *Adv. Mater.* **2010**, *22*, 4198–4203.
- (15) Li, R.; Ward, J. W.; Smilgies, D.-M.; Payne, M. M.; Anthony, J. E.; Jurchescu, O. D.; Amassian, A. Direct Structural Mapping of Organic Field-Effect Transistors Reveals Bottlenecks to Carrier Transport. *Adv. Mater.* **2012**, *24*, 5553–5558.
- (16) Gundlach, D. J.; Royer, J. E.; Park, S. K.; Subramanian, S.; Jurchescu, O. D.; Hamadani, B. H.; Moad, A. J.; Kline, R. J.; Teague, L. C.; Kirillov, O.; et al. Contact-Induced Crystallinity for High-Performance Soluble Acene-Based Transistors and Circuits. *Nat. Mater.* **2008**, *7*, 216–221.
- (17) Ward, J. W.; Loth, M. a.; Kline, R. J.; Coll, M.; Ocal, C.; Anthony, J. E.; Jurchescu, O. D. Tailored Interfaces for Self-Patterning Organic Thin-Film Transistors. *J. Mater. Chem.* **2012**, *22*, 19047.
- (18) Kano, M.; Minari, T.; Tsukagoshi, K. Improvement of Subthreshold Current Transport by Contact Interface Modification in p -Type Organic Field-Effect Transistors. *Appl. Phys. Lett.* **2009**, *94*, 143304.
- (19) Mannsfeld, S. C. B.; Tang, M. L.; Bao, Z. Thin Film Structure of Triisopropylsilylethynyl-Functionalized Pentacene and Tetraceno[2,3-b]Thiophene from Grazing Incidence X-Ray Diffraction. *Adv. Mater.* **2011**, *23*, 127–131.
- (20) Anthony, J. E.; Eaton, D. L.; Parkin, S. R. A Road Map to Stable, Soluble, Easily Crystallized Pentacene Derivatives. *Org. Lett.* **2002**, *4*, 15–18.
- (21) Jurchescu, O. D.; Subramanian, S.; Kline, R. J.; Hudson, S. D.; Anthony, J. E.; Jackson, T. N.; Gundlach, D. J. Organic Single-Crystal Field-Effect Transistors of a Soluble Anthradithiophene. *Chem. Mater.* **2008**, *20*, 6733–6737.
- (22) Subramanian, S.; Sung, K. P.; Parkin, S. R.; Podzorov, V.; Jackson, T. N.; Anthony, J. E. Chromophore Fluorination Enhances Crystallization and Stability of Soluble Anthradithiophene Semiconductors. *J. Am. Chem. Soc.* **2008**, *130*, 2706–2707.

- (23) Izawa, T.; Miyazaki, E.; Takimiya, K. Molecular Ordering of High-Performance Soluble Molecular Semiconductors and Re-Evaluation of Their Field-Effect Transistor Characteristics. *Adv. Mater.* **2008**, *20*, 3388–3392.
- (24) Leonardi, F.; Casalini, S.; Zhang, Q.; Galindo, S.; Gutiérrez, D.; Mas-Torrent, M. Electrolyte-Gated Organic Field-Effect Transistor Based on a Solution Sheared Organic Semiconductor Blend. *Adv. Mater.* **2016**, *28*, 10311–10316.
- (25) Ebata, H.; Izawa, T.; Miyazaki, E.; Takimiya, K.; Ikeda, M.; Kuwabara, H.; Yui, T. Highly Soluble [1]Benzothieno[3,2-b]Benzothiophene (BTBT) Derivatives for High-Performance, Solution-Processed Organic Field-Effect Transistors. *J. Am. Chem. Soc.* **2007**, *129*, 15732–15733.
- (26) Liu, C.; Minari, T.; Lu, X.; Kumatani, A.; Takimiya, K.; Tsukagoshi, K. Solution-Processable Organic Single Crystals with Bandlike Transport in Field-Effect Transistors. *Adv. Mater.* **2011**, *23*, 523–526.
- (27) Colella, S.; Ruzié, C.; Schweicher, G.; Arlin, J.-B.; Karpinska, J.; Geerts, Y.; Samorì, P. High Mobility in Solution-Processed 2,7-Dialkyl-[1]Benzothieno[3,2-b][1]Benzothiophene-Based Field-Effect Transistors Prepared with a Simplified Deposition Method. *Chempluschem* **2014**, *79*, 371–374.
- (28) Giri, G.; Verploegen, E.; Mannsfeld, S. C. B.; Atahan-Evrenk, S.; Kim, D. H.; Lee, S. Y.; Becerril, H. a.; Aspuru-Guzik, A.; Toney, M. F.; Bao, Z. Tuning Charge Transport in Solution-Sheared Organic Semiconductors Using Lattice Strain. *Nature* **2011**, *480*, 504–508.
- (29) Niazi, M. R.; Li, R.; Qiang Li, E.; Kirmani, A. R.; Abdelsamie, M.; Wang, Q.; Pan, W.; Payne, M. M.; Anthony, J. E.; Smilgies, D.-M.; et al. Solution-Printed Organic Semiconductor Blends Exhibiting Transport Properties on Par with Single Crystals. *Nat. Commun.* **2015**, *6*, 8598.
- (30) Diao, Y.; Tee, B. C.-K.; Giri, G.; Xu, J.; Kim, D. H.; Becerril, H. a; Stoltenberg, R. M.; Lee, T. H.; Xue, G.; Mannsfeld, S. C. B.; et al. Solution Coating of Large-Area Organic Semiconductor Thin Films with Aligned Single-Crystalline Domains. *Nat. Mater.* **2013**, *12*, 665.
- (31) Park, B.; Jeon, H. G.; Choi, J.; Kim, Y. K.; Lim, J.; Jung, J.; Cho, S. Y.; Lee, C. High-Performance Organic Thin-Film Transistors with Polymer-Blended Small-Molecular Semiconductor Films, Fabricated Using a Pre-Metered Coating Process. *J. Mater. Chem.* **2012**, *22*, 5641.
- (32) Pierre, A.; Sadeghi, M.; Payne, M. M.; Facchetti, A.; Anthony, J. E.; Arias, A. C. All-Printed Flexible Organic Transistors Enabled by Surface Tension-Guided Blade Coating. *Adv. Mater.* **2014**, *26*, 5722–5727.
- (33) Minari, T.; Kano, M.; Miyadera, T.; Wang, S. D.; Aoyagi, Y.; Tsukagoshi, K. Surface

- Selective Deposition of Molecular Semiconductors for Solution-Based Integration of Organic Field-Effect Transistors. *Appl. Phys. Lett.* **2009**, *94*, 093307.
- (34) Minari, T.; Kanehara, Y.; Liu, C.; Sakamoto, K.; Yasuda, T.; Yaguchi, A.; Tsukada, S.; Kashizaki, K.; Kanehara, M. Room-Temperature Printing of Organic Thin-Film Transistors with Pi-Junction Gold Nanoparticles. *Adv. Funct. Mater.* **2014**, *24*, 4886–4892.
- (35) Cho, J. M.; Higashino, T.; Mori, T. Band-like Transport down to 20 K in Organic Single-Crystal Transistors Based on Dioctylbenzothienobenzothiophene. *Appl. Phys. Lett.* **2015**, *106*, 193303.
- (36) Molina-Lopez, F.; Yan, H.; Gu, X.; Kim, Y.; Toney, M. F.; Bao, Z. Electric Field Tuning Molecular Packing and Electrical Properties of Solution-Shearing Coated Organic Semiconducting Thin Films. *Adv. Funct. Mater.* **2017**, 1605503.
- (37) Haase, K.; Teixeira da Rocha, C.; Hauenstein, C.; Zheng, Y.; Hamsch, M.; Mannsfeld, S. C. B. High-Mobility, Solution-Processed Organic Field-Effect Transistors from C8-BTBT:Polystyrene Blends. *Adv. Electron. Mater.* **2018**, *4*, 1800076.
- (38) Mas-Torrent, M.; Masirek, S.; Hadley, P.; Crivillers, N.; Oxtoby, N. S.; Reuter, P.; Veciana, J.; Rovira, C.; Tracz, A. Organic Field-Effect Transistors (OFETs) of Highly Oriented Films of Dithiophene-Tetrathiafulvalene Prepared by Zone Casting. *Org. Electron.* **2008**, *9*, 143–148.
- (39) Zhang, Q.; Leonardi, F.; Casalini, S.; Temiño, I.; Mas-Torrent, M. High Performing Solution-Coated Electrolyte-Gated Organic Field-Effect Transistors for Aqueous Media Operation. *Sci. Rep.* **2016**, *6*, 39623.
- (40) Cramer, T.; Kyndiah, A.; Murgia, M.; Leonardi, F.; Casalini, S.; Biscarini, F. Double Layer Capacitance Measured by Organic Field Effect Transistor Operated in Water. *Appl. Phys. Lett.* **2012**, *100*, 143302.
- (41) Kergoat, L.; Herlogsson, L.; Braga, D.; Piro, B.; Pham, M. C.; Crispin, X.; Berggren, M.; Horowitz, G. A Water-Gate Organic Field-Effect Transistor. *Adv. Mater.* **2010**, *22*, 2565–2569.





## CHAPTER 3

---

# Role of the vertical phase separation on the performance and stability of OFETs fabricated from organic semiconductor:insulating polymer blends\*

### 3.1 INTRODUCTION AND OBJECTIVES

---

Solution-based deposition techniques for small molecule organic semiconductors (OSCs) are especially attractive to promote low-cost manufacturing of organic field-effect transistors (OFETs) by high-throughput processes compatible with flexible substrates.<sup>1</sup> However, these technologies encounter problems related with dewetting and lack of control over the nucleation and growth of the molecular crystallites, which lead to a lack of reproducibility and homogeneity of the crystalline films and large performance disparity among the devices.<sup>2–4</sup> In this sense, one of the major advances in solution processing comes from the idea of blending the small semiconducting molecule with an amorphous insulating polymer to benefit from the high carrier mobility of the crystalline component and the processability enhancement provided by the polymer.<sup>5–8</sup> Moreover, this strategy has led to an overall rise in charge carrier mobility accompanied by an improvement of devices reproducibility and stability.<sup>9–11</sup> The superior performance achieved by the OSC blend OFETs seems to be related with the vertical phase separation of the two material components, with an underlying polymeric layer that passivates the OSC/dielectric interface ensuring a low density of traps.<sup>9,12,13</sup> This stratification has been confirmed by *ex situ* measurements, such as transmission electron microscopy (TEM),<sup>13</sup> secondary ion mass spectrometry (SIMS),<sup>14</sup> neutron reflectivity<sup>15</sup> or variable angle spectroscopic ellipsometry.<sup>15</sup>

---

\* This work has been published in Pérez-Rodríguez, A.; Temiño, I.; Ocal, C.; Mas-Torrent, M.; Barrena, E. Decoding the Vertical Phase Separation and Its Impact on C8-BTBT/PS Transistors Properties. *ACS Appl. Mater. Interfaces* **2018**, *10*, 7296–7303.

The OSC family of benzothieno[3,2-b][1]benzothiophene (BTBT) has demonstrated to give rise to high performance devices, being one of the most promising small semiconducting molecules due to their proven high hole mobility.<sup>13,16–20</sup> In particular, blends employing the soluble alkylated derivative C8-BTBT and polystyrene (PS), shown in **Figure 3.1 (a)**, have reported an enhanced film reproducibility and homogeneity<sup>10</sup> and remarkable field-effect mobilities up to  $12 \text{ cm}^2/\text{V}\cdot\text{s}$ .<sup>21</sup> Moreover, evidences of the vertical phase separation of both components in off-centre spin-coated films, with the PS segregated to the semiconductor/dielectric interface, have been provided by cross-sectional TEM (**Figure 3.1 (b)**).<sup>13</sup>

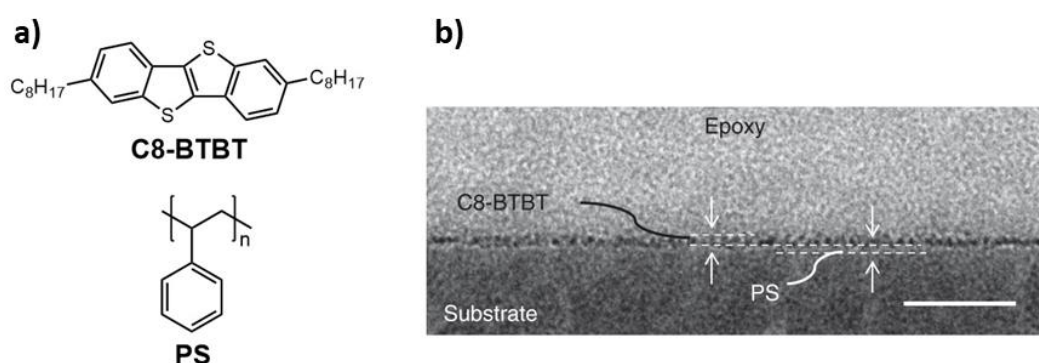


**Figure 3.1.** (a) Molecular structures of C8-BTBT and PS. (b) Cross-sectional TEM image showing the vertical phase separation between C8-BTBT and PS in a thin film processed by off-centre spin-coating. The scale bar is 100 nm. Extracted from ref. 13.

Nevertheless, the detailed vertical structure of this type of films at the nanometre scale has not been fully determined yet. To address this important question with such precision, atomic force microscopy (AFM) techniques are of great usefulness and importance.

### AFM as tool for materials characterisation

In atomic force microscopy a force sensor consisting on a nanometre-sized tip attached to a cantilever is used to measure the interaction forces acting between the probe and the surface. These forces cause the bending and torsion of the cantilever, which are usually sensed by an optical beam detection method (as schematised in **Figure 3.2 (a-b)**).<sup>22</sup> By sweeping the cantilever along the samples surface, interaction maps are obtained. The forces acting between the tip and the sample have different origins and contributions, giving rise to a wide variety of derived AFM techniques that provide different information about the scanned surface. In the following, the techniques used along this work will be briefly described.

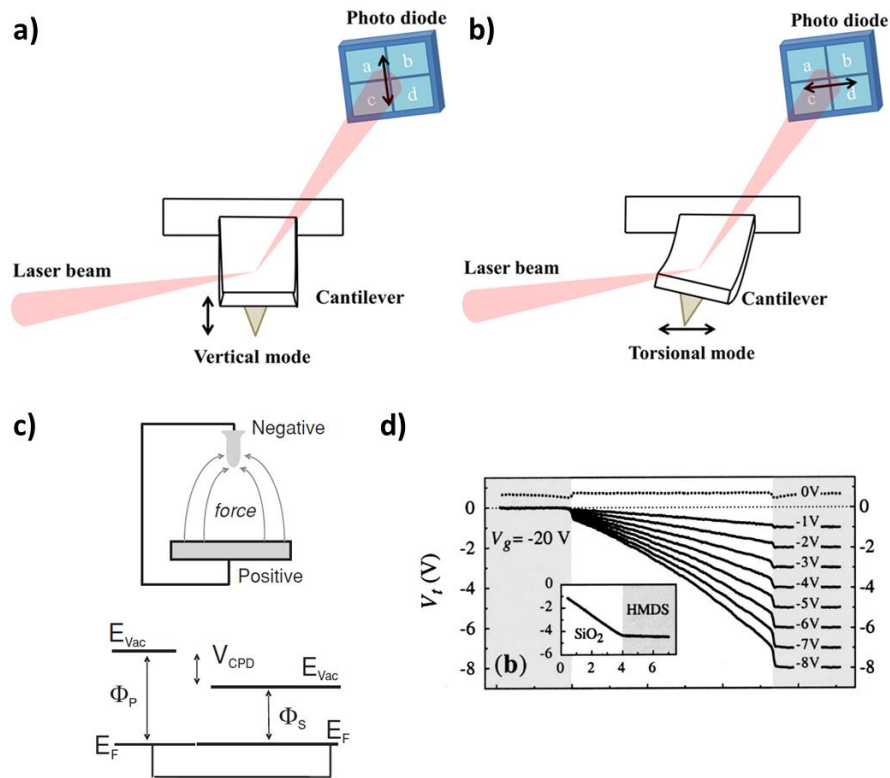


**Figure 3.2.** Scheme of the optical beam detection method employed to sense the bending and torsion of the cantilever due to (a) normal and (b) lateral forces, respectively. Extracted from ref. 22. (c) Setup for contact potential difference (CPD) measurements including an energy level diagram showing the Fermi levels ( $E_F$ ) and the contact potential difference ( $V_{CPD}$ ). Extracted from ref. 26. (d) KPFM of a P3HT thin-film field-effect transistor at different  $V_{SD}$  keeping the gate voltage constant. Extracted from ref.27.

### ► Topography

Topographic images are generated by recording the vertical movement of the cantilever (**Figure 3.2 (a)**). This kind of mapping can be done in contact mode, placing the tip in direct contact with the sample, or in dynamic mode, oscillating the cantilever at a given distance to the surface. In the latter case, the interactions induce variations in the phase, frequency and amplitude of the initial tip oscillation, providing additional information about the scanned surface.

### ► Friction force microscopy

In friction force microscopy (FFM), also known as lateral force imaging, the lateral force opposite to the relative tip-sample motion is measured by recording the torsion of the cantilever (**Figure 3.2 (b)**). When the tip encounters a region with different frictional behaviour the magnitude of the torsion changes, allowing to perform relative studies of friction. Since the FFM technique can be sensitive to the chemical termination, packing, molecular order or hydrophobicity of the surface, it conforms a powerful tool to reveal structural and compositional details that are otherwise difficult to visualise in topography

images. In particular, it has proven to be useful in identifying materials with a different chemical nature (such as graphene flakes<sup>23,24</sup> or organic islands on a substrate<sup>25</sup>) in heterogeneous samples.

### ► Kelvin probe force microscopy

Kelvin probe force microscopy (KPFM) uses the electrostatic interaction between the tip and the sample, which are electrically connected, to measure the contact potential difference (CPD) and thus map the surface potential distribution (**Figure 3.2 (c)**).<sup>26</sup> This method is commonly used to obtain a direct measure of the work-function of metals. In addition, information about the charge transport and carrier injection can be obtained from the evaluation of the surface potential in operating OFETs,<sup>27–29</sup> which is of great interest for this work. In particular, the surface potential in the channel of a thin-film transistor operated in the linear regime follows the electrostatic potential in the accumulation layer, which varies linearly along the channel, as depicted in **Figure 3.2 (d)**.<sup>27</sup> The measurement of abrupt potential drops at the source and drain interfaces with the semiconductor facilitates contact resistance determination.

## Objectives

The main objective of this chapter is to perform a detailed nanoscale characterisation of the vertical distribution of C8-BTBT and PS in blended thin films in order to understand the different macroscopic electrical performance measured when they are employed as active layers in OFET devices. First, thin films prepared by the deposition of solutions with different C8-BTBT:PS weight ratios (i.e., 1:2, 1:1 and 4:1) by BAMS were electrically characterised. Then, topographic AFM images in combination with FFM were used to gain a full understanding on the thin-film morphology and stratification. Finally, the contact resistance was investigated by KPFM measurements in operating devices.

### 3.2 DEVICE FABRICATION AND ELECTRICAL CHARACTERISATION

Thin films based on C8-BTBT and PS were deposited by bar-assisted meniscus shearing (BAMS) from blend solutions in chlorobenzene (2 wt%) prepared at different C8-BTBT:PS weight ratios: 1:2, 1:1 and 4:1. The molecular weight of PS (10 kg/mol) and the use of chlorobenzene as solvent were selected considering the previously optimised experimental conditions shown in Chapter 2.<sup>10</sup> Bottom-gate top-contact devices (**Figure 3.3 (a)**) were fabricated onto Si/SiO<sub>2</sub> substrates with top MoO<sub>3</sub>/Au electrodes (7 nm of MoO<sub>3</sub> and 35 nm of Au) evaporated through a shadow mask. This process resulted in OFETs with channel lengths from  $L = 30$  to  $100 \mu\text{m}$  and fixed channel width of  $W = 4 \text{ mm}$ .

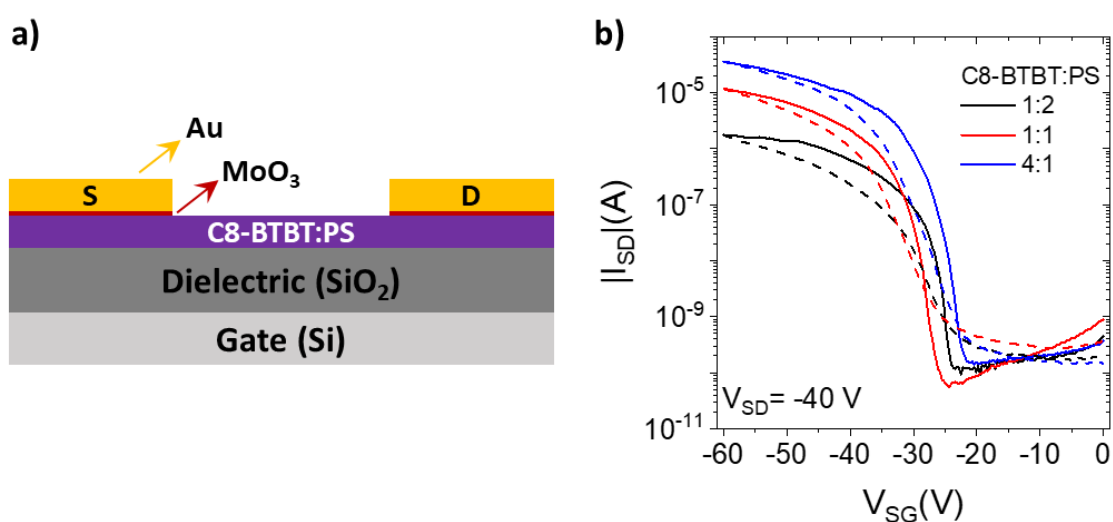


**Figure 3.3.** (a) Scheme of the bottom-gate top-contact OFETs employed in this work, showing the cross-section of the devices. (b) Transfer characteristics in the saturation regime of typical C8-BTBT:PS OFET devices ( $L = 30 \mu\text{m}$ ) based on different blend ratios: 1:2, 1:1 and 4:1. Straight and dashed lines correspond to forward and reverse sweeps of source-gate voltage, respectively.

Devices fabricated from the 1:2, 1:1 and 4:1 blend ratios were electrically characterised and representative transfer curves of the three types of devices (with a  $30 \mu\text{m}$  channel length) are shown in **Figure 3.3 (b)**. C8-BTBT:PS 4:1 OFETs exhibited an average hole field-effect mobility of  $0.3 \text{ cm}^2/\text{V}\cdot\text{s}$  in the saturation regime.<sup>10</sup> In addition, the reproducibility was significantly high for this ratio, with over 90% of the devices showing a good performance. On the contrary, for the 1:1 ratio the reproducibility dropped around 80%, and for 1:2 it reached 50%. The performance of the latter formulations also diminished with respect to the 4:1 ratio up to one order of magnitude, giving field-effect mobilities smaller by a 1/2 and a 1/10 factor, respectively.

### 3.3 MORPHOLOGICAL CHARACTERISATION

In order to understand how the formulation affects the vertical phase separation taking place in each film and the impact this has on the electrical properties of the devices, a full morphological characterisation has been performed.

The optical microscope images for the three different blend ratios are depicted in **Figure 3.4 (a)**. While 1:1 and 4:1 thin films show a similar morphology, for the 1:2 film the optical images reflect significantly smaller crystal domains. On the other hand, the topographic AFM images in **Figure 3.4 (b)** show very similar features for the three investigated blend ratios, hampering carrying out a direct correlation between thin-film morphology or crystallinity and electrical performance of the devices.

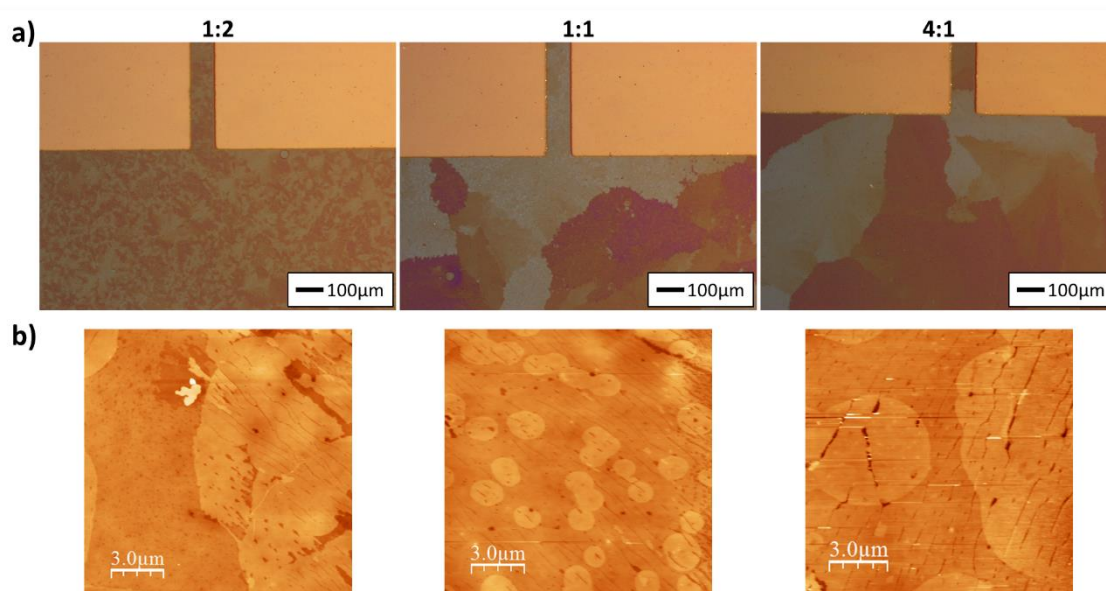


**Figure 3.4.** (a) Optical microscope and (b) topographic AFM images of thin films fabricated using different C8-BTBT:PS blend ratios (1:2, 1:1 and 4:1).

A close inspection of the organic film topography inside the OFET channel reveals a uniform and smooth surface consisting of large flat platforms or terraces with lateral sizes in the micrometre range (**Figure 3.5 (a)**). The height of each terrace was estimated to be  $3.1 \pm 0.2$  nm or multiples of it, as shown in the profile in **Figure 3.5 (b)**. This is only slightly higher than the inter-planar distance of the reported C8-BTBT thin-film structure consisting of a layered herringbone packing with the lamellar planes parallel to the surface. It should be noted that this is the most favourable orientation for charge transport in OFETs.<sup>30,31</sup>

When inspecting the lateral force signal, two different contrasts arose indicating two different levels of friction. This was more remarkable for the 1:2 films, hence the following friction study was performed with this sample. In **Figure 3.5 (c)** the lateral force signal that was recorded simultaneously with the topography in **Figure 3.5 (a)** is shown. Here, a substantial contrast between some areas is observed, where a darker colour corresponds to lower friction. On the terraces exhibiting the highest friction (lightest colour), molecular-resolved images were obtained (**Figure 3.5 (d)**). The estimated in-plane lattice constant ( $\approx 0.6 \pm 0.1$  nm) is in agreement with the next neighbours distance of C8-BTBT molecules in the herringbone packing within the plane ( $a = 0.59$  nm,  $b = 0.78$  nm),<sup>19</sup> evidencing the high crystalline quality of the C8-BTBT layer. Moreover, the lateral force signal allows relating the friction contrast with material composition, i.e., high friction for crystalline C8-BTBT and low friction for PS areas, respectively. As a matter of fact, molecular order was not observed on those terraces with low friction as expected from the amorphous structure of PS.

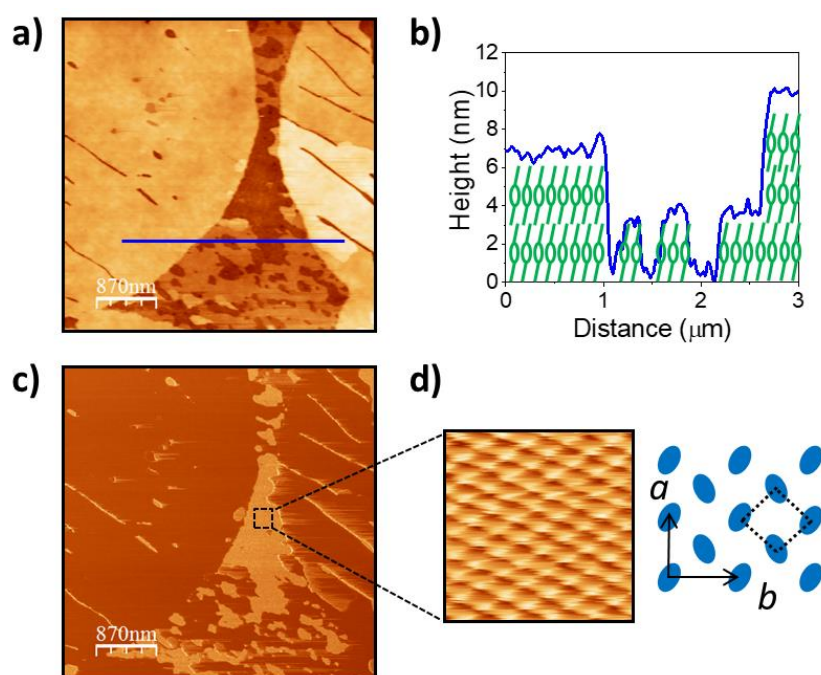


**Figure 3.5.** (a) Topographic and (c) lateral force images obtained within the channel of a C8-BTBT:PS 1:2 OFET. (b) Height profile along the marked line in (a) including a schematic illustration of the proposed molecular packing and layer thickness (the height of the molecules is at scale). (d) Magnified molecular resolution image (5 nm x 5 nm) of C8-BTBT and top view model of the in-plane herringbone unit cell, where blue ellipsoids represent the BTBT cores.



Interestingly, by consecutive scanning these low friction areas (or slightly increasing the imaging load) an extremely thin layer was peeled off by the swept action of the tip, leaving uncovered a surface that exhibited the friction contrast and molecular order of C8-BTBT. An example of how C8-BTBT areas are uncovered upon sweeping is shown in **(Figure 3.6 (a-b))**, while the topographic profile in **Figure 3.6 (c)** shows the height difference between the topmost layer and the C8-BTBT revealed underneath. The thickness of this PS layer was further investigated by analysing two consecutive topographic images, as depicted in **Figure 3.6 (d-e)**. In the profile shown in **Figure 3.6 (f)** a height decrease between 0.5 and 2 nm upon sweeping is manifested. This key observation permits firmly establishing the existence of an ultrathin skin layer of PS covering large areas of the crystalline C8-BTBT.

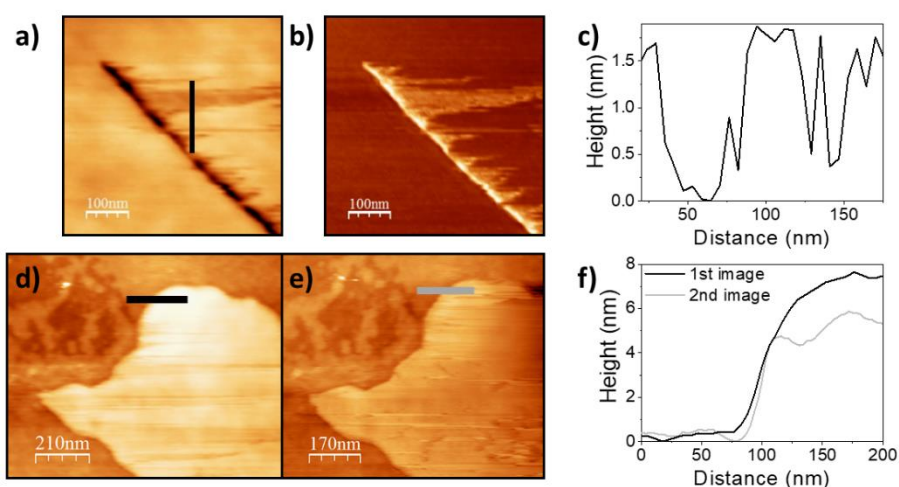


**Figure 3.6.** (a) Topographic and (b) forward lateral force images obtained during PS layer removal. (c) Height profile along the marked line in (a). (d-e) Consecutive topographic AFM images and (f) height profile along the marked lines showing the height drop upon sweeping.

Correlating topography and friction is particularly helpful for gaining information about the phase separation and determining the resulting vertical structure of the system. For this task, the 1:2 films were again of big relevance since there are regions where the C8-BTBT film is not complete leaving exposed areas at lower vertical level. The topographic and lateral force images illustrated in **Figure 3.7 (a)** show areas with different heights and friction contrast. In particular, it can be observed that the frictional signal of the base level terrace is lower than that of the surrounding C8-BTBT film and similar to that of the PS skin layer on the topmost level. In fact, no molecular order is observed at neither of these regions suggesting a similar composition for the skin and bottom layers.

In order to clarify whether the lowest level in **Figure 3.7 (a)** corresponds to the substrate or to the presence of an underlying PS buffer layer, the film was locally scratched by scanning at a higher load ( $> 1$  nN) until reaching the substrate. This scratching led to a

square cavity exposing the bare substrate, as observed in the topography image obtained after the process (**Figure 3.7 (b)**). Conveniently, the uncovered  $\text{SiO}_2$  serves as a reference to evaluate the thickness of the different layers as well as that of the overall film following the path marked in red. The height analysis in **Figure 3.7 (c)** confirms the existence of a layer of  $\sim 2\text{-}3\text{ nm}$  laying under the C8-BTBT film identified by FFM as PS rich. Hence, it was concluded that the C8-BTBT:PS blended films have a vertically phase segregated structure consisting of a C8-BTBT crystalline film sandwiched between two PS layers, one at the bottom and one on the top, as suggested in the illustration from **Figure 3.7 (c)**. The interface between the different layers is very smooth and structurally well defined. It should also be noted that the segregation of PS at both interfaces, with  $\text{SiO}_2$  and air, despite their dissimilar surface energy, suggests a phase separation driven by the crystallisation of the C8-BTBT rather than by surface energy minimisation. The formation of a bottom PS layer has been suggested in the literature to serve as a nonpolar dielectric medium that assures low charge trapping between the dielectric and the OSC.<sup>9,12,13</sup> On the other hand, although the presence of a thin PS film covering the crystalline layer has been proposed before, as far as we know it had not yet been experimentally proven for this type of systems.

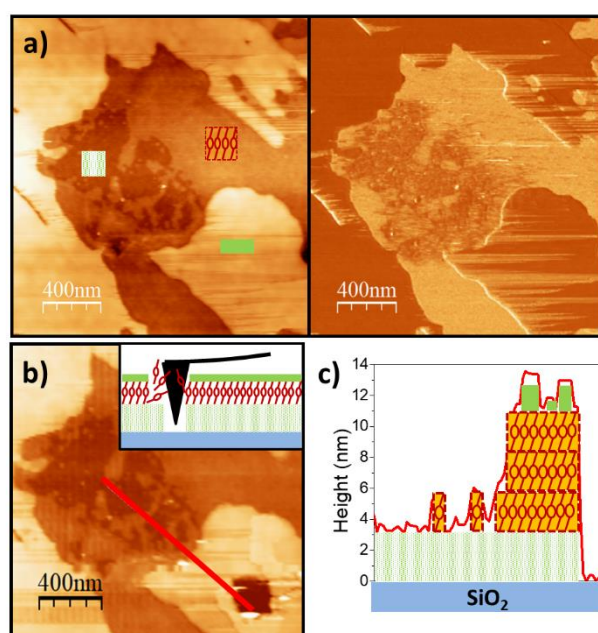


**Figure 3.7.** (a) Topographic (left) and lateral force (right) images obtained within the channel of a C8-BTBT:PS 1:2 OFET and (b) the same area after scratching the film. Inset: schematic illustration of the scratching experiments. (c) Height profile along the marked line in (b) including a schematic illustration of the proposed vertical structure.

Following the above described procedure the vertical distribution of PS and C8-BTBT was characterised with nanometre precision for all the fabricated thin films. A total thickness of  $\approx 16$ , 13 and 25 nm was determined for the 1:2, 1:1 and 4:1 based films, respectively. Quantitative differences in the individual thickness of the three-layers of the structure were also found, as schematically summarised in **Figure 3.8**.

It is noteworthy that for the 4:1 ratio, with the thickest C8-BTBT layer, the extracted current and mobility were the highest, whereas for the 1:2 film, where not even a complete C8-BTBT layer is formed, a poor performance and lack of reproducibility was obtained. Indeed, for the 1:2 blend the heterogeneous distribution of heights leaves uncovered some areas of the bottom PS layer. For the other blends, the hole transporting layer consists of two complete C8-BTBT layers for the 1:1 ratio and three complete layers for the 4:1 ratio. Thus, more than two molecular monolayers of the organic semiconductor are needed to ensure high OFET performance. Remarkably, the PS bottom layer and skin layer have the same thickness for all compositional ratios. This result indicates that the ratio between blend components affects the number of complete C8-BTBT crystalline layers formed, but it does not alter the thickness of both bottom and top PS layers.

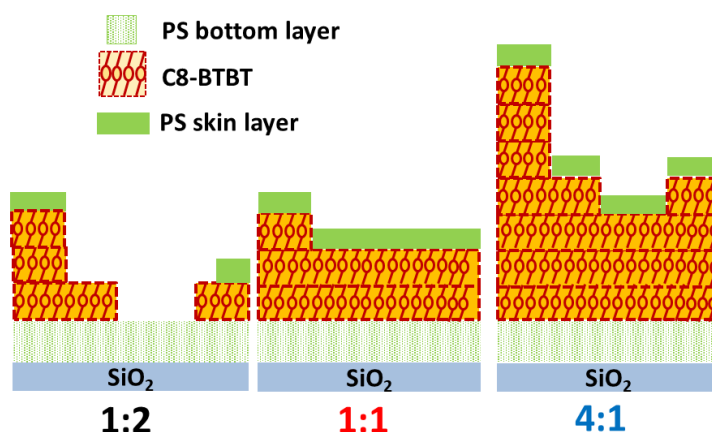


**Figure 3.8.** Deduced structure for the 1:2, 1:1 and 4:1 C8-BTBT:PS thin films.

### 3.4 ROLE OF PS IN THE FILMS SHELF-STABILITY

In order to understand the role of the PS layers in the shelf-stability of the thin films, two types of samples were investigated by AFM as a function of time: the above described C8-BTBT:PS 4:1 blend, which gave the best OFET performance, and a control sample processed under similar conditions but containing only C8-BTBT. A comparison of the very same samples just as prepared (fresh) and after several months is depicted in **Figure 3.9**. The topographic images reveal that the single component C8-BTBT films suffer from a strong dewetting with time. The initial 30 nm thick and laterally continuous film (**Figure 3.9 (a)**) evolves, after 4 months, to 90 nm high islands that leave uncovered large substrate regions (**Figure 3.9 (b)**). Indeed, dewetting of this molecule has been reported even after only few hours from the film preparation, and it is further enhanced at elevated temperatures.<sup>32</sup> This tendency for island growth and structuration in multi-layers has been related to the relatively high surface energy of the dielectric surface (SiO<sub>2</sub>).<sup>33</sup>

Remarkably, for the C8-BTBT:PS blend aging is negligible from a morphological and structural point of view, since the film presents basically the same appearance at the nanoscale after more than one year from preparation (**Figure 3.9 (c-d)**). It has already been reported that the hydrophobicity of the underlying PS buffer layer leads to an enhancement of the OFET stability and reduces the trap density at the OSC/dielectric interface.<sup>9,12,13</sup> In addition, these results suggest that the formation of both, top and bottom, PS layers acts as an encapsulation film for C8-BTBT impeding the dewetting of the crystalline layer upon time. This is of crucial importance for achieving long-term operating devices.

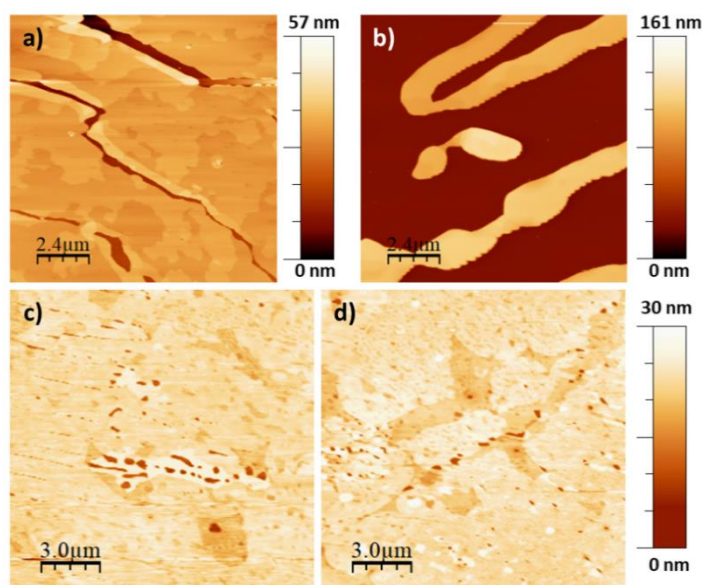


**Figure 3.9.** Topographic images of (a) a freshly prepared C8-BTBT film (without PS), (b) same sample 4 months later, (c) a freshly prepared C8-BTBT:PS film (4:1), and (d) same sample 14 months later.

### 3.5 KELVIN PROBE FORCE MICROSCOPY IN OPERANDO OFETS

The previous morphological study has shown that the measured C8-BTBT thickness for each C8-BTBT:PS blend correlates with the different electrical performance measured for the OFETs. To better understand the implications of the vertically phase segregated structure on the device performance, a KPFM nanoscale characterisation of the OFETs under operation was performed. Employing this technique, information about the charge transport and carrier injection can be obtained from the contact potential difference (CPD) maps.

#### Accumulation layer

The formation or not of the accumulation layer in the OFETs was locally evaluated by measuring the CPD within the channel as a function of the applied gate voltage ( $V_{SG}$ ), as plotted in **Figure 3.10 (a)** for 1:2 and 4:1 blend ratios. In order to get information from the whole tri-layer structure (including the top and bottom PS layers), these measurements were performed at locations well away from any film void or topographic defect.

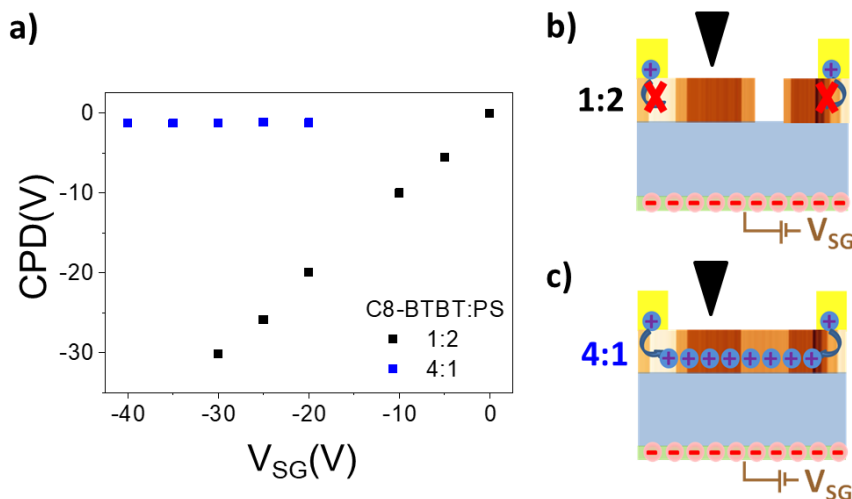


**Figure 3.10.** (a) CPD values inside the channel of C8-BTBT:PS OFETs based on the 1:2 and 4:1 ratios for  $V_{SD} = 0$  V upon applied  $V_{SG}$  bias. Schematic illustration of the formation or not of the charge accumulation layer upon  $V_{SG}$  application for (b) 1:2 and (c) 4:1 devices.

Results show a completely different tendency for each type of device. In the device with a blend ratio 1:2 (in black), the measured CPD coincides with  $V_{SG}$ , implying that no charges are injected into the device to screen the applied gate bias and, consequently, the charge accumulation channel is not formed. This fact is directly related to the lateral discontinuity of the transport layer, consisting of an incomplete C8-BTBT film for this ratio. This interpretation is schematically illustrated in **Figure 3.10 (b)**. Additionally, a largely defective film coverage was also found at the electrodes borders for these devices, with large areas of uncovered C8-BTBT, suggesting degradation of the film upon evaporation of the top electrodes. This can be observed in **Figure 3.11**, in which the topographic image of the channel taken by AFM in dynamic mode together with the corresponding excitation signal are shown. These inhomogeneities at the film/electrode boundary hinder at some extent the injection of charges needed to form the transport channel; however, since the OFET characteristics could be measured, there must be conductive paths connecting source and drain electrodes and allowing the device to work at macroscopic level although with low  $I_{SD}$  (see **Figure 3.3 (b)**).

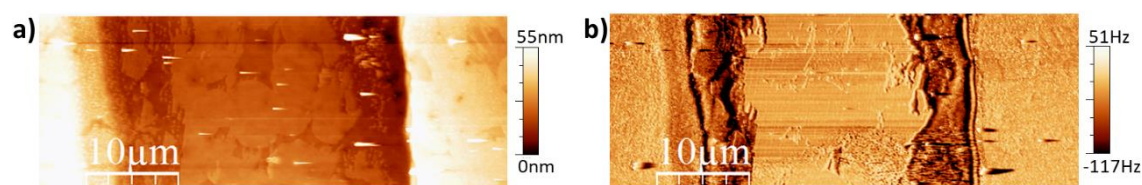


**Figure 3.11.** (a) Topographic and (b) excitation images obtained in the channel of the 1:2 C8-BTBT:PS OFET. The two electrode edges were imaged to illustrate the defective characteristics of the film at the boundary.

Conversely to the above description, devices based on the 4:1 blend show the expected behaviour for an operating OFET. In this case, the CPD in the channel (in blue) does not change upon the application of  $V_{SG}$ , implying that charges are rapidly injected from the electrodes into the channel and forming the accumulation layer that screens the gate bias (see scheme in **Figure 3.10 (c)**).

### Contact resistance

It is noteworthy that even for the optimal 4:1 ratio, the hole field-effect mobility extracted from the devices saturation transfer characteristics ( $\mu_{FE} = 0.3 \text{ cm}^2/\text{V}\cdot\text{s}$ , in average<sup>10</sup>) is lower than that reported in the literature for C8-BTBT based OFETs. For example, an average saturation mobility of  $16.4 \text{ cm}^2/\text{V}\cdot\text{s}$  was extracted for single-crystal C8-BTBT devices fabricated by inkjet-printing.<sup>34</sup> In another work, thin films processed by plate-



shearing gave rise to mobilities around  $12 \text{ cm}^2/\text{V}\cdot\text{s}$ ;<sup>21</sup> however, given the low shearing speed employed (0.25 mm/s) and the long temperature annealing step applied afterwards (70 h), this methodology could be rather regarded as a slow assisted crystallisation process. One of the critical issues that can severely affect the OFET performance is the contact resistance between the metal electrodes and the semiconductor layer.<sup>35</sup> Indeed, for C8-BTBT a hole injection barrier exists due to the large mismatch between the OSC highest occupied molecular orbital (HOMO  $\sim -5.7 \text{ eV}$ ) and the work-function of the gold electrode, which is commonly ameliorated by using self-assembled monolayers (SAMs),<sup>36</sup> inserting a charge injection layer,<sup>37</sup> doping the contacts with inorganic or organic compounds<sup>38,39</sup>, or using a conducting organic charge-transfer complex.<sup>40</sup> In this work, a  $\text{MoO}_3$  layer has been incorporated underneath the Au contacts, but still a high average threshold voltage of  $V_{th} = -29 \text{ V}$  was found.<sup>10</sup> Considering all this, the electrodes were studied by KPFM and the contact resistance was determined in order to understand its influence on the mobility extraction.

**Figure 3.12 (a)** displays representative CPD line profiles at two different  $V_{SD}$  values ( $V_{SD} = 0 \text{ V}$  and  $V_{SD} = -5 \text{ V}$ ) and using  $V_{SG} = -40 \text{ V}$  for a 4:1 C8-BTBT:PS OFET with  $\text{MoO}_3/\text{Au}$  contacts. As can be noticed, microscopically the contact resistance ( $R_C$ ) manifests by a sudden voltage drop at the source (marked in yellow). First, in order to assure the ohmic behaviour of the contact in the device, the CPD drop was measured as a function of the applied  $V_{SD}$ . The plot in **Figure 3.12 (c)** confirms their linear dependency, permitting to extract  $R_C$  values by Ohm's law. Thus, a resistance of  $R_C \cdot W = 23.9 \text{ k}\Omega \cdot \text{cm}$  was determined for the source  $\text{MoO}_3/\text{Au}$  contact when the OFET is operated in linear regime ( $V_{SD} = -5 \text{ V}$  and  $V_{SG} = -40 \text{ V}$ ). Likewise, the channel resistance, estimated from the total resistance in the OFET, is  $R_{ch} \cdot W = 0.74 \text{ k}\Omega \cdot \text{cm}$ . This evidences the large relative contribution of the contact resistance and suggests a considerably higher intrinsic charge carrier mobility for this material than the effective value extracted from the current-voltage characteristics.

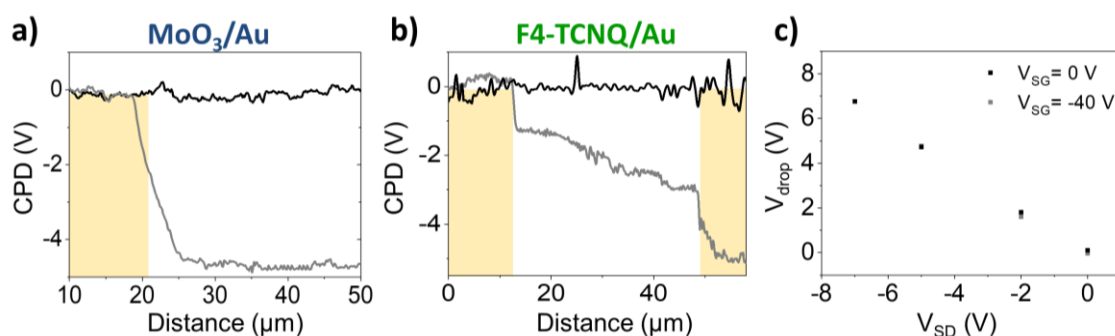


**Figure 3.12.** CPD profiles of C8-BTBT:PS 4:1 OFETs with (a)  $\text{MoO}_3/\text{Au}$  and (b)  $\text{F4-TCNQ}/\text{Au}$  contacts ( $L = 40 \mu\text{m}$ ) measured at  $V_{SD} = 0 \text{ V}$  and  $V_{SG} = -40 \text{ V}$  (off state, in black) and  $V_{SD} = -5 \text{ V}$  and  $V_{SG} = -40 \text{ V}$  (linear regime, in grey). (c) Measured  $V_{drop}$  in the CPD profiles as a function of the applied  $V_{SD}$ .

Proven that the devices operation is strongly limited by the contacts, 2,3,5,6-tetrafluoro-7,7,8,8-tetracyanoquinodimethane (F4-TCNQ) was incorporated as a doping interlayer aiming to improve the injection properties. The strong acceptor character of this molecule (with an electron affinity around 5.2 eV) has already shown to enable contact doping in C8-BTBT based devices, successfully reducing the threshold voltage.<sup>41,42</sup> In the following, the same 4:1 C8-BTBT:PS thin films were employed as active layer and OFET devices were fabricated by the evaporation of F4-TCNQ/Au top contacts. To do so, 20 nm of the organic dopant were evaporated prior to the gold evaporation. The CPD profiles in **Figure 3.12 (b)** show that the modification of the electrodes architecture results in a reduced voltage drop with very similar values in both source and drain. As a consequence, the obtained resistances are very similar ( $R_C \cdot W = 5.5 \text{ k}\Omega \cdot \text{cm}$  and  $R_C \cdot W = 2.1 \text{ k}\Omega \cdot \text{cm}$  for drain and source contacts, respectively) and lower by about one order of magnitude than the one extracted for MoO<sub>3</sub>/Au electrodes. This injection improvement is generally attributed to a thinning of the depletion region (thus allowing tunneling injection) and to the reduction of traps density in the metal/semiconductor interface.<sup>38</sup> On the other hand, the estimated channel resistance ( $R_{ch} \cdot W = 0.88 \text{ k}\Omega \cdot \text{cm}$ ) is comparable to that of the devices with MoO<sub>3</sub>/Au electrodes, in agreement with a channel free of dopants.

In addition, the decrease in the contact resistance results in a significantly higher device mobility of  $1.5 \text{ cm}^2/\text{V}\cdot\text{s}$ , determined on average from 11 devices in the saturation regime. The transfer and output characteristics plotted in **Figure 3.13** show the improvement achieved in the injection by the use of F4-TCNQ/Au contacts: a steeper switch-on, closer to 0 V, higher  $I_{SD}$  current and improved linearity at low source-drain voltage in the output curves. In particular, the switch-on voltage and mobility values obtained were  $V_{on} = -13 \text{ V}$  and  $\mu_{FE} = 0.45 \text{ cm}^2/\text{V}\cdot\text{s}$  for the device with MoO<sub>3</sub>/Au, and  $V_{on} = -2.1 \text{ V}$  and  $\mu_{FE} = 0.94 \text{ cm}^2/\text{V}\cdot\text{s}$  for the device with F4-TCNQ/Au.

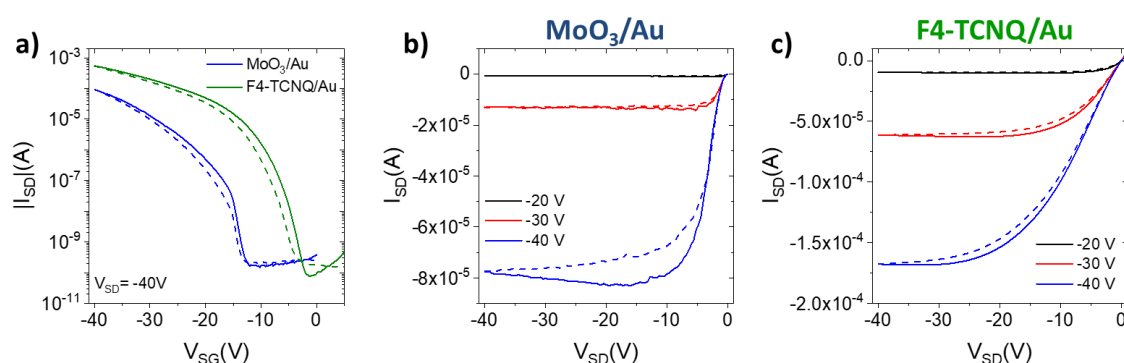


**Figure 3.13.** Electrical characteristics of C8-BTBT:PS 4:1 OFETs with MoO<sub>3</sub>/Au and F4-TCNQ/Au contacts ( $L = 40 \mu\text{m}$ ). (a) Transfer characteristics in the saturation regime. (b-c) Output characteristics. Straight and dashed lines correspond to forward and reverse sweeps, respectively.



Moreover, the effect of the contacts can be excluded to obtain the intrinsic field-effect mobility along the channel in the linear regime. Considering  $V_{SD} \ll V_{SG} - V_{th}$ , the source-drain current can be approximated as:<sup>43,44</sup>

$$I_{SD} = \mu_{FE} \cdot \frac{C \cdot W}{L} [(V_{SG} - V_{th}) \cdot V_{SD}] \quad (3.1)$$

where  $C$  is the dielectric capacitance per unit area. Then, the channel mobility ( $\mu_{FE,ch}$ ) can be calculated substituting the total  $V_{SD}$  for the voltage drop along the channel,  $\Delta V_{ch}$ :

$$\mu_{FE,ch} = \left[ \frac{I_{SD} \cdot L}{C \cdot W} \right] \frac{1}{(V_{SG} - V_{th}) \cdot \Delta V_{ch}} \quad (3.2)$$

where  $\Delta V_{ch} = V_{SD} - \Delta V_S - \Delta V_D$ , being  $\Delta V_S$  and  $\Delta V_D$  the potential drops determined from the CPD profiles at the source and drain contacts, respectively. For the F4-TCNQ/Au device the calculated channel mobility excluding the contact resistance is found to be  $\mu_{FE,ch} = 10 \pm 1 \text{ cm}^2/\text{V}\cdot\text{s}$ , which is one order of magnitude higher than the mobility extracted from the linear characteristics of this device,  $1.1 \text{ cm}^2/\text{V}\cdot\text{s}$ . Such high channel mobilities are of the order of the ones reported for C8-BTBT single-crystal devices fabricated by inkjet-printing,<sup>34</sup> evidencing the high crystalline quality and the good connectivity between domain boundaries in the 4:1 ratio film prepared by BAMS. Indeed, these results point out that a further optimisation of the contacts would make feasible to reach hole mobility values close to those reported for single-crystal C8-BTBT devices employing thin films processed by high throughput solution methodologies.

### 3.6 SUMMARY

---

In summary, the vertical structure of C8-BTBT:PS thin films of three different blending ratios has been investigated with nanometre precision by combining topographical and tribologic (FFM) images. From this morphological study it was concluded that the films consist of a C8-BTBT crystalline layer sandwiched between two PS layers, one at the bottom and an ultra-thin skin PS layer on the top, which confer stability by impeding the dewetting upon time.

Results also explain how the thickness of the C8-BTBT, which varies from a laterally incomplete film for the C8-BTBT:PS 1:2 blend to three complete molecular layers for the 4:1 blend, correlates with the different macroscopic electrical performance measured for the OFETs. In particular, KPFM measurements in operando OFETs revealed that the thickness and continuity of the crystalline layer play a fundamental role in the transport channel formation.

Finally, it was also demonstrated that the contact resistance is the critical factor limiting the devices performance, which is significantly improved by doping the contacts with a F4-TCNQ interlayer. By excluding the contact resistance, a hole mobility in the channel as large as  $\mu_{ch} = 10 \pm 1 \text{ cm}^2/\text{V}\cdot\text{s}$  was obtained for the 4:1 OFET, giving evidence of the excellent transport properties of the film. Next chapter will be devoted to further optimising the performance of C8-BTBT:PS based devices by exploring various doping strategies.

3.7 REFERENCES

---

- (1) Xu, Y.; Liu, C.; Khim, D.; Noh, Y.-Y. Development of High-Performance Printed Organic Field-Effect Transistors and Integrated Circuits. *Phys. Chem. Chem. Phys.* **2015**, *17*, 26553–26574.
- (2) Mas-Torrent, M.; Rovira, C. Novel Small Molecules for Organic Field-Effect Transistors: Towards Processability and High Performance. *Chem. Soc. Rev.* **2008**, *37*, 827–838.
- (3) Diao, Y.; Shaw, L.; Mannsfeld, S. C. B. Morphology Control Strategies for Solution-Processed Organic Semiconductor Thin Films. *Energy Environ. Sci.* **2014**, *7*, 2145–2159.
- (4) Virkar, A. A.; Mannsfeld, S.; Bao, Z.; Stingelin, N. Organic Semiconductor Growth and Morphology Considerations for Organic Thin-Film Transistors. *Adv. Mater.* **2010**, *22*, 3857–3875.
- (5) Hamilton, R.; Smith, J.; Ogier, S.; Heeney, M.; Anthony, J. E.; McCulloch, I.; Veres, J.; Bradley, D. D. C.; Anthopoulos, T. D. High-Performance Polymer-Small Molecule Blend Organic Transistors. *Adv. Mater.* **2009**, *21*, 1166–1171.
- (6) Lee, W. H.; Lim, J. A.; Kwak, D.; Cho, J. H.; Lee, H. S.; Choi, H. H.; Cho, K. Semiconductor-Dielectric Blends: A Facile All Solution Route to Flexible All-Organic Transistors. *Adv. Mater.* **2009**, *21*, 4243–4248.
- (7) Zhao, K.; Wodo, O.; Ren, D.; Khan, H. U.; Niazi, M. R.; Hu, H.; Abdelsamie, M.; Li, R.; Li, E. Q.; Yu, L.; et al. Vertical Phase Separation in Small Molecule:Polymer Blend Organic Thin Film Transistors Can Be Dynamically Controlled. *Adv. Funct. Mater.* **2016**, *26*, 1737–1746.
- (8) Riera-Galindo, S.; Leonardi, F.; Pfattner, R.; Mas-Torrent, M. Organic Semiconductor/Polymer Blend Films for Organic Field-Effect Transistors. *Adv. Mater. Technol.* **2019**, 1900104.
- (9) del Pozo, F. G.; Fabiano, S.; Pfattner, R.; Georgakopoulos, S.; Galindo, S.; Liu, X.; Braun, S.; Fahlman, M.; Veciana, J.; Rovira, C.; et al. Single Crystal-Like Performance in Solution-Coated Thin-Film Organic Field-Effect Transistors. *Adv. Funct. Mater.* **2016**, *26*, 2379–2386.
- (10) Temiño, I.; Del Pozo, F. G.; Ajayakumar, M. R.; Galindo, S.; Puigdollers, J.; Mas-Torrent, M. A Rapid, Low-Cost, and Scalable Technique for Printing State-of-the-Art Organic Field-Effect Transistors. *Adv. Mater. Technol.* **2016**, *1*, 1600090.
- (11) Niazi, M. R.; Li, R.; Qiang Li, E.; Kirmani, A. R.; Abdelsamie, M.; Wang, Q.; Pan, W.; Payne, M. M.; Anthony, J. E.; Smilgies, D.-M.; et al. Solution-Printed Organic

- Semiconductor Blends Exhibiting Transport Properties on Par with Single Crystals. *Nat. Commun.* **2015**, *6*, 8598.
- (12) Leonardi, F.; Casalini, S.; Zhang, Q.; Galindo, S.; Gutiérrez, D.; Mas-Torrent, M. Electrolyte-Gated Organic Field-Effect Transistor Based on a Solution Sheared Organic Semiconductor Blend. *Adv. Mater.* **2016**, *28*, 10311–10316.
- (13) Yuan, Y.; Giri, G.; Ayzner, A. L.; Zoombelt, A. P.; Mannsfeld, S. C. B.; Chen, J.; Nordlund, D.; Toney, M. F.; Huang, J.; Bao, Z. Ultra-High Mobility Transparent Organic Thin Film Transistors Grown by an off-Centre Spin-Coating Method. *Nat. Commun.* **2014**, *5*, 3005.
- (14) Ohe, T.; Kuribayashi, M.; Yasuda, R.; Tsuboi, A.; Nomoto, K.; Satori, K.; Itabashi, M.; Kasahara, J. Solution-Processed Organic Thin-Film Transistors with Vertical Nanophase Separation. *Appl. Phys. Lett.* **2008**, *93*, 053303.
- (15) Shin, N.; Kang, J.; Richter, L. J.; Prabhu, V. M.; Kline, R. J.; Fischer, D. A.; Delongchamp, D. M.; Toney, M. F.; Satija, S. K.; Gundlach, D. J.; et al. Vertically Segregated Structure and Properties of Small Molecule-Polymer Blend Semiconductors for Organic Thin-Film Transistors. *Adv. Funct. Mater.* **2013**, *23*, 366–376.
- (16) Schweicher, G.; Lemaire, V.; Niebel, C.; Ruzié, C.; Diao, Y.; Goto, O.; Lee, W. Y.; Kim, Y.; Arlin, J. B.; Karpinska, J.; et al. Bulky End-Capped [1]Benzothieno[3,2-b]Benzothiophenes: Reaching High-Mobility Organic Semiconductors by Fine Tuning of the Crystalline Solid-State Order. *Adv. Mater.* **2015**, *27*, 3066–3072.
- (17) Ebata, H.; Izawa, T.; Miyazaki, E.; Takimiya, K.; Ikeda, M.; Kuwabara, H.; Yui, T. Highly Soluble [1]Benzothieno[3,2-b]Benzothiophene (BTBT) Derivatives for High-Performance, Solution-Processed Organic Field-Effect Transistors. *J. Am. Chem. Soc.* **2007**, *129*, 15732–15733.
- (18) Amin, A. Y.; Khassanov, A.; Reuter, K.; Meyer-friedrichsen, T.; Halik, M. Low-Voltage Organic Field Effect Transistors with a 2-Tridecyl[1]Benzothieno[3,2-b][1]Benzothiophene Semiconductor Layer. *J. Am. Chem. Soc.* **2012**, *134*, 16548–16550.
- (19) Gbabode, G.; Dohr, M.; Niebel, C.; Balandier, J.-Y.; Ruzié, C.; Négrier, P.; Mondieig, D.; Geerts, Y. H.; Resel, R.; Sferrazza, M. X-Ray Structural Investigation of Nonsymmetrically and Symmetrically Alkylated [1]Benzothieno[3,2-b]Benzothiophene Derivatives in Bulk and Thin Films. *ACS Appl. Mater. Interfaces* **2014**, *6*, 13413–13421.
- (20) Paterson, A. F.; Treat, N. D.; Zhang, W.; Fei, Z.; Wyatt-Moon, G.; Faber, H.; Vourlias, G.; Patsalas, P. A.; Solomeshch, O.; Tessler, N.; et al. Small Molecule/Polymer Blend Organic Transistors with Hole Mobility Exceeding 13  $\text{cm}^2 \text{V}^{-1} \text{s}^{-1}$ . *Adv. Mater.* **2016**, *28*, 7791–7798.

- (21) Haase, K.; Teixeira da Rocha, C.; Hauenstein, C.; Zheng, Y.; Hambsch, M.; Mannsfeld, S. C. B. High-Mobility, Solution-Processed Organic Field-Effect Transistors from C8-BTBT:Polystyrene Blends. *Adv. Electron. Mater.* **2018**, *4*, 1800076.
- (22) Arima, E.; Wen, H.; Naitoh, Y.; Li, Y. J.; Sugawara, Y. Development of Low Temperature Atomic Force Microscopy with an Optical Beam Deflection System Capable of Simultaneously Detecting the Lateral and Vertical Forces. *Rev. Sci. Instrum.* **2016**, *87*, 093113.
- (23) Choi, J. S.; Kim, J.-S.; Byun, I.-S.; Lee, D. H.; Lee, M. J.; Park, B. H.; Lee, C.; Yoon, D.; Cheong, H.; Lee, K. H.; et al. Friction Anisotropy-Driven Domain Imaging on Exfoliated Monolayer Graphene. *Science* **2011**, *333*, 607–610.
- (24) Miranzo, P.; López-Mir, L.; Román-Manso, B.; Belmonte, M.; Osendi, M. I.; Ocal, C. Prominent Local Transport in Silicon Carbide Composites Containing In-Situ Synthesized Three-Dimensional Graphene Networks. *J. Eur. Ceram. Soc.* **2016**, *36*, 3073–3081.
- (25) Aghamohammadi, M.; Fernández, A.; Schmidt, M.; Pérez-Rodríguez, A.; Goñi, A. R.; Fraxedas, J.; Sauthier, G.; Paradinas, M.; Ocal, C.; Barrena, E. Influence of the Relative Molecular Orientation on Interfacial Charge-Transfer Excitons at Donor/Acceptor Nanoscale Heterojunctions. *J. Phys. Chem. C* **2014**, *118*, 14833–14839.
- (26) Glatzel, T.; Lux-Steiner, M. C.; Strassburg, E.; Boag, A.; Rosenwaks, Y. Principles of Kelvin Probe Force Microscopy. In *Scanning Probe Microscopy: Electrical and Electromechanical Phenomena at the Nanoscale*; Kalinin, S., Gruverman, A., Eds.; Springer New York: New York, NY, 2007; pp 113–131.
- (27) Bürgi, L.; Siringhaus, H.; Friend, R. H. Noncontact Potentiometry of Polymer Field-Effect Transistors. *Appl. Phys. Lett.* **2002**, *80*, 2913–2915.
- (28) Palermo, V.; Palma, M.; Samori, P. Electronic Characterization of Organic Thin Films by Kelvin Probe Force Microscopy. *Adv. Mater.* **2006**, *18*, 145–164.
- (29) Yamagishi, Y.; Noda, K.; Kobayashi, K.; Yamada, H. Interlayer Resistance and Edge-Specific Charging in Layered Molecular Crystals Revealed by Kelvin-Probe Force Microscopy. *J. Phys. Chem. C* **2015**, *119*, 3006–3011.
- (30) Tsutsumi, J.; Matsuoka, S.; Inoue, S.; Minemawari, H.; Yamada, T.; Hasegawa, T. N-Type Field-Effect Transistors Based on Layered Crystalline Donor–Acceptor Semiconductors with Dialkylated Benzothienobenzothiophenes as Electron Donors. *J. Mater. Chem. C* **2015**, *3*, 1976–1981.
- (31) Jones, A. O. F.; Geerts, Y. H.; Karpinska, J.; Kennedy, A. R.; Resel, R.; Röthel, C.; Ruzié, C.; Werzer, O.; Sferrazza, M. Substrate-Induced Phase of a [1]Benzothieno[3,2-b]Benzothiophene Derivative and Phase Evolution by Aging and Solvent Vapor

- Annealing. *ACS Appl. Mater. Interfaces* **2015**, *7*, 1868–1873.
- (32) Dohr, M.; Werzer, O.; Shen, Q.; Salzmann, I.; Teichert, C.; Ruzié, C.; Schweicher, G.; Geerts, Y. H.; Sferrazza, M.; Resel, R. Dynamics of Monolayer-Island Transitions in 2,7-Dioctyl- Benzothienobenzothiophene Thin Films. *ChemPhysChem* **2013**, *14*, 2554–2559.
- (33) Amin, A. Y.; Reuter, K.; Meyer-friedrichsen, T.; Halik, M. Interface Engineering in High-Performance Low-Voltage Organic Thin-Film Transistors Based on 2,7-Dialkyl-[1]Benzothieno[3,2-b][1]Benzothiophenes. *Langmuir* **2011**, *27*, 15340–15344.
- (34) Minemawari, H.; Yamada, T.; Matsui, H.; Tsutsumi, J.; Haas, S.; Chiba, R.; Kumai, R.; Hasegawa, T. Inkjet Printing of Single-Crystal Films. *Nature* **2011**, *475*, 364–367.
- (35) Liu, C.; Xu, Y.; Noh, Y. Y. Contact Engineering in Organic Field-Effect Transistors. *Mater. Today* **2015**, *18*, 79–96.
- (36) Mei, Y.; Fogel, D.; Chen, J.; Ward, J. W.; Payne, M. M.; Anthony, J. E.; Jurchescu, O. D. Interface Engineering to Enhance Charge Injection and Transport in Solution-Deposited Organic Transistors. *Org. Electron.* **2017**, *50*, 100–105.
- (37) Kano, M.; Minari, T.; Tsukagoshi, K. Improvement of Subthreshold Current Transport by Contact Interface Modification in p -Type Organic Field-Effect Transistors. *Appl. Phys. Lett.* **2009**, *94*, 143304.
- (38) Minari, T.; Darmawan, P.; Liu, C.; Li, Y.; Xu, Y.; Tsukagoshi, K. Highly Enhanced Charge Injection in Thienoacene-Based Organic Field-Effect Transistors with Chemically Doped Contact. *Appl. Phys. Lett.* **2012**, *100*, 093303.
- (39) Tietze, M. L.; Burtone, L.; Riede, M.; Lüssem, B.; Leo, K. Fermi Level Shift and Doping Efficiency in P-Doped Small Molecule Organic Semiconductors: A Photoelectron Spectroscopy and Theoretical Study. *Phys. Rev. B* **2012**, *86*, 035320.
- (40) Georgakopoulos, S.; Pérez-Rodríguez, A.; Campos, A.; Temiño, I.; Galindo, S.; Barrena, E.; Ocal, C.; Mas-Torrent, M. Spray-Coated Contacts from an Organic Charge Transfer Complex Solution for Organic Field-Effect Transistors. *Org. Electron.* **2017**, *48*, 365–370.
- (41) Soeda, J.; Hirose, Y.; Yamagishi, M.; Nakao, A.; Uemura, T.; Nakayama, K.; Uno, M.; Nakazawa, Y.; Takimiya, K.; Takeya, J. Solution-Crystallized Organic Field-Effect Transistors with Charge-Acceptor Layers: High-Mobility and Low-Threshold-Voltage Operation in Air. *Adv. Mater.* **2011**, *23*, 3309–3314.
- (42) Zhang, F.; Dai, X.; Zhu, W.; Chung, H.; Diao, Y. Large Modulation of Charge Carrier Mobility in Doped Nanoporous Organic Transistors. *Adv. Mater.* **2017**, *29*, 1700411.
- (43) Natali, D.; Fumagalli, L.; Sampietro, M. Modeling of Organic Thin Film Transistors:

Effect of Contact Resistances. *J. Appl. Phys.* **2007**, *101*, 014501.

- (44) Bittle, E. G.; Basham, J. I.; Jackson, T. N.; Jurchescu, O. D.; Gundlach, D. J. Mobility Overestimation Due to Gated Contacts in Organic Field-Effect Transistors. *Nat. Commun.* **2015**, *7*, 10908.

## CHAPTER 4

# Doping methodologies for the optimisation of the performance of C8-BTBT based OFETs\*

### 4.1 INTRODUCTION AND OBJECTIVES

For the fabrication of organic field-effect transistors (OFETs) exhibiting high electrical performance, it is crucial to achieve an efficient charge injection from the electrodes to the organic semiconductor (OSC).<sup>1</sup> However, when the highest occupied molecular orbital (HOMO) of the OSC and the work-function of the electrodes are not aligned, injection is significantly hindered by the high energetic barrier and, macroscopically, high contact resistance values are extracted. As a result, in some cases, despite the good charge transport properties of the OSC, the performance of the fabricated OFETs (e.g current and mobility) and their possible applications are limited due to the high voltages required to power and turn on the resulting devices. For example, OFETs based on the organic semiconductor 2,7-dioctyl[1]benzothieno[3,2-b][1]benzothiophene (C8-BTBT, shown in **Figure 4.1 (a)**) have been reported to exhibit remarkable field-effect mobilities<sup>2-5</sup> but also large negative threshold voltage values,<sup>6-8</sup> as a result of the large mismatch between the HOMO of this molecule ( $\sim -5.7$  eV)<sup>9</sup> and the work-function of gold ( $\sim -5.1$  eV), which is commonly employed for top evaporated electrodes. Indeed, in the previous chapter (Chapter 3) it was evidenced that the high potential of C8-BTBT based transistors is not completely exploited, as the intrinsic hole mobility of the material ( $\sim 10$  cm<sup>2</sup>/V·s) was found to be one order of magnitude higher than the overall device mobility value.<sup>10</sup> In order to confront these contact resistance issues, different contact engineering approaches have been proposed.<sup>1</sup> For example, by using self-assembled monolayers (SAMs) the work-function of the metal electrodes can be tuned,<sup>11</sup> although this is only possible when a bottom-contact configuration is employed. An alternative is doping the semiconductor, which is a well-established strategy for inorganic transistors and has had great success in organic optoelectronic and energy devices. Hence, OFET doping is now

---

\* This work has been carried out in collaboration with Dr. Tommaso Salzillo, Manuel España and Jinghai Li (ICMAB).



being intensively investigated since it can be a key enabler for achieving high-performance devices.<sup>12–14</sup>

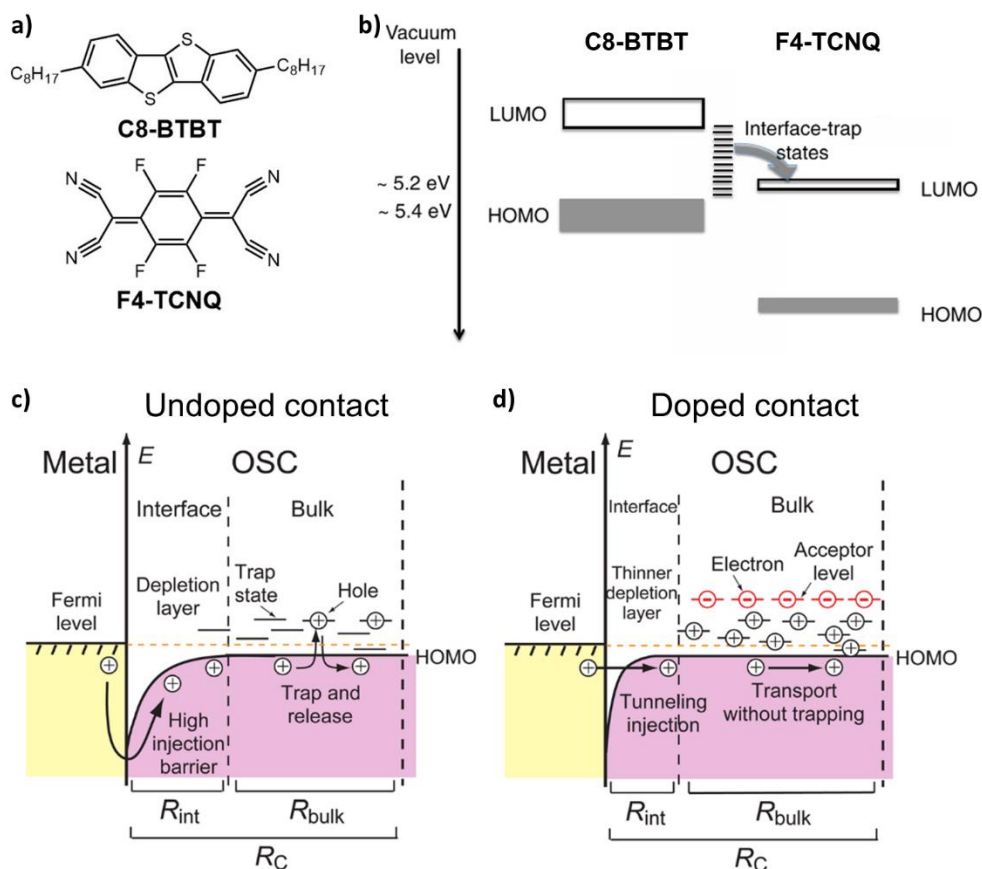


**Figure 4.1.** (a) Molecular structures of C8-BTBT and F4-TCNQ. (b) Energy diagram showing the charge-transfer between C8-BTBT and F4-TCNQ, thus filling the in-gap traps levels at the interface of the OSC.

Extracted from ref. 23. Schematic energy diagrams of the organic semiconductor/metal contact: (c) without doping, the depletion layer is very thick and hole injection is by thermal activation through a high-energy barrier, (d) with acceptor doping, so that the depletion thickness decreases, the tunneling injection becomes predominant, and trap states are occupied. Extracted from ref. 15.

A large variety of acceptor materials has been explored for p-doping purposes, which can be mainly classified as metals and metal oxides,<sup>9,15</sup> carbon-based nanostructures,<sup>4</sup> small organic molecules,<sup>16</sup> and organic-metallic complexes.<sup>17</sup> Among these, the fully fluorinated derivative of tetracyanoquinodimethane, F4-TCNQ (shown in **Figure 4.1 (a)**), is one of the most widely used p-type dopants for both polymeric and small molecule organic semiconductors.<sup>18–24</sup> Its effectiveness relies on its strong electron-withdrawing ability, as it has a deep lowest unoccupied molecular orbital (LUMO, around -5.2 eV) that is energetically in the vicinity of the HOMO level of many organic semiconductors, thus enabling doping via charge transfer. In particular, there are some works in which F4-TCNQ was used as dopant in C8-BTBT based OFETs, facilitating charge injection.<sup>23,24</sup> In this same

line, in Chapter 3 the contact resistance of transistors based on a blend of C8-BTBT and polystyrene (PS) was successfully reduced by about one order of magnitude by employing F4-TCNQ/Au top electrodes.<sup>10</sup> Two reasons have been suggested to explain the observed decrease in the contact resistance ( $R_C$ ). Firstly, doping at the contacts can increase the charge density in the depletion region, which becomes thinner (see **Figure 4.1 (c-d)**).<sup>15</sup> Consequently, charge tunnelling is favoured and the interface contact resistance ( $R_{int}$ ) is lowered. Secondly, it has been proposed that the reduction of traps density in the organic semiconductor/metal interface plays a role decreasing the bulk contact resistance ( $R_{bulk}$ ). As shown in **Figure 4.1 (b)**,<sup>23</sup> given the LUMO and HOMO levels of F4-TCNQ and C8-BTBT, respectively, it could be expected that most of the in-gap trap levels of the OSC are filled by a charge transfer process, thus facilitating charge transport through this bulk region. In addition, thanks to the low energy of the C8-BTBT HOMO, no additional mobile charges are generated in the semiconductor (i.e., it is not essentially oxidised). This is a very interesting point, since it makes possible to improve injection without increasing the off current, as it has been observed for other OSCs with higher HOMO energy, such as pentacene ( $\sim -4.8$  eV).<sup>23</sup>

Moreover, it is possible to distinguish between selective and bulk doping, that is, whether the semiconductor film is doped only at the desired areas (for example, at the OSC/electrode interface) or homogeneously doped. This substantially depends on the doping methodology employed, which can be basically divided into thermal evaporation, solution-based and physisorption processes, as described in the following and depicted in **Figure 4.2**.<sup>13,14</sup>

#### ► Thermal evaporation

The thermal evaporation of dopants has been widely investigated since it offers a high control over the doping dose.<sup>10,15,20–22</sup> The co-deposition of the dopant and the OSC gives rise to doped films in which the mixing ratio can be easily controlled by adjusting their individual evaporation rates. An alternative is to sequentially evaporate a dopant layer over the already formed OSC film; in this case, doping can be controlled by adjusting the dopant layer thickness. In addition, by using shadow masks dopant interlayers can be inserted at the OSC/electrode interface, thus selectively doping the contact area only.

#### ► Solution-based processes

Depositing dopant molecules from solution is very attractive as solution-based methodologies provide the additional benefit of low-cost manufacturing. The simplest solution-based approach consists on depositing a solution of the dopant molecule and the OSC.<sup>18,19</sup> In this way, a precise control of the relative dopant weight or molar ratio to the OSC can be achieved. However, solubility issues (such as aggregation or precipitation) usually arise; as a result, improving the dopants solubility in common organic solvents has attracted plenty of attention.<sup>25</sup> Another option is the sequential deposition of the OSC and the dopant molecule by solution methodologies, such as coating<sup>24</sup> or dipping<sup>23</sup>. In this

case, orthogonal solvents should be selected for the dopant and the OSC in order to avoid dissolving the pre-deposited film.

### ► Physisorption

Organic semiconductors can also be doped by physisorption, which is mainly accomplished by exposing the OSC thin film to vapours of the dopant. For example, using iodine ( $I_2$ ) as p-type dopant has demonstrated to give rise to remarkable performance improvements in terms of charge carrier mobility and total resistance even employing short exposure times ( $\sim 5$  s).<sup>12,26</sup> In spite of the simplicity of this method, the lack of control over the doping level and homogeneity is an important disadvantage for real applications. In this sense, the superficial exposure of the organic layer to an aqueous solution of the dopant agent provides a better control over dopant concentration and exposure time. This solution-based approach was recently exploited in our group for mercury-mediated surface doping of organic semiconductor transistors.<sup>27</sup>

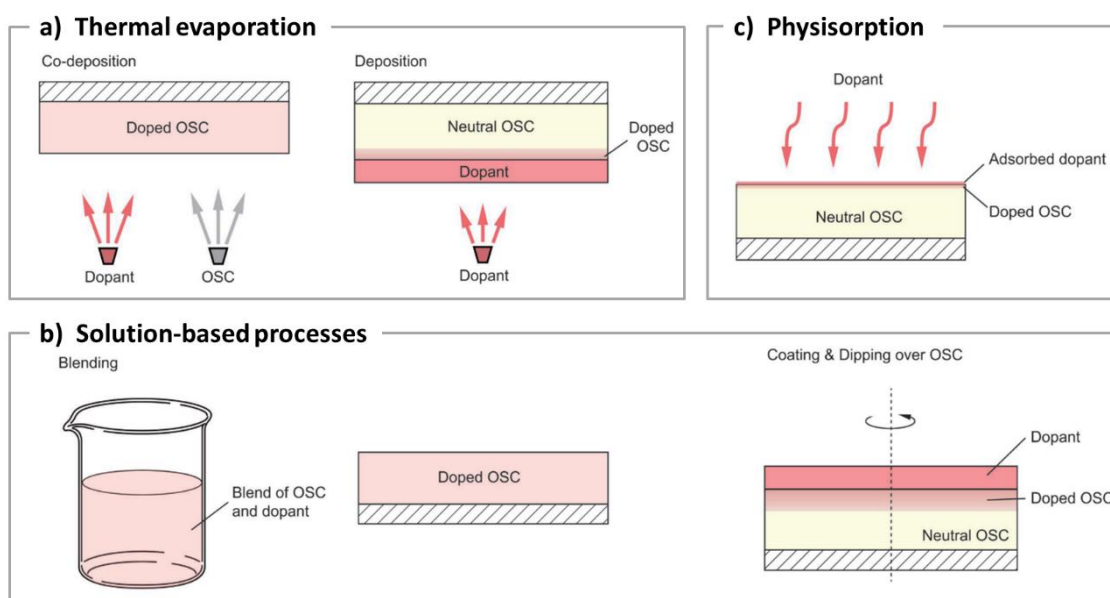


**Figure 4.2.** Schematic illustration of organic semiconductor doping techniques: (a) thermal evaporation, (b) solution-based processes and (c) physisorption. Adapted from ref. 14.

All in all, OFET doping is a developing field that requires further optimisation in order to ensure device reliability. Given the vast library of OSCs, dopant molecules and processing methodologies, fundamental understanding on doping mechanisms and related processes, such as doping diffusion, is still lacking. However, there are some general ideas that should be taken into account.<sup>12–14</sup> First, in the case of bulk doping (i.e., when the whole organic semiconductor film is doped) some detrimental effects can be anticipated, especially at high doping ratios. These mainly concern changes in the semiconductor

morphology and microstructure, which surely affect the electrical characteristics. On the other hand, when sequential doping is chosen, although it is possible that the OSC layer retains its inherent molecular packing, stability arises as an additional challenge. Because the dopant molecules are not covalently bonded to the organic semiconductor, they are free to diffuse with time and under an applied electric field. This is especially true for small-sized dopants and small molecule OSC layers.

## Objectives

Thus, the objective of this chapter is to explore various doping methodologies in order to improve the performance of C8-BTBT based OFETs, which typically exhibit contact resistance issues. Thin films based on blends of C8-BTBT and PS, deposited from solution by bar-assisted meniscus shearing (BAMS), were used as platform for testing different doping strategies. On one hand, contact doping was investigated by inserting a F4-TCNQ interlayer at the OSC/electrode interface. On the other hand, doping the semiconductor film from solution was addressed both by adding F4-TCNQ in the OSC solution and depositing such ink solution by BAMS, and by exposing the surface of a pre-deposited C8-BTBT based film to an iodine water solution. In all cases, focus was set on optimising the performance by adjusting the amount of dopant employed and also studying the devices stability in time.

## 4.2 INSERTING A DOPING INTERLAYER AT THE OSC/ELECTRODE INTERFACE

---

As it was previously mentioned, the performance of C8-BTBT based OFETs is strongly limited by contact resistance. In Chapter 3 it was demonstrated that by incorporating a 20 nm thick interlayer of F4-TCNQ under the Au top electrodes charge injection is ameliorated, resulting in a higher device mobility.<sup>10</sup> However, due to the small size and planarity of the F4-TCNQ dopant molecule, it has been reported that it can diffuse and intercalate in the organic semiconducting layer giving rise to an enhancement of disorder and structural defects. Thus, doping can ultimately result in a reduction of the devices stability in time or even an oxidation of the OSC, causing an increase of the off current.<sup>28</sup> In this sense, optimising the amount of dopant employed in order to achieve the desired performance improvement but avoiding (or at least minimising) these detrimental effects is crucial. Hence, electrodes comprising F4-TCNQ layers with different thickness have been considered in this work. Moreover, given the vertical phase separation found for C8-BTBT:PS thin films (Chapter 3), PS with different molecular weight ( $M_w$ ) have been employed in order to investigate how this factor affects the OFET performance as well as the device stability.

### Device fabrication

Thin films based on C8-BTBT and PS were deposited on Si/SiO<sub>2</sub> substrates by bar-assisted meniscus shearing (BAMS) from blend solutions in chlorobenzene (2 wt%) prepared at a 4:1 weight ratio. The use of chlorobenzene as solvent as well as the blending ratio were selected considering the previously optimised experimental conditions shown in Chapter 2 and 3.<sup>10,29</sup> PS with a  $M_w$  of 10 and 100 kg/mol (namely PS10k and PS100k, respectively) were employed. It is worth mentioning that films based on C8-BTBT only were not considered as they presented too many cracks along the crystalline layer, thus disrupting charge transport. Bottom-gate top-contact devices (**Figure 4.3**) were fabricated by evaporating F4-TCNQ/Au electrodes (10 or 20 nm of F4-TCNQ and 25 nm of Au) through a shadow mask; devices with Au only electrodes (25 nm thick) were also fabricated for comparison. The evaporation process resulted in OFETs with channel lengths from  $L = 30$  to 80  $\mu\text{m}$  and fixed channel width of  $W = 1$  mm. In summary, 6 different types of devices, based on two different formulations (C8-BTBT:PS10k and C8-BTBT:PS100k) and three different electrodes architecture (Au, 10 nm F4-TCNQ/Au and 20 nm F4-TCNQ/Au), were employed along this work.

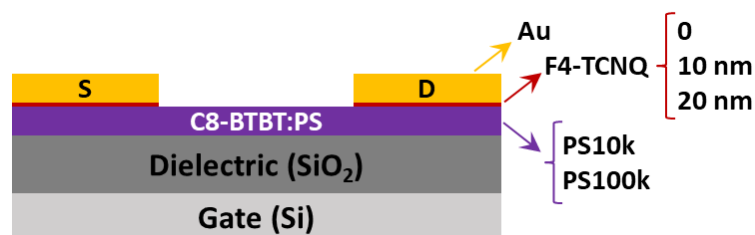


**Figure 4.3.** Scheme of the bottom-gate top-contact OFETs employed in this work, showing the cross-section of the devices and the employed materials (molecular weight of PS and thickness of the F4-TCNQ interlayer).

### Thin-film characterisation

The polarised optical microscope images of the C8-BTBT:PS10k and C8-BTBT:PS100k thin films are shown in **Figure 4.4**, where it can be observed that both formulations give rise to a similar morphology with plate-like crystal domains of various hundreds of microns. To further characterise the thin-film morphology, atomic force microscopy (AFM) images were acquired (**Figure 4.5**). AFM topography images shown in **Figure 4.5 (a-b)** indicate that both types of C8-BTBT:PS films have a uniform and smooth surface, with a root mean square roughness (*rms*) of 5.6 and 4.0 nm for films with PS10k and PS100k, respectively. In addition, the thickness of the films, estimated from the height profiles in **Figure 4.5 (e-f)**, was found to be between 20 and 30 nm, which is in agreement with our previous work employing C8-BTBT:PS10k with a 4:1 weight ratio (see Chapter 3).<sup>10</sup>

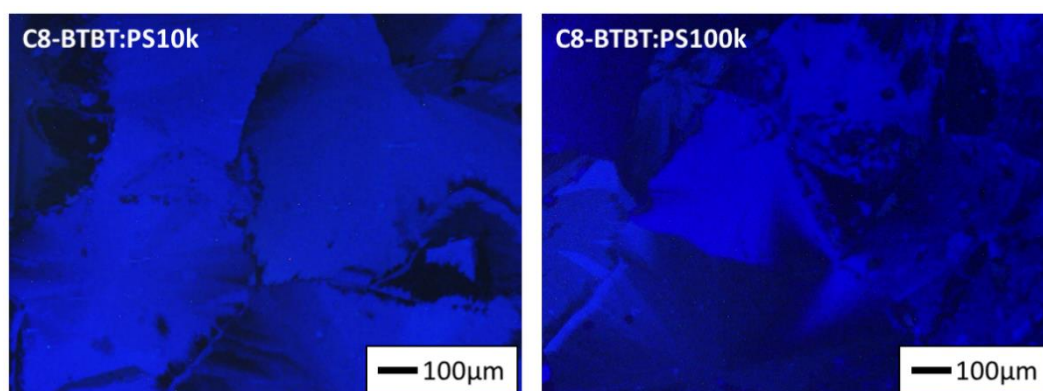


**Figure 4.4.** Crossed-polarised optical microscope images of thin films based on C8-BTBT blended with PS10k (left) and PS100k (right).



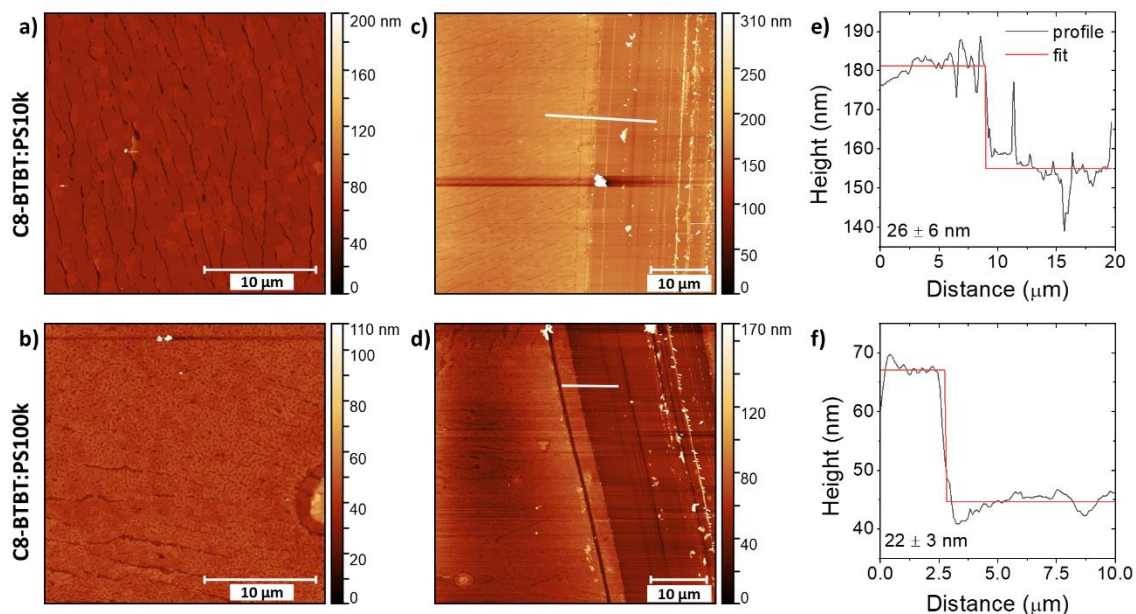


**Figure 4.5.** (a-d) AFM topography images and (e-f) height profiles obtained from the height step in (c-d) for thickness estimation of thin films based on C8-BTBT blended with PS10k and PS100k. The bar indicates the path in which the height profile has been obtained.

The high degree of crystallinity was confirmed by the X-ray diffractograms in **Figure 4.6**. C8-BTBT:PS10k and C8-BTBT:PS100k thin films exhibited identical diffraction patterns in agreement with the monoclinic phase previously reported for this material, which presents a herringbone packing.<sup>30</sup> In addition, only (00l) type reflections were observed, indicating that crystallites are highly oriented with respect to the substrate.

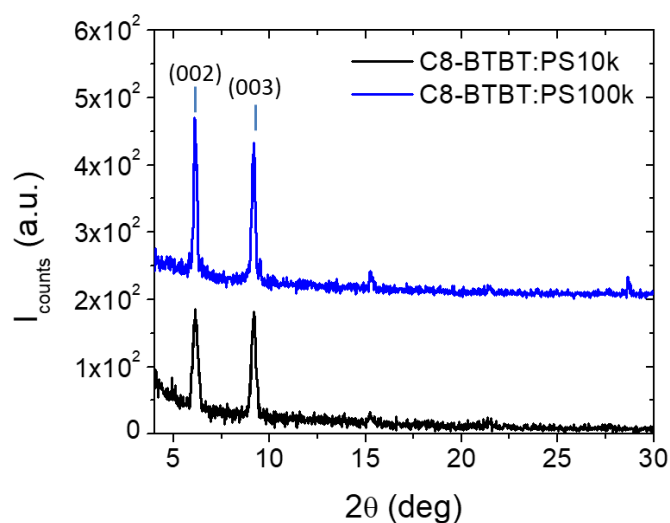


**Figure 4.6.** X-ray diffractograms of thin films based on C8-BTBT blended with PS10k and PS100k. Diffraction curves have been shifted along the y-axis for clarity.

## OFET electrical characterisation

OFET devices were electrically characterised right after fabrication under ambient conditions. In order to statistically evaluate the different performance resulting from the different C8-BTBT:PS blends and electrodes architecture employed, 8 devices of each type were measured. Typical saturation transfer characteristics are shown in **Figure 4.7**, while the corresponding output curves are collected in **Figure 4.8**. The main parameters of the measured OFETs, including average and standard deviation values, are summarised in **Table 4.1**.

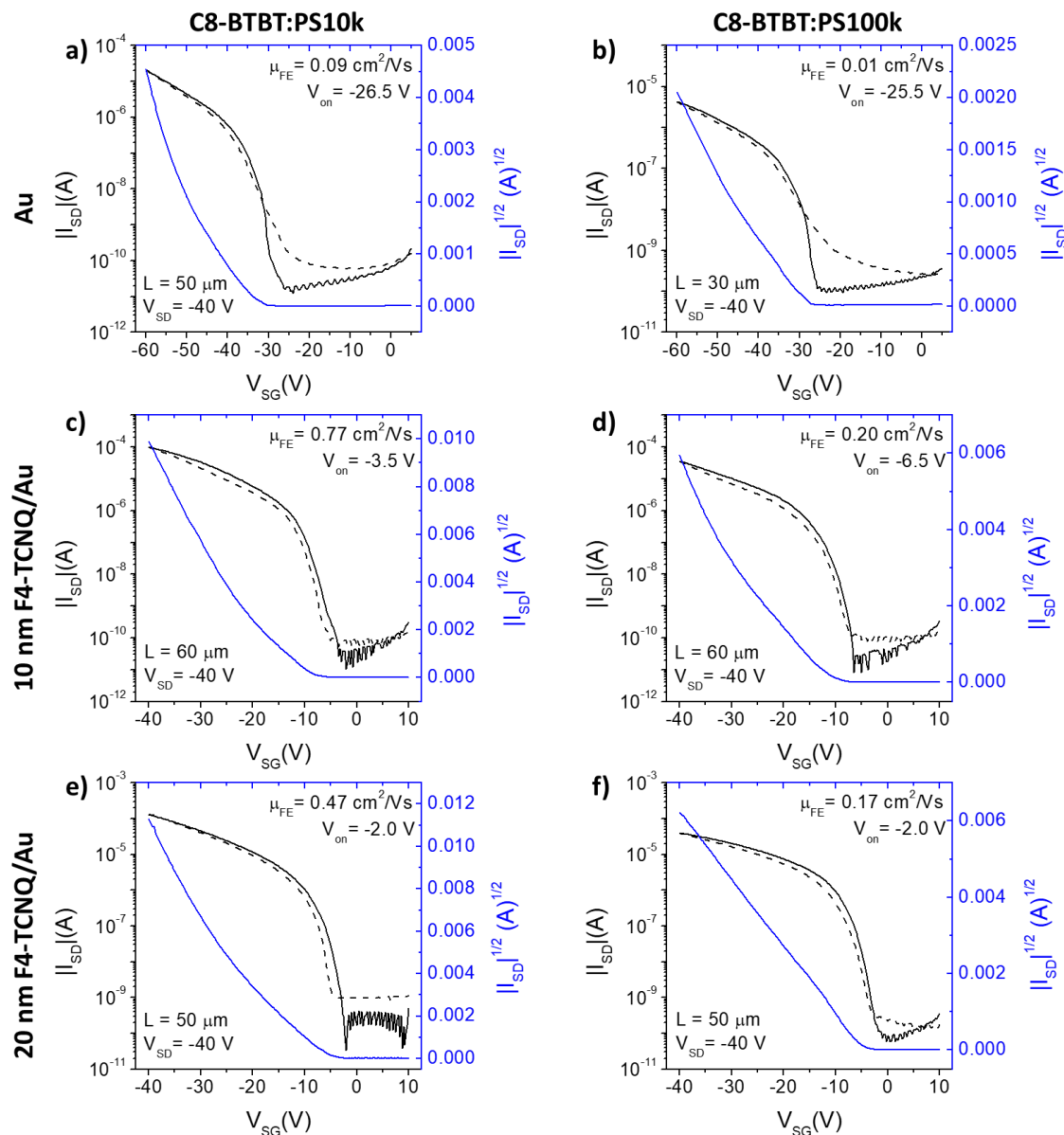


**Figure 4.7.** Transfer characteristics in the saturation regime and square root of the absolute value of the source-drain current vs. source-gate voltage for the extraction of field effect mobility of typical OFET devices based on C8-BTBT:PS10k (left) and C8-BTBT:PS100k (right) blends and with Au or F4-TCNQ/Au top electrodes. Straight and dashed lines correspond to forward and reverse sweeps of source-gate voltage, respectively.



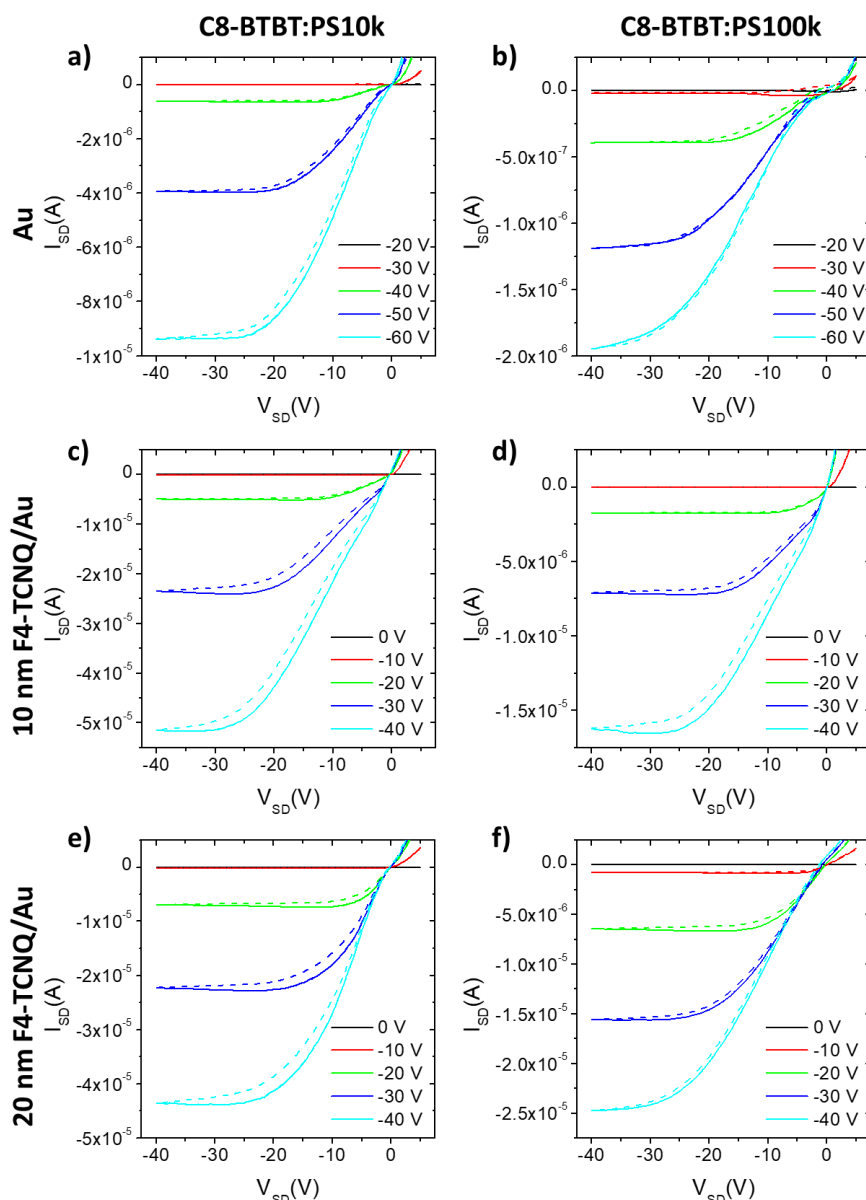


**Figure 4.8.** Output characteristics of typical OFET devices based on C8-BTBT:PS10k (left) and C8-BTBT:PS100k (right) blends and with Au or F4-TCNQ/Au top electrodes. Straight and dashed lines correspond to forward and reverse sweeps of source-drain voltage, respectively.

Firstly, from the electrical measurements of C8-BTBT:PS10k and C8-BTBT:PS100k devices with Au contacts large (negative) switch-on voltage ( $V_{on}$ ) values, of -27 and -28 V in average, were extracted, respectively (see **Table 4.1**). This finding is in agreement with previously reported results employing this organic semiconductor.<sup>6-8,10</sup> Moreover, it evidences how the large mismatch between the C8-BTBT HOMO and the gold work-function limits the operability of C8-BTBT based OFETs. This issue has also an impact on the output characteristics of the devices, which exhibit low linearity at low source-drain voltage (see **Figure 4.8 (a-b)**). Contact resistance ( $R_C W$ ) was extracted by the Y-function

method, which allows obtaining contact resistance values of single devices from their linear transfer characteristics.<sup>1,31</sup> For C8-BTBT:PS10k devices with Au electrodes, an average contact resistance of 26 k $\Omega$ ·cm was calculated, which agrees well with the resistance value extracted by Kelvin probe force microscopy in Chapter 3 (23.9 k $\Omega$ ·cm) for the source MoO<sub>3</sub>/Au contact.<sup>10</sup> By comparing both blends, C8-BTBT:PS10k and C8-BTBT:PS100k, it is noteworthy that devices with PS100k exhibit a field-effect mobility ( $\mu_{FE}$ ) and an *on/off* ratio almost ten times smaller than that of devices with PS10k (see **Figure 4.7 (a-b)**), indicating that the higher molecular weight of the binding polymer negatively affects the OFET performance. Indeed, a higher contact resistance (80 k $\Omega$ ·cm, on average) was extracted for this type of devices.

On the other hand, in the devices with a doping interlayer (i.e., with F4-TCNQ/Au electrodes) the overall OFET performance was enhanced as a result of the improved charge injection. For these devices the switch-on is closer to 0 V, with average  $V_{on}$  values ranging between -3 and -5 V when 10 nm of F4-TCNQ were incorporated and around -2 V when the maximum thickness of F4-TCNQ considered, 20 nm, was evaporated (see **Table 4.1**). Along with this remarkable improvement of the switch-on voltage, devices with doped contacts exhibited an improved linearity of the output curves at low source-drain voltage (see **Figure 4.8 (c-f)**). This result is related to the smaller contact resistance extracted for OFETs with F4-TCNQ/Au electrodes, which is at least half of that extracted for devices with Au contacts, as shown in **Table 4.1**. Indeed, a better injection but also extraction of holes might be responsible for the reduction of the hysteresis registered between the forward and reverse transfer characteristics; the high off current shown by C8-BTBT:PS devices with Au contacts in the reverse sweep is no longer appreciated when F4-TCNQ/Au electrodes are employed. Finally, it is easy to see from the transfer curves in **Figure 4.7 (c-f)** that the use of F4-TCNQ/Au contacts results in a higher source-drain on current ( $I_{on}$ ) and an enhanced field-effect mobility, with average values as high as 0.5 cm<sup>2</sup>/V·s. However, as it is commonly found in contact doping, an increase of almost one order of magnitude in the off current ( $I_{off}$ ) was observed, hampering the enhancement of the total *on/off* ratio. This issue also results in a less steep switching for devices with doped contacts, as evidenced by the higher subthreshold swing ( $SS$ ) values collected in **Table 4.1**, which point towards a more disordered organic semiconductor/electrode interface. Interestingly, although a remarkable improvement of the OFET performance is achieved by using F4-TCNQ/Au electrodes, no great differences are observed between the 10 and the 20 nm thick interlayer.

It is important to highlight that, regardless of the electrodes architecture, devices based on the C8-BTBT:PS10k blend exhibited a smaller contact resistance resulting in a higher field-effect mobility and an overall improved OFET performance in comparison with C8-BTBT:PS100k based devices. This indicates that using PS with a high  $M_w$ , 100 kg/mol in this case, hinders achieving an efficient charge injection. Assuming that both formulations

undergo the same vertical phase separation discussed in Chapter 3, a thicker underlying PS layer when PS100k is present in the blend could be suggested as a possible explanation for these results. However, a structural study should be conducted to confirm this idea. Anyhow, this highlights the importance of carefully choosing not only the type of polymer but also the  $M_w$  employed, as it can determine the final characteristics of small molecule:polymer blend films.<sup>32</sup>

**Table 4.1.** Main OFET parameters of C8-BTBT:PS10k and C8-BTBT:PS100k devices with Au and F4-TCNQ/Au electrodes extracted in the saturation regime from a set of 8 devices of each formulation measured right after fabrication.

PS	F4-TCNQ interlayer	$I_{on}$ ( $\mu A$ )	$I_{off}$ (nA)	$on/off$	$\mu_{FE}$ ( $cm^2/V \cdot s$ )	$V_{on}$ (V)	SS (V/dec)	$R_C \cdot W$ ( $k\Omega \cdot cm$ )
10k	-	30	0.05	$8 \cdot 10^5$	$0.12 \pm 0.05$	$-27 \pm 4$	$1.3 \pm 0.3$	$26 \pm 2$
100k	-	7	0.2	$1 \cdot 10^5$	$0.02 \pm 0.01$	$-28 \pm 1$	$1.2 \pm 0.4$	$80 \pm 20$
10k	10 nm	70	8	$5 \cdot 10^5$	$0.5 \pm 0.3$	$-5 \pm 5$	$3.2 \pm 1.2$	$11 \pm 6$
100k	10 nm	40	2	$4 \cdot 10^5$	$0.2 \pm 0.1$	$-3 \pm 4$	$2.9 \pm 0.8$	$40 \pm 20$
10k	20 nm	100	0.1	$1 \cdot 10^6$	$0.4 \pm 0.1$	$-2 \pm 4$	$1.6 \pm 1.2$	$12 \pm 7$
100k	20 nm	70	20	$7 \cdot 10^5$	$0.3 \pm 0.2$	$-2 \pm 3$	$2.1 \pm 1.2$	$30 \pm 10$

### Time stability

The electrical stability of the fabricated OFETs was investigated in order to evaluate the possible degradation of the devices performance in time. To do so, devices based on both formulations, C8-BTBT:PS10k and C8-BTBT:PS100k, were monitored for up to 91 days (3 months). The evolution in time of some relevant electrical parameters, on and off currents, mobility and switch-on voltage, is shown in **Figure 4.9** for devices with Au electrodes, in **Figure 4.10** for devices with 10 nm F4-TCNQ/Au electrodes and in **Figure 4.11** for devices with 20 nm F4-TCNQ/Au electrodes. Moreover, the final values extracted for the main OFET parameters (i.e., after 3 months) are summarised in **Table 4.2**.

Firstly, the evolution of the source-drain current of C8-BTBT:PS devices with Au contacts (shown in **Figure 4.9 (a-b)**) points towards a quite stable behaviour. It should be noted that the extracted values for the  $I_{on}$  and  $I_{off}$  displayed large variability, ranging over more than one order of magnitude. For this reason, in this kind of plot the bars do not

correspond to a standard deviation but to the minimum and maximum registered values, so that the ranging interval is better illustrated. Nevertheless, a slight decrease of the  $I_{on}$  and a notable increase of the  $I_{off}$  was observed during the last month (i.e., from day 63 onwards) for both formulations. In this line, the field-effect mobility increased after fabrication until an abrupt decrease was observed starting from day 63 (**Figure 4.9 (c-d)**). The key to understand this trend is at the interface between the top electrodes and the organic semiconducting film. The initial enhancement of mobility values can be ascribed to a better contact between the metal electrodes and the organic semiconductor layer, facilitating charge injection. Indeed, smaller contact resistance values were extracted for C8-BTBT:PS10k and C8-BTBT:PS100k based OFETs after 1 month from fabrication ( $R_C \cdot W = 16$  and  $70 \text{ k}\Omega \cdot \text{cm}$ , respectively). As a result,  $\mu_{FE}$  reached values up to 3.5 and 2.5 times higher than the original ones exhibited by each formulation. The posterior decrease in mobility can be related to a degradation of this interface in terms of crystallinity and structural order, hindering charge injection as indicated by the higher contact resistance extracted after 3 months from fabrication (see **Table 4.2**). Finally, the switch-on voltage increased (i.e., it shifted towards values closer to 0 V) almost monotonously (see **Figure 4.9 (e-f)**), reaching an average shift of +6 V for both types of devices. Bearing in mind that the devices were stored and measured in ambient conditions, the effects of continuous exposure to air and the possible introduction of unintentional doping from the environment should not be disregarded. It is noteworthy that the device-to-device variability increased with time, as manifested by the growing error bars in some of these plots.

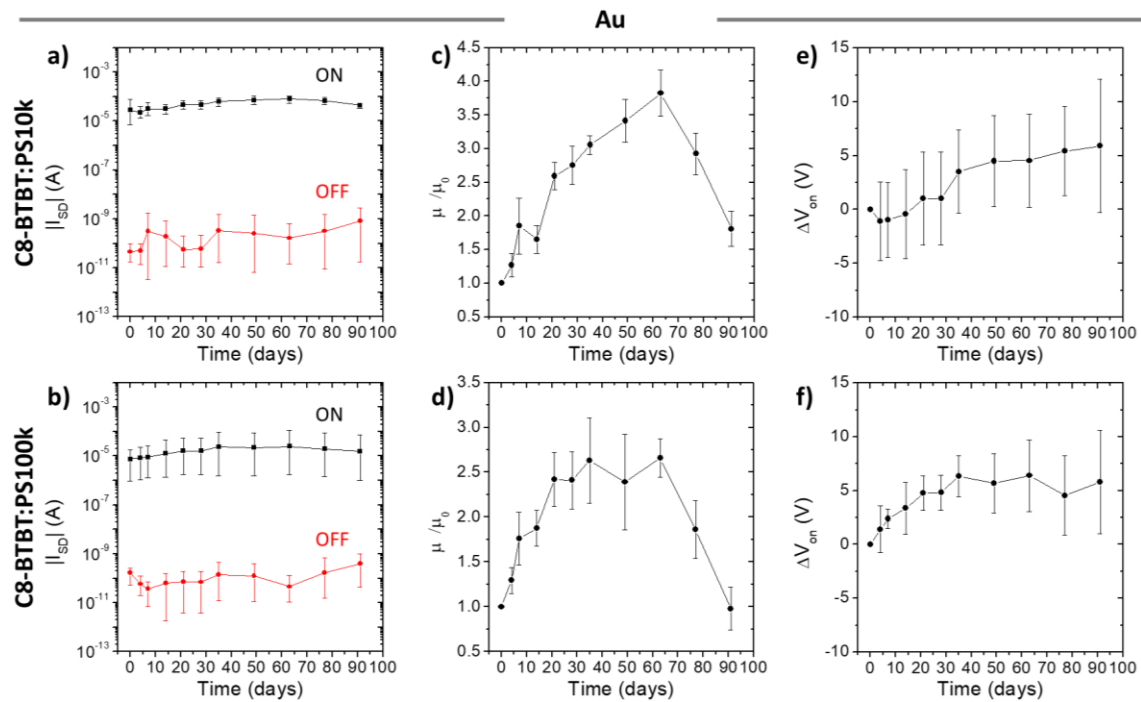


**Figure 4.9.** Stability over time of some relevant electrical parameters of OFET devices based on C8-BTBT:PS10k (top) and C8-BTBT:PS100k (bottom) blends and with Au top electrodes: (a-b) mobility variation relative to the initial value ( $\mu_0$ ), (c-d) evolution of the on and off source-drain current, and (e-f) switch-on voltage shift.

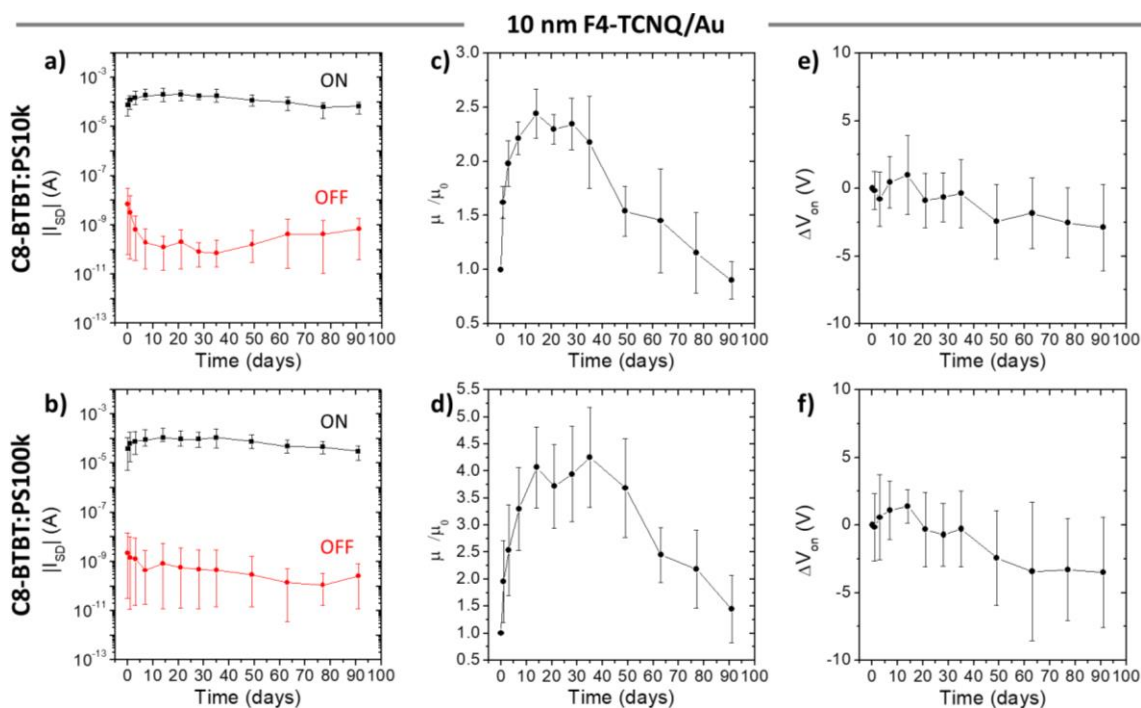


**Figure 4.10.** Stability over time of some relevant electrical parameters of OFET devices based on C8-BTBT:PS10k (top) and C8-BTBT:PS100k (bottom) blends and with 10 nm F4-TCNQ/Au top electrodes: (a-b) mobility variation relative to the original value ( $\mu_0$ ), (c-d) evolution of the on and off source-drain current, and (e-f) switch-on voltage shift.

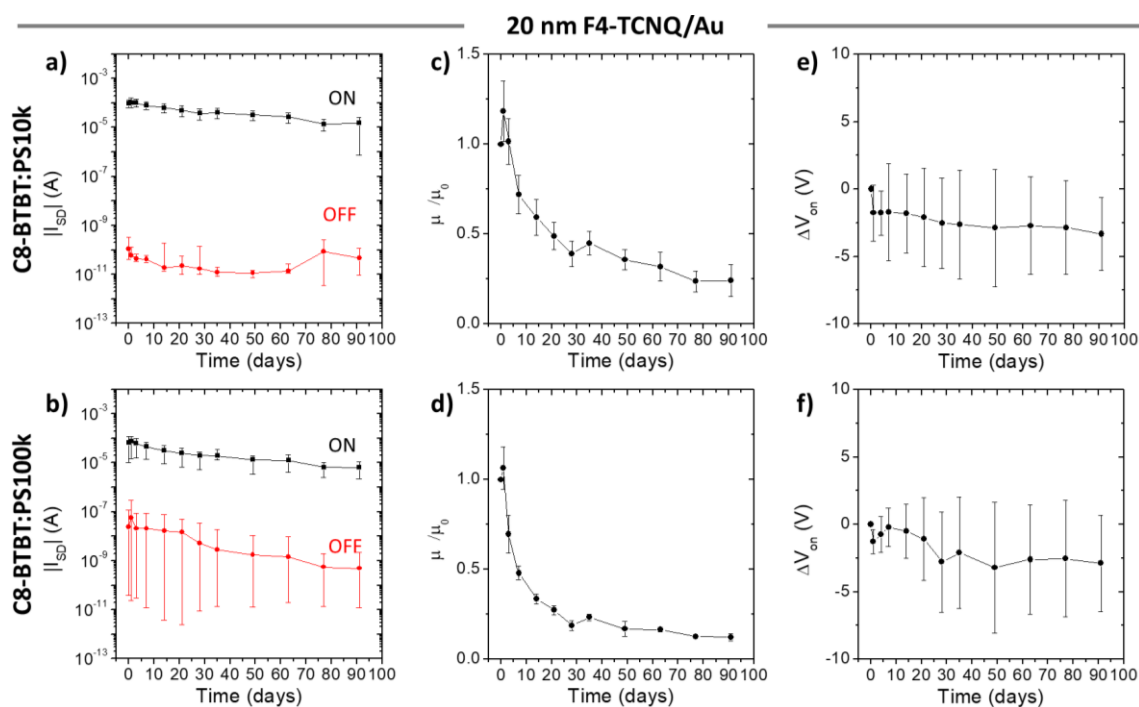


**Figure 4.11.** Stability over time of some relevant electrical parameters of OFET devices based on C8-BTBT:PS10k (top) and C8-BTBT:PS100k (bottom) blends and with 20 nm F4-TCNQ/Au top electrodes: (a-b) mobility variation relative to the original value ( $\mu_0$ ), (c-d) evolution of the on and off source-drain current, and (e-f) switch-on voltage shift.

In the devices with F4-TCNQ/Au electrodes, although a very similar improvement of the OFETs performance was achieved by using a doping interlayer of either 10 or 20 nm, the stability of the electrical characteristics clearly differs. For the devices with 10 nm F4-TCNQ/Au top electrodes an increase of the on current (**Figure 4.10 (a-b)**) along with the field-effect mobility (**Figure 4.10 (c-d)**) was registered during the first days after fabrication up to day 14; then, both parameters stabilised and slowly decreased with time. As a result, mobility values after 3 months were almost equal to those exhibited by C8-BTBT:PS10k and C8-BTBT:PS100k based OFETs right after fabrication (see **Table 4.2**). The observed trends can be explained by the same processes mentioned above: a better contact of the top electrodes with the organic semiconductor layer, thus improving charge injection, followed by the degradation of the organic layer at such interface, resulting in a higher contact resistance (see **Table 4.2**). Moreover, with the inserted doping interlayer, the diffusion of F4-TCNQ molecules into the C8-BTBT layer, thus disordering its crystalline structure, may explain the accelerated degradation. In fact, devices with 20 nm F4-TCNQ/Au contacts exhibited peak  $I_{on}$  and  $\mu_{FE}$  values (shown in **Figure 4.11 (a-b)** and **Figure 4.11 (c-d)**, respectively) after 1 day from fabrication. After that, both values decreased rapidly, in such a way that the final OFET mobility values were between 4 and 10 times smaller than the original ones (see **Table 4.2**). This rapid degradation can be ascribed to a faster diffusion of F4-TCNQ as a result of the thicker layer evaporated in

these devices. Indeed, a bigger hysteresis in the transfer characteristics was experimentally observed upon measuring, probably related to the disorder induced by the dopant molecules. However, from a microscopic point of view no morphological changes could be appreciated at the edge of the electrodes. Finally, it is worth mentioning that the switch-on voltage of all C8-BTBT:PS OFETs with doped contacts shifted towards more negative values by around -3 V (Figure 4.10 (e-f) and Figure 4.11 (e-f)), indicating that no doping of the OSC channel is taking place.

**Table 4.2.** Main OFET parameters of C8-BTBT:PS10k and C8-BTBT:PS100k devices with Au and F4-TCNQ/Au electrodes extracted in the saturation regime from a set of 8 devices of each formulation measured after 3 months from fabrication.

PS	F4-TCNQ interlayer	$I_{on}$ ( $\mu$ A)	$I_{off}$ (nA)	$on/off$	$\mu_{FE}$ ( $cm^2/V\cdot s$ )	$V_{on}$ (V)	SS (V/dec)	$R_C \cdot W$ ( $k\Omega \cdot cm$ )
10k	-	40	0.8	$9 \cdot 10^5$	$0.3 \pm 0.1$	$-21 \pm 3$	$1.1 \pm 0.8$	$30 \pm 10$
100k	-	20	0.4	$7 \cdot 10^4$	$0.02 \pm 0.01$	$-22 \pm 5$	$2.3 \pm 1.6$	$150 \pm 40$
10k	10 nm	70	0.7	$3 \cdot 10^5$	$0.5 \pm 0.2$	$-7 \pm 3$	$2.0 \pm 1.9$	$40 \pm 30$
100k	10 nm	30	0.3	$7 \cdot 10^5$	$0.3 \pm 0.1$	$-7 \pm 4$	$1.7 \pm 1.1$	$100 \pm 10$
10k	20 nm	20	0.05	$6 \cdot 10^5$	$0.10 \pm 0.05$	$-6 \pm 6$	$0.8 \pm 0.4$	$20 \pm 10$
100k	20 nm	6	0.5	$1 \cdot 10^5$	$0.04 \pm 0.02$	$-5 \pm 2$	$1.9 \pm 0.9$	$80 \pm 50$

All in all, controlling the amount of dopant evaporated in the top electrodes architecture seems crucial in order to achieve OFETs with a stable performance. In particular, the use of thick doping layers (20 nm, in this case) is not advisable in the long term since it induces a fast degradation of the organic layer and the device electrical characteristics. Although in devices with 10 nm F4-TCNQ/Au contacts degradation was slower, mobility showed a decreasing, and not yet stabilised, trend after 3 months from fabrication. Hence, a doping methodology that allows to improve charge injection at the organic semiconductor/electrodes interface but also ensures time stability for the organic layer and the devices characteristics should be further investigated.

In parallel, it has been observed that the molecular weight of the PS employed, either PS10k or PS100k, does not have a considerable impact on the degradation of the OFETs performance. Consequently, given that C8-BTBT:PS100k based devices exhibited a problematic charge injection and worse OFET characteristics (higher contact resistance and lower field-effect mobility), using the C8-BTBT:PS10k blend would be preferable.



### 4.3 DOPING THE OSC FILM BY SOLUTION-BASED METHODOLOGIES

---

In this section, two different methodologies for doping semiconductor films based on C8-BTBT from solution will be explored: i) mixing F4-TCNQ and C8-BTBT in solution to deposit a doped thin film, and ii) carrying out a superficial treatment of a pre-deposited C8-BTBT based film employing an iodine aqueous solution.

#### 4.3.1 ADDING THE DOPANT MOLECULE IN THE OSC INK SOLUTION

As mentioned in the introduction section, F4-TCNQ has already been exploited as dopant for C8-BTBT based transistors. However, in the few works employing solution-based doping methodologies, which are of high interest for large-area processing, surface doping was achieved either by dipping a C8-BTBT film into a F4-TCNQ solution<sup>23</sup> or by spin-coating the dopant onto a nanoporous thin film.<sup>24</sup> These approaches not only require using orthogonal solvents to avoid dissolving the pre-deposited C8-BTBT film, but they essentially imply an additional post-treatment step. On the other hand, mixing F4-TCNQ with C8-BTBT in solution is a much simpler strategy, allowing to deposit in one step only a doped organic semiconductor layer. Also, working in this way, it is possible to precisely control the doping concentration by regulating the relative dopant/OSC molar ratio. However, adding the dopant in the OSC ink solution might also cause some detrimental effects, mainly concerning the semiconductor microstructure and the device electrical characteristics, especially at high doping ratios.<sup>14</sup> Hence, C8-BTBT layers with different amounts of F4-TCNQ have been considered in this part of the work and special attention was paid to the OFETs performance as well as the devices stability.

#### Device fabrication and thin-film characterisation

Thin films based on C8-BTBT and PS with a molecular weight of 10 kg/mol were deposited on Si/SiO<sub>2</sub> substrates by bar-assisted meniscus shearing (BAMS), employing the same experimental conditions previously described in section 4.2 (chlorobenzene solution with a 2 wt% concentration and a C8-BTBT:PS blending ratio of 4:1 in weight). The dopant molecule, F4-TCNQ, was added in the semiconductor ink employing different molar ratios ranging from 1/100 to 5/100 (mols of F4-TCNQ/mols of C8-BTBT). More details regarding the preparation of these solutions can be found in the experimental methods chapter (Chapter 7). Bottom-gate top-contact devices were fabricated by evaporating Au electrodes (25 nm thick) through a shadow mask, resulting in OFETs with channel lengths



from  $L = 30$  to  $80 \mu\text{m}$  and fixed channel width of  $W = 1 \text{ mm}$ . Devices without dopant were also fabricated for comparison and, for simplicity, they will be referred to as 0/100.

The polarised optical microscope images of the prepared C8-BTBT:PS thin films, with a F4-TCNQ molar content between 0 and 5/100, are shown in **Figure 4.12**. It can be observed that when the formulation does not include dopant, the organic semiconductor crystallises forming plate-like crystal domains (**Figure 4.12 (a)**), as it was found in the previous section. In contrast, the addition of F4-TCNQ gives rise to a different morphology with domains that are rather spherulitic than planar, even for the smallest dopant molar ratio considered, 1/100. Significant alterations of the semiconductor film morphology have already been reported for other dopant/OSC blends, in which a reduction of the domains size was also observed.<sup>16</sup>

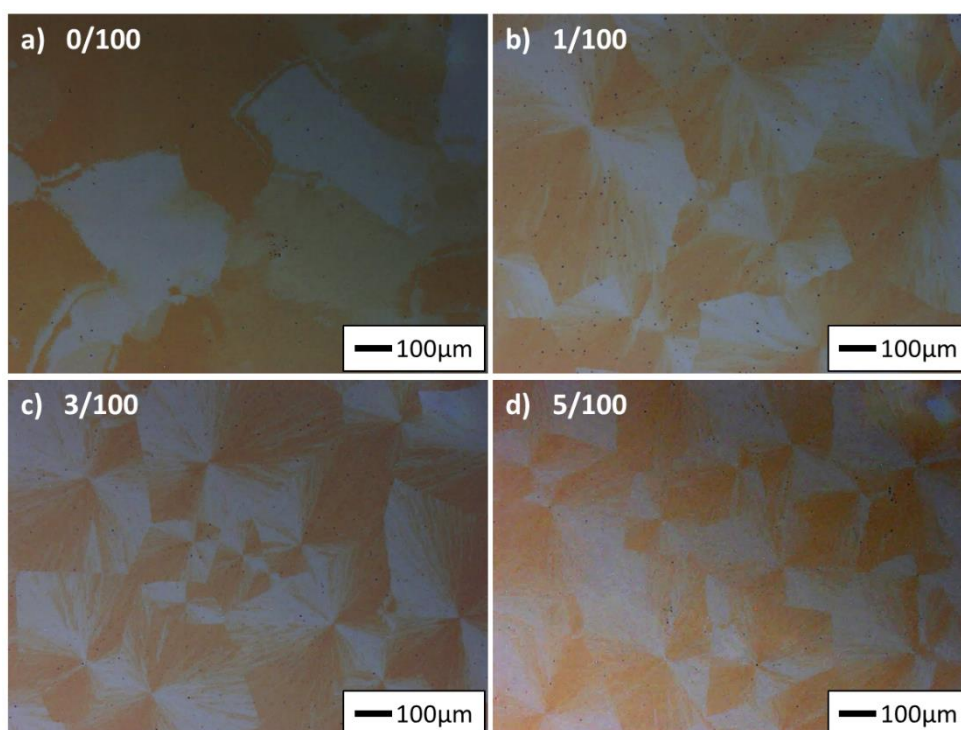


**Figure 4.12.** Crossed-polarised optical microscope images of C8-BTBT:PS thin films with a molar content of F4-TCNQ ranging between 0 and 5/100.

In spite of the different morphology exhibited by C8-BTBT:PS films with and without F4-TCNQ, X-ray diffraction (**Figure 4.13**) confirmed that the same crystalline structure is present in both types of films as identical diffraction patterns were measured from 0/100 (in black) and 5/100 (in blue) samples. Moreover, the position of the diffraction peaks is in agreement with the monoclinic phase previously reported for C8-BTBT.<sup>30</sup> In addition, the fact that only  $(00l)$  type reflections were observed indicates that crystallites are highly oriented with respect to the substrate.

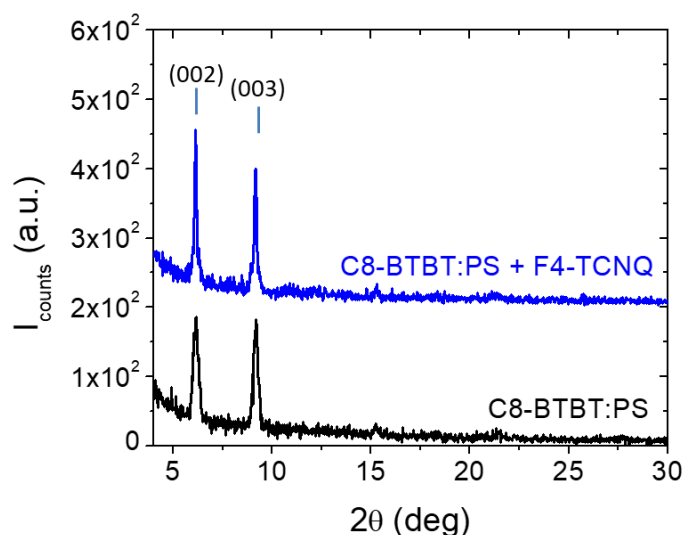


**Figure 4.13.** X-ray diffractograms of thin films based on C8-BTBT:PS without F4-TCNQ (in black) and C8-BTBT:PS with a 5/100 molar ratio of F4-TCNQ (in blue). Diffraction curves have been shifted along the y-axis for clarity.

### OFET electrical characterisation

OFET devices were electrically measured under ambient conditions right after fabrication (i.e., after the deposition of Au top electrodes). In **Figure 4.14**, typical transfer and output characteristics of devices based on C8-BTBT:PS (left) and C8-BTBT:PS with F4-TCNQ (right) are shown. The main OFET parameters, statistical analysed using 5 devices of each type, are summarised in **Table 4.3**.

From the characteristic curves of C8-BTBT:PS devices without dopant, a mean switch-on voltage ( $V_{on}$ ) around -24 V was extracted. This high negative value is in agreement with previously reported results employing this organic semiconductor<sup>6-8</sup> and former results presented in this thesis.<sup>10</sup> Indeed, the output characteristics exhibited low linearity at low source-drain voltage (see **Figure 4.14 (c)**), indicative of a high injection barrier. Contact resistance was extracted by the Y-function method, giving an average value of  $R_C \cdot W = 26 \pm 15 \text{ k}\Omega \cdot \text{cm}$ , which is similar to that calculated in section 4.2 for this formulation and structure ( $26 \pm 2 \text{ k}\Omega \cdot \text{cm}$ ). On the contrary, for devices with F4-TCNQ present in the organic active layer an improved linearity was appreciated in the output curves even when only a 1/100 molar ratio was employed (**Figure 4.14 (d)**). Along with this, doping with a 1/100 F4-TCNQ molar ratio resulted in an enhancement of the on current ( $I_{on}$ ) and the field-effect mobility ( $\mu_{FE}$ ) of around a 50%, thus reaching  $\mu_{FE} = 0.6 \text{ cm}^2/\text{V}\cdot\text{s}$ . This improved performance is explained by the smaller contact resistance values extracted for this type of devices, of  $9 \text{ k}\Omega \cdot \text{cm}$  on average (see **Table 4.3**). It is interesting to note that such reduction of the contact resistance was achieved in section 4.2 by inserting a 10 or 20 nm

thick F4-TCNQ interlayer at the C8-BTBT/electrodes interface, giving  $R_C \cdot W \approx 11\text{-}12 \text{ k}\Omega\cdot\text{cm}$ . Thus, it could be assumed that the observed performance enhancement is not related to the change in the thin-film morphology. Importantly, the positive shift of  $V_{on}$  (of over 20 V) obtained by using F4-TCNQ/Au electrodes is not observed in this case. Moreover, by increasing the content of F4-TCNQ up to doping ratios of 3/100 and 5/100 the electrical characteristics and the transport properties of the active layer are worsened, which is evidenced by the decrease of the  $I_{on}$  and  $\mu_{FE}$  values (see **Figure 4.14 (b)** and **Table 4.3**). This is not a surprising result, as reduced mobility is often observed at high doping ratios; the dopant molecules act as impurities that interfere in the molecular organisation and disrupt crystallisation, causing energetic disorder to the charge transport.<sup>14</sup> In fact, such effect is also correlated with the high contact resistance extracted for devices with a 5/100 F4-TCNQ molar ratio, of over 100  $\text{k}\Omega\cdot\text{cm}$ . It is also worth noting that the off current ( $I_{off}$ ) does not significantly increase even for the highest F4-TCNQ doping ratios, meaning that using 3/100 and 5/100 ratios is excessive in terms of induced structural disorder but not in terms of doping due to charge transfer. Indeed, the fact that the switch-on does not shift towards 0 V indicates that C8-BTBT itself is not doped, that is, that no additional mobile charges are generated.

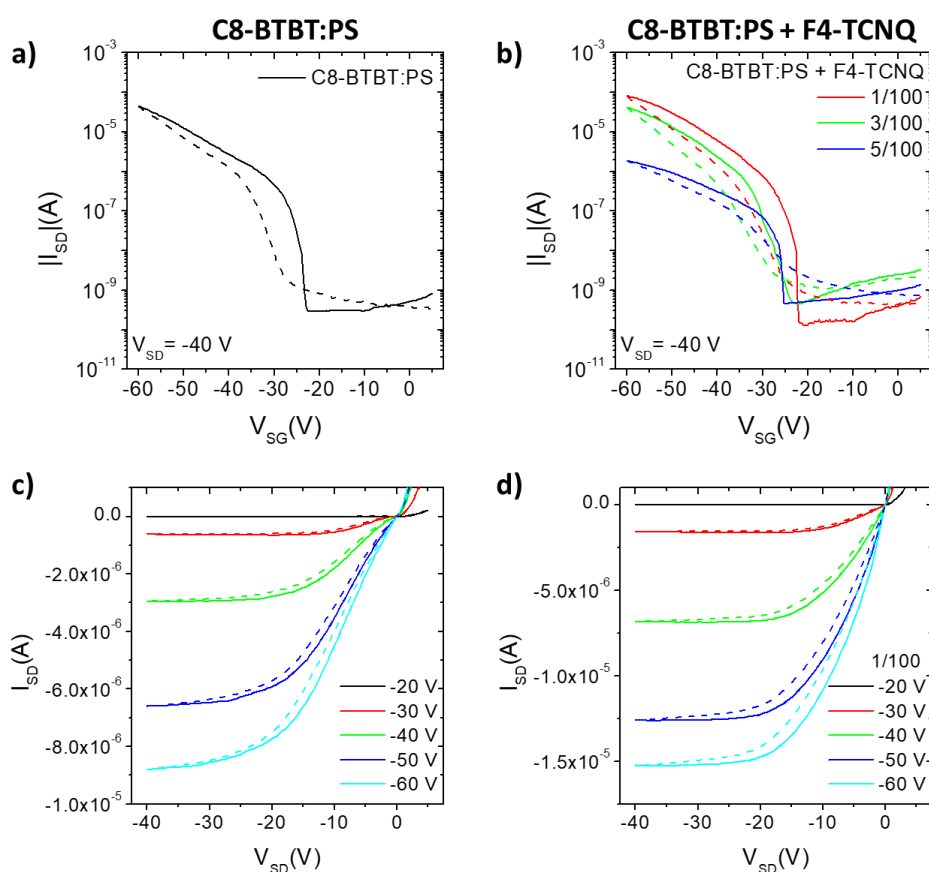


**Figure 4.14.** Electrical characteristics of typical OFET devices based on C8-BTBT:PS (left) and C8-BTBT:PS with F4-TCNQ (right), comprising Au top electrodes. (a-b) Transfer characteristics in the saturation regime. (c-d) Output characteristics. Straight and dashed lines correspond to forward and reverse sweeps, respectively, for both transfer and output characteristics.

**Table 4.3.** Main OFET parameters of C8-BTBT:PS based devices with a molar content of F4-TCNQ ranging between 0 and 5/100 and Au top electrodes extracted in the saturation regime from a set of 5 devices of each type measured right after fabrication.

F4-TCNQ molar ratio	$I_{on}$ ( $\mu\text{A}$ )	$I_{off}$ (pA)	$on/off$	$\mu_{FE}$ ( $\text{cm}^2/\text{V}\cdot\text{s}$ )	$V_{on}$ (V)	$R_C \cdot W$ ( $\text{k}\Omega \cdot \text{cm}$ )
0/100	50	300	$2 \cdot 10^5$	$0.4 \pm 0.2$	$-24 \pm 3$	$26 \pm 15$
1/100	70	200	$4 \cdot 10^5$	$0.6 \pm 0.3$	$-23 \pm 2$	$9 \pm 1$
3/100	40	400	$1 \cdot 10^5$	$0.3 \pm 0.1$	$-24 \pm 1$	$20 \pm 2$
5/100	3	300	$1 \cdot 10^4$	$0.013 \pm 0.008$	$-24 \pm 1$	$300 \pm 100$

In summary, the performance improvement achieved by adding F4-TCNQ in the C8-BTBT solution at a 1/100 molar ratio is not remarkable in comparison with the results obtained with F4-TCNQ/Au top electrodes. Although similar  $R_C \cdot W$ ,  $I_{on}$  and  $\mu_{FE}$  values were obtained, no  $V_{on}$  shift towards values closer to zero was achieved by solution mixing F4-TCNQ and C8-BTBT, proving it is a rather inefficient strategy. In this sense, a methodology that allows to fabricate dopant/organic semiconductor thin films from solution in only one deposition step, but also prevents dopant molecules from disturbing the OSC well-packed crystal structure, is highly desirable. A possible approach to this idea could consist in favouring segregation of the dopant from the OSC crystalline layer by using, for example, solvent mixtures or bulky dopants molecules.

#### Time stability

As it was previously mentioned, structural disorder and defects in the active layer due to the presence of dopant molecules can be enhanced in time, giving rise to a deteriorated device performance. Considering this, the stability of OFETs based on C8-BTBT:PS with a 1/100 F4-TCNQ molar ratio (i.e., the formulation that gave the best performance) was investigated in order to evaluate the possible degradation of the devices electrical characteristics in time. For comparison, the stability of C8-BTBT:PS OFETs without dopant (0/100) was also studied. To do so, devices based on both formulations were electrically measured after 8 and 58 days (around 1 week and 2 months, respectively) from fabrication. The evolution of the main OFET parameters, considering 5 devices of each type, is summarised in Table 4.4.

**Table 4.4.** Evolution in time of the main OFET parameters of C8-BTBT:PS based devices without dopant and with a molar content of F4-TCNQ of 1/100. All values were extracted from a set of 5 devices.

F4-TCNQ molar ratio	Time (days)	$I_{on}$ ( $\mu$ A)	$I_{off}$ (pA)	$on/off$	$\mu_{FE}$ ( $cm^2/V\cdot s$ )	$V_{on}$ (V)	$R_C\cdot W$ ( $k\Omega\cdot cm$ )
0/100	0	50	300	$2 \cdot 10^5$	$0.4 \pm 0.2$	$-24 \pm 3$	$26 \pm 15$
	8	130	100	$2 \cdot 10^6$	$1.2 \pm 0.9$	$-24 \pm 1$	$11 \pm 8$
	58	180	300	$8 \cdot 10^5$	$1.5 \pm 0.6$	$-23 \pm 2$	$5 \pm 1$
1/100	0	70	200	$4 \cdot 10^5$	$0.6 \pm 0.3$	$-23 \pm 2$	$9 \pm 1$
	8	180	200	$1 \cdot 10^6$	$1.7 \pm 0.7$	$-22 \pm 1$	$5 \pm 1$
	58	140	100	$3 \cdot 10^6$	$1.3 \pm 0.8$	$-21 \pm 3$	$5 \pm 1$

After 8 days from fabrication, the on current and the field-effect mobility exhibited by the devices was more than twice higher than the original values (reaching  $\mu_{FE} > 1 \text{ cm}^2/\text{V}\cdot\text{s}$ ), while the switch-on voltage remained practically unaltered (see Table 4.4). This enhancement of the devices performance could be ascribed to a better contact of the Au electrodes on top of the organic layer, thus facilitating charge injection at the OSC/metal interface. This process resulted in a smaller contact resistance after only one week for both 0/100 and 1/100 films, which was estimated to be around 11 and 5  $k\Omega\cdot\text{cm}$ , respectively. Indeed, this behaviour was already observed in section 4.2 for C8-BTBT:PS based OFETs with Au top contacts.

Interestingly, OFET measurements after 58 days from fabrication reveal that  $I_{on}$  and  $\mu_{FE}$  further increase in time for C8-BTBT:PS devices without dopant, for which contact resistance reaches values as low as  $R_C\cdot W = 5 \pm 1 \text{ k}\Omega\cdot\text{cm}$  (see Table 4.4). In contrast, for devices with a 1/100 F4-TCNQ molar ratio the value of such transport parameters is slightly smaller after 2 months in comparison with measurements after 1 week from fabrication. Given that the contact resistance did not vary for 1/100 doped OFETs upon this period of time, the degradation of their electrical characteristics could be ascribed to an enhancement of the structural disorder induced by the presence and diffusion of F4-TCNQ molecules in the C8-BTBT crystalline layer. Also, the effect of oxygen and water present in the environment, as samples were stored and measured in ambient conditions, should be considered. However, stability should be investigated for a longer period of time to check the degradation rate. Again, the possibility to fabricate from solution dopant/organic semiconductor thin films in which the dopant and the OSC are segregated would be convenient to improve the stability of the devices performance.



### 4.3.2 SUPERFICIAL EXPOSURE OF THE OSC FILM TO A DOPANT WATER SOLUTION

As mentioned in the introduction section, p-type doping can also be achieved by exposure to oxidising gases such as iodine, which was already investigated as dopant for polyacetylene films in the 1970's and later applied to pentacene single crystals and thin films.<sup>12</sup> However, although exposing the semiconductor layer to dopant vapours is simple from a technical point of view, with this doping methodology there is an important lack of control over the doping level and homogeneity. Considering this, and also inspired by our recent report of surface p-doping of an organic semiconducting layer by exposing it to an aqueous solution of the dopant agent (in this case, mercury),<sup>27</sup> we decided to approach iodine-doping from a solution-based perspective. Thus, in this part of the work doping C8-BTBT based films employing iodine water solutions has been explored. It is worth highlighting that iodine-doping is known to be rather unstable over time since iodine tends to desorb in ambient conditions due to its very low vapour pressure (around 40 Pa at room temperature). Bearing this in mind, the stability of iodine-doped devices was considered.

#### Device fabrication and superficial exposure doping procedure

OFET devices based on C8-BTBT and PS with a molecular weight of 10 kg/mol were fabricated by depositing such blend on Si/SiO<sub>2</sub> substrates by bar-assisted meniscus shearing (BAMS). The experimental conditions were identical to that of the devices reported in section 4.3.1, that is, solutions were prepared in chlorobenzene with a 2 wt% concentration and a C8-BTBT:PS blending ratio of 4:1 in weight was employed. Indeed, the resulting thin films exhibited the same morphological and structural features as those previously presented, with plate-like crystal domains (see **Figure 4.12 (a)**) and high crystallinity and orientation with respect to the substrate (see **Figure 4.13**, black line). As well, bottom-gate top-contact devices were fabricated by evaporating 25 nm thick Au electrodes on top of the active layer through a shadow mask (**Figure 4.15 (a)**). This process gave rise to OFETs with channel lengths ranging from  $L = 30$  to  $80 \mu\text{m}$  and fixed channel width of  $W = 1 \text{ mm}$ . As it was previously mentioned, doping was done by exposing the top surface of the devices to an iodine water solution. To do so, a saturated iodine solution was prepared in MilliQ water beforehand (concentration  $\sim 0.3 \text{ mg/ml}$ ) and a droplet was casted on the device covering completely the OFET channel, as shown in the photograph in **Figure 4.15 (b)**. After a waiting time of 3 minutes, which was enough to allow iodine to be adsorbed into the organic layer and dope the semiconductor by charge transfer, the devices were abundantly washed with more MilliQ water and dried.

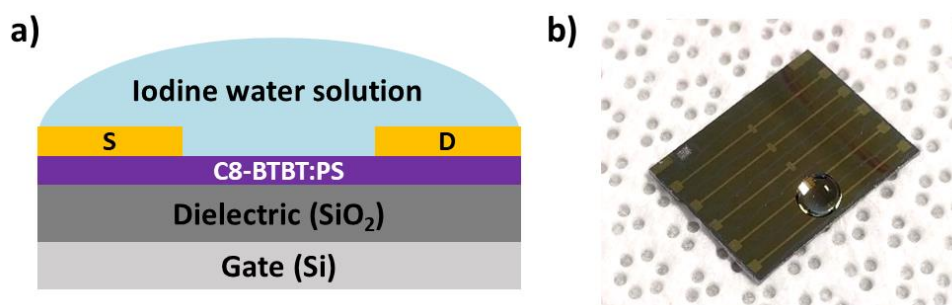


**Figure 4.15.** (a) Scheme of the bottom-gate top-contact OFETs employed in this work, showing the superficial exposure method. (b) Photograph of a real device with a drop of iodine solution on top.

### OFET electrical characterisation

OFET devices were electrically measured under ambient conditions before and after doping with iodine. In **Figure 4.16 (a)**, which shows the transfer characteristics in saturation regime before and after exposure to the iodine solution, a large current enhancement can be observed. Indeed, it can be observed that both the on current ( $I_{on}$ ) and the field-effect mobility ( $\mu_{FE}$ ) increased approximately 4 times as a result of iodine-doping, reaching values as high as  $\mu_{FE} = 4.4 \text{ cm}^2/\text{V}\cdot\text{s}$  (**Figure 4.16 (b)**). In order to test reproducibility, a total of 5 devices were characterised following the same procedure and the main OFET parameters were extracted before and after exposure, as summarised in **Table 4.5**. In all cases a remarkable enhancement of conductivity ( $I_{on}$  and  $\mu_{FE}$ ) was observed, while the off current ( $I_{off}$ ) did not increase and the switch-on voltage ( $V_{on}$ ) did not shift towards more positive values, meaning that no additional mobile charges are generated. In contrast, in the previous work exploiting mercury aqueous solutions, an increment of both  $I_{off}$  and  $V_{on}$  were reported.<sup>27</sup> This different behaviour could be ascribed to the smaller oxidation capability of iodine (with a standard oxidation potential of 0.62 V, smaller than that of mercury ions, 0.85 V) and the lower HOMO energy of C8-BTBT in comparison with the OSC employed in that study (around -5.7 eV and -5.0 eV, respectively).<sup>33</sup> In addition, previous works employing superficial exposure doping methods have already reported that the dopant is only adsorbed in the top surface of the active layer, thus avoiding excessive doping in the OFET conductive channel (which is at the bottom OSC/dielectric interface).<sup>26,27</sup> The improvement achieved by exposing the C8-BTBT layer to iodine can be related to a decrease in the hole trap density since a reduction of the subthreshold swing ( $SS$ ) was obtained after doping, as shown in **Figure 4.16 (a)**. In addition, the extracted contact resistance values ( $R_C \cdot W$ ) were also reduced by half after exposure to iodine (see **Table 4.5**), which points towards an improved charge injection at the OSC/electrode interface thanks to contact doping.<sup>26</sup>

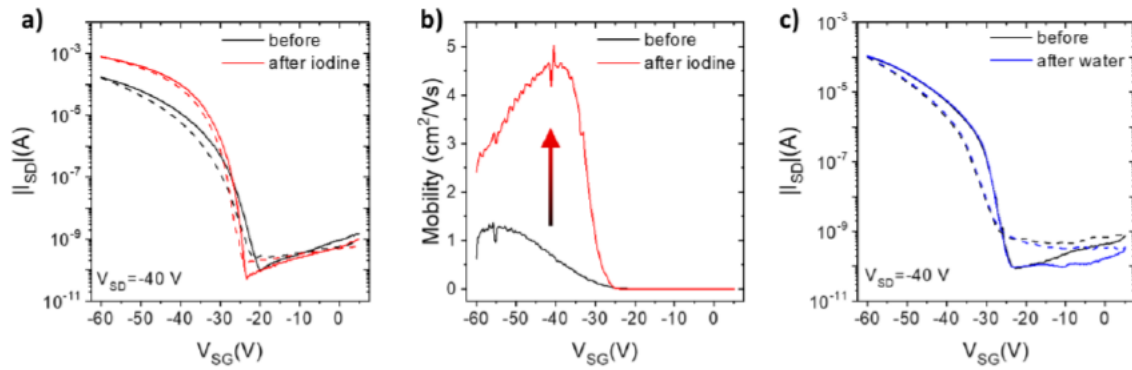


**Figure 4.16.** Electrical characteristics of OFET devices based on C8-BTBT:PS before and after they were subjected to a superficial exposure to an iodine water solution, or only water, for 3 minutes. (a, c) Transfer characteristics in the saturation regime before and after exposure to (a) iodine and (c) water, respectively. Straight and dashed lines correspond to forward and reverse sweeps, respectively. (b) Mobility profile in the saturation regime vs. source-gate voltage for a device before and after iodine exposure.

**Table 4.5.** Main OFET parameters of C8-BTBT:PS based devices measured before and after carrying out the superficial exposure to an iodine water solution, values were extracted in the saturation regime from a set of 5 devices.

Exposure to iodine solution	$I_{on}$ ( $\mu\text{A}$ )	$I_{off}$ (pA)	on/off	$\mu_{FE}$ ( $\text{cm}^2/\text{V}\cdot\text{s}$ )	$V_{on}$ (V)	SS (V/dec)	$R_C \cdot W$ ( $\text{k}\Omega \cdot \text{cm}$ )
Before	170	800	$7 \cdot 10^5$	$0.9 \pm 0.3$	$-21 \pm 1$	$2.4 \pm 0.4$	$5.7 \pm 0.8$
After	700	400	$8 \cdot 10^6$	$3.4 \pm 0.9$	$-22 \pm 3$	$1.0 \pm 0.2$	$2.1 \pm 0.3$

During doping tests, it was realised that OFET devices not directly exposed to the iodine solution but close to those that were, also showed changes in their electrical performance. To rule out a doping effect arising from washing the whole sample with MilliQ water, the same procedure was repeated exposing a new C8-BTBT:PS sample to only water for 3 minutes. As an example, the transfer characteristics in saturation regime measured for an OFET before and after it was exposed to MilliQ water are shown in Figure 4.16 (c). Here, it can be observed that the electrical performance was practically identical in both cases. This means that when a drop of iodine solution is casted on top of an OFET channel, the nearby devices are somehow affected by iodine too, pointing out the diffusion of iodine through the film and the rapid doping effect.

In addition, employing a second batch of C8-BTBT:PS samples to test iodine-doping, the role of the thin-film morphology was evidenced. The effect that iodine had on these OFET devices was clearly smaller, with an increase of the  $I_{on}$  around the 60% and the  $\mu_{FE}$  rising between a 10 and a 50%. Indeed, as shown in Figure 4.17 (b), the transfer characteristics



changed slightly after exposure to the iodine solution, but far less than the effect previously measured (shown in **Figure 4.16 (a)**). Since the exposure procedure remained the same, focus was set on the differences exhibited by the C8-BTBT:PS thin films. First of all, it was observed that in the new batch of samples the semiconductor crystallised forming domains of bigger size in comparison with those observed in previous films (see **Figure 4.17 (a)** and **Figure 4.12 (a)**). Considering this, it could be suggested that the boundaries between crystal domains facilitate doping the organic layer, offering an easy way for iodine ions to diffuse and be adsorbed. In other words, doping could be taking place at these boundaries, thus increasing the conductivity at the most resistive part of the semiconducting layer. In fact, the formation of highly conductive grain boundaries was already reported in a previous work, where such effect was attributed to the conduction assistance provided by the semiconducting polymer employed as binder.<sup>34</sup> In the case of iodine-doping, bigger crystal domains (i.e., less inter-domains boundaries) would lead to a less significant doping effect. On the other hand, the bigger crystal domains also resulted in OFETs with a higher mobility, of  $\mu_{FE} = 1.6 \text{ cm}^2/\text{V}\cdot\text{s}$ . Although one could think that with this high value there is less room for improvement, mobility only increased up to  $1.9 \text{ cm}^2/\text{V}\cdot\text{s}$  after exposure to iodine, which is much smaller than the mobility value achieved with the first batch of samples ( $4.4 \text{ cm}^2/\text{V}\cdot\text{s}$ ).

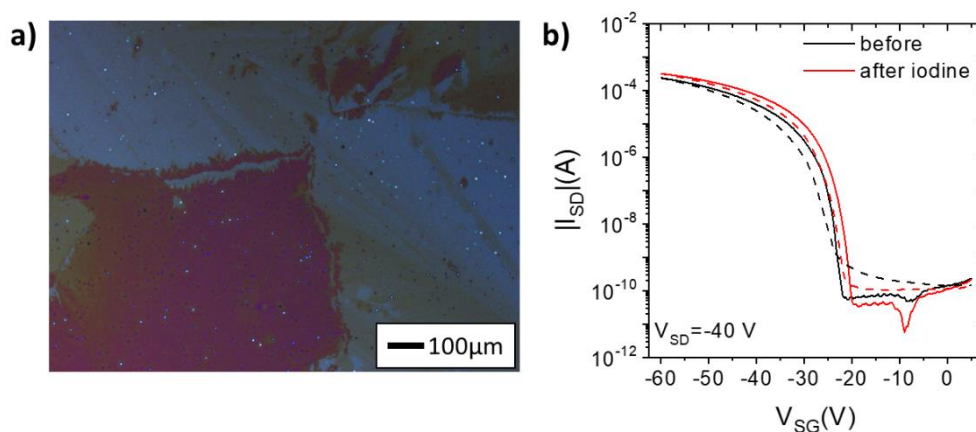


**Figure 4.17.** (a) Crossed-polarised optical microscope image of a C8-BTBT:PS thin film with large sized crystal domains. (b) Transfer characteristics in the saturation regime of an OFET device based on the film shown in (a) before and after exposure to an iodine solution for 3 minutes. Straight and dashed lines correspond to forward and reverse sweeps, respectively.

In summary, the enhancement of the OFETs performance after exposing the surface of the organic semiconductor layer to an iodine solution can be attributed to iodine-doping. This process is somehow correlated with the thin-film morphology, but many interesting factors remain unknown, for example, the extent of iodine diffusion and adsorption, or the doping dose achieved. To assess this, future work should include using some spectroscopic and surface characterisation techniques such as energy-dispersive X-ray

spectroscopy (EDX), electron paramagnetic resonance spectroscopy (EPR), Raman spectroscopy, infrared spectroscopy (IR) or conductive AFM.

### Time stability

As it was previously mentioned, iodine-doping is usually unstable. Indeed, although it has been known for several years as an effective oxidising agent, its tendency to rapidly diffuse out of films on time scales of minutes to hours has limited the use of iodine as p-dopant for practical purposes.<sup>12</sup> Considering this, the stability of the C8-BTBT:PS OFET showing the highest mobility enhancement after exposure to iodine was monitored over time. The device was electrically measured repeatedly for 29 days (approximately one month) and the respective transfer curves and mobility profiles are shown in **Figure 4.18 (a-b)**. The main effects that can be observed here are a slight increase of the  $SS$  along with a shift of the  $V_{on}$ , which recovers its initial value, and a progressive decrease of the field-effect mobility. The evolution of the extracted mobility over time is shown in **Figure 4.18 (c)**, where measurements from another device that was exposed to only water have also been included for comparison. In this plot values have been normalised to the mobility extracted right after exposure to iodine or water, respectively. In this way, the remarkable increase achieved as a result of iodine-doping can be clearly appreciated. Also, it can be observed that mobility decreases more rapidly for the doped C8-BTBT OFET. Although this degradation of the performance could be attributed to de-doping (i.e., to iodine desorption), a mobility as high as  $3 \text{ cm}^2/\text{V}\cdot\text{s}$  was still measured after 1 month. However, stability should be investigated for a longer period of time in order to know whether de-doping stabilises or not. Interestingly, in a previous work it was suggested that iodine was retained in the OSC film, and mostly near the OSC/metal interface, even after thermal annealing (which promotes desorption and thus de-doping).<sup>26</sup> Also, depositing an encapsulation layer could be explored as a way to block iodine desorption.

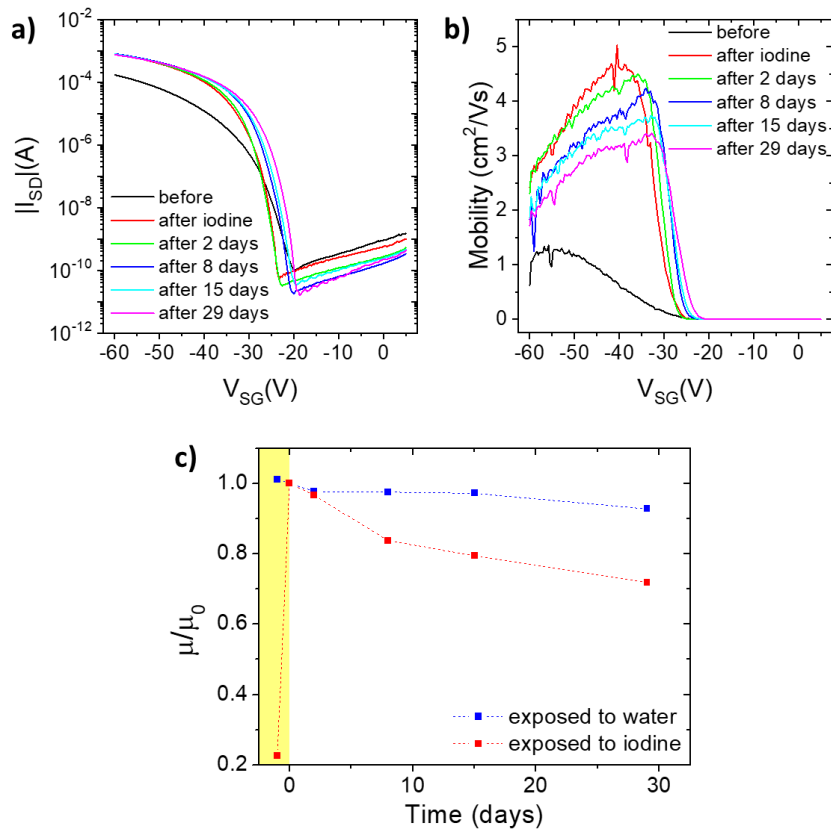


**Figure 4.18.** Evolution over time of the (a) transfer characteristics in the saturation regime and (b) mobility profiles in the saturation regime vs. source-gate voltage measured for a C8-BTBT:PS OFET device exposed to an iodine water solution. (c) Evolution up to 29 days of field-effect mobility of a C8-BTBT:PS device exposed to an iodine water solution (in red) and comparison with a device exposed to only water (in blue). Values have been normalised to the those obtained right after exposure to iodine or water, respectively.

## 4.4 SUMMARY

---

In summary, three different doping methodologies have been employed aiming to optimise the performance of OFETs based on C8-BTBT:PS blends.

Firstly, contact doping was investigated by inserting a F4-TCNQ interlayer at the C8-BTBT/Au interface, which resulted to be the most effective strategy in terms of switch-on voltage shift, thus allowing to reduce the voltage needed to turn on and operate the devices. In this study it was concluded that using a binding polymer with a higher molecular weight can hinder achieving an efficient charge injection, as higher contact resistance and lower mobility values were extracted when using PS100k instead of PS10k. Also, it was found that the thickness of the F4-TCNQ layer determined the rate of degradation of the OFETs performance.

Secondly, doping the C8-BTBT film by adding F4-TCNQ in the OSC solution and depositing it by bar-assisted meniscus shearing demonstrated to be a simple technique leading to a reduced contact resistance. However, morphology was affected by the presence of the dopant molecules and, as a result, charge transport was deteriorated at high doping ratios.

Thirdly, surface doping was achieved carrying out a superficial exposure of the prepared C8-BTBT:PS OFETs to an iodine aqueous solution, which lead to remarkably high mobility values. Although this effect seems to be correlated with the thin-film morphology, and more specifically to the size of the crystal domains, further research is needed to understand the processes governing iodine-doping (adsorption, diffusion and desorption).

In general, the results found in the herein presented work showed that doping organic field-effect transistors is a rather unexplored tool that could enable achieving high performance devices. Hence, simple but efficient doping methodologies should be developed. In addition, doping stability has shown to be a very complex matter that deserves further research and preventing dopant diffusion and, thus, device degradation, is highly desirable.

## 4.5 REFERENCES

- (1) Liu, C.; Xu, Y.; Noh, Y. Y. Contact Engineering in Organic Field-Effect Transistors. *Mater. Today* **2015**, *18*, 79–96.
- (2) Minemawari, H.; Yamada, T.; Matsui, H.; Tsutsumi, J.; Haas, S.; Chiba, R.; Kumai, R.; Hasegawa, T. Inkjet Printing of Single-Crystal Films. *Nature* **2011**, *475*, 364–367.
- (3) Yuan, Y.; Giri, G.; Ayzner, A. L.; Zoombelt, A. P.; Mannsfeld, S. C. B.; Chen, J.; Nordlund, D.; Toney, M. F.; Huang, J.; Bao, Z. Ultra-High Mobility Transparent Organic Thin Film Transistors Grown by an off-Centre Spin-Coating Method. *Nat. Commun.* **2014**, *5*, 3005.
- (4) Paterson, A. F.; Treat, N. D.; Zhang, W.; Fei, Z.; Wyatt-Moon, G.; Faber, H.; Vourlias, G.; Patsalas, P. A.; Solomeshch, O.; Tessler, N.; et al. Small Molecule/Polymer Blend Organic Transistors with Hole Mobility Exceeding  $13 \text{ cm}^2 \text{ V}^{-1} \text{ s}^{-1}$ . *Adv. Mater.* **2016**, *28*, 7791–7798.
- (5) Haase, K.; Teixeira da Rocha, C.; Hauenstein, C.; Zheng, Y.; Hamsch, M.; Mannsfeld, S. C. B. High-Mobility, Solution-Processed Organic Field-Effect Transistors from C8-BTBT:Polystyrene Blends. *Adv. Electron. Mater.* **2018**, *4*, 1800076.
- (6) Ebata, H.; Izawa, T.; Miyazaki, E.; Takimiya, K.; Ikeda, M.; Kuwabara, H.; Yui, T. Highly Soluble [1]Benzothieno[3,2-b]Benzothiophene (BTBT) Derivatives for High-Performance, Solution-Processed Organic Field-Effect Transistors. *J. Am. Chem. Soc.* **2007**, *129*, 15732–15733.
- (7) Liu, C.; Minari, T.; Lu, X.; Kumatani, A.; Takimiya, K.; Tsukagoshi, K. Solution-Processable Organic Single Crystals with Bandlike Transport in Field-Effect Transistors. *Adv. Mater.* **2011**, *23*, 523–526.
- (8) Colella, S.; Ruzié, C.; Schweicher, G.; Arlin, J.-B.; Karpinska, J.; Geerts, Y.; Samorì, P. High Mobility in Solution-Processed 2,7-Dialkyl-[1]Benzothieno[3,2-b][1]Benzothiophene-Based Field-Effect Transistors Prepared with a Simplified Deposition Method. *Chempluschem* **2014**, *79*, 371–374.
- (9) Kano, M.; Minari, T.; Tsukagoshi, K. Improvement of Subthreshold Current Transport by Contact Interface Modification in p-Type Organic Field-Effect Transistors. *Appl. Phys. Lett.* **2009**, *94*, 143304.
- (10) Pérez-Rodríguez, A.; Temiño, I.; Ocal, C.; Mas-Torrent, M.; Barrena, E. Decoding the Vertical Phase Separation and Its Impact on C8-BTBT/PS Transistor Properties. *ACS Appl. Mater. Interfaces* **2018**, *10*, 7296–7303.
- (11) Mei, Y.; Fogel, D.; Chen, J.; Ward, J. W.; Payne, M. M.; Anthony, J. E.; Jurchescu, O. D. Interface Engineering to Enhance Charge Injection and Transport in Solution-

- Deposited Organic Transistors. *Org. Electron.* **2017**, *50*, 100–105.
- (12) Lüssem, B.; Keum, C. M.; Kasemann, D.; Naab, B.; Bao, Z.; Leo, K. Doped Organic Transistors. *Chem. Rev.* **2016**, *116*, 13714–13751.
- (13) Jacobs, I. E.; Moulé, A. J. Controlling Molecular Doping in Organic Semiconductors. *Adv. Mater.* **2017**, *29*, 1703063.
- (14) Xu, Y.; Sun, H.; Liu, A.; Zhu, H.-H. H.; Li, W.; Lin, Y.-F. F.; Noh, Y.-Y. Y. Doping: A Key Enabler for Organic Transistors. *Adv. Mater.* **2018**, *30*, 1801830.
- (15) Minari, T.; Darmawan, P.; Liu, C.; Li, Y.; Xu, Y.; Tsukagoshi, K. Highly Enhanced Charge Injection in Thienoacene-Based Organic Field-Effect Transistors with Chemically Doped Contact. *Appl. Phys. Lett.* **2012**, *100*, 093303.
- (16) Zhang, F.; Kahn, A. Investigation of the High Electron Affinity Molecular Dopant F6-TCNNQ for Hole-Transport Materials. *Adv. Funct. Mater.* **2018**, *28*, 1703780.
- (17) Qi, Y.; Sajoto, T.; Barlow, S.; Kim, E. G.; Brédas, J. L.; Marder, S. R.; Kahn, A. Use of a High Electron-Affinity Molybdenum Dithiolene Complex to p-Dope Hole-Transport Layers. *J. Am. Chem. Soc.* **2009**, *131*, 12530–12531.
- (18) Zhang, Y.; Boer, B. De; Blom, P. W. M. Controllable Molecular Doping and Charge Transport in Solution-Processed Polymer Semiconducting Layers. *Adv. Funct. Mater.* **2009**, *19*, 1901–1905.
- (19) Zhang, Y.; Blom, P. W. M. Enhancement of the Hole Injection into Regioregular Poly(3-Hexylthiophene) by Molecular Doping. *Appl. Phys. Lett.* **2010**, *97*, 083303.
- (20) Lu, G.; Blakesley, J.; Himmelberger, S.; Pingel, P.; Frisch, J.; Lieberwirth, I.; Salzmann, I.; Oehzelt, M.; Di Pietro, R.; Salleo, A.; et al. Moderate Doping Leads to High Performance of Semiconductor/Insulator Polymer Blend Transistors. *Nat. Commun.* **2013**, *4*, 1588.
- (21) Harada, K.; Sumino, M.; Adachi, C.; Tanaka, S.; Miyazaki, K. Improved Thermoelectric Performance of Organic Thin-Film Elements Utilizing a Bilayer Structure of Pentacene and 2,3,5,6-Tetrafluoro-7,7,8,8-Tetracyanoquinodimethane (F4-TCNQ). *Appl. Phys. Lett.* **2010**, *96*, 253304.
- (22) Hählen, T.; Vanoni, C.; Wäckerlin, C.; Jung, T. A.; Tsujino, S. Surface Doping in Pentacene Thin-Film Transistors with Few Monolayer Thick Channels. *Appl. Phys. Lett.* **2012**, *101*, 033305.
- (23) Soeda, J.; Hirose, Y.; Yamagishi, M.; Nakao, A.; Uemura, T.; Nakayama, K.; Uno, M.; Nakazawa, Y.; Takimiya, K.; Takeya, J. Solution-Crystallized Organic Field-Effect Transistors with Charge-Acceptor Layers: High-Mobility and Low-Threshold-Voltage Operation in Air. *Adv. Mater.* **2011**, *23*, 3309–3314.

- (24) Zhang, F.; Dai, X.; Zhu, W.; Chung, H.; Diao, Y. Large Modulation of Charge Carrier Mobility in Doped Nanoporous Organic Transistors. *Adv. Mater.* **2017**, *29*, 1700411.
- (25) Mascal, M.; Yin, B.; Stroeve, P.; Li, J.; Zhang, G.; Holm, D. M.; Moulé, A. J.; Jacobs, I. E. Introducing Solubility Control for Improved Organic P-Type Dopants. *Chem. Mater.* **2015**, *27*, 5765–5774.
- (26) Lee, B. H.; Bazan, G. C.; Heeger, A. J. Doping-Induced Carrier Density Modulation in Polymer Field-Effect Transistors. *Adv. Mater.* **2016**, *28*, 57–62.
- (27) Zhang, Q.; Leonardi, F.; Casalini, S.; Mas-Torrent, M. Mercury-Mediated Organic Semiconductor Surface Doping Monitored by Electrolyte-Gated Field-Effect Transistors. *Adv. Funct. Mater.* **2017**, *27*, 1703899.
- (28) Kim, Y.; Chung, S.; Cho, K.; Harkin, D.; Hwang, W.-T.; Yoo, D.; Kim, J.-K.; Lee, W.; Song, Y.; Ahn, H.; et al. Enhanced Charge Injection Properties of Organic Field-Effect Transistor by Molecular Implantation Doping. *Adv. Mater.* **2019**, *31*, 1806697.
- (29) Temiño, I.; Del Pozo, F. G.; Ajayakumar, M. R.; Galindo, S.; Puigdollers, J.; Mas-Torrent, M. A Rapid, Low-Cost, and Scalable Technique for Printing State-of-the-Art Organic Field-Effect Transistors. *Adv. Mater. Technol.* **2016**, *1*, 1600090.
- (30) Izawa, T.; Miyazaki, E.; Takimiya, K. Molecular Ordering of High-Performance Soluble Molecular Semiconductors and Re-Evaluation of Their Field-Effect Transistor Characteristics. *Adv. Mater.* **2008**, *20*, 3388–3392.
- (31) Xu, Y.; Minari, T.; Tsukagoshi, K.; Chroboczek, J. A.; Ghibaudo, G. Direct Evaluation of Low-Field Mobility and Access Resistance in Pentacene Field-Effect Transistors. *J. Appl. Phys.* **2010**, *107*, 114507.
- (32) Riera-Galindo, S.; Leonardi, F.; Pfattner, R.; Mas-Torrent, M. Organic Semiconductor/Polymer Blend Films for Organic Field-Effect Transistors. *Adv. Mater. Technol.* **2019**, 1900104.
- (33) Patnaik, P. *Dean's Analytical Chemistry Handbook*; McGraw-Hill New York, 2004.
- (34) Hunter, S.; Anthopoulos, T. D. Observation of Unusual, Highly Conductive Grain Boundaries in High-Mobility Phase Separated Organic Semiconducting Blend Films Probed by Lateral-Transport Conductive-AFM. *Adv. Mater.* **2013**, *25*, 4320–4326.

## CHAPTER 5

---

# Mechanical stress response of bendable OFETs and relationship with the thin-film morphology\*

### 5.1 INTRODUCTION AND OBJECTIVES

---

One of the most demanded features for emerging electronic applications is, undoubtedly, mechanical flexibility. Indeed, the possibility of conforming devices and entire electronic systems to non-planar surfaces could enable their actual integration on daily-life objects, which is of high interest for applications in fields related to smart-packaging as well as for people and goods tracking.<sup>1</sup> Moreover, achieving mechanically robust devices, such that they would stand a continuous or cyclic application of bending deformations without significant permanent variations in the electrical performance, is key for applications ranging from the so-called “tattoo-electronics”<sup>2–4</sup> to wearable electronics and e-textiles.<sup>5,6</sup> All these novel applications promise to have a strong impact on human life, causing an increment in the number of studies aiming at the development of flexible electronic devices.

Among the different technologies, organic electronics is generally considered the most suitable for its exploitation in flexible electronics. Indeed, the use of solution processing techniques to deposit organic materials at low temperature would allow the large-area fabrication of low-cost electronic devices<sup>7,8</sup> on flexible substrates, including plastic,<sup>9–11</sup> paper<sup>12,13</sup> and fabric.<sup>14,15</sup> For this reason, many efforts have been made to implement organic field-effect transistor (OFET) systems in applications requiring either high sensitivity or high stability, i.e., bending sensors or strain-insensitive circuitry.<sup>16</sup>

---

\* This work has been published in Lai, S.; Temiño, I.; Cramer, T.; del Pozo, F. G.; Fraboni, B.; Cosseddu, P.; Bonfiglio, A.; Mas-Torrent, M. Morphology Influence on the Mechanical Stress Response in Bendable Organic Field-Effect Transistors with Solution-Processed Semiconductors. *Adv. Electron. Mater.* **2018**, *4*, 1700271.



As a matter of fact, organic semiconductor films can be severely affected by the application of mechanical deformations. When a mechanical deformation is applied such that the substrate is positioned in a convex or concave position, as illustrated in **Figure 5.1**, a tensile or compressive strain is induced, respectively. In the case of thin-film devices, where the overall thickness of the device is negligible with respect to the one of the substrate ( $t_{sub}$ ), the strain ( $\epsilon$ ) in the outermost crystalline layer obtained by bending the substrate with a certain bending radius ( $R$ ) is given by the relationship:<sup>17</sup>

$$\epsilon = t_{sub}/2R \quad (5.1)$$

This surface strain induced on the active layer can give rise to variations in the conductivity of the devices, which are generally more significant for polycrystalline semiconducting thin films than for amorphous ones. This mechanical sensitivity has been thoroughly investigated for pentacene films, where it has been correlated to morphological changes taking place in the active layer, that, in turn, modify the hopping energy barrier for charge transport.<sup>18–22</sup> Both changes in the spacing between molecules and changes in the lateral spacing between individual adjacent crystallites have been suggested. However, the most recent works demonstrated that strain caused morphological rather than structural changes; hence, they identified the latter case, i.e., changes in the inter-grain distance, as the main reason behind the observed sensitivity.<sup>21</sup> Thus, when an elongation or compression parallel to the channel length is applied, a dislocation of the crystalline domains in the semiconductor film is induced (that is, they are brought apart or closer to each other, respectively), altering the charge transport mechanisms and the device electrical behaviour. As a result, mechanical sensitivity arises as a decrease or increase in the OFET current and carrier mobility upon elongation and compression, respectively.

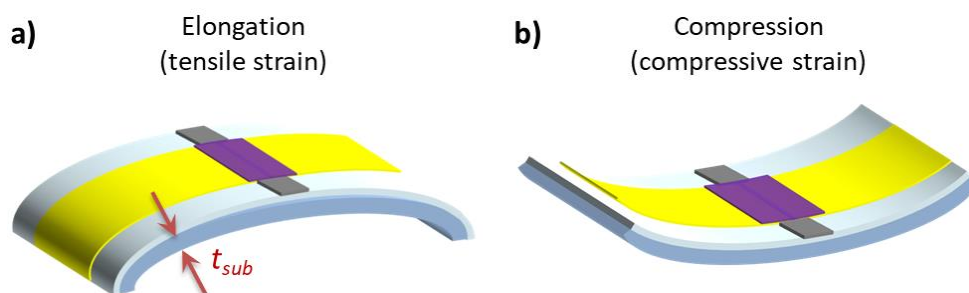


**Figure 5.1.** Illustration of an organic field-effect transistor under (a) elongation or tensile strain and (b) compression or compressive strain.

In this sense, attention is being particularly focused on studying the way mechanical deformation affects the semiconductor morphology, and so what kind of morphological features should be obtained to modulate the bending response from high sensitivity to high stability. For instance, the influence of the processing parameters in determining the morphology of the semiconductor layer, and thus the sensitivity to tensile mechanical deformation, has been investigated for evaporated pentacene films.<sup>22</sup> Interestingly, a linear dependence between the device electrical response, in terms of current variation, and the applied strain was observed. Further, by enhancing the crystal domain size by reducing the evaporation rate, an increased strain sensitivity was achieved (see **Figure 5.2 (a)**). However, it would be highly desirable to perform this type of study on solution-processed organic semiconductor thin films, since they are more appealing for industrial applications as they can be printed employing low-cost roll-to-roll processes. Indeed, the soluble derivative TIPS-pentacene (**Figure 5.2 (b)**) has been exploited for the fabrication of organic flexible tactile sensors and memories showing a remarkable mechanical stability thanks to the reduction of the substrate thickness to few  $\mu\text{m}$ , thus minimising the surface strain.<sup>23,24</sup> Yet, in these works the organic semiconductor was deposited by drop-casting, which is far from being compatible with up-scaling and high throughput processes. Moreover, the impact of the thin-film morphology on the bending sensitivity, as well as the possibility of tuning this sensitivity by changing the morphological features of the deposited films, are still substantially unexplored.

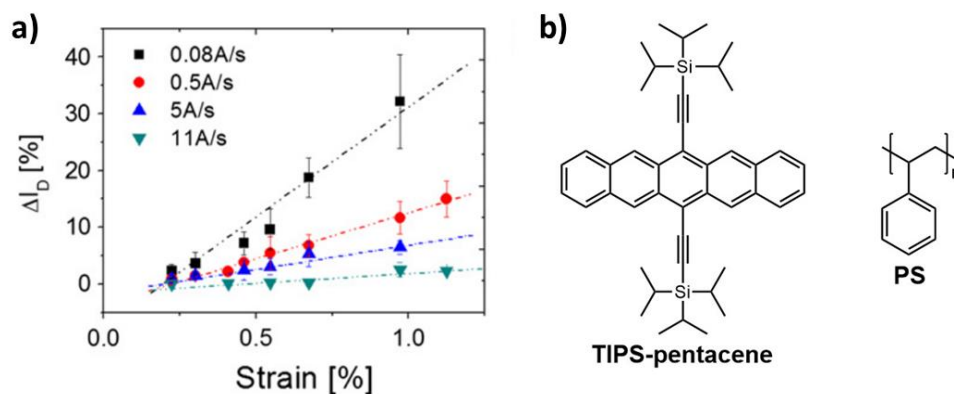


**Figure 5.2.** (a) Current variation vs. tensile strain for pentacene-based transistors fabricated using different evaporation rates resulting in different crystal sizes. Extracted from ref. 22. (b) Molecular structures of TIPS-pentacene and PS.

Many solution-processing techniques have recently faced the challenge of controlling thin-film morphology during printing/coating processes,<sup>8,25</sup> among which bar-assisted meniscus shearing (BAMS) has attracted a significant interest thanks to its scalability, high coating speed and easiness-in-use.<sup>26,27</sup> With this technique it has already been demonstrated that by tuning the deposition parameters, such as temperature or speed,

as well as the ink formulation, it is possible to modulate the thin-film morphology.<sup>28</sup> Further, blending the organic semiconductor with an insulating polymer, such as polystyrene (PS, **Figure 5.2 (b)**), has shown to be an efficient strategy to enhance the material processability, the thin-film crystallinity and homogeneity, and the device environmental stability.<sup>29–31</sup>

### Objectives

Thus, the objective of this thesis chapter is to investigate the influence of the organic semiconductor thin-film morphology on the device response to mechanical stress, and to explore the possibility of tuning such response by controlling the coating parameters. To do so, flexible OFETs were fabricated on plastic substrates by depositing TIPS-pentacene:PS thin films employing BAMS processing technique and varying the shearing direction, resulting in crystal domains of different size. After characterizing the OFET performance of such devices, their response when subjected to bending deformation was investigated, considering their recovery and stability. Finally, a morphological study including atomic force microscopy and Kelvin probe force microscopy was performed to rationalise the relationship between the morphological features and the electrical response of the devices.

## 5.2 DEVICE FABRICATION AND THIN-FILM CHARACTERISATION

Bottom-gate bottom-contact OFETs based on a TIPS-pentacene:PS blend were fabricated using 175  $\mu\text{m}$  thick polyethylene terephthalate (PET) substrates with an aluminium gate and aluminium oxide (8 nm)/Parylene C (170 nm) as gate insulator (**Figure 5.3 (a-b)**). Patterning of gold source and drain electrodes resulted in OFETs with a channel perfectly aligned with the gate and with a width and length of  $W = 5 \text{ mm}$  and  $L = 30 \text{ }\mu\text{m}$ , respectively. A more detailed description of the fabrication of such flexible devices can be found on the experimental methods chapter (Chapter 7). Employing this structure, that combines a hybrid organic/inorganic dielectric layer with an aligning process to minimise the overlap between source/drain and gate contacts, low operating voltages are ensured.<sup>32,33</sup> TIPS-pentacene and PS with a molecular weight of 10 kg/mol were blended in a 4:1 weight ratio in chlorobenzene (2 wt%) and deposited by bar-assisted meniscus shearing (BAMS), considering the experimental conditions optimised in Chapter 2.<sup>27</sup> However, in this case the material of the bar was changed from the standard stainless steel to polytetrafluoroethylene (PTFE or Teflon), since changing the surface energy of the shearing bar facilitated the growth of crystalline films on the hydrophobic Parylene C surface. The thin-film deposition was performed in two orthogonal directions, choosing the shearing direction to be either orthogonal or parallel to the channel length, as depicted in **Figure 5.3 (c-d)**. In the following, these coatings will be referred to as orthogonal (o-) or parallel (p-) coating.

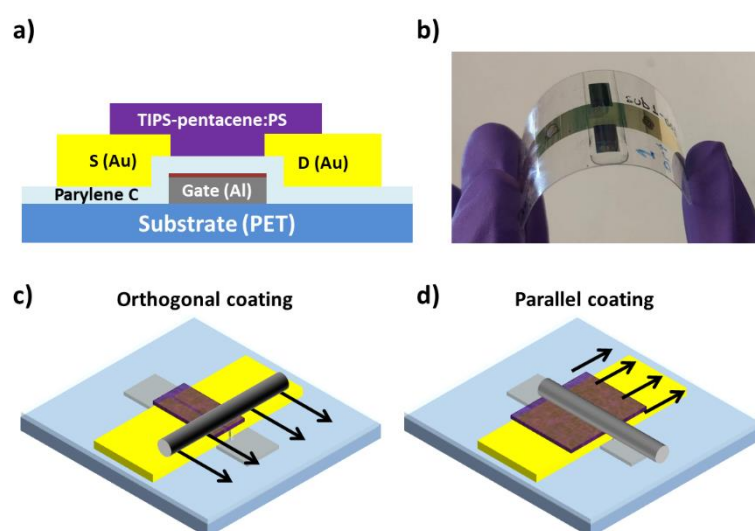


**Figure 5.3.** (a) Scheme of the flexible bottom-gate bottom-contact OFETs employed in this work, showing the cross-section of the devices. (b) Photograph of a real device. (c-d) Schematic illustration of the thin-film deposition performed by BAMS technique in a direction orthogonal and parallel to the channel length, respectively.

The polarised optical microscope images of the prepared orthogonal and parallel coatings are shown in **Figure 5.4 (a)** and **(b)**, respectively, where the formation of highly crystalline and uniform films with spherulitic domains can be observed in both cases. However, for p-coated devices the size of the crystal domains is clearly smaller on the device channel area than on the contact pads. On the other hand, for o-coated devices domains are very well connected from one pad to the other, through the channel. The reduction in domain size in the p-coating might be related to the relatively high step between the gold contacts and the Parylene C (ranging around 60-80 nm) and also to the different wettability of these materials, making the crystallisation reliant on the surface. Although deciphering the cause for this different morphology was out of the scope of this work, it was interesting to find that using the same device structure, materials and deposition parameters, a different crystallisation could be obtained when the meniscus was moved parallel to the channel width (o-coating) or parallel to the channel length (p-coating). Profilometry measurements were performed by scratching the organic semiconductor from the gold surface, generating a height step. Thus, the film thickness was found to be in the range of 100 to 200 nm (**Figure 5.4 (c-d)**).

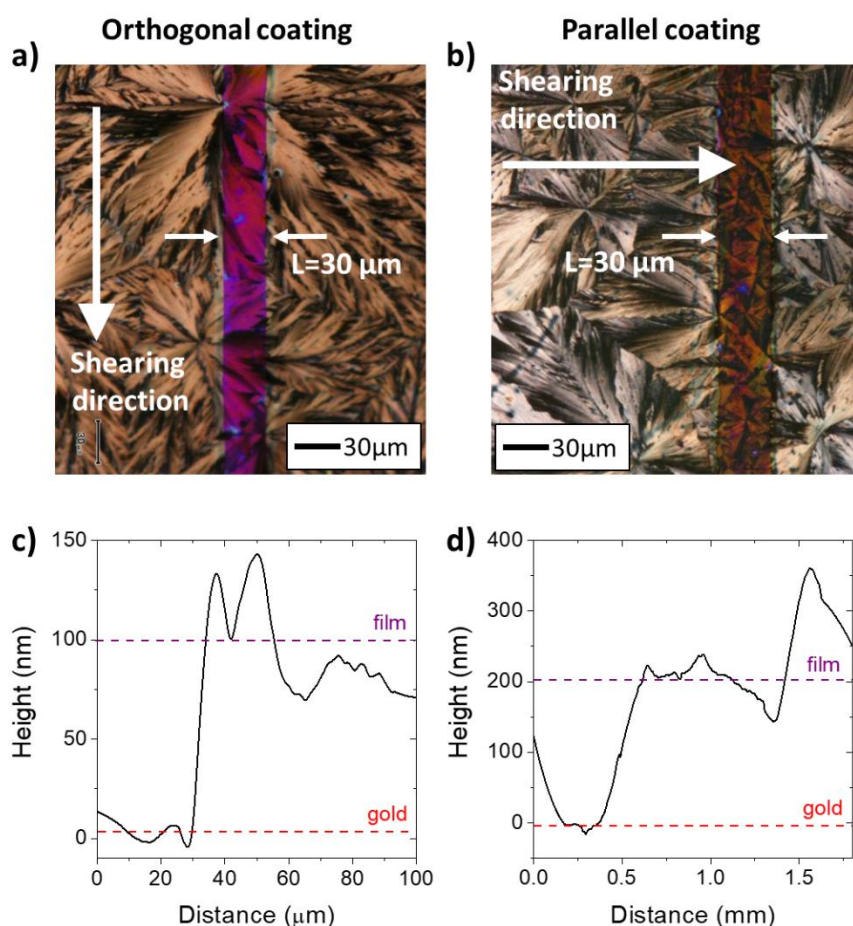


**Figure 5.4.** (a-b) Crossed-polarised optical microscope images in the channel area and (c-d) contact profilometry for thickness estimation of the o- and p-coatings.

Thin films were also characterised by X-ray diffraction to ensure that the different morphological features are not associated with structural changes. **Figure 5.5** shows identical diffraction patterns in agreement with the triclinic phase previously reported for TIPS-pentacene,<sup>34,35</sup> evidencing the high degree of crystallinity of the deposited films. In this plot, an X-ray diffractogram obtained from a substrate with no film has been included to show that the peak centred at 13.9° is due to the contribution of the gold contacts. In addition, only (00 $l$ ) type reflections were observed, indicating that crystallites are highly oriented with respect to the substrate.

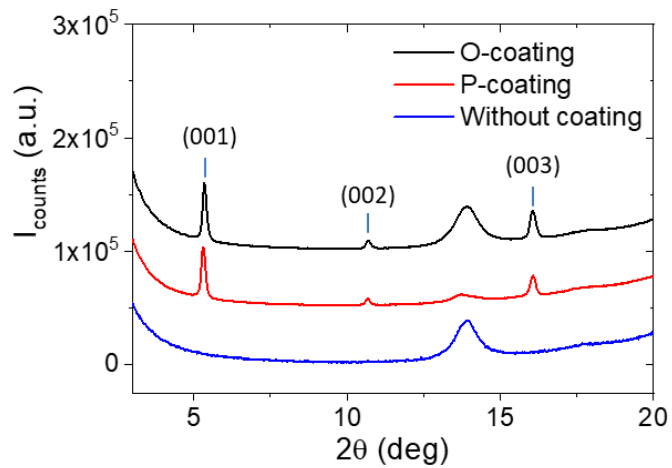


**Figure 5.5.** X-ray diffractograms of the orthogonal and parallel TIPS-pentacene:PS coatings and from a substrate with no film, showing that the peak centred at 13.9° is due to the contribution of the gold contacts. Diffraction curves have been shifted along the y-axis for clarity.

## 5.3 OFET ELECTRICAL CHARACTERISATION

Before applying any mechanical deformation on the fabricated devices, the pristine o-coated and p-coated OFETs were electrically characterised. Thanks to the device architecture and materials employed, transfer and output characteristics could be measured in a low voltage range, reaching -5 V at maximum for both  $V_{SD}$  and  $V_{SG}$ . Typical saturation transfer characteristics of both the orthogonal and parallel coated devices are shown in **Figure 5.6 (a-b)**, where a very small hysteresis can be observed between the forward and reverse sweeps. Also, the output characteristics in **Figure 5.6 (c-d)** show no significant injection problems.

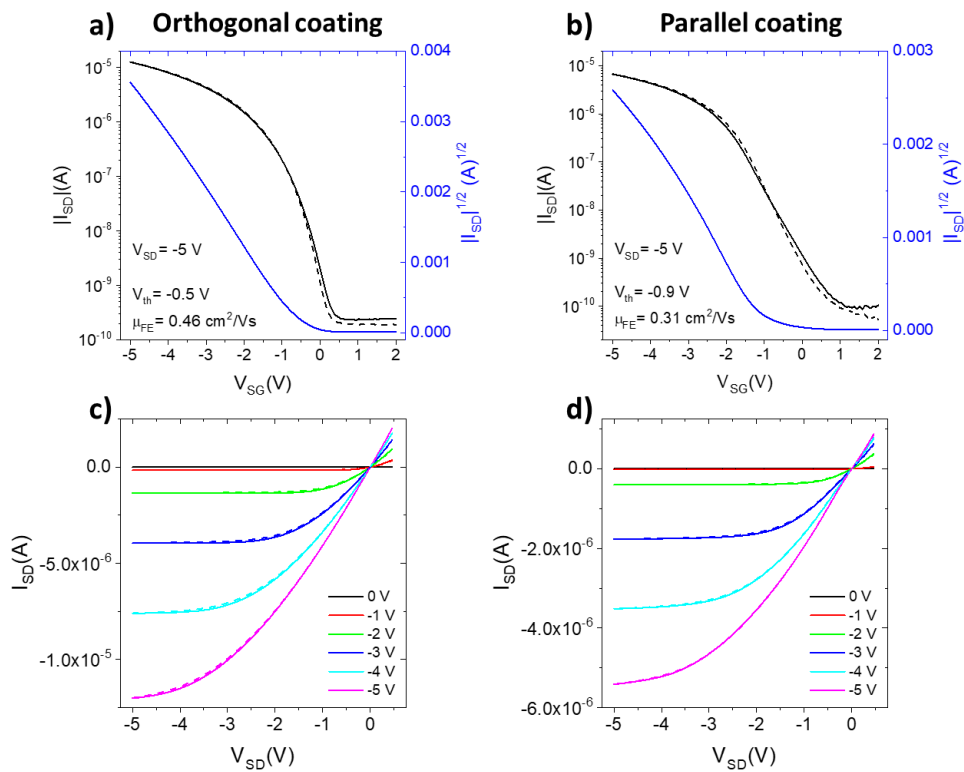


**Figure 5.6.** Electrical characteristics of typical o-coated and p-coated TIPS-pentacene:PS OFET devices.

(a-b) Transfer characteristics in the saturation regime and square root of the absolute value of the source-drain current vs. source-gate voltage for the extraction of field-effect mobility and threshold voltage. (c-d) Output characteristics. Straight and dashed lines correspond to forward and reverse sweeps, respectively, for both transfer and output characteristics.

A statistical analysis was performed considering 15-20 devices for each type of coating. The main parameters of the measured OFETs, including average and standard deviation values, are summarised in **Table 5.1**. O-coated devices exhibited an average field-effect mobility ( $\mu_{FE}$ ) around  $0.39 \text{ cm}^2/\text{V}\cdot\text{s}$ , and a threshold voltage ( $V_{th}$ ) with an average value



of -0.6 V, both extracted in the saturation regime. Likewise, for p-coated devices an average field-effect mobility and threshold voltage of  $0.32 \text{ cm}^2/\text{V}\cdot\text{s}$  and -1.1 V, respectively, were extracted. Both types of devices showed an *on/off* ratio on the order of  $10^4$ - $10^5$ . These results indicate that the different thin-film morphology (i.e., crystalline domain size in the channel area) between o- and p-coatings is not significantly affecting the overall device performance in terms of mobility values, pointing out that the crystallites are very well interconnected in both types of coating. However, p-coated devices showed a less steep switching resulting in an average subthreshold swing (*SS*) of 0.7 V/dec, higher than that found for o-coated devices, 0.28 V/dec. This difference in the subthreshold behaviour can be related to the greater number of crystallites (and thus, grain boundaries) present in the p-coating.

**Table 5.1.** Main OFET parameters of the studied o-coated and p-coated TIPS-pentacene:PS OFET devices extracted in the saturation regime considering 15-20 devices.

Type of coating	<i>on/off</i>	$\mu_{FE}$ ( $\text{cm}^2/\text{V}\cdot\text{s}$ )	$V_{th}$ (V)	<i>SS</i> (V/dec)
Orthogonal	$10^4$ - $10^5$	$0.39 \pm 0.26$	$-0.6 \pm 0.3$	$0.28 \pm 0.07$
Parallel	$10^4$ - $10^5$	$0.32 \pm 0.17$	$-1.1 \pm 0.4$	$0.7 \pm 0.2$



## 5.4 CHARACTERISATION UPON BENDING DEFORMATION

In order to understand the effect that the application of a bending deformation has on the performance of o- and p-coated devices, the variation of basic electronic parameters such as charge carrier mobility and threshold voltage upon elongation and compression was investigated. The recovery of the original electrical performance after such mechanical stress as well as the stability upon cyclic bending were also investigated.

### Strain response

To electrically characterise the devices while applying a mechanical deformation, OFETs were contacted with silver paint and Ag-coated nylon threads, as depicted in **Figure 5.7 (a)**. Then, substrates were held in a fixed position, either flat or bent, by laboratory clamps (**Figure 5.7 (b)**). Using reference cylinders of various sizes, six different bending radii ( $R$ ) between 4.5 and 0.5 cm were applied during both elongation and compression experiments, as summarised in **Table 5.2**. Deformation was induced along the larger dimension of the substrates, which was parallel to the channel length of the device and large enough (6 cm) to guarantee the application of a radial deformation on the channel area. Being all the considered radii much larger than the channel length, the applied thin-film strain can be considered uniform. Thus, strain values ( $\epsilon$ ) calculated from **Equation 5.1**, which vary between 0.19 and 1.75%, are shown in **Table 5.2**.

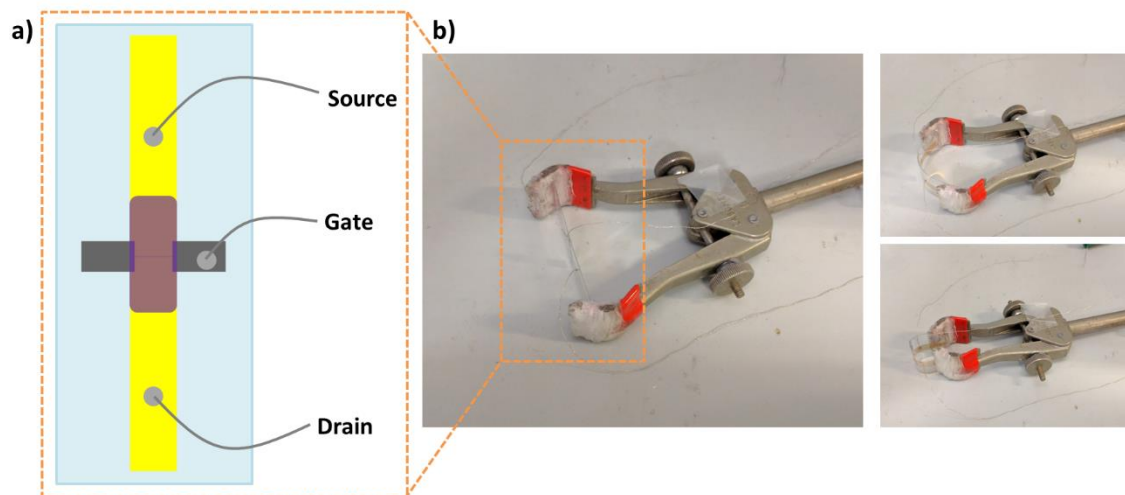


**Figure 5.7.** (a) Scheme of the flexible OFET devices and the electrical connections employed during the bending deformation tests. (b) Photographs of a real device hold by laboratory clamps in flat or bent position.

**Table 5.2.** Bending radii and strain values applied during elongation and compression experiments.

Bending radius $R$ (cm)	4.5	3	2	1	0.75	0.5
Strain $ \epsilon $ (%)	0.19	0.29	0.44	0.88	1.17	1.75

Strain response upon elongation and compression are reported in **Figure 5.8 (a)** and **(b)**, respectively, in terms of percentage relative mobility variation  $\Delta\mu/\mu_0 = (\mu - \mu_0)/\mu_0$ , being  $\mu_0$  the field-effect mobility of the pristine device while flat, and  $\mu$  the value recorded while the device is bent. Likewise, **Figure 5.8 (c-d)** shows the absolute threshold voltage variation respect to the value of the pristine device. In this part of the work at least three devices were measured, so that each point corresponds to the average value and its deviation. As expected, when the devices were elongated, a mobility reduction was observed for both types of coating (**Figure 5.8 (a)**). The devices response is substantially linear, although the o-coating resulted in a slightly larger sensitivity than the p-coating, reaching a mobility variation up to -80%. Interestingly, the difference between the two coatings is more evident when devices are compressed (**Figure 5.8 (b)**). In this case, o-coated devices did not show a significant trend in their response since the mobility variation reached a plateau for strain values larger than -0.44%. On the contrary, devices with p-coated semiconductor showed a linear variation of the mobility over the whole range of applied strain, being significantly more sensitive to compression than devices with o-coated film. Regarding the threshold voltage (**Figure 5.8 (c-d)**), no substantial variations were observed for both coatings and both kinds of deformation. The width of the error bars in elongation account for device-to-device variations, but a direct relationship between threshold voltage and strain was not clearly observed. This is in accordance with previous works employing pentacene evaporated films, which showed that mechanical deformation generally does not affect the semiconductor/insulator interface in a significant way.<sup>20,22</sup> Instead, they suggested that the current and, thus, mobility variation induced by surface strain are mainly related to an alteration of the charge carrier transport mechanisms, probably due to a change in distance between adjacent crystal domains.

Remarkably, the sensitivity exhibited by the o- and p-coatings demonstrates not only that the response to bending is reliant on the morphological properties of the films, but also that it can be tuned according to the bar shearing direction.

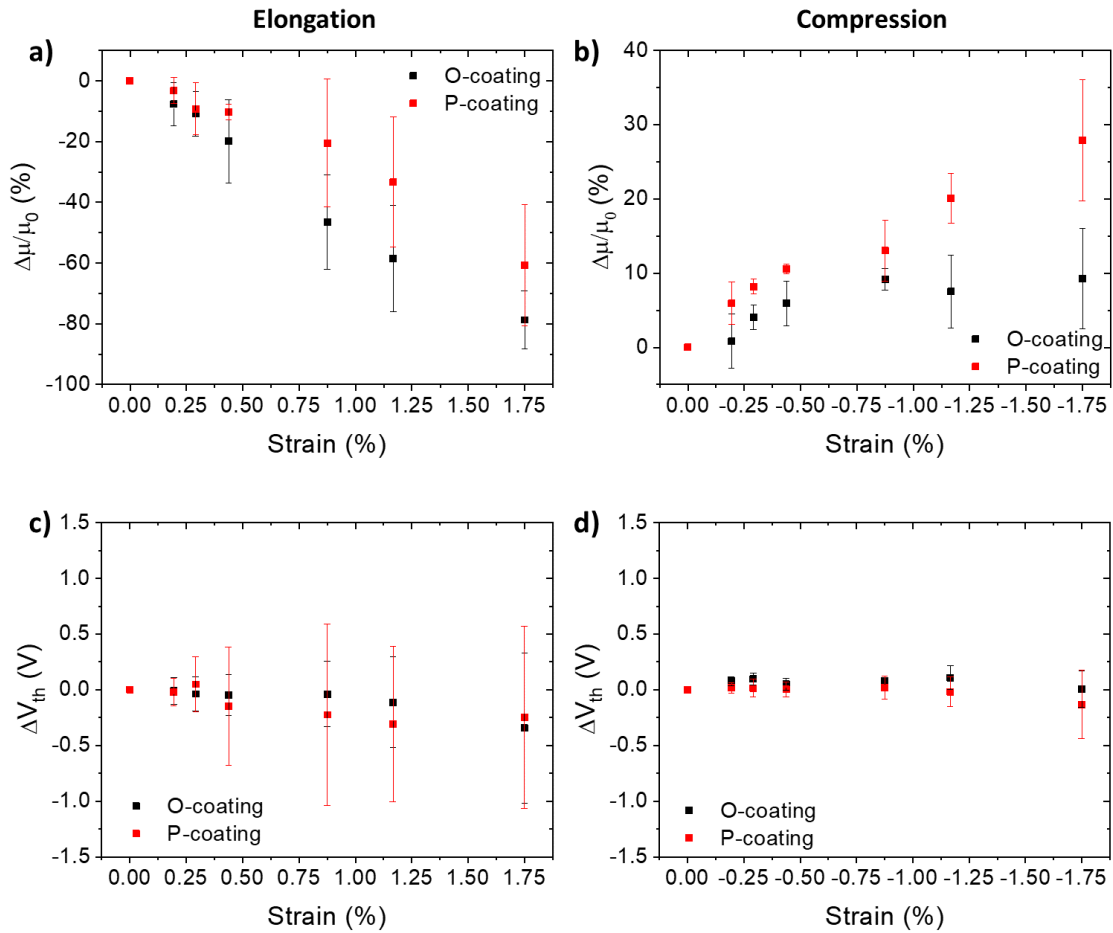


**Figure 5.8.** (a-b) Average percentage mobility variation and (c-d) average threshold voltage variation as a function of the applied strain upon elongation and compression for o-coated and p-coated devices.

### Recovery after deformation

In an ideal case, when a flexible device is brought back to flat state after the application of a deformation, its electrical parameters should recover their original value. However, as reported by previous literature,<sup>36</sup> the application of a deformation larger than a certain value can result in long standing or possibly permanent variations in the electrical properties of the device, which is mainly related to permanent deformations of the substrate, damages in the device structure and cracking of the crystalline layer. Thus, it is of great interest to investigate the critical value of strain causing irreversible variations for both the o- and p-coatings.

To assess this, experiments were performed in a sequence from lower to higher deformations, bringing the devices back to flat state after the application of each different strain value and measuring the electrical characteristics of the devices in all bended and flat positions. These results are reported in **Figure 5.9**; note that the values for mobility

variation while bending are the same shown in **Figure 5.8 (a-b)** and only the values obtained in the intermediate flat step have been added. In the case of elongation (**Figure 5.9 (a)**), a significant shift of the mobility value in flat state towards lower values can be observed for both kinds of coating. In particular, after the application of a bending radius of 2 cm ( $\epsilon = 0.44\%$ ), error bars start to be significantly large, proving that devices do not recover from the applied stress in the same way. Despite the width of the error bars, it can be observed that the recovering ability of devices with o-coated semiconductor is averagely lower than the one of p-coated devices. Furthermore, after the application of a critical strain value of  $\epsilon = 1.17\%$  ( $R = 0.75$  cm), none of the investigated devices recovered the original mobility value. Interestingly, the effect of the mechanical stress was significantly lower when a compressive deformation was applied on the devices (**Figure 5.9 (b)**). In that case, and for both kinds of coating, the devices substantially recover the pristine mobility value when brought back to flat state after compression. As in the case of elongation, o-coated devices showed a larger mobility variation in flat state than p-coated ones, although the difference is less evident. From this plot, and according to the amplitude of error bars, a higher variability is observed after the application of a bending radius of 0.75 cm ( $\epsilon = -1.17\%$ ) for both kinds of coating.

Considering all the above results, it can be concluded that films based on smaller crystallites (i.e., p-coating) seem to adapt more easily to deformations better recovering the pristine electrical performance. Undoubtedly, the critical strain values found here could be correlated with both the crystallinity of the TIPS-pentacene and the plasticity/elasticity of the PS present in the active layer.<sup>37</sup> However, this would require an in-depth comparison between different device structures and ink formulations, which will be further investigated in future work.

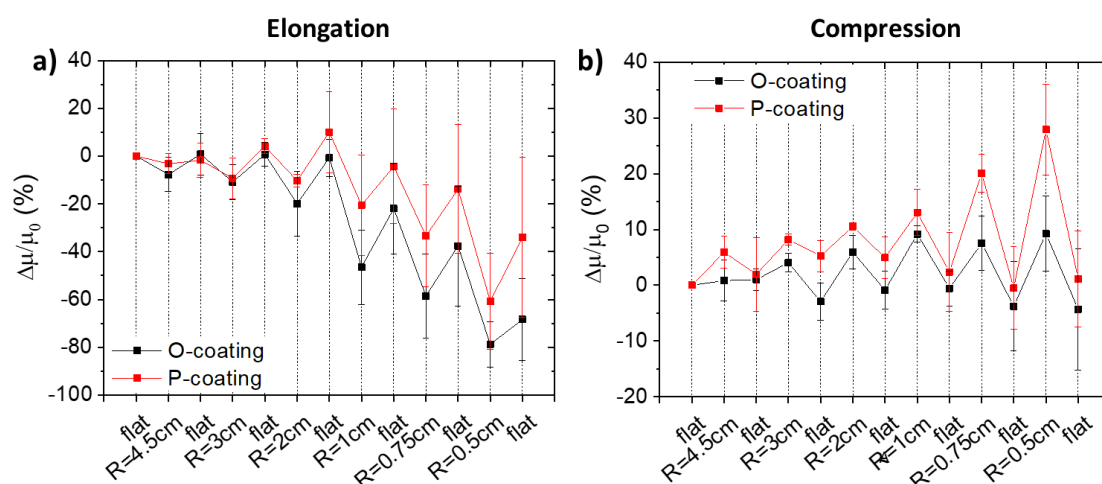


**Figure 5.9.** Average percentage mobility variation as a function of the applied bending radius ( $R$ ) and in flat state for o-coated and p-coated devices. Response to (a) elongation and (b) compression.

## Cyclic stability

In order to further investigate the effects of mechanical stress on devices with different kinds of coating, OFETs were subjected to several cycles of mechanical deformation by using an automated system provided with a mechanical indenter. Each bending cycle consisted in the application of an elongation with a bending radius of 2 cm ( $\epsilon = 0.44\%$ ) for 5 seconds and a relaxation time of 10 seconds. Note that this strain value is below the critical strain that has previously shown to cause irreversible damage. The transfer characteristic curves of o- and p-coated devices were recorded in flat state in pristine conditions and after a certain number of deformations (100, 300, 600 and 1000 cycles), as shown in **Figure 5.10 (a-b)**, but devices were not biased during the deformation. For both kinds of coating, such a large number of bending cycles lead to a clear shift of the characteristic curves. For o-coated devices, transfer curves changed significantly specially after the first 300 cycles, while the following variations were much smaller. In particular, there is not a significant difference between the curves recorded after 600 and 1000 bending cycles. On the contrary, in the case of p-coated devices, more than 100 cycles were necessary to observe a significant shift of the curves; after that, variations were substantially linear with the number of cycles. Indeed, these changes are reflected in how the threshold voltage is affected by the cyclic application of mechanical strain, shown in **Figure 5.10 (c)**. After 1000 bending cycles, threshold voltage shifted up to 700 mV towards more negative values for both kinds of coating, although the different trends reflect the different dynamics of the electrical curves degradation. This  $V_{th}$  shift is probably caused by a modification of the insulator/semiconductor and/or electrode/semiconductor interfaces. In the transfer curves this effect is combined with changes in the device mobility (i.e., the slope of the curves); however, these variations were limited to +10% and did not show a significant trend.

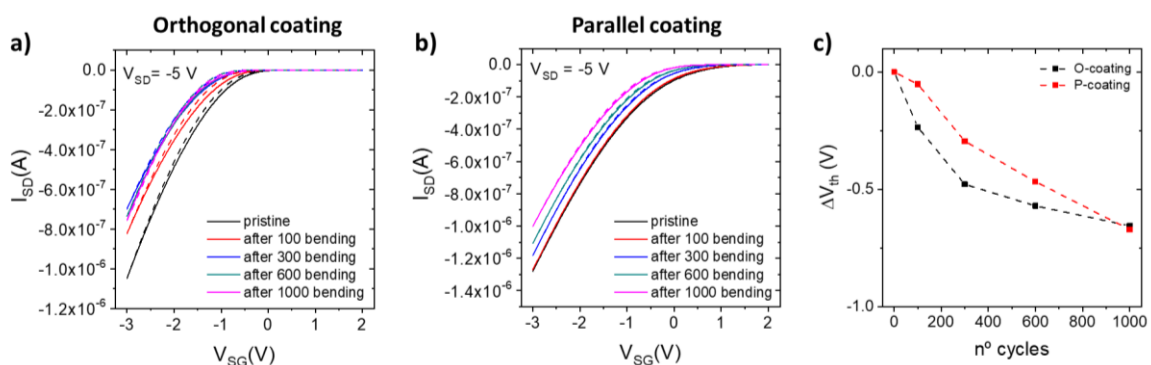


**Figure 5.10.** Transfer characteristics recorded in flat state for (a) o-coated and (b) p-coated devices in pristine conditions and after the application of an increasing number of elongations ( $R = 2$  cm,  $\epsilon = 0.44\%$ ). Straight and dashed lines correspond to forward and reverse sweeps of  $V_{SG}$ , respectively. (c) Threshold voltage variation as a function of the number of applied deformations.

Apart from the OFET stability upon cyclic bending, it is also interesting to consider the reproducibility of the response when a bending deformation is applied repetitively. Again, devices were subjected to elongation cycles by applying a bending radius of 2 cm ( $\epsilon = 0.44\%$ ) but in this test the OFETs current was continuously monitored. To do this, a constant drain voltage of -5 V was applied, while a square-waved gate voltage, between 0 and -3 V ( $f = 10$  Hz), was employed to reduce bias stress. **Figure 5.11 (a)** and **(b)** report, respectively, the total current measured for o- and p-coated devices in a time window of 30 minutes approximately. Here, aside of the current drift related to bias stress effects, a very stable response to bending (i.e., the difference between the current recorded in the “relaxed” and “elongated” states) can be noticed. Thus, these tests on the application of elongation cycles demonstrated that both types of devices show not only good OFET stability but also remarkable response reproducibility over prolonged stress.

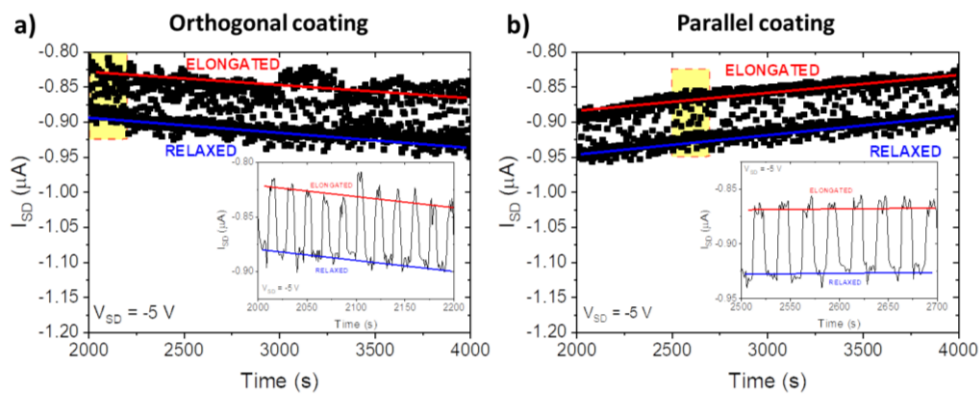


**Figure 5.11.** Current monitoring upon the application of cyclic bending ( $R = 2$  cm,  $\epsilon = 0.44\%$ ) onto an (a) o-coated and (b) p-coated device for approximately 30 min. The inset shows the square pulses resulting from the elongation for a shorter period of time (highlighted in yellow).



## 5.5 MORPHOLOGICAL AND LOCAL ELECTRICAL CHARACTERISATION

---

Considering all the previous results, understanding the relationship between the response to bending and the effects of mechanical stress, on one side, and the different morphology of the o- and p-coated devices, on the other, stood out as an important issue. To assess this, atomic force microscopy (AFM) and Kelvin probe force microscopy (KPFM) analysis were carried out on devices based on both kinds of coating and considering the pristine, elongated and compressed conditions. Along with the topography maps obtained by AFM, KPFM gives access to the surface potential distribution in the transistor. In particular, when a thin-film transistor is operated in the linear regime, the surface potential in the channel follows the electrostatic potential in the accumulation layer, which varies linearly along the channel, providing valuable information on local carrier concentration, variations in mobility and contact resistance.<sup>38,39</sup> Thus, during our KPFM scans the transistors were kept at a constant drain and gate bias of  $V_{SD} = -1$  V and  $V_{SG} = -5$  V.

**Figure 5.12 (a)** and **(c)** show the topography and surface potential maps obtained on pristine transistors fabricated with o- and p-coating, respectively. Overall, both coatings show a very homogeneous surface topography in the channel area, attributed to the successful embedding of the semiconducting microcrystals in the PS matrix. In contrast with the o-coating, the p-coating exhibits smaller surface structures hinting to an overall smaller feature size of TIPS-pentacene microcrystals, as previously observed by optical microscopy. Images show that, for both types of coating, the semiconductor layer is thicker in the channel area than on the electrodes. Moreover, a significant increase in surface height at the channel/electrode interface is observed. This accumulation of material in the spatially confined channel can be attributed to the larger affinity of the TIPS-pentacene:PS ink to the Parylene C surface in the channel instead of the gold surface from the electrodes.

In the corresponding surface potential maps in **Figure 5.12 (a)** and **(c)**, the source and drain electrodes can be identified as isopotential surfaces at 0 V and -1 V, respectively. For both kinds of coatings, the potential drops significantly at the channel/electrode interface due to contact resistance effects, whereas a homogeneous decrease in potential is observed along the channel. Here, local inhomogeneities indicating high electric fields due to traps or transport barriers are not present. The potential profiles along the channel obtained from these surface potential maps of pristine transistors are shown in **Figure 5.12 (b)** and **(d)**. In addition, the profiles obtained from transistors that were subjected to elongation or compression (reaching the maximum strain value considered,  $\varepsilon = 1.75\%$  or  $\varepsilon = -1.75\%$ , respectively) and then repositioned in flat state for the KPFM characterisation have been included. From these graphs, two important observations can be made. On one hand, there is a strong increase in contact resistance for elongated transistors. In fact,

almost all the potential variation occurs at the semiconductor/electrode interfaces, showing that a strong electric field is required here to inject or extract carriers from the semiconductor. On the other hand, compression has the opposite effect: the contact resistances are reduced. However, stronger variations in the profile slope are observed in the channel, indicating the formation of local barriers for charge carrier transport.

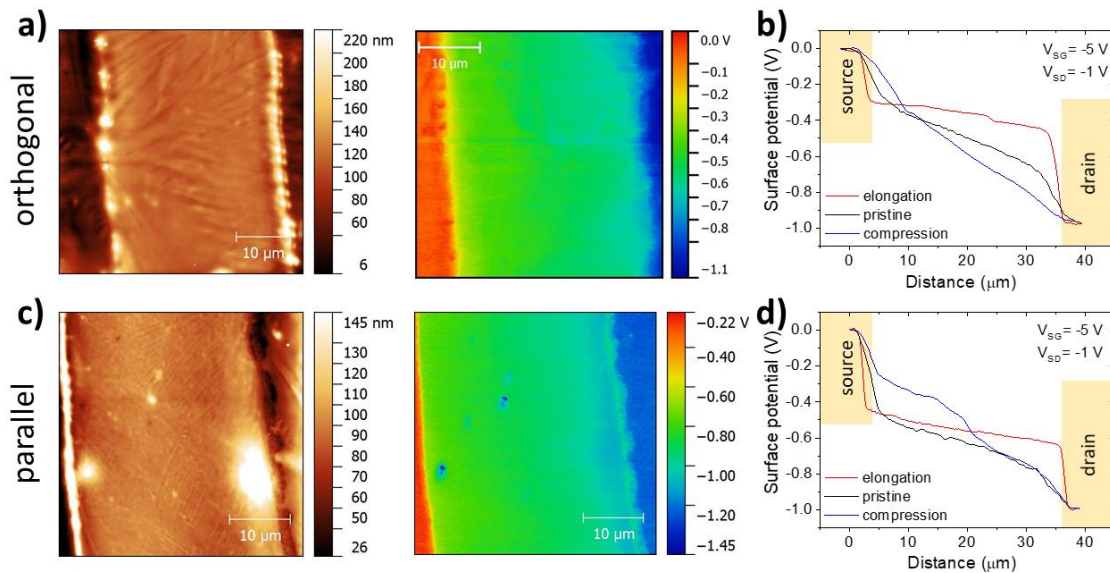


**Figure 5.12.** (a, c) Topography (left) and surface potential (right) images of the whole channel of pristine o-coated and p-coated devices. (b, d) Surface potential profiles of o-coated and p-coated devices in pristine conditions, and after elongation and compression. During KPFM measurements, transistors were kept at a constant drain and gate bias of  $V_{SD} = -1$  V and  $V_{SG} = -5$  V.

If the potential profiles of o- and p-coated devices are compared, it is easy to observe that the contact resistance for a pristine device is larger in the latter case, probably as a consequence of the morphology variation at the channel/electrode interface. Moreover, p-coated devices showed a larger contact resistance reduction than o-coated ones as a result of compression, thus explaining the larger sensitivity of p-coated devices to this kind of deformation. In contrast, o-coated devices showed a larger increase of contact resistance than p-coated ones after elongation, justifying the larger mobility reduction registered in the elongation tests.

The reason for the increase in contact resistance after elongation was further investigated by acquiring AFM and KPFM images of the electrodes border region in higher resolution, as shown in **Figure 5.13 (a)** and **(c)**. From the o-coating images it can be observed that the smooth surface morphology is interrupted by nanocracks that extend in the direction orthogonal to the current. Coincident with these cracks, a strong decrease in surface potential is observed (see the height and potential drops in **Figure 5.13 (b)**). A similar finding was made for the parallel coating; in this case, however, cracks do not extent



linearly in a single direction but are more distributed and not fully interconnected. This different cracking behaviour can be related to the smaller microcrystals identified in the less homogeneous p-coating. In **Figure 5.13 (d)** a decrease in surface potential caused, again, by the formation of cracks can be observed for p-coated devices, although now the variation is more gradual and smaller in magnitude.

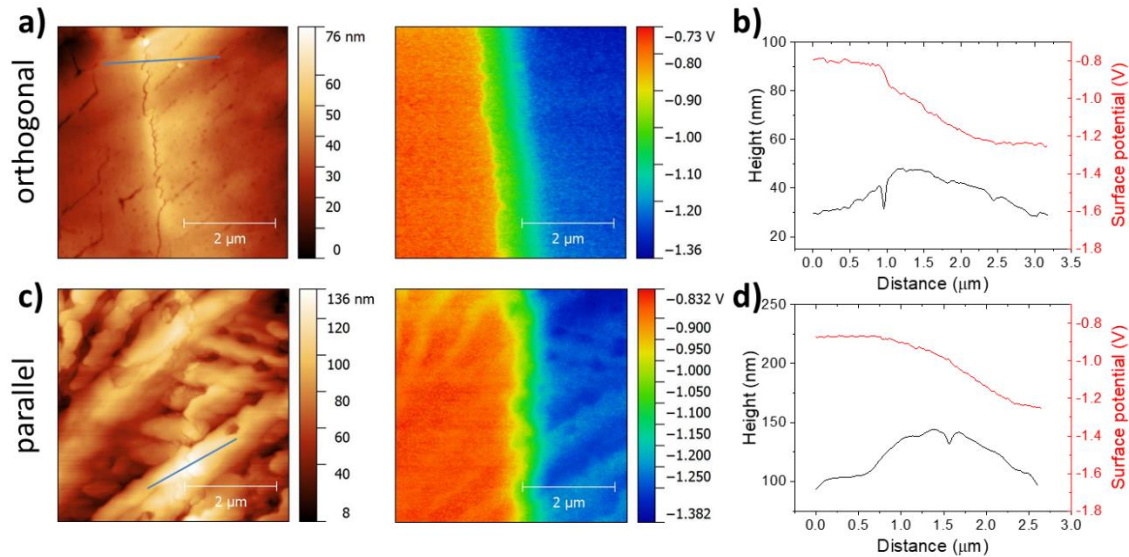


**Figure 5.13.** (a, c) Topography (left) and surface potential (right) images of the contact region in higher resolution of o-coated and p-coated devices after elongation. (b, d) Height and surface potential characteristic profiles obtained along the marked lines. During KPFM measurements, transistors were kept at a constant drain and gate bias of  $V_{SD} = -1$  V and  $V_{SG} = -5$  V.

The described crack formation at the electrodes border can be attributed to high local strain due to the presence of a surface step probably caused by the thickness of the underlying bottom source and drain electrodes. As microcrystals must adapt to this height step at the channel/electrode interface, a pre-strain is already present in the pristine flat state. Then, elongation leads to an increase in strain and when a critical value is reached, strain localisation and crack opening occur mainly in this region instead of in the channel area. As evidenced by the recovery tests (**Figure 5.9**), such a crack formation is irreversible and cracks do not close when the transistor is brought back to flat state. This interpretation of the crack formation can also explain other observations made upon the application of bending deformations. For example, the smaller microcrystals found in the parallel coating lead to a distributed crack opening and less interconnected cracks. As a consequence, some transport pathways remain open after deformation and degradation due to strain is less severe (**Figure 5.9**). Also, the different dynamics of OFET degradation upon cyclic deformation (**Figure 5.10**) can now be rationalised. On one side, the large shift observed in o-coated devices after the first 300 bending cycles can be explained by the formation of the majority of the deep cracks in this stage of the experiment, thus pre-

conditioning the crystalline layer. This relatively rapid cracking can be associated to the large crystal domains of the o-coating, which result in a certain stiffness of the active layer. On the other side, the smaller crystal dimension of p-coated devices contributes to enhance the elasticity of the active layer: the cracks are thus not only scarcely connected, but also formed over a more prolonged stress and also uniformly with the number of deformations.

As a summary, all the above conclusions regarding the relationship between the response to bending and the damaging effects of mechanical stress and the different morphology of the o- and p-coatings are briefly presented in **Table 5.3**.

**Table 5.3.** Summary of the bending sensitivity (upon elongation and compression) and the recovering ability of the o- and p-coated devices in relation with their different morphology.

	Orthogonal coating	Parallel coating
<b>Morphology</b>	Larger crystal domains, stiffer crystalline layer	Smaller crystals domains on the channel area
<b>Elongation</b>	Larger sensitivity than p-coated devices	
<b>Compression</b>	Larger sensitivity than o-coated devices	
<b>Recovery</b>	The recovering ability is lower due to the formation of deep interconnected cracks	Better recovering since cracks are more distributed and less interconnected
<b>Stability</b>	Rapid cracking due to high layer stiffness (large crystal domains)	Cracks are formed uniformly with bending cycles

## 5.6 SUMMARY

---

In summary, bar-assisted meniscus shearing has been exploited for the fabrication of bendable TIPS-pentacene:PS OFETs sensitive to the application of mechanical deformations. Changing the shearing direction between orthogonal (o-coating) and parallel (p-coating) to the channel length allowed tuning the thin-film morphology in the channel area from large to small crystal domain sizes, respectively. Both types of devices showed similar electrical characteristics, but they exhibited an enhanced response to the application of a specific deformation. In particular, it was demonstrated that devices with o- and p-coating showed a larger sensitivity upon elongation and compression, respectively, thus proving the influence of the semiconductor thin-film morphology tuned upon deposition on the bending response.

AFM and KPFM images provided a clear explanation for the electrical response to deformation: an increase (a decrease) of the contact resistance was observed for elongated (compressed) devices, thus justifying the observed current and mobility decrease (increase). Moreover, the formation of cracks in the semiconductor film prevents the devices from recovering their pristine electrical performance, especially in the case of the orthogonal coating, for which cracks are more interconnected due to the larger crystal size.

Finally, the application of cyclic bending demonstrated a good OFET stability and a remarkable response reproducibility over prolonged stress for both types of devices.

## 5.7 REFERENCES

---

- (1) Zhan, Y.; Mei, Y.; Zheng, L. Materials Capability and Device Performance in Flexible Electronics for the Internet of Things. *J. Mater. Chem. C* **2014**, *2*, 1220–1232.
- (2) Greco, F.; Zucca, A.; Taccola, S.; Mazzolai, B.; Mattoli, V. Patterned Free-Standing Conductive Nanofilms for Ultraconformable Circuits and Smart Interfaces. *ACS Appl. Mater. Interfaces* **2013**, *5*, 9461–9469.
- (3) Reuveny, A.; Lee, S.; Yokota, T.; Fuketa, H.; Siket, C. M.; Lee, S.; Sekitani, T.; Sakurai, T.; Bauer, S.; Someya, T. High-Frequency, Conformable Organic Amplifiers. *Adv. Mater.* **2016**, *28*, 3298–3304.
- (4) Nawrocki, R. A.; Matsuhisa, N.; Yokota, T.; Someya, T. 300-Nm Imperceptible, Ultraflexible, and Biocompatible e-Skin Fit with Tactile Sensors and Organic Transistors. *Adv. Electron. Mater.* **2016**, *2*, 1500452.
- (5) Wang, X.; Liu, Z.; Zhang, T. Flexible Sensing Electronics for Wearable/Attachable Health Monitoring. *Small* **2017**, *13*, 1602790.
- (6) Li, Y. Q.; Huang, P.; Zhu, W. Bin; Fu, S. Y.; Hu, N.; Liao, K. Flexible Wire-Shaped Strain Sensor from Cotton Thread for Human Health and Motion Detection. *Sci. Rep.* **2017**, *7*, 45013.
- (7) Xu, Y.; Liu, C.; Khim, D.; Noh, Y.-Y. Development of High-Performance Printed Organic Field-Effect Transistors and Integrated Circuits. *Phys. Chem. Chem. Phys.* **2015**, *17*, 26553–26574.
- (8) Diao, Y.; Shaw, L.; Mannsfeld, S. C. B. Morphology Control Strategies for Solution-Processed Organic Semiconductor Thin Films. *Energy Environ. Sci.* **2014**, *7*, 2145–2159.
- (9) Conti, S.; Lai, S.; Cosseddu, P.; Bonfiglio, A. An Inkjet-Printed, Ultralow Voltage, Flexible Organic Field Effect Transistor. *Adv. Mater. Technol.* **2017**, *2*, 1600212.
- (10) Grau, G.; Subramanian, V. Fully High-Speed Gravure Printed, Low-Variability, High-Performance Organic Polymer Transistors with Sub-5 V Operation. *Adv. Electron. Mater.* **2016**, *2*, 1500328.
- (11) Feng, L.; Jiang, C.; Ma, H.; Guo, X.; Nathan, A. All Ink-Jet Printed Low-Voltage Organic Field-Effect Transistors on Flexible Substrate. *Org. Electron.* **2016**, *38*, 186–192.
- (12) Huang, J.; Zhu, H.; Chen, Y.; Preston, C.; Rohrbach, K.; Cumings, J.; Hu, L. Highly Transparent and Flexible Nanopaper Transistors. *ACS Nano* **2013**, *7*, 2106–2113.

- (13) Peng, B.; Ren, X.; Wang, Z.; Wang, X.; Roberts, R. C.; Chan, P. K. L. High Performance Organic Transistor Active-Matrix Driver Developed on Paper Substrate. *Sci. Rep.* **2014**, *4*, 6430.
- (14) Mattana, G.; Cosseddu, P.; Fraboni, B.; Malliaras, G. G.; Hinestroza, J. P.; Bonfiglio, A. Organic Electronics on Natural Cotton Fibres. *Org. Electron.* **2011**, *12*, 2033–2039.
- (15) Kim, W.; Kwon, S.; Lee, S. M.; Kim, J. Y.; Han, Y.; Kim, E.; Choi, K. C.; Park, S.; Park, B. C. Soft Fabric-Based Flexible Organic Light-Emitting Diodes. *Org. Electron.* **2013**, *14*, 3007–3013.
- (16) Fukuda, K.; Hikichi, K.; Sekine, T.; Takeda, Y.; Minamiki, T.; Kumaki, D.; Tokito, S. Strain Sensitivity and Durability in P-Type and n-Type Organic Thin-Film Transistors with Printed Silver Electrodes. *Sci. Rep.* **2013**, *3*, 2048.
- (17) Lewis, J. Material Challenge for Flexible Organic Devices. *Mater. Today* **2006**, *9*, 38–45.
- (18) Sekitani, T.; Kato, Y.; Iba, S.; Shinaoka, H.; Someya, T.; Sakurai, T.; Takagi, S. Bending Experiment on Pentacene Field-Effect Transistors on Plastic Films. *Appl. Phys. Lett.* **2005**, *86*, 073511.
- (19) Sekitani, T.; Iba, S.; Kato, Y.; Someya, T. Bending Effect of Organic Field-Effect Transistors with Polyimide Gate Dielectric Layers. *Jpn. J. Appl. Phys.* **2005**, *44*, 2841–2843.
- (20) Cosseddu, P.; Milita, S.; Bonfiglio, A. Strain Sensitivity and Transport Properties in Organic Field-Effect Transistors. *IEEE Electron Device Lett.* **2012**, *33*, 113–115.
- (21) Scenev, V.; Cosseddu, P.; Bonfiglio, A.; Salzman, I.; Severin, N.; Oehzelt, M.; Koch, N.; Rabe, J. P. Origin of Mechanical Strain Sensitivity of Pentacene Thin-Film Transistors. *Org. Electron.* **2013**, *14*, 1323–1329.
- (22) Cosseddu, P.; Tiddia, G.; Milita, S.; Bonfiglio, A. Continuous Tuning of the Mechanical Sensitivity of Pentacene OTFTs on Flexible Substrates: From Strain Sensors to Deformable Transistors. *Org. Electron.* **2013**, *14*, 206–211.
- (23) Viola, F. A.; Spanu, A.; Ricci, P. C.; Bonfiglio, A.; Cosseddu, P. Ultrathin, Flexible and Multimodal Tactile Sensors Based on Organic Field-Effect Transistors. *Sci. Rep.* **2018**, *8*, 8073.
- (24) Cosseddu, P.; Lai, S.; Casula, G.; Raffo, L.; Bonfiglio, A. High Performance, Foldable, Organic Memories Based on Ultra-Low Voltage, Thin Film Transistors. *Org. Electron.* **2014**, *15*, 3595–3600.
- (25) Riera-Galindo, S.; Tamayo, A.; Mas-Torrent, M. Role of Polymorphism and Thin-Film

- Morphology in Organic Semiconductors Processed by Solution Shearing. *ACS Omega* **2018**, *3*, 2329–2339.
- (26) del Pozo, F. G.; Fabiano, S.; Pfattner, R.; Georgakopoulos, S.; Galindo, S.; Liu, X.; Braun, S.; Fahlman, M.; Veciana, J.; Rovira, C.; et al. Single Crystal-Like Performance in Solution-Coated Thin-Film Organic Field-Effect Transistors. *Adv. Funct. Mater.* **2016**, *26*, 2379–2386.
- (27) Temiño, I.; Del Pozo, F. G.; Ajayakumar, M. R.; Galindo, S.; Puigdollers, J.; Mas-Torrent, M. A Rapid, Low-Cost, and Scalable Technique for Printing State-of-the-Art Organic Field-Effect Transistors. *Adv. Mater. Technol.* **2016**, *1*, 1600090.
- (28) Galindo, S.; Tamayo, A.; Leonardi, F.; Mas-Torrent, M. Control of Polymorphism and Morphology in Solution Sheared Organic Field-Effect Transistors. *Adv. Funct. Mater.* **2017**, *27*, 1700526.
- (29) Hamilton, R.; Smith, J.; Ogier, S.; Heeney, M.; Anthony, J. E.; McCulloch, I.; Veres, J.; Bradley, D. D. C.; Anthopoulos, T. D. High-Performance Polymer-Small Molecule Blend Organic Transistors. *Adv. Mater.* **2009**, *21*, 1166–1171.
- (30) Lee, W. H.; Lim, J. A.; Kwak, D.; Cho, J. H.; Lee, H. S.; Choi, H. H.; Cho, K. Semiconductor-Dielectric Blends: A Facile All Solution Route to Flexible All-Organic Transistors. *Adv. Mater.* **2009**, *21*, 4243–4248.
- (31) Riera-Galindo, S.; Leonardi, F.; Pfattner, R.; Mas-Torrent, M. Organic Semiconductor/Polymer Blend Films for Organic Field-Effect Transistors. *Adv. Mater. Technol.* **2019**, 1900104.
- (32) Cosseddu, P.; Lai, S.; Barbaro, M.; Bonfiglio, A. Ultra-Low Voltage, Organic Thin Film Transistors Fabricated on Plastic Substrates by a Highly Reproducible Process. *Appl. Phys. Lett.* **2012**, *100*, 093305.
- (33) Lai, S.; Cosseddu, P.; Gazzadi, G. C.; Barbaro, M.; Bonfiglio, A. Towards High Frequency Performances of Ultra-Low Voltage OTFTs: Combining Self-Alignment and Hybrid, Nanosized Dielectrics. *Org. Electron.* **2013**, *14*, 754–761.
- (34) Mannsfeld, S. C. B.; Tang, M. L.; Bao, Z. Thin Film Structure of Triisopropylsilylethynyl-Functionalized Pentacene and Tetraceno[2,3-b]Thiophene from Grazing Incidence X-Ray Diffraction. *Adv. Mater.* **2011**, *23*, 127–131.
- (35) Anthony, J. E.; Eaton, D. L.; Parkin, S. R. A Road Map to Stable, Soluble, Easily Crystallized Pentacene Derivatives. *Org. Lett.* **2002**, *4*, 15–18.
- (36) Cramer, T.; Travaglini, L.; Lai, S.; Patruno, L.; De Miranda, S.; Bonfiglio, A.; Cosseddu, P.; Fraboni, B. Direct Imaging of Defect Formation in Strained Organic Flexible Electronics by Scanning Kelvin Probe Microscopy. *Sci. Rep.* **2016**, *6*, 38203.

- (37) Gurmessa, B. J.; Croll, A. B. Onset of Plasticity in Thin Polystyrene Films. *Phys. Rev. Lett.* **2013**, *110*, 074301.
- (38) Bürgi, L.; Sirringhaus, H.; Friend, R. H. Noncontact Potentiometry of Polymer Field-Effect Transistors. *Appl. Phys. Lett.* **2002**, *80*, 2913–2915.
- (39) Palermo, V.; Palma, M.; Samori, P. Electronic Characterization of Organic Thin Films by Kelvin Probe Force Microscopy. *Adv. Mater.* **2006**, *18*, 145–164.

## CHAPTER 6

# X-ray sensitivity of OFET based detectors tuned by controlling the processing parameters\*

### 6.1 INTRODUCTION AND OBJECTIVES

The detection of ionising radiation, either as high-energy photons (X- and gamma-rays) or particles (neutrons or electrons) is demanded by many industrial and socially relevant fields, such as microelectronics, quality control, nuclear waste monitoring or medical imaging.<sup>1,2</sup> Up to now, inorganic semiconductor materials such as silicon exhibit the best detecting performances thanks to their superior charge transport properties. Such applications are of high commercial interest but ensuring high material purity and uniformity is expensive. Consequently, amorphous silicon (a-Si), amorphous selenium (a-Se), and polycrystalline cadmium zinc telluride (poly-CZT) are often exploited for the realisation of large-area detectors.<sup>3-7</sup> An alternative approach is based on the employment of organic semiconductors as active material for radiation detection systems, which has attracted great attention from the research community. Above all, the possibility to employ solution-based processing techniques to fabricate large-area, low-cost and flexible organic devices would allow overcoming the limitations of traditional inorganic semiconductor devices, which are typically rigid, heavy, power-consuming and with a small active detection area. The attractive features offered by organic materials are key to open the way for several innovative applications, spanning from medical diagnostics to public safety, space, cultural heritage and environmental monitoring.

Organic semiconductor materials were first suggested for the indirect detection of ionising radiation in the early 1960s, when the primary interest in these materials was on their scintillating properties.<sup>8-10</sup> As illustrated in **Figure 6.1 (a)**, in the indirect detection

---

\* This work has been carried out during a 3 month stay at the University of Bologna in collaboration with the group of Prof. Beatrice Fraboni. Manuscript submitted. Temiño, I.; Basiricò, L.; Fratelli I.; Tamayo A.; Ciavatti A.; Mas-Torrent, M.; Fraboni, B. Morphology and Mobility as Tools to Control and Unprecedentedly Enhance X-Ray Sensitivity in Organic Thin-Film Devices.



mechanism the incoming ionising radiation is transduced into an electrical output signal in two steps: first, a scintillator transforms the ionising radiation into visible photons, and then, a photodiode converts this signal into an electrical one.<sup>2</sup> However, in the direct detection mechanism (**Figure 6.1 (b)**) the ionising radiation is transduced into an electrical signal within the same device, which is a more effective process than the indirect one since it improves the signal-to-noise ratio and it reduces the device response time.

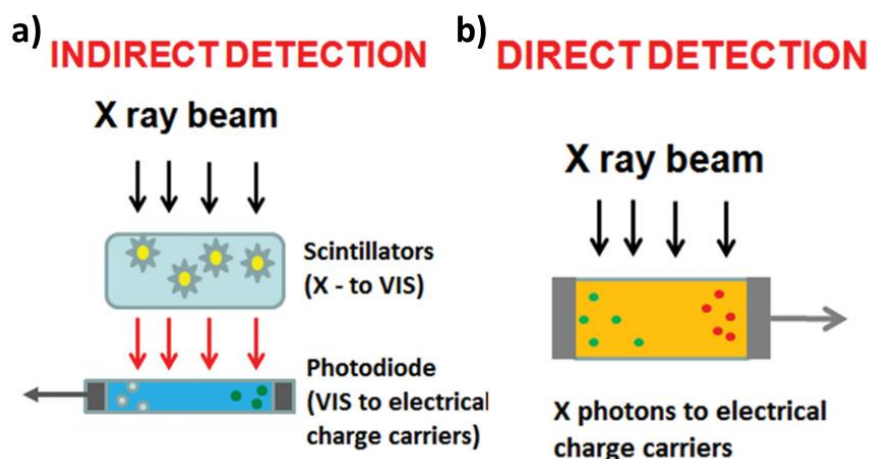


**Figure 6.1.** Schematic illustration of the (a) indirect and (b) direct radiation detection mechanisms. Extracted from ref. 2.

The direct detection approach employing organic semiconductors has been extensively investigated in the last decade. As a result, several examples based on conjugated polymer films,<sup>11,12</sup> single crystals,<sup>13,14</sup> and small molecule polycrystalline films<sup>15,16</sup> have been reported exhibiting in most cases a linear electrical photoresponse to increasing radiation dose rates. In this field, two important characteristics have been mainly considered in order to achieve high performance direct radiation detectors: the transport characteristics and the absorbance properties of the active organic layer.

First, in order to reduce energy loss due to charge recombination and to achieve an efficient charge collection, a high charge carrier mobility is desirable. In this sense, the focus is set in semiconducting materials exhibiting high crystallinity, resulting in enhanced charge transport and X-ray detection properties.<sup>17</sup> For instance, a two-terminal photodetector based on micro-crystalline 6,13-bis(triisopropylsilylethynyl)pentacene (TIPS-pentacene, **Figure 6.2 (a)**) drop-casted onto flexible poly(ethyleneterephthalate) (PET) substrates reported an X-ray sensitivity of 200 nC/Gy.<sup>15</sup> Furthermore, by exploiting the structure of an organic field-effect transistor (OFET), the detection ability of the devices could be tuned by the biasing conditions (**Figure 6.2 (b)**), and an enhanced sensitivity of 1200 nC/Gy was achieved in this case.<sup>16</sup>

Secondly, the amount of radiation absorbed should be favoured as much as possible since the low stopping power of organic materials, which is related to their low atomic number  $Z$ , limits the detection capability of such devices. The employment of thick films to increase the active volume is generally avoided because it results in an increase of the operating voltage and limits the bendability of the devices, thus sacrificing the potential advantages of organic materials. Alternative solutions to enhance the absorbance of the organic layer, such as blending high  $Z$  elements as nanoparticles or quantum dots, or inserting carbon nanotubes in the organic matrix have been proposed.<sup>18–23</sup> More recently, tailoring the molecular structure of TIPS-pentacene to include high- $Z$  atoms (i.e., substituting Si with Ge atoms to give TIPGe-pentacene, shown in **Figure 6.2 (a)**) has been investigated,<sup>24</sup> resulting in transistor devices with a remarkable sensitivity of 4460 nC/Gy (18  $\mu\text{C}/\text{Gy}\cdot\text{cm}^2$ , per unit area). This is a record value for organic thin-film X-ray detectors, and, moreover, it is competitive with the performance of some state-of-the-art inorganic materials currently used to fabricate large-area detectors (typical sensitivity values for a-Se are around 30  $\mu\text{C}/\text{Gy}\cdot\text{cm}^2$ ).<sup>7</sup>

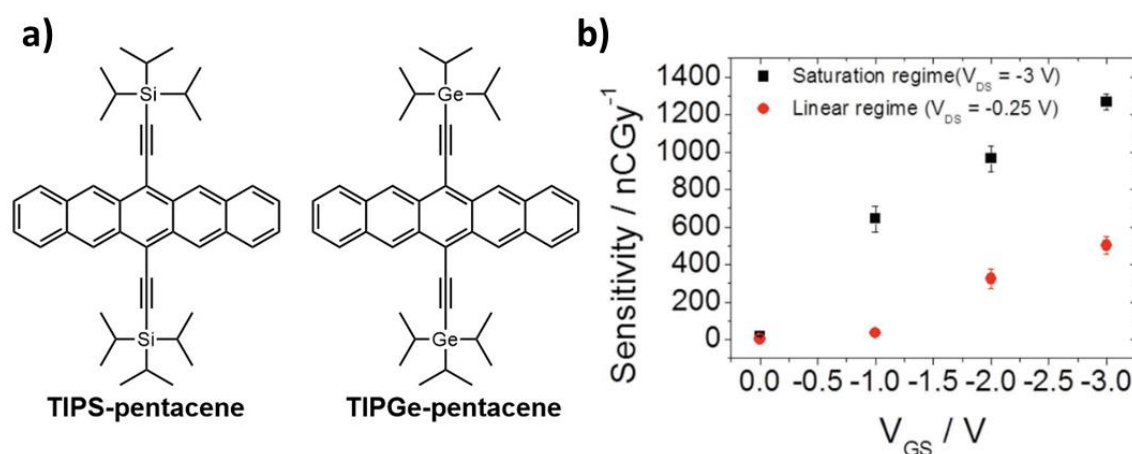


**Figure 6.2.** (a) Molecular structures of TIPS-pentacene and TIPGe-pentacene. (b). Sensitivity modulated by the source-gate voltage in linear and saturation regime. Extracted from ref. 16.

Besides research aiming to the obtention of organic direct X-ray detectors with higher sensitivities, attention has also been focused on studying the physical processes ruling the detection mechanism of high-energy photons in such low  $Z$  molecular systems. The X-ray sensitivity displayed by inorganic semiconductors is generally explained by the generation of electron-hole pairs. Under the effect of an applied electric field (i.e., when a potential difference is applied between two electrodes), the charge carriers separate and drift to the respective electrodes, thus generating a photocurrent. In this process, recombination and phonon formation represent losses. However, it was recently reported by L. Basiricò et al. that the photocurrent produced by X-ray photons in a micro-crystalline TIPS-pentacene thin film was higher by two orders of magnitude than the estimated signal

considering only the collection of photogenerated charges.<sup>15</sup> To explain this remarkable result, a photoconductive gain mechanism based on the accumulation of photogenerated charges in the material was proposed. As schematically illustrated in **Figure 6.3**, this mechanism consists of the following processes. First, additional electrons and holes are generated under X-ray irradiation (1). Then, while holes drift along the electric field until they reach the collecting electrode, electrons remain trapped in deep trap states within the organic material (2). To guarantee charge neutrality, holes are continuously emitted from the injecting electrode, and, consequently, for each electron-hole pair created more than one hole contributes to the photocurrent leading to a photoconductive gain effect (3). Finally, charge recombination counterbalances the charge photogeneration process in the steady-state (4). Thus, it was concluded that the modulation of the current signal experimentally measured upon X-rays exposure is correlated to an electron traps assisted photoconductive gain mechanism. At this point, the possibility of tuning the density of such electron traps within the active material in order to enhance the X-ray sensitivity of organic based detectors is an interesting question yet to be explored.

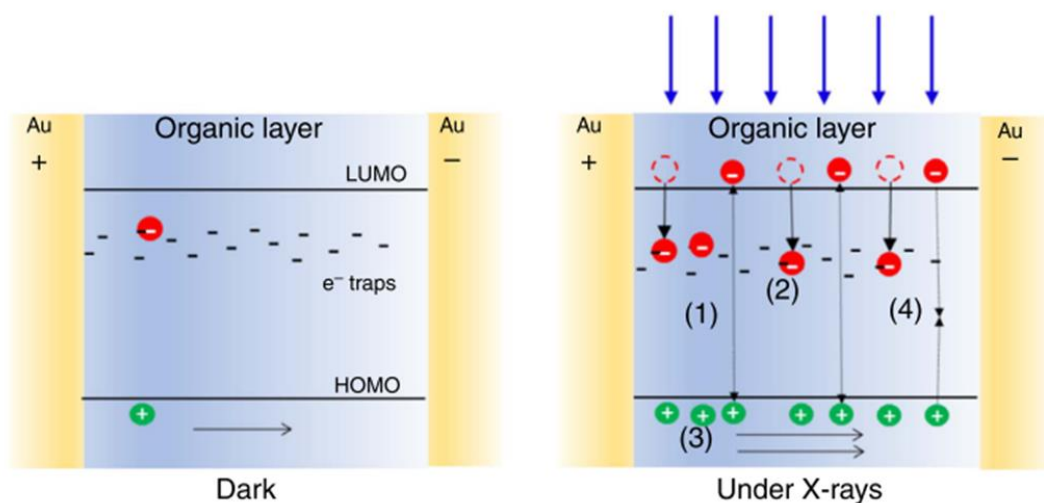


**Figure 6.3.** Schematic of the photoconductive gain mechanism that modulates the current induced by X-rays exposure of TIPS-pentacene films. Extracted from ref. 15.

Although the impact of the thin-film morphology on the X-ray sensitivity could be anticipated, this matter has been scarcely investigated probably due to the poor control on the final morphological features offered by some solution-based techniques. Some innovative approaches for controlling the thin-film morphology upon deposition from solution have been proposed,<sup>25,26</sup> among which bar-assisted meniscus shearing (BAMS) has attracted a significant interest mainly thanks to its scalability, high coating speed and easiness-in-use.<sup>27</sup> BAMS technique has demonstrated to be able to cover large areas with uniform and highly crystalline organic semiconducting thin films, leading to OFETs with

high and reproducible field-effect mobility values.<sup>28</sup> Interestingly, as it has already been reported, it is possible to modulate the morphology of thin films processed by BAMS by tuning the deposition parameters, such as temperature or speed, as well as the ink formulation.<sup>29,30</sup> Moreover, the use of blends consisting of a small molecule organic semiconductor and an insulating polymer (such as polystyrene, PS) has shown to be an efficient strategy to enhance thin-film processability and homogeneity, as well as device environmental stability.<sup>31-33</sup>

## Objectives

Thus, the main objective of this chapter is to exploit OFETs for the direct detection of X-ray radiation, and to investigate the physical processes behind photoconversion by understanding the relationship between the devices sensing capability and the morphological and transport properties of the polycrystalline organic semiconductor layers. To do so, the control of the processing parameters employing BAMS as solution deposition technique has been explored, aiming to maximise the devices response. Firstly, TIPS-pentacene thin films were deposited at different coating speeds, resulting in a tuned thin-film morphology. Also, tuning the OFET mobility by using TIPS-pentacene:PS blends with different blending ratios was explored. Finally, important features for the implementation of organic X-ray detectors in real-life applications, such as device stability, reliability and limit of detection, were tested.

## 6.2 TIPS-PENTACENE OFETS AS X-RAY DETECTORS

Bottom-gate bottom-contact OFETs based on TIPS-pentacene were fabricated on Si/SiO<sub>2</sub> substrates with interdigitated gold electrodes with a channel width and length of  $W = 2.5 \text{ mm}$  and  $L = 25 \text{ }\mu\text{m}$ , respectively. Source/drain electrodes were treated with a self-assembled monolayer of pentafluorobenzenethiol (PFBT), as optimised in Chapter 2.<sup>28</sup> TIPS-pentacene thin films were deposited from chlorobenzene solutions (4 wt%) by bar-assisted meniscus shearing (BAMS) at a speed of 10 mm/s. This process resulted in polycrystalline thin films with high coverage, homogeneity, crystallinity, and spherulitic domains, as shown in the polarised optical microscope image in **Figure 6.4**.

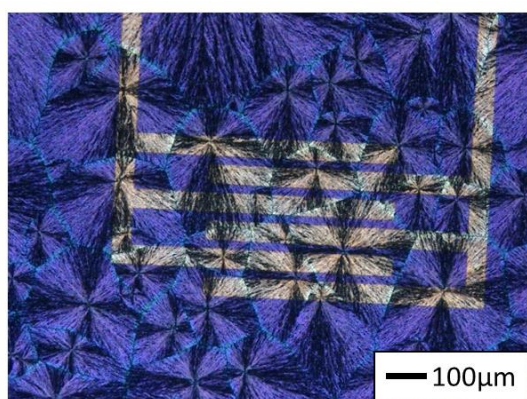


**Figure 6.4.** Crossed-polarised optical microscope image of a TIPS-pentacene thin film deposited by BAMS at 10 mm/s.

Devices were electrically measured under ambient conditions, with  $V < 20 \text{ V}$  for both  $V_{SD}$  and  $V_{SG}$ . A typical saturation transfer curve is reported in **Figure 6.5 (a)**, showing a good current modulation and a small but noticeable hysteresis. Also, the output characteristics in **Figure 6.5 (b)** indicate a negligible contact resistance. The main OFET parameters were extracted in the saturation regime and statistically analysed for a set of 10 devices. Devices exhibited an average field-effect mobility of  $\mu_{FE} = 10^{-2} \text{ cm}^2/\text{V}\cdot\text{s}$  and a mean threshold voltage of  $V_{th} = 6 \pm 2 \text{ V}$ , indicating that the devices are slightly doped. The *on/off* ratio was around  $10^3$ , a rather small value that can be related to a not so steep switch-on of the devices (the average subthreshold swing was  $SS = 1.6 \pm 0.4 \text{ V/dec}$ ). This result points towards the presence of defects or charge traps at the semiconductor/dielectric interface, which alter the switch-on of the devices and cause the observed hysteresis.

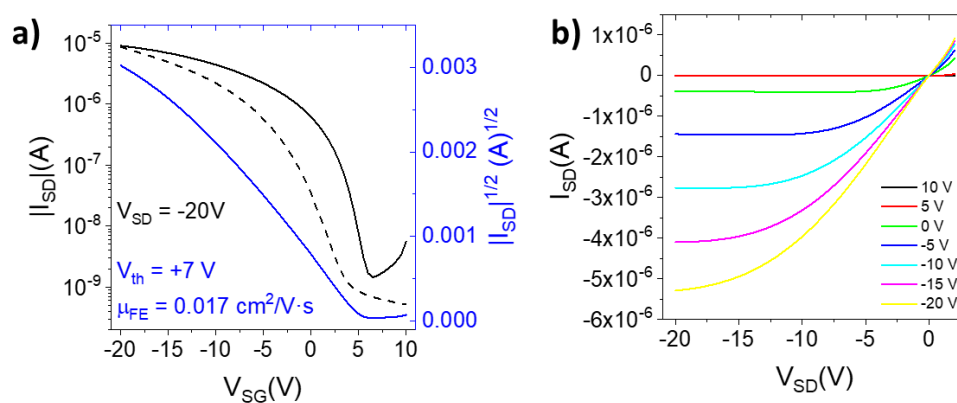


**Figure 6.5.** Electrical characteristics of a typical TIPS-pentacene OFET device in which the semiconductor was deposited by BAMS at 10 mm/s. (a) Transfer characteristics in the saturation regime and square root of the absolute value of the source-drain current vs. source-gate voltage for the extraction of field-effect mobility and threshold voltage. Straight and dashed lines correspond to forward and reverse sweeps, respectively. (b) Output characteristics.

TIPS-pentacene devices were subsequently characterised as X-ray detectors employing the setup shown in **Figure 6.6 (a)**, comprising a Mo-target X-ray tube. Devices were exposed to multiple on/off beam switching cycles with a time window of 60 s and an increasing dose rate, varying from 6 to 53 mGy/s. Meanwhile OFETs were biased with  $V_{SD} = -20$  V and  $V_{SG} = -15$  V, as preliminary tests indicated that the devices response is maximised when the transistor is on and biased in the saturation regime, in agreement with previous reports (see also **Figure 6.2 (b)**).<sup>16</sup> More details on the experimental setup can be found on the experimental methods chapter (Chapter 7). The induced real-time response of a TIPS-pentacene device measured in these conditions is shown in **Figure 6.6 (b)**. As it was previously mentioned,<sup>15,16</sup> the observed photocurrent response can be ascribed to a photoconductive gain mechanism related to electron traps. The subsequent stretched exponential decrease of the current after the exposure to X-rays is attributed to a slow relaxation of the trapped charge carriers. The X-ray induced photocurrent can be evaluated as the amplitude of the on peaks with respect to the current base line. As it is shown in **Figure 6.6 (c)**, a linear dependency of the photocurrent with the dose rate of the incident radiation is observed. From the slope of this plot a sensitivity  $S = 1.60$   $\mu\text{C}/\text{Gy}$  was estimated, which, considering the pixel area of the interdigitated devices ( $A = 4.25 \cdot 10^{-3}$   $\text{cm}^2$ ), yields a normalised sensitivity of  $3.8 \cdot 10^2$   $\mu\text{C}/\text{Gy}\cdot\text{cm}^2$ . Remarkably, this value is about two orders of magnitude higher than the previously reported results employing detectors based on drop-casted TIPS-pentacene OFETs (a sensitivity of 1.2  $\mu\text{C}/\text{Gy}$  was reported in this case, but the large active area of the employed devices, 0.25  $\text{cm}^2$ , gives a normalised value of 4.8  $\mu\text{C}/\text{Gy}\cdot\text{cm}^2$ ).<sup>16</sup> Moreover, it is also higher by a factor of 20 than the sensitivity exhibited by transistor devices based on drop-casted TIPGe-pentacene (18  $\mu\text{C}/\text{Gy}\cdot\text{cm}^2$ ).<sup>24</sup>



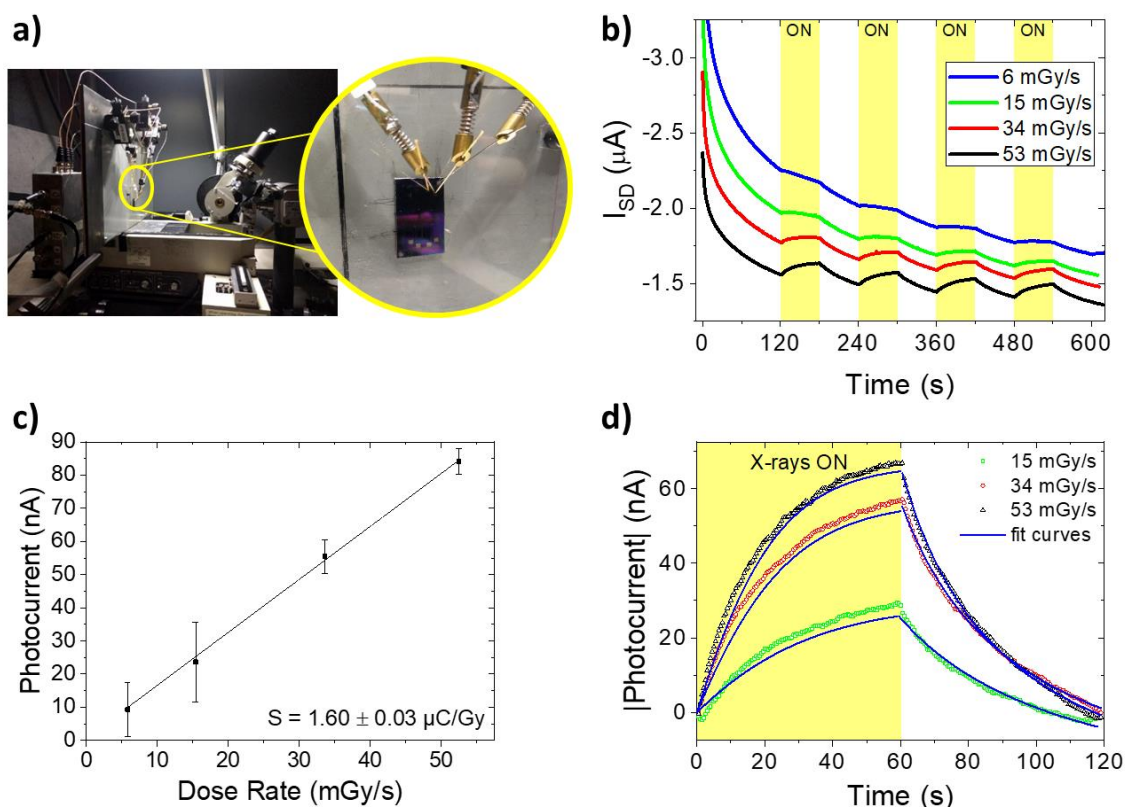


**Figure 6.6.** (a) Photograph of the experimental setup for the samples irradiation with a Mo-target X-ray tube. (b) X-ray induced photocurrent response of a pure TIPS-pentacene device upon four on/off switching cycles (yellow areas, time windows of 60 s) employing an increasing dose rate from 6 to 53 mGy/s. (c) X-ray induced photocurrent versus dose rate plot for X-ray sensitivity estimation. (d) Experimental and fitted curves of the dynamic response for different dose rates.

Furthermore, the dynamic behaviour of the photocurrent signal was fitted by the same photoconductive gain model previously developed for TIPS-pentacene two-terminal devices on PET substrates.<sup>15</sup> The fitted curves shown in **Figure 6.6 (d)** were obtained using a single set of fitting parameters for all the different dose rates employed, which allowed extracting a gain value ( $G$ ) of  $2 \cdot 10^6$  upon exposure to 15 mGy/s X-rays radiation. More details regarding the fitting process and the equations employed can be found on Chapter 7. Again, this value, which is one order of magnitude higher than that reported for drop-casted TIPS-pentacene OFETs ( $3 \cdot 10^5$ ),<sup>16</sup> points out the huge amplification of the induced photocurrent achieved by these devices.

### 6.3 SENSITIVITY VS. THIN-FILM MORPHOLOGY: CONTROLLING THE COATING SPEED

The modification of the deposition speed is known to influence the crystallisation regime of the thin film, affecting the morphology, the domain size and even the molecular orientation.<sup>26,34</sup> In this part of the work, the control of the BAMS coating speed was employed as a tool to modify the active layer morphology in order to study its influence on the X-ray detection mechanism. Hence, TIPS-pentacene thin films were deposited at lower and higher speeds than the one previously used, 10 mm/s.

The polarised optical microscope images in **Figure 6.7** show that thin films deposited at a low and high coating speed (4 and 28 mm/s, respectively) exhibit the same spherulitic domains, but in the former case the crystal domains size is considerably bigger. To further characterise the thin-film morphology, atomic force microscopy (AFM) topography images were obtained (**Figure 6.8**). The thin-films thickness', estimated from the height profiles in **Figure 6.8 (b-c)** and reported in **Table 6.1**, were found to range from 70 to 120 nm. In addition, images in **Figure 6.8 (a)** show morphological features that indicate a bigger size of TIPS-pentacene crystallites for the low-speed processed thin film. The grain size was analysed employing a dedicated Gwyddion tool (the software employed for the analysis of AFM images), and calculated values are reported in **Table 6.1**. Although great differences are observed between films deposited at 4 and 28 mm/s, it should also be noted that increasing the coating speed from 10 to 28 mm/s does not significantly affect the thin-film morphology. Indeed, processing at a speed in the range 10-30 mm/s gives rise to similar crystal domains (see **Figure 6.4** and **Figure 6.7 (b)**) and grain sizes (see **Figure 6.8 (a)** and **Table 6.1**). Increasing further the coating speed leads to thin films with smaller domains; however, due to the lack of uniformity, higher speeds have been avoided in this work in order to achieve reproducible thin films.

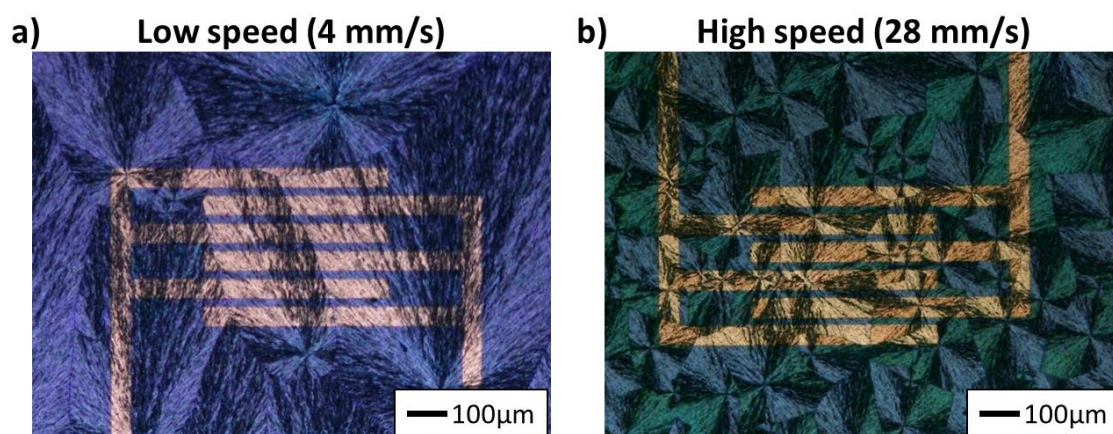


**Figure 6.7.** Crossed-polarised optical microscope images of TIPS-pentacene thin films deposited by BAMS at (a) low speed (4 mm/s) and (b) high speed (28 mm/s).



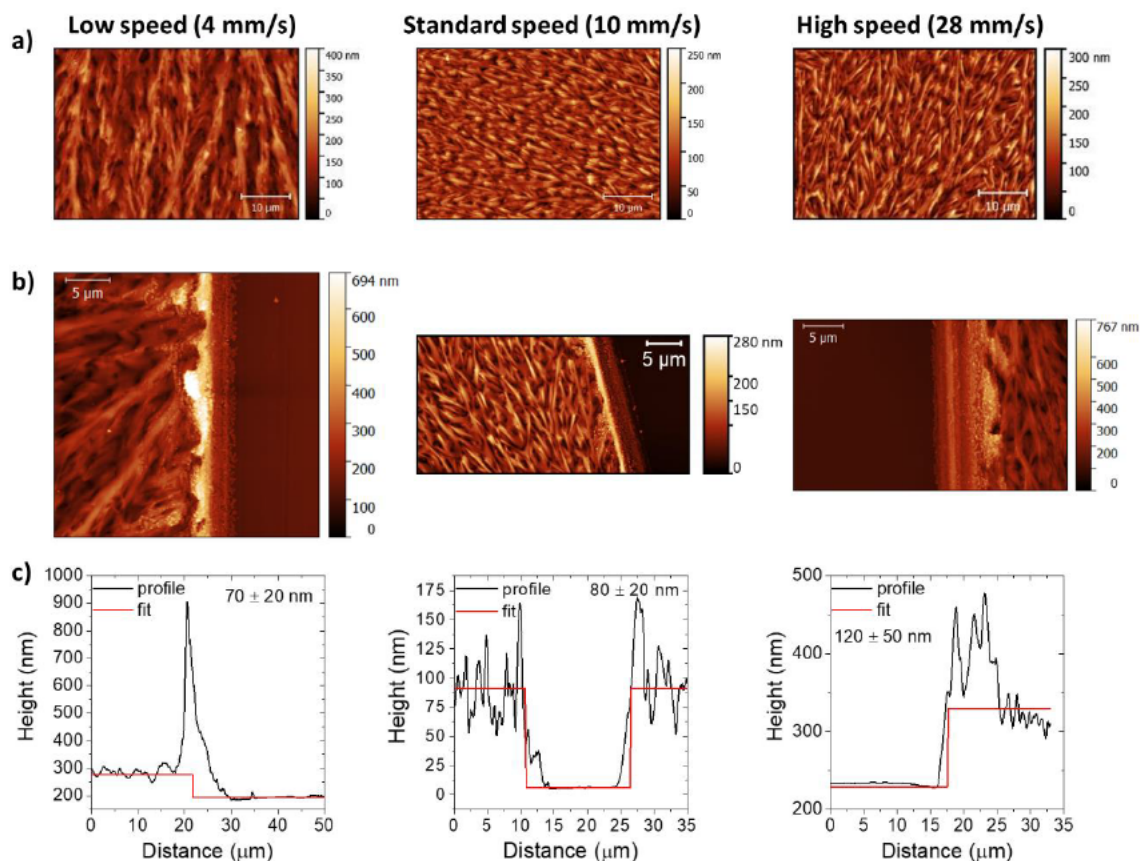


**Figure 6.8.** (a-b) AFM topography images of TIPS-pentacene thin films deposited at low, standard and high coating speed. (c) Height profile obtained from the height step in (b), employed for thickness estimation.

**Table 6.1.** Comparison between low-, standard- and high-speed deposition, of different parameters of the TIPS-pentacene thin films, the TIPS-pentacene OFET devices and their X-ray sensing performance. The error of the grain size, film thickness, and X-ray sensitivity was deduced from the experimental calculations, while the error shown for the OFET mobility and the density of hole traps ( $N_T$ ) is a standard deviation.

Deposition speed (mm/s)	Grain size ( $\mu\text{m}^2$ )	Thickness (nm)	$\mu_{FE}$ ( $\text{cm}^2/\text{V}\cdot\text{s}$ )	$N_T$ ( $10^{12} \text{ eV}^{-1}\text{cm}^{-2}$ )	Sensitivity ( $\mu\text{C}/\text{Gy}\cdot\text{cm}^2$ )	Gain
Low (4)	$17 \pm 3$	$70 \pm 20$	$(2.5 \pm 0.7) \cdot 10^{-2}$	$1.7 \pm 0.4$	$(1.0 \pm 0.2) \cdot 10^2$	$7 \cdot 10^5$
Standard (10)	$6 \pm 2$	$80 \pm 20$	$(1.7 \pm 0.5) \cdot 10^{-2}$	$1.8 \pm 0.5$	$(3.8 \pm 0.1) \cdot 10^2$	$2 \cdot 10^6$
High (28)	$6 \pm 3$	$120 \pm 50$	$(2.4 \pm 0.6) \cdot 10^{-2}$	$1.6 \pm 0.4$	$(3.8 \pm 1.2) \cdot 10^2$	$4 \cdot 10^6$

OFETs based on TIPS-pentacene thin films deposited at low and high speed were electrically measured and exhibited similar characteristics. The field-effect mobility ( $\mu_{FE}$ ) values extracted from **Figure 6.9 (a)**, where the square root of  $|I_{SD}|$  is plotted versus  $V_{SG}$ , are around  $2 \cdot 10^{-2} \text{ cm}^2/\text{V}\cdot\text{s}$  (**Table 6.1**). The hole trap density values ( $N_T$ ), calculated from the subthreshold swing, are also comparable for both types of devices. Regarding the X-ray detection capability, the devices processed at high speed showed a sensitivity more than three times higher than that of the low-speed processed devices:  $3.8 \cdot 10^2$  and  $1 \cdot 10^2 \mu\text{C}/\text{Gy}\cdot\text{cm}^2$ , respectively (see **Figure 6.9 (b)** and **Table 6.1**). Since the OFET parameters extracted from the electrical characteristics (i.e.,  $\mu_{FE}$  and  $N_T$ ) are comparable, the differences observed in the X-ray response between the low- and high-speed processed devices can be ascribed to their different thin-film morphologies and, in particular, to the different density of grain boundaries. Indeed, it is noteworthy that the similar thin-film morphology obtained by coating at 10 and 28 mm/s results in similar X-ray sensitivity values too. The photoconductive gain was calculated for the low- and high-speed processed devices by fitting again the photocurrent signal to the photoconductive gain model. As reported in **Table 6.1**, the higher gain value estimated for the high-speed processed device points out that in this type of samples there is a higher number of electron traps inducing a greater amplification of the photocurrent.

These results indicate that the reduction of the grains size (that is, an increase in the density of grain boundaries) in the active layer is an efficient strategy to increase the X-ray sensitivity of organic polycrystalline thin-film devices, as an enhancement of the electron trap density is achieved. In this case, morphological changes are easily modulated by the coating speed of the TIPS-pentacene films.

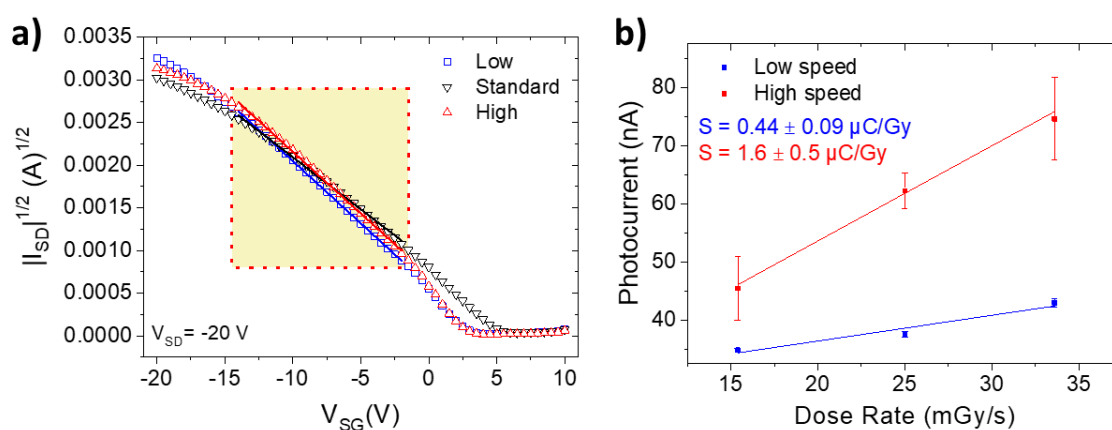


**Figure 6.9.** (a) Square root of the absolute value of the source-drain current vs. source-gate voltage for OFET devices prepared at low, standard and high coating speed, employed for the extraction of field-effect mobility by fitting in the highlighted area. (b) X-ray induced photocurrent versus dose rate plot for the low- and high-speed processed devices.

## 6.4 SENSITIVITY VS. CHARGE CARRIER MOBILITY: CONTROLLING THE TIPS-PENTACENE:PS RATIO

The addition of an insulating polymer such as polystyrene (PS) to a small molecule organic semiconductor ink is known to be an effective way to improve thin-film processability and stability, and to boost the performance of the transistors.<sup>28,31</sup> Indeed, OFETs based on blends of TIPS-pentacene and PS with a molecular weight of 10 kg/mol with a TIPS-pentacene:PS weight ratio of 4:1 were optimised in Chapter 2 and further applied onto flexible plastic substrates in Chapter 5. In this case, thin films based on different TIPS-pentacene:PS blending ratios, 4:1, 2:1 and 1:1, were deposited by BAMS in order to investigate the effect of the blending ratio on the OFET performance and, in turn, on the devices X-ray detection capability. The addition of the polymer allowed lowering the concentration of the chlorobenzene solution from 4 to 2 wt%, while the coating speed remained fixed at 10 mm/s. Devices based on only TIPS-pentacene and processed at the same speed, which have been reported in the previous sections of this chapter, will be used for comparison and, for simplicity, they will be referred to as 1:0 films.

The polarised optical microscope images of the 4:1, 2:1 and 1:1 deposited thin films are shown in **Figure 6.10**, where it can be observed that in all cases TIPS-pentacene crystallises in uniform films with the same spherulitic morphology previously observed for the 1:0 thin films (see **Figure 6.4**). The X-ray diffractograms presented in **Figure 6.11** for films based on the 1:0, 4:1, 2:1 and 1:1 blends evidence their high degree of crystallinity. The four blends exhibit identical diffraction patterns in agreement with the triclinic phase previously reported for this molecule,<sup>35</sup> ensuring that the same crystal phase is present in all of them. In addition, only sets of  $(00l)$  peaks were observed, indicative of the high orientation of the crystallites with respect to the substrate. It is worth commenting that the broader diffraction peaks registered for TIPS-pentacene:PS films is explained by the reduction of the crystalline domains size observed in the microscope images.

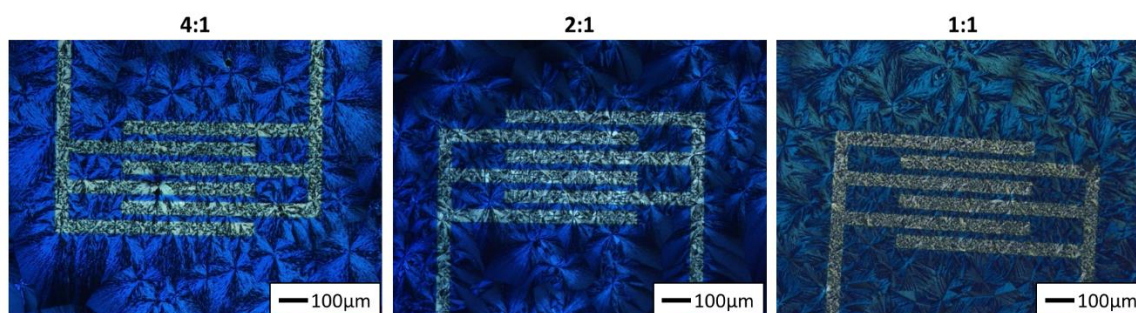


**Figure 6.10.** Crossed-polarised optical microscope images of TIPS-pentacene:PS thin films based on different blending ratios (4:1, 2:1, 1:1).

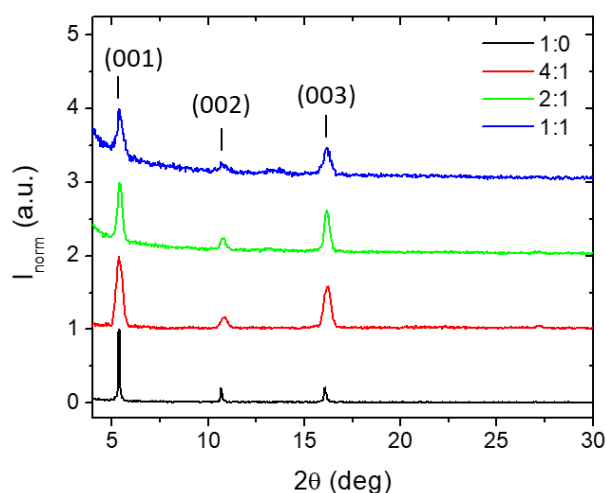


**Figure 6.11.** Normalised X-ray diffractograms of the 1:0, 4:1, 2:1 and 1:1 TIPS-pentacene:PS thin films. Diffraction curves have been shifted along the y-axis for clarity.

The morphology of the TIPS-pentacene:PS deposited thin films was further characterised by AFM, as reported in **Figure 6.12**. The thin-film thickness estimated from the height profiles was found to be between 40 and 90 nm (note TIPS-pentacene only was 80 nm thick). In addition, it can be clearly appreciated that PS-containing thin films present a smoother top surface in comparison with TIPS-pentacene films as shown in **Figure 6.8 (a)**. In fact, the root mean square roughness (*rms*) was estimated to be 6, 9 and 2 nm for the 4:1, 2:1 and 1:1 blends, respectively, and 37 nm for TIPS-pentacene only films. The increased smoothness of the TIPS-pentacene:PS thin films is a proof of the uniformity provided by the polymer, and an indication that TIPS-pentacene crystals are embedded in a polymeric matrix.<sup>27</sup>

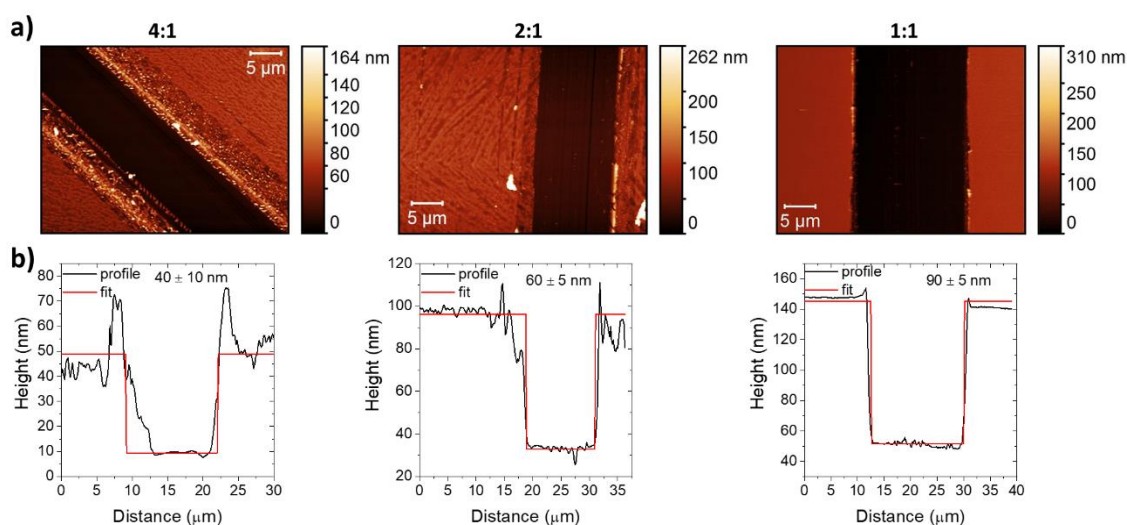


**Figure 6.12.** (a) AFM topography images with a height step and (b) height profile for thickness estimation of TIPS-pentacene:PS thin films based on different blending ratios (4:1, 2:1, 1:1).

OFET devices based on the 4:1, 2:1 and 1:1 TIPS-pentacene:PS blends were electrically characterised and a statistical analysis of the main OFET parameters extracted in the saturation regime was carried out employing a set of 10 devices for each formulation in order to test reproducibility. Average and standard deviation values are summarised in **Table 6.2**, where 1:0 devices have been included for comparison. In addition, a box-plot representation of the statistics obtained for the *on/off* ratio, the field-effect mobility ( $\mu_{FE}$ ), the threshold voltage ( $V_{th}$ ) and the hole trap density ( $N_T$ ) is shown in **Figure 6.13**. In this kind of plot, all the data between the first and the third quartile is included inside the box, and the mean, the maximum and the minimum values are also clearly indicated, in such a way that the dispersion between identical devices and differences between formulations can be easily appreciated.

Comparison between all studied blends shows a general improvement of the electrical performance when PS is added to the formulation. Firstly, it can be observed that the *on/off* ratio and the field-effect mobility are higher for PS-containing devices (**Figure 6.13 (a-b)**). In particular, for 4:1 and 2:1 blends the average values reach  $4 \cdot 10^5$  and  $0.5 \text{ cm}^2/\text{V}\cdot\text{s}$ , respectively, which represents an increase of almost two orders of magnitude with respect to the pure TIPS-pentacene devices. Another benefit provided by the addition of PS is found in the threshold voltage (**Figure 6.13 (c)**), that shifts from positive values around 6 V for devices based on only TIPS-pentacene to  $V_{th}$  mean values between -1 and -2 V for the devices based on blends. Moreover, a steeper turn-on, and thus a lower subthreshold swing ( $SS$ ), was found for PS-containing devices, indicating a smaller interfacial hole trap density (**Figure 6.13 (d)**). Indeed, a vertical phase separation between the organic semiconductor (OSC) molecule and the polystyrene, where the crystalline semiconducting layer is formed on top of a PS buffering layer, has been reported for various OSC:PS blends processed by solution.<sup>31,36–38</sup> Thanks to this stratification, the surface of the  $\text{SiO}_2$  dielectric is passivated by the underlying PS layer and, thus, the density of hole traps at the OSC/dielectric interface is reduced, justifying the overall performance improvement of the TIPS-pentacene:PS OFETs.



**Table 6.2.** Main OFET parameters of 1:0, 4:1, 2:1 and 1:1 TIPS-pentacene:PS devices extracted in the saturation regime from a set of 10 devices of each formulation.

Blend ratio	$on/off$	$\mu_{FE}$ ( $cm^2/V \cdot s$ )	$V_{th}$ (V)	$SS$ (V/dec)	$N_T$ ( $10^{12} eV^{-1}cm^{-2}$ )
1:0	$(4 \pm 2) \cdot 10^3$	$(1.0 \pm 0.3) \cdot 10^{-2}$	$6 \pm 2$	$1.6 \pm 0.4$	$2.7 \pm 0.7$
4:1	$(3 \pm 2) \cdot 10^5$	$(5 \pm 2) \cdot 10^{-1}$	$-1 \pm 2$	$0.6 \pm 0.2$	$1.0 \pm 0.3$
2:1	$(4 \pm 2) \cdot 10^5$	$(5 \pm 3) \cdot 10^{-1}$	$-1 \pm 1$	$0.5 \pm 0.1$	$0.8 \pm 0.1$
1:1	$(1.4 \pm 0.9) \cdot 10^5$	$(6 \pm 4) \cdot 10^{-2}$	$-2 \pm 1$	$0.7 \pm 0.1$	$1.2 \pm 0.2$

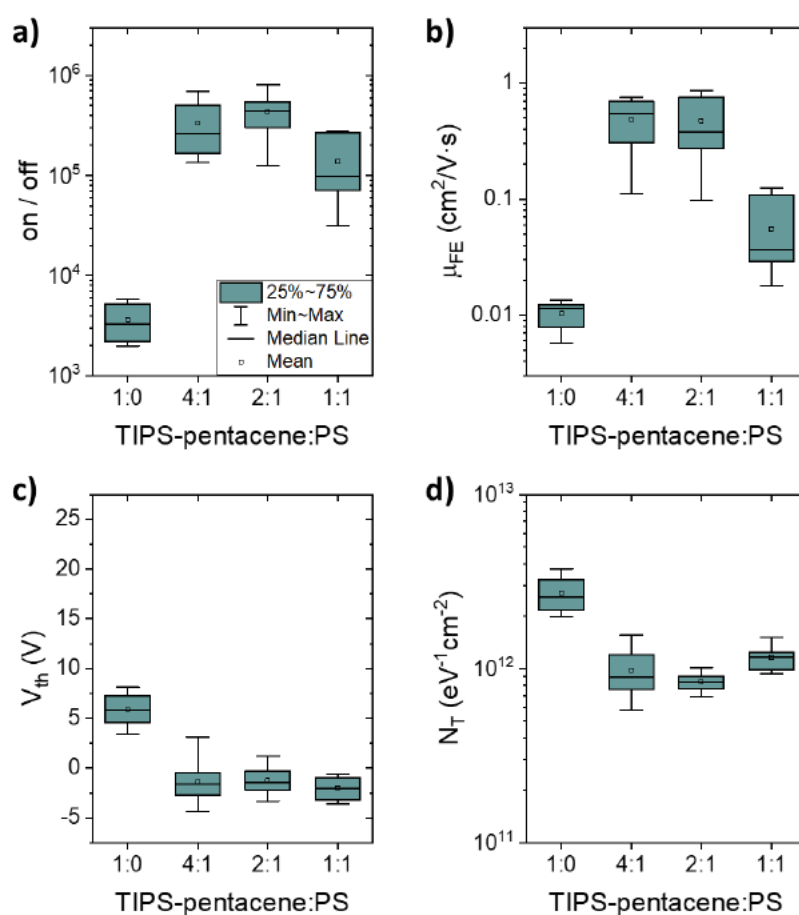


**Figure 6.13.** Box-plot statistics for the main OFET parameters, (a) on/off ratio, (b) field-effect mobility, (c) threshold voltage and (d) hole trap density, obtained from 10 devices of each TIPS-pentacene:PS blend ratio (1:0, 4:1, 2:1 and 1:1). For each data set, the box includes all the data between the first and the third quartile (25-75%), the line inside each box is the second quartile or median, the square represents the mean value and the extremes are the maxima and minima data found.

The response to X-rays was tested for all the TIPS-pentacene:PS blends, 1:0, 4:1, 2:1 and 1:1, biasing the OFET devices in saturation regime ( $V_{SD} = -20$  V and  $V_{SG} = -15$  V), as in the previous sections. The estimated sensitivity values, which are collected in **Figure 6.14 (a)** for all formulations, are higher for PS-containing devices, especially for 4:1 and 2:1 blends. Remarkably, an outstanding X-ray sensitivity as high as  $54 \mu\text{C}/\text{Gy}$  was obtained for the 4:1 TIPS-pentacene:PS device, which yields to  $1.3 \cdot 10^4 \mu\text{C}/\text{Gy}\cdot\text{cm}^2$  when normalised to the pixel area. This is the highest value reported for organic thin-film X-ray detectors, highly surpassing by three orders of magnitude that exhibited by TIPGe-pentacene transistor devices ( $18 \mu\text{C}/\text{Gy}\cdot\text{cm}^2$ ).<sup>24</sup> Moreover, a typical parameter employed for organic X-ray detectors is the sensitivity per unit of active volume, setting the focus on the material property rather than on the detector performance. The value achieved in this case,  $3.2 \cdot 10^9 \mu\text{C}/\text{Gy}\cdot\text{cm}^3$ , is exceptionally high because of the low thickness of the active layer (40 nm), significantly outperforming again the previously top reported value,  $9 \cdot 10^5 \mu\text{C}/\text{Gy}\cdot\text{cm}^3$ .<sup>24</sup> In order to better compare the herein presented results with the top sensitivity values recently reported in the literature for X-ray detectors based on inorganic,<sup>7</sup> hybrid organic/inorganic,<sup>20,21</sup> organic,<sup>16,24</sup> and perovskite active layers<sup>39</sup>, a summary is presented in **Table 6.3**. Here, sensitivity per unit area ( $S_A$ ) and per unit volume ( $S_V$ ) have been calculated employing the device information reported in the referenced papers and expressed in the same units of measurement. Among the hybrid organic/inorganic devices, a value of  $1.7 \cdot 10^6 \mu\text{C}/\text{Gy}\cdot\text{cm}^3$  was reported for a vertical diode architecture consisting of an organic bulk heterojunction (P3HT:PC<sub>70</sub>BM) with embedded Bi<sub>2</sub>O<sub>3</sub> nanoparticles (NPs).<sup>20</sup> However, such a high value was achieved employing thicknesses around 10-30  $\mu\text{m}$ , which is three orders of magnitude thicker than the active layers employed in this work. In fact, the photoconductive gain mechanism and the transport/collection of the photogenerated charges are so efficient in the TIPS-pentacene:PS blended devices that the X-ray sensitivity values are comparable with that of direct detectors based on 830  $\mu\text{m}$  thick polycrystalline perovskite devices ( $1.1 \cdot 10^4 \mu\text{C}/\text{Gy}\cdot\text{cm}^2$ ).<sup>39</sup> Furthermore, the achieved sensitivity is about three and two orders of magnitude higher than the reference value for a-Se ( $30 \mu\text{C}/\text{Gy}\cdot\text{cm}^2$ ) and poly-CZT ( $300 \mu\text{C}/\text{Gy}\cdot\text{cm}^2$ ) X-ray detectors, respectively, i.e., the inorganic semiconductor materials presently used for large-area direct radiation detectors.<sup>7</sup>

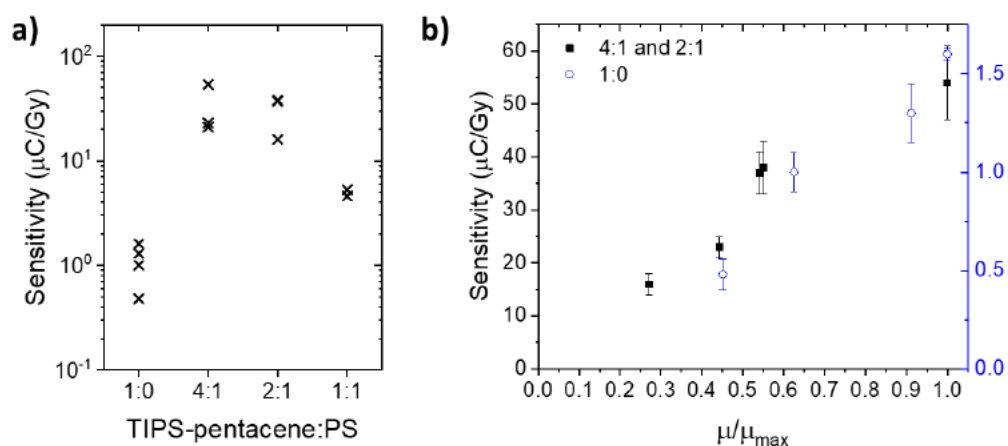


**Figure 6.14.** (a) X-ray sensitivity of 1:0, 4:1, 2:1 and 1:1 TIPS-pentacene:PS devices. (b) Sensitivity versus normalised mobility, for 4:1 and 2:1 TIPS-pentacene:PS devices (in black, left axis) and 1:0 devices (in blue, right axis).

**Table 6.3.** Comparison between state-of-the-art sensitivities values normalised per unit area and per unit volume and those reported in this work. \*Values extracted employing the device information reported in the referenced papers.

Active layer material	$S_A$ ( $\mu\text{C}/\text{Gy}\cdot\text{cm}^2$ )	$S_V$ ( $\mu\text{C}/\text{Gy}\cdot\text{cm}^3$ )	Ref.
Stabilised a-Se	30		(7)
poly-CZT	300		(7)
P3HT:PC <sub>70</sub> BM + NP-Bi <sub>2</sub> O <sub>3</sub>	$3.9 \cdot 10^3$ *	$1.7 \cdot 10^6$	(20)
P3HT:PC <sub>70</sub> BM + NP-Bi <sub>2</sub> O <sub>3</sub>	$2.8 \cdot 10^3$ *	$1.6 \cdot 10^5$	(21)
Organometallic perovskite (MAPbI <sub>3</sub> )	$1.1 \cdot 10^4$	$1.3 \cdot 10^4$ *	(39)
TIPS-pentacene	4.8 *	$4.8 \cdot 10^5$ *	(16)
TIPGe-pentacene	18 *	$9 \cdot 10^5$	(24)
TIPS-pentacene:PS	$1.3 \cdot 10^4$	$3.2 \cdot 10^9$	This work

Noteworthy, the observed trend of X-ray sensitivity versus TIPS-pentacene:PS ratio (Figure 6.14 (a)) is very similar to the one shown by the OFET mobility (Figure 6.13 (b)). In order to assess if both device parameters are correlated, the X-ray sensitivity has been plotted in Figure 6.14 (b) as a function of the mobility normalised to its maximum value. In this plot, devices based on only TIPS-pentacene (1:0) are shown in blue, while the



devices based on the 4:1 and 2:1 blends have been grouped (in black) considering the similar morphological features they presented in their corresponding thin films. In this way, it can be appreciated that for a given thin-film morphology, sensitivity is strongly dependant on device mobility. This is a very relevant result, since it indicates that improving the electrical performance of the transistors (i.e., the transport properties of the semiconducting layer) allows to optimise the devices for the detection of X-ray radiation. In this case this is achieved by adding PS to the formulation and controlling the TIPS-pentacene:PS blend ratio.

At this point, it is worth noting that the fact that PS-containing devices reveal high X-ray sensitivity implies that the electron traps responsible for the photoconductive gain (or at least the majority of them) are not affected by the addition of the polymer. This further supports the previous results correlating the presence of active electron traps with grain boundaries. All in all, tuning either the thin-film morphology and/or the OFET mobility have proven to be two independent and excellent strategies to enhance X-ray sensitivity.

## 6.5 RELIABILITY AND STABILITY: TOWARDS REAL X-RAY SENSORS

---

Up to now the focus has been set on obtaining high X-ray sensitivities, which has been achieved by tuning the morphology and the electrical performance of TIPS-pentacene:PS devices. However, if organic thin films are to be applied in direct X-ray detectors, the reliability and stability of the devices response must be also considered. This matter will be addressed herein by studying their shelf-stability and limit of detection, as well as by realising an X-ray sensor based on a Wheatstone bridge geometry.

### Shelf-stability

The stability in time of devices based on the best performing blends, 4:1 and 2:1, was investigated by monitoring the performance of the detectors for up to 80 days. It should be noted that during this period the devices were stored and measured under dark and ambient conditions. In **Figure 6.15 (a)** the evolution of the X-ray sensitivity and the field-effect mobility, normalised to the initial value, are depicted. For both blends, a decrease in the X-ray response of around 30-40% was observed after more than 2 months from fabrication, as well as a device mobility drop of 45% on average. These changes in the OFET performance are often attributed in the literature to degradation due to ambient humidity, an issue that is usually avoided by depositing an encapsulation layer on top of the organic film.<sup>40,41</sup> Although this additional processing step was not performed for the here reported devices, TIPS-pentacene:PS OFETs show a more stable behaviour than those based on TIPS-pentacene only (1:0), which are strongly doped and exhibit a fast increase of device mobility after a few days from fabrication, as shown in **Figure 6.15 (b)**. These results point out that the addition of PS provides the organic semiconductor thin films with an enhanced stability, making TIPS-pentacene:PS blended films an excellent material platform for the fabrication of long-lasting sensor devices.

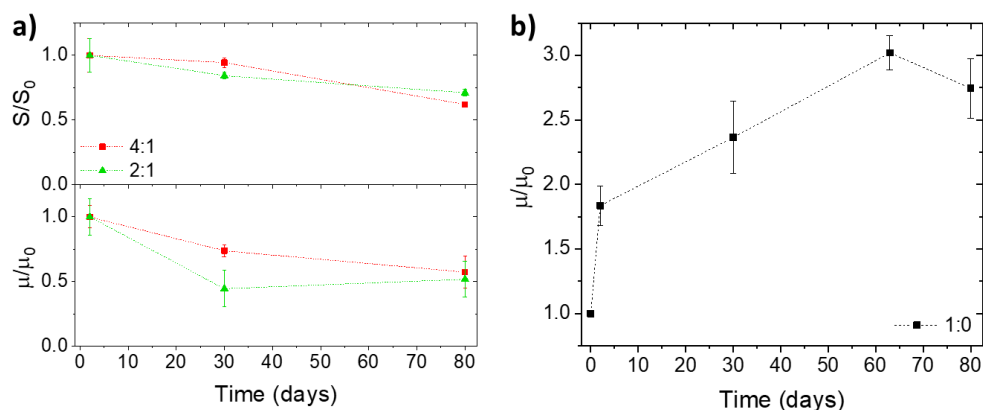


**Figure 6.15.** Evolution over time up to 80 days of (a) X-ray sensitivity (up) and field-effect mobility (down) of 4:1 and 2:1 TIPS-pentacene:PS devices and (b) field-effect mobility of 1:0 devices. Values have been normalised to the initial values.

### Limit of detection

The possibility to detect very low radiation doses is a very appealing characteristic for medical applications, where the intensity of the delivered radiation should be as low as possible. Thus, the minimum detectable dose rate is a fundamental figure of merit that allows to fully characterise the performance of X-ray detectors. The photocurrent response of a device based on the 4:1 TIPS-pentacene:PS blend, the formulation that exhibited the highest X-ray sensitivity, was evaluated employing very low dose rates. To do so, a system of aluminium filters was built to attenuate the dose rate provided by the X-ray tube, allowing to reach values as low as a few  $\mu\text{Gy/s}$ . Also, in order to minimise noise and light-induced photogenerated charges, the sample was kept in dark in a metal Faraday cage for a long period of time (2 months), which ensured a stable electrical behaviour. In addition, the device was biased at a source-gate voltage of 0 V to decrease the dark current. Measurements performed in these conditions are shown in **Figure 6.16 (a)**, where the photocurrent generated by the irradiation of the sample at several dose rates is reported. The obtained results show that the devices are capable to detect dose rates as low as  $35 \mu\text{Gy/s}$ . Even employing such low doses, a current signal in the order of pA can be detected in a time scale around 500 ms, i.e., the response can be reasonably measured and in a short time.

Furthermore, by plotting the photocurrent response versus the applied dose rate, as shown in **Figure 6.16 (b)**, it can be observed that they are no longer linearly dependent when considering a wide dose rate range (0.035–4.3 mGy/s, i.e., two orders of magnitude). This behaviour is in accordance with the photoconductive gain model (see fitted red line) and previously reported results that showed the highest sensitivity values when employing long exposure times and low dose rates.<sup>15,16</sup> This implies that, by decreasing

the dose of radiation it is possible to operate the detector in the most sensitive range. In particular, in the steepest region of the curve a sensitivity as high as  $134 \pm 7$  nC/Gy ( $32 \pm 2$   $\mu\text{C}/\text{Gy}\cdot\text{cm}^2$ ) was calculated.

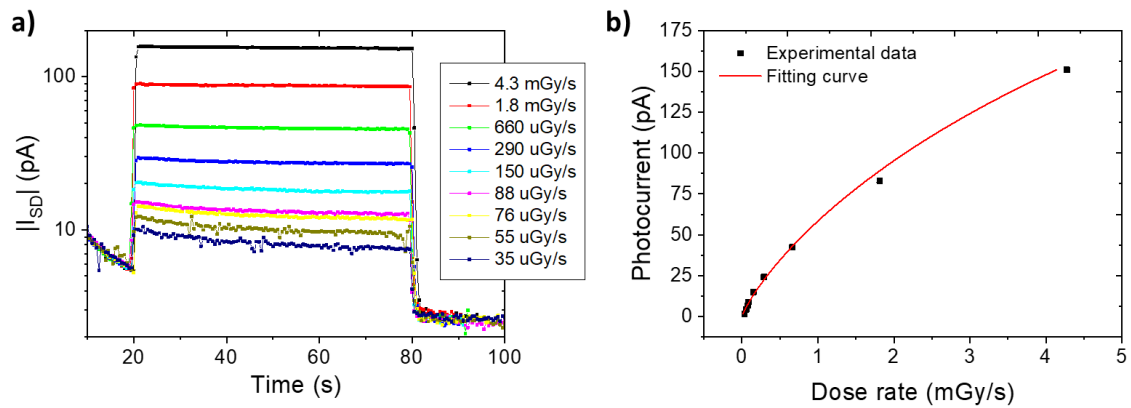


**Figure 6.16.** (a) X-ray induced photocurrent response of a TIPS-pentacene:PS 4:1 device at several dose rates, down to  $35$   $\mu\text{Gy}/\text{s}$ . (b) X-ray induced photocurrent versus dose rate, including the fitting curve resulting from theoretical calculations.

### Wheatstone bridge

The excellent X-ray sensing capability exhibited by TIPS-pentacene:PS based devices encouraged us to develop a more reliable sensor with minimised dark current (i.e., the signal measured without exposure to X-rays), a highly desirable feature for radiation detectors. To do so, a 4-pixel detector based on a Wheatstone bridge geometry was implemented.

The circuit in **Figure 6.17 (a)** shows the connections and components of a Wheatstone bridge architecture,<sup>42</sup> which consists of 4 resistors ( $R_1$ ,  $R_2$ ,  $R_3$  and  $R_4$ ) arranged in two branches ( $ACB$  and  $ADB$ ) biased by a common  $V_{AB}$  potential. This device architecture was originally conceived to measure unknown resistance values but, since it allows to detect small changes in resistance, it is also typically used in resistive sensor systems. The working principle of this circuit is based on the equivalence of the four resistances. If the bridge is balanced (i.e., the four resistances are equal,  $R_1 = R_2 = R_3 = R_4 = R$ ) the current flowing in both branches is the same and the voltage difference between nodes C and D is  $V_{out} = 0$  V. If the bridge is unbalanced, the electrical current flowing in these two branches is different and  $V_{out} \neq 0$  V. Therefore, by measuring  $V_{out}$  it is possible to employ the Wheatstone bridge architecture as a detector sensitive to external stimuli able to modify the resistance of at least one of the resistors of the system. In particular, if two opposite resistors are modified, for example  $R_1 = R_4 = R + \Delta R$ , the output signal is given by:

$$V_{out} = -V_{AB} \cdot \frac{\Delta R}{2R + \Delta R} \quad (6.1)$$

Considering all these features of the Wheatstone bridge architecture, achieving resistors with similar electrical behaviour is mandatory in the development of new organic detectors; hence, it is crucial to employ processing techniques able to deposit uniform thin films over large areas. In the work presented herein, uniformity is granted by using BAMS to deposit the organic semiconducting layer based on the 4:1 TIPS-pentacene:PS blend. Thus, a Wheatstone bridge consisting of four OFETs that operate as resistors was realised employing the layout depicted in **Figure 6.17 (b)**. As it has been previously shown, when X-ray photons impact onto the organic layer, the photogenerated charges induce an increase in the measured current, that is, the OFET channel resistance decreases ( $\Delta R < 0$ ). Thus, by exposing to X-rays devices  $R_1$  and  $R_4$  the bridge state is switched from the balanced to the unbalanced state, causing a change in the registered output voltage. Devices were biased employing  $V_{AB} = -20$  V and  $V_{SG} = -5$  V, and the  $\Delta V_{out}$  signal was recorded upon exposure to X-rays with various dose rates, as shown in **Figure 6.17 (c)**. Remarkably, a very stable and constant dark current was obtained. Moreover, as it can be observed in **Figure 6.17 (d)**, the Wheatstone bridge response to increasing dose rates is linear, as previously observed for single OFET detectors. This result points out the potential of organic devices for the realisation of real direct detectors for X-ray radiation.

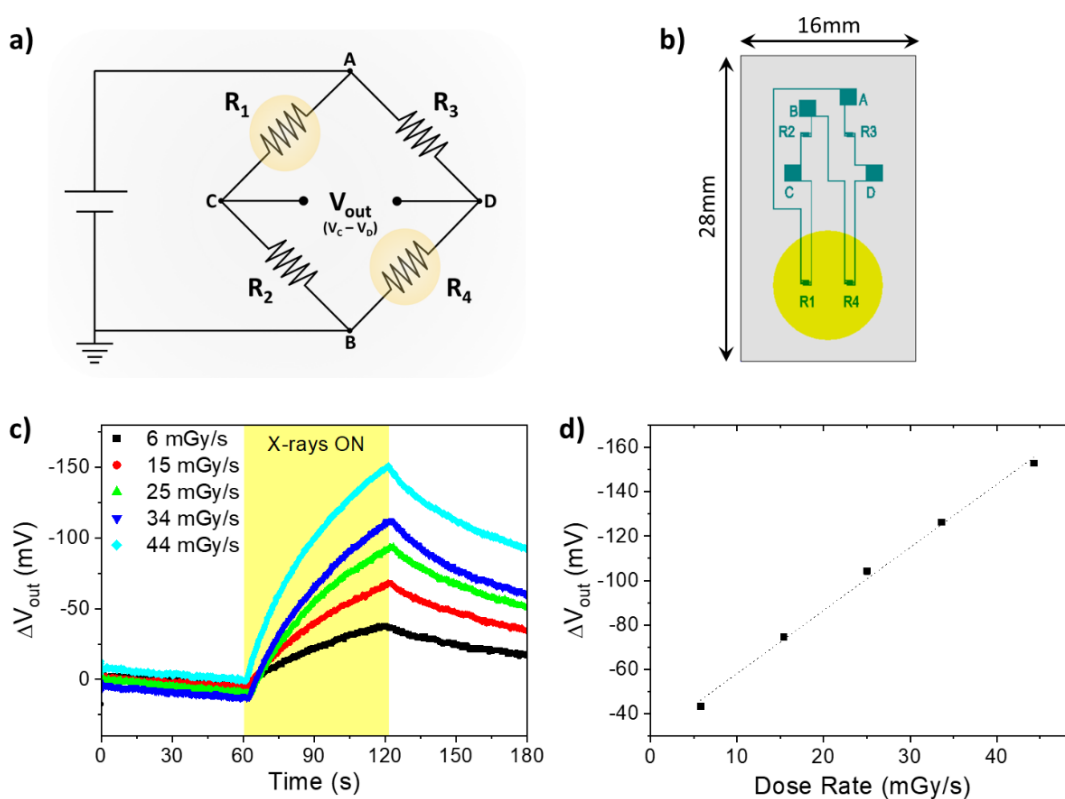


**Figure 6.17.** (a) Wheatstone bridge circuit. (b) Schematic representation of the layout designed for the fabrication of the devices. (c)  $\Delta V_{out}$  generated by different dose rates and applying  $V_{AB} = -20$  V and  $V_{SG} = -5$  V. (d)  $\Delta V_{out}$  linear dependency with dose rate.

## 6.6 SUMMARY

---

In summary, TIPS-pentacene based OFETs processed by bar-assisted meniscus shearing have been exploited as direct X-ray detectors. Interestingly, tuning the active layer's morphology and the OFETs mobility by controlling the processing parameters have proven to be excellent strategies to enhance the X-ray sensitivity of such devices. On one side, employing a higher coating speed allowed obtaining thin films with smaller grain size (or an increased density of grain boundaries), resulting in an improved X-ray sensitivity as an enhancement of the electron trap density within the organic material was achieved. On the other side, by adding polystyrene to the TIPS-pentacene solution and controlling the blending ratio, the hole trap density at the semiconductor/dielectric interface was reduced and OFETs exhibited a higher charge carrier mobility, resulting in an enhanced device X-ray sensitivity.

Importantly, these results help to understand the origin of the physical processes and parameters governing the photoconductive gain effect, correlating the devices sensing capability with the morphological and transport properties of the organic semiconductor layer. Moreover, by controlling both factors, an outstanding sensitivity of  $1.3 \cdot 10^4 \mu\text{C}/\text{Gy}\cdot\text{cm}^2$  was achieved, which is a record value among organic thin-film X-ray detectors and competitive with the inorganic materials currently used to fabricate large-area detectors (such as a-Se and poly-CZT).

Finally, the stability, reliability and limit of detection, of the optimised TIPS-pentacene:PS devices were tested, as they are relevant features for the implementation of organic X-ray detectors in real-life applications. The shelf-stability of the devices was improved by the addition of PS, which helps to protect the organic semiconductor from degradation due to ambient humidity; however, it is realised that degradation could be further prevented by depositing an encapsulation layer on top of the organic layer. Also, a very low minimum detectable dose rate of  $35 \mu\text{Gy}/\text{s}$  was obtained, resulting in a signal in the order of pA that can be detected in a short time ( $\sim 500$  ms). Last, thanks to the high uniformity provided by the BAMS deposition technique, a proof-of-concept X-ray sensor based on a Wheatstone bridge geometry was implemented, obtaining a very reliable sensor with a stable and low dark current, a highly desirable feature for radiation detectors.

6.7 REFERENCES

---

- (1) Chung, F. H.; Smith, D. K. *Industrial Applications of X-Ray Diffraction*; CRC press, 1999.
- (2) Fraboni, B.; Fraleoni-Morgera, A.; Zaitseva, N. Ionizing Radiation Detectors Based on Solution-Grown Organic Single Crystals. *Adv. Funct. Mater.* **2016**, *26*, 2276–2291.
- (3) Zygmanski, P.; Abkai, C.; Han, Z.; Shulevich, Y.; Menichelli, D.; Hesser, J. Low-cost Flexible Thin-film Detector for Medical Dosimetry Applications. *J. Appl. Clin. Med. Phys.* **2014**, *15*, 311–326.
- (4) Kasap, S. O. X-Ray Sensitivity of Photoconductors: Application to Stabilized a-Se. *J. Phys. D. Appl. Phys.* **2000**, *33*, 2853–2865.
- (5) Kasap, S.; Frey, J. B.; Belev, G.; Tousignant, O.; Mani, H.; Greenspan, J.; Laperriere, L.; Bubon, O.; Reznik, A.; DeCrescenzo, G.; et al. Amorphous and Polycrystalline Photoconductors for Direct Conversion Flat Panel X-Ray Image Sensors. *Sensors* **2011**, *11*, 5112–5157.
- (6) Owens, A.; Peacock, A. Compound Semiconductor Radiation Detectors. *Nucl. Instruments Methods Phys. Res. Sect. A Accel. Spectrometers, Detect. Assoc. Equip.* **2004**, *531*, 18–37.
- (7) Kabir, M. Z.; Kasap, S. Photoconductors for X-Ray Image Detectors. In *Springer Handbook of Electronic and Photonic Materials*; Kasap, S., Capper, P., Eds.; Springer International Publishing, 2017.
- (8) Kallmann, H. Scintillation Counting with Solutions. *Phys. Rev.* **1950**, *78*, 621–622.
- (9) Brooks, F. D. Development of Organic Scintillators. *Nucl. Instruments Methods* **1979**, *162*, 477–505.
- (10) Yoshino, K.; Hayashi, S.; Inuishi, Y. Effects of Electron Irradiation on Electrical Conductivity of Polyacetylene. *Jpn. J. Appl. Phys.* **1982**, *21*, L569–L570.
- (11) Newman, C. R.; Siringhaus, H.; Blakesley, J. C.; Speller, R. Stability of Polymeric Thin Film Transistors for X-Ray Imaging Applications. *Appl. Phys. Lett.* **2007**, *91*, 142105.
- (12) Boroumand, F. A.; Zhu, M.; Dalton, A. B.; Keddie, J. L.; Sellin, P. J.; Gutierrez, J. J. Direct X-Ray Detection with Conjugated Polymer Devices. *Appl. Phys. Lett.* **2007**, *91*, 033509.
- (13) Fraboni, B.; Ciavatti, A.; Merlo, F.; Pasquini, L.; Cavallini, A.; Quaranta, A.; Bonfiglio, A.; Fraleoni-Morgera, A. Organic Semiconducting Single Crystals as next Generation

- of Low-Cost, Room-Temperature Electrical X-Ray Detectors. *Adv. Mater.* **2012**, *24*, 2289–2293.
- (14) Ciavatti, A.; Capria, E.; Fraleoni-Morgera, A.; Tromba, G.; Dreossi, D.; Sellin, P. J.; Cosseddu, P.; Bonfiglio, A.; Fraboni, B. Toward Low-Voltage and Bendable X-Ray Direct Detectors Based on Organic Semiconducting Single Crystals. *Adv. Mater.* **2015**, *27*, 7213–7220.
- (15) Basiricò, L.; Ciavatti, A.; Cramer, T.; Cosseddu, P.; Bonfiglio, A.; Fraboni, B. Direct X-Ray Photoconversion in Flexible Organic Thin Film Devices Operated below 1 V. *Nat. Commun.* **2016**, *7*, 13063.
- (16) Lai, S.; Cosseddu, P.; Basiricò, L.; Ciavatti, A.; Fraboni, B.; Bonfiglio, A. A Highly Sensitive, Direct X-Ray Detector Based on a Low-Voltage Organic Field-Effect Transistor. *Adv. Electron. Mater.* **2017**, *3*, 1600409.
- (17) Intaniwet, A.; Keddie, J. L.; Shkunov, M.; Sellin, P. J. High Charge-Carrier Mobilities in Blends of Poly(Triarylamine) and TIPS-Pentacene Leading to Better Performing X-Ray Sensors. *Org. Electron.* **2011**, *12*, 1903–1908.
- (18) Intaniwet, A.; Mills, C. A.; Shkunov, M.; Sellin, P. J.; Keddie, J. L. Heavy Metallic Oxide Nanoparticles for Enhanced Sensitivity in Semiconducting Polymer X-Ray Detectors. *Nanotechnology* **2012**, *23*, 235502.
- (19) Ciavatti, A.; Cramer, T.; Carroli, M.; Basiricò, L.; Fuhrer, R.; De Leeuw, D. M.; Fraboni, B. Dynamics of Direct X-Ray Detection Processes in High-Z Bi<sub>2</sub>O<sub>3</sub> Nanoparticles-Loaded PFO Polymer-Based Diodes. *Appl. Phys. Lett.* **2017**, *111*, 183301.
- (20) Thirimanne, H. M.; Jayawardena, K. D. G. I.; Parnell, A. J.; Bandara, R. M. I.; Karalasingam, A.; Pani, S.; Huerdler, J. E.; Lidzey, D. G.; Tedde, S. F.; Nisbet, A.; et al. High Sensitivity Organic Inorganic Hybrid X-Ray Detectors with Direct Transduction and Broadband Response. *Nat. Commun.* **2018**, *9*, 2926.
- (21) Jayawardena, K. D. G. I.; Thirimanne, H. M.; Tedde, S. F.; Huerdler, J. E.; Parnell, A. J.; Bandara, R. M. I.; Mills, C. A.; Silva, S. R. P. Millimeter-Scale Unipolar Transport in High Sensitivity Organic-Inorganic Semiconductor X-Ray Detectors. *ACS Nano* **2019**, *13*, 6973–6981.
- (22) Ankah, G. N.; Büchele, P.; Poulsen, K.; Rauch, T.; Tedde, S. F.; Gimmler, C.; Schmidt, O.; Kraus, T. PbS Quantum Dot Based Hybrid-Organic Photodetectors for X-Ray Sensing. *Org. Electron.* **2016**, *33*, 201–206.
- (23) Han, H.; Lee, S.; Seo, J.; Mahata, C.; Cho, S.; Han, A.-R.; Hong, K.-S.; Park, J.-H.; Soh, M.-J.; Park, C.; et al. Enhancement of X-Ray Detection by Single-Walled Carbon Nanotube Enriched Flexible Polymer Composite. *Nanoscale Res. Lett.* **2014**, *9*, 610.
- (24) Ciavatti, A.; Basiricò, L.; Fratelli, I.; Lai, S.; Cosseddu, P.; Bonfiglio, A.; Anthony, J. E.;



- Fraboni, B. Boosting Direct X-Ray Detection in Organic Thin Films by Small Molecules Tailoring. *Adv. Funct. Mater.* **2019**, *29*, 1806119.
- (25) Diao, Y.; Shaw, L.; Mannsfeld, S. C. B. Morphology Control Strategies for Solution-Processed Organic Semiconductor Thin Films. *Energy Environ. Sci.* **2014**, *7*, 2145–2159.
- (26) Riera-Galindo, S.; Tamayo, A.; Mas-Torrent, M. Role of Polymorphism and Thin-Film Morphology in Organic Semiconductors Processed by Solution Shearing. *ACS Omega* **2018**, *3*, 2329–2339.
- (27) del Pozo, F. G.; Fabiano, S.; Pfattner, R.; Georgakopoulos, S.; Galindo, S.; Liu, X.; Braun, S.; Fahlman, M.; Veciana, J.; Rovira, C.; et al. Single Crystal-Like Performance in Solution-Coated Thin-Film Organic Field-Effect Transistors. *Adv. Funct. Mater.* **2016**, *26*, 2379–2386.
- (28) Temiño, I.; Del Pozo, F. G.; Ajayakumar, M. R.; Galindo, S.; Puigdollers, J.; Mas-Torrent, M. A Rapid, Low-Cost, and Scalable Technique for Printing State-of-the-Art Organic Field-Effect Transistors. *Adv. Mater. Technol.* **2016**, *1*, 1600090.
- (29) Galindo, S.; Tamayo, A.; Leonardi, F.; Mas-Torrent, M. Control of Polymorphism and Morphology in Solution Sheared Organic Field-Effect Transistors. *Adv. Funct. Mater.* **2017**, *27*, 1700526.
- (30) Lai, S.; Temiño, I.; Cramer, T.; del Pozo, F. G.; Fraboni, B.; Cosseddu, P.; Bonfiglio, A.; Mas-Torrent, M. Morphology Influence on the Mechanical Stress Response in Bendable Organic Field-Effect Transistors with Solution-Processed Semiconductors. *Adv. Electron. Mater.* **2018**, *4*, 1700271.
- (31) Hamilton, R.; Smith, J.; Ogier, S.; Heeney, M.; Anthony, J. E.; McCulloch, I.; Veres, J.; Bradley, D. D. C.; Anthopoulos, T. D. High-Performance Polymer-Small Molecule Blend Organic Transistors. *Adv. Mater.* **2009**, *21*, 1166–1171.
- (32) Lee, W. H.; Lim, J. A.; Kwak, D.; Cho, J. H.; Lee, H. S.; Choi, H. H.; Cho, K. Semiconductor-Dielectric Blends: A Facile All Solution Route to Flexible All-Organic Transistors. *Adv. Mater.* **2009**, *21*, 4243–4248.
- (33) Riera-Galindo, S.; Leonardi, F.; Pfattner, R.; Mas-Torrent, M. Organic Semiconductor/Polymer Blend Films for Organic Field-Effect Transistors. *Adv. Mater. Technol.* **2019**, 1900104.
- (34) Giri, G.; Verploegen, E.; Mannsfeld, S. C. B.; Atahan-Evrenk, S.; Kim, D. H.; Lee, S. Y.; Becerril, H. a.; Aspuru-Guzik, A.; Toney, M. F.; Bao, Z. Tuning Charge Transport in Solution-Sheared Organic Semiconductors Using Lattice Strain. *Nature* **2011**, *480*, 504–508.
- (35) Mannsfeld, S. C. B.; Tang, M. L.; Bao, Z. Thin Film Structure of

- Triisopropylsilylethynyl-Functionalized Pentacene and Tetraceno[2,3-b]Thiophene from Grazing Incidence X-Ray Diffraction. *Adv. Mater.* **2011**, *23*, 127–131.
- (36) Zhao, K.; Wodo, O.; Ren, D.; Khan, H. U.; Niazi, M. R.; Hu, H.; Abdelsamie, M.; Li, R.; Li, E. Q.; Yu, L.; et al. Vertical Phase Separation in Small Molecule:Polymer Blend Organic Thin Film Transistors Can Be Dynamically Controlled. *Adv. Funct. Mater.* **2016**, *26*, 1737–1746.
- (37) Yuan, Y.; Giri, G.; Ayzner, A. L.; Zoombelt, A. P.; Mannsfeld, S. C. B.; Chen, J.; Nordlund, D.; Toney, M. F.; Huang, J.; Bao, Z. Ultra-High Mobility Transparent Organic Thin Film Transistors Grown by an off-Centre Spin-Coating Method. *Nat. Commun.* **2014**, *5*, 3005.
- (38) Pérez-Rodríguez, A.; Temiño, I.; Ocal, C.; Mas-Torrent, M.; Barrena, E. Decoding the Vertical Phase Separation and Its Impact on C8-BTBT/PS Transistor Properties. *ACS Appl. Mater. Interfaces* **2018**, *10*, 7296–7303.
- (39) Kim, Y. C.; Kim, K. H.; Son, D. Y.; Jeong, D. N.; Seo, J. Y.; Choi, Y. S.; Han, I. T.; Lee, S. Y.; Park, N. G. Printable Organometallic Perovskite Enables Large-Area, Low-Dose X-Ray Imaging. *Nature* **2017**, *550*, 87–91.
- (40) De Angelis, F.; Cipolloni, S.; Mariucci, L.; Fortunato, G. Aging Effects in Pentacene Thin-Film Transistors: Analysis of the Density of States Modification. *Appl. Phys. Lett.* **2006**, *88*, 193508.
- (41) Kim, S. H.; Yoon, W. M.; Jang, M.; Yang, H.; Park, J. J.; Park, C. E. Damage-Free Hybrid Encapsulation of Organic Field-Effect Transistors to Reduce Environmental Instability. *J. Mater. Chem.* **2012**, *22*, 7731–7738.
- (42) Hoffmann, K. *Applying the Wheatstone Bridge Circuit*; HBM Germany, 1974.



## CHAPTER 7

# Materials and experimental methods

---

### 7.1 MATERIALS

---

#### Organic semiconductors

**6,13-bis(triisopropylsilylethynyl)pentacene (TIPS-pentacene)** was purchased from Ossila and was used without any further purification.

**2,8-difluoro-5,11-bis(triethylsilylethynyl)anthradithiophene (diF-TES-ADT)** was purchased from Lumtec and was used without any further purification.

**2,7-dioctyl[1]benzothieno[3,2-b][1]benzothiophene (C8-BTBT)** was purchased from Sigma Aldrich and was used without any further purification.

**Dithiophenetetrathiafulvalene (DT-TTF)** was synthesised in our group by Dr. Ajayakumar M. Rathamony following the previously described procedure.<sup>1</sup>

#### Insulating polymers

**Polystyrene (PS)** with molecular weight of 1 kg/mol (PS1k), 10 kg/mol (PS10k) and 100 kg/mol (PS100k), were purchased from Sigma Aldrich and were used without any further purification.

#### Solvents

**Anhydrous chlorobenzene (CB) and toluene (Tol)** were purchased from Sigma Aldrich.

**Acetone and isopropanol** (HPLC grade) were purchased from Teknocroma Analítica S.A.

### Molecules for self-assembled monolayers (SAMs)

**2,3,4,5,6-pentafluorobenzenethiol (PFBT)** was purchased from Sigma Aldrich.

### Materials for semiconductor doping

**2,3,5,6-tetrafluoro-7,7,8,8-tetracyanoquinodimethane (F4-TCNQ)** was purchased from TCI Europe and was used without any further purification.

**Molybdenum oxide (MoO<sub>3</sub>)** was purchased from Kurt J. Lesker.

**Iodine** was purchased from Sigma Aldrich.

### Substrates and materials for electrode fabrication

**Highly n-doped silicon wafers** were purchased from SiMat with the following characteristics: 200 nm SiO<sub>2</sub>; Diameter: 100 mm; Type/Dopant: N/Sb; Orientation: <100>; Resistivity: 0.05-0.02 Ω·cm; Thickness: 525 ± 25 μm; Front Surface: Polished; Back Surface: Etched; Flats: SEMI Standard.

**Shiplot Microposit S1813 positive photoresist** was purchased from Shiplot.

**Shiplot Microposit MF-319 developer** was purchased from Shiplot.

**Gold and chromium** for metal evaporation were 99.99 % pure and were purchased from Kurt J. Lesker.

**Shadow masks E201 and E292 and evaporation stacks E191 and E281**, used to deposit top-contact electrodes, were purchased from Ossila. The stacks hold up to 12 substrates of an approximate size of 20 by 15 mm. The E201 mask gives six transistors per substrate, with channel length (*L*) of 30, 40, 50, 60, 80 and 100 μm and a constant width (*W*) of 4 mm. The E292 mask gives five transistors per substrate, with channel length (*L*) of 30, 40, 50, 60 and 80 μm and a constant width (*W*) of 1 mm.

**Flexible substrates** consisting on 175 μm thick polyethylene terephthalate (PET) were purchased from Goodfellow.

**Parylene C** employed as dielectric for flexible devices was purchased from Specialty Coating Systems.

## 7.2 OFET FABRICATION

---

### Bottom-contact Si/SiO<sub>2</sub> substrates

Source and drain interdigitated gold electrodes for bottom-gate bottom-contact (BGBC) configuration devices were fabricated on the aforementioned Si/SiO<sub>2</sub> wafers by photolithography. The fabrication process was carried out in a clean room class 10.000. First, the desired electrode design was patterned using a Micro-writer from Durham Magneto Optics Ltd. Afterwards, chromium and gold metal layers were deposited by thermal evaporation at  $2 \cdot 10^{-6}$  mbar using an Evaporation System Auto 306 from Boc Edwards. The whole process consisted in the following steps:

1. A nitrogen flux was used to remove any traces of dust on the Si/SiO<sub>2</sub> wafer.
2. The photoresist Shipley Microposit S1813 was spin-coated at 5000 rpm for 25 s. Right after the deposition, the photoresist was baked by placing the wafer on a hotplate at 95 °C for 60 s.
3. For the writing process, the wafer was loaded in the Micro-writer and the desired pattern, previously designed by the software CleWin4, was charged into the system.
4. In order to develop all the exposed photoresist, the wafer was immersed in Shipley Microposit MF-319 developer for 1 minute. Then, the wafer was rinsed with ultrapure water to remove the remaining developer on the wafer and finally dried with a nitrogen gun.
5. Subsequently, the patterned wafer was placed inside the evaporator and the vacuum pumps were switched on. Once the pressure reached  $2 \cdot 10^{-6}$  mbar, first chromium (5 nm) and then gold (40 nm) were evaporated.
6. The wafer was cut into individual substrates with the help of a ruler and a diamond scribe. Afterwards, the lift-off was done by immersing and sonicating the substrates in acetone for 15 minutes, three times. Then, this process was repeated again in isopropanol.
7. Finally, the substrates were dried with a nitrogen gun and stored until used.

The dielectric thickness (200 nm SiO<sub>2</sub>) offers a capacitance per unit area of  $C = 17.3$  nF/cm<sup>2</sup>. Different channel widths ( $W$ ) and lengths ( $L$ ), as well as pattern designs, were used for the different works. Accordingly, different substrate sizes were employed depending on the application. However, an illustration of a substrate is presented in **Figure 7.1** as an example.

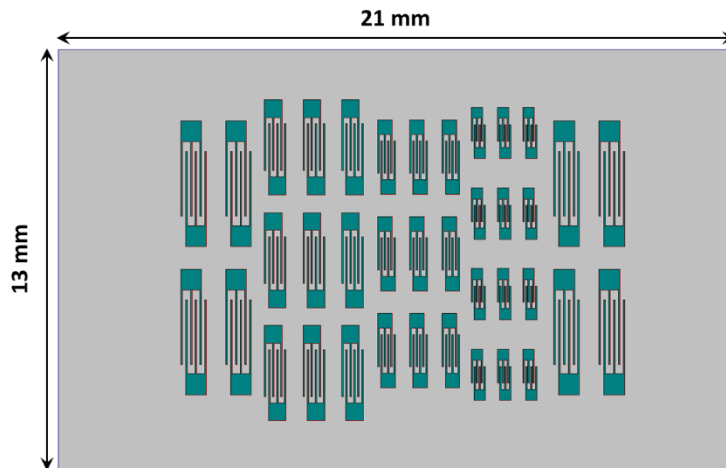


**Figure 7.1.** Example of a Si/SiO<sub>2</sub> substrate with differently sized interdigitated electrodes for bottom-gate bottom-contact transistor fabrication.

### Bottom-contact flexible substrates

Flexible substrates employed for the mechanical stress response study in Chapter 5 were fabricated by our collaborators from the University of Cagliari (Prof. Annalisa Bonfiglio) following the procedure developed in a previous work.<sup>2</sup> As shown in the vertical cross-section in **Figure 7.2 (a)**, the substrates consist on several stacked layers prepared according to the following steps:

1. PET substrates (6 × 2.5 cm, 175 μm thick) were cleaned with multiple rinsing of acetone, isopropanol, and deionised water, and dried with nitrogen.
2. An aluminium layer (nominal thickness of 100 nm) was then deposited by thermal evaporation (pressure: 5·10<sup>-5</sup> Torr). The shape of the gate was defined by means of photolithography.
3. After that, a nanosized aluminium oxide layer (nominal thickness of 8 nm) was grown on the gate by an annealing process, storing the substrate overnight at a temperature of 50 °C.
4. A Parylene C layer with a nominal thickness of 170 nm was deposited by means of chemical vapour deposition.
5. Afterwards, a photoresist was patterned onto the gate electrode using a self-alignment process.
6. A gold layer with a nominal thickness of 60-80 nm was thermally evaporated onto the substrate (pressure: 5·10<sup>-5</sup> Torr) using a shadow mask. The excess of gold, i.e., the part deposited onto the photoresist layer covering the channel, was removed by lift-off. Thus, source and drain electrodes were defined in the channel area with a minimum overlap between source/drain and the gate electrode.

The hybrid organic/inorganic dielectric layer (Parylene C/aluminium oxide) offers a capacitance per unit area of  $C = 18 \text{ nF/cm}^2$ . The channel width and length of the fabricated electrodes was  $W = 5 \text{ mm}$  and  $L = 30 \text{ }\mu\text{m}$ , respectively, as depicted in **Figure 7.2 (b)**.

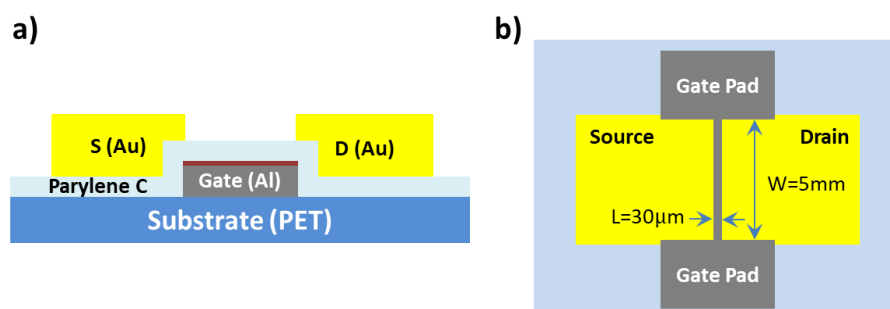


**Figure 7.2.** Scheme of the flexible substrates employed for bottom-gate bottom-contact transistor fabrication: (a) vertical cross-section and (b) top view.

### Top-contact electrodes fabrication

Top-contact gold electrodes were fabricated using the shadow masks and evaporation stacks purchased from Ossila. First, Si/SiO<sub>2</sub> wafers were cut into substrates of an approximate size of 20 by 15 mm. Once the substrates were coated with the semiconducting thin film, they were sandwiched between the shadow mask and the magnetic layer (see **Figure 7.3**). To deposit the gold source and drain electrodes, the whole stack was placed in the evaporation chamber and 20–40 nm of Au were deposited at a rate of 0.1–0.5 Å/s and a pressure of  $2 \cdot 10^{-6}$  mbar. Devices with channel lengths varying from 30 to 100 μm and a constant channel width of 1 or 4 mm were obtained.

In Chapters 2 and 3, the fabrication of gold top electrodes with an interlayer of MoO<sub>3</sub> was carried out. This evaporation was performed with the same shadow mask, but prior to the Au deposition a thin layer of 7 nm of MoO<sub>3</sub> was deposited at a rate of 0.1–0.2 Å/s. This process was carried out in an evaporation chamber equipped with two different available sources, so that it was not necessary to depressurise the system between the two evaporations. In Chapters 3 and 4, F4-TCNQ/Au contacts were deposited following the same procedure (an interlayer of 10 or 20 nm of F4-TCNQ was evaporated in this case).



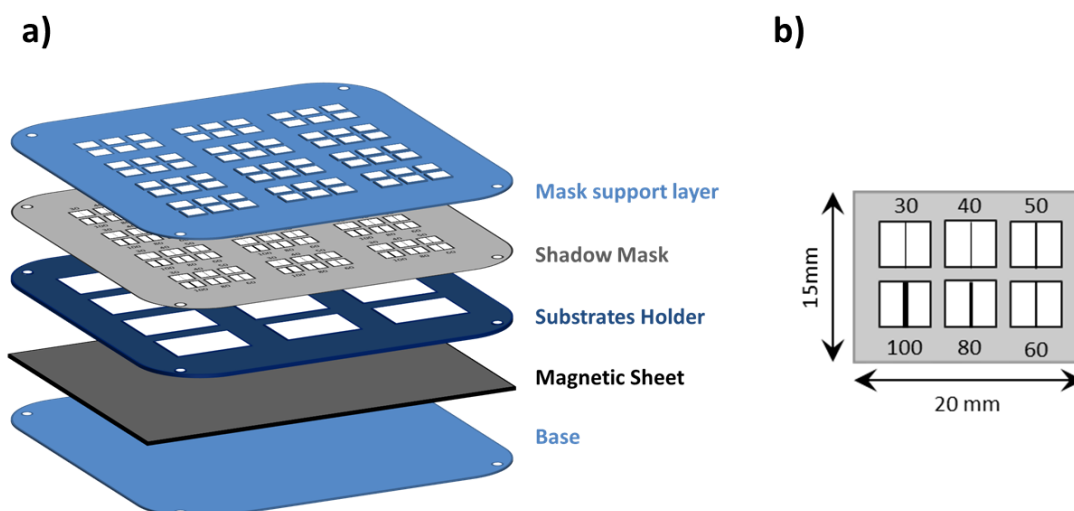


**Figure 7.3.** (a) Schematic illustration of all the layers of the evaporation stack for top-contact electrode deposition. (b) Closer look to the pattern given by the shadow mask E201 onto the area of one substrate. The numbers correspond to the channel length in  $\mu\text{m}$ . The channel width is 4 mm.

### Self-assembled monolayer formation

Self-assembled monolayers (SAMs) of PFBT were formed on the gold bottom contacts by immersion in a 15 mM solution of PFBT in isopropanol. The substrates were first cleaned and activated using an ultraviolet ozone treatment for 25 minutes, and then placed immediately into the prepared solution for 15 minutes. After that time, the substrates were removed from the solution and rinsed with pure isopropanol.

However, in the preparation of a PFBT SAM on gold contacts from flexible PET/Parylene C substrates (Chapter 5) the ultraviolet ozone treatment was not performed in order to avoid damaging the dielectric surface.

### Organic semiconductor ink formulation

The ink solutions based on blends of organic semiconductors (OSCs) and polystyrene used in Chapters 2 to 6, were prepared using a common methodology. Generally, the binding polymer and the OSC were separately dissolved in chlorobenzene (CB) employing the same concentration (2 wt%, which is equivalent to 22.6 mg/ml) and heating if necessary to totally dissolve them. Then, solutions were accurately mixed at the desired weight ratio using a micropipette.

When solutions without polystyrene were also prepared, usually the lack of viscosity made obtaining a uniform thin film more difficult. In these cases, the concentration was increased up to 4 wt%.

The dopant and OSC blend solutions employed in Chapter 4 were prepared adjusting the F4-TCNQ/C8-BTBT molar ratio (mols of F4-TCNQ/mols of C8-BTBT). To prepare such ink solutions, first C8-BTBT and polystyrene were mixed at a 4:1 weight ratio in a concentrated CB solution. Then, the necessary amount of F4-TCNQ dissolved in CB (1 mg/ml) was added according to the desired doping ratio, ranging between 1/100 and 5/100. Finally, additional CB was added to keep the C8-BTBT:PS concentration at a 2 wt%.

Solutions were always stored in darkness to protect the OSCs against the possible harmful effects of light. Also, amber vials were used for protection during use.

### Semiconducting film deposition

To deposit the semiconducting films bar-assisted meniscus shearing (BAMS) was used.<sup>3</sup> This technique was used both on substrates with bottom electrodes and on plain Si/SiO<sub>2</sub> substrates for subsequent top-contact evaporation. Typically, 20-40  $\mu$ l of the ink solution were placed in the gap between the metallic bar and the substrate, and immediately after that the bar (or the substrate) was sheared usually at a speed of 10 mm/s and at a temperature of 105 °C. The ink solutions were heated on the coating bed prior to the film deposition to ensure that the OSC was fully dissolved and thus avoid the formation of holes or bubbles caused by particles in suspension.

In the case of TIPS-pentacene devices fabricated on flexible PET/Parylene C substrates (Chapter 5), the standard stainless steel bar was changed for a polytetrafluoroethylene (PTFE or Teflon) bar to facilitate obtaining a crystalline film on the more hydrophobic Parylene C surface.

### 7.3 THIN-FILM CHARACTERISATION

---

**Optical microscopy and cross-polarised optical microscopy** images were obtained using an Olympus BX51 equipped with a light polariser and an analyser.

**Atomic force microscopy (AFM) images** were acquired in ambient conditions with three different measurement systems:

- AFM images in Chapter 2 and 4 were acquired in tapping mode using a 5100 SPM system from Agilent Technologies. Images were subsequently analysed using Gwyddion software.
- AFM measurements in Chapter 3 were carried out using a commercial head and control unit from Nanotec Electrónica S.L. The contact mode friction force microscopy (FFM) study was carried out using Si tips mounted in soft ( $k \approx 0.01\text{--}0.1 \text{ N m}^{-1}$ ) cantilevers from Veeco. Unless otherwise indicated, the load was always kept as low as possible (close to the pull-off force) during the FFM scanning. In Kelvin probe force microscopy (KPFM) measurements, contact potential difference (CPD) maps were obtained simultaneously with the topography in a single pass. For this, CrPt-coated Si tips in cantilevers with nominal  $k = 3 \text{ N m}^{-1}$  from BudgetSensors were used. In this study, data was analysed with the WSxM freeware.
- AFM images in Chapter 5 and 6 were acquired using a Park NX10 system with PPP-NCST-Au probes (Nanosensors) in non-contact mode. For the Kelvin probe force microscopy (KPFM) measurements in Chapter 5, height and surface potential images were acquired in parallel using a setup with two lock-in amplifiers. During the measurements, a bias was applied to transistor source, drain and gate contacts using a Keysight 2912B source measure unit. Grain size analysis in Chapter 6 was done applying adaptive scan-rate to slow down the scan speed at crystallite borders. Subsequent data analysis was carried out using Gwyddion software. In particular, setting a height threshold value a dedicated tool of this software can recognise different grains laying on the same thin film, thus enabling grain size estimation.

**Profilometry** measurements in Chapter 4 were carried out with a Dektak XT stylus profiler (Bruker).

**X-ray powder diffraction** measurements in Chapter 2 and 5 were performed using a PANalytical X'PERT MRD diffractometer, while a Siemens D-5000 diffractometer was used for measurements in Chapter 4 and 6.

**X-ray photoelectron spectroscopy (XPS)** was employed in Chapter 2 to analyse the chemical composition at the surface of OSC:PS blended thin films. Measurements were performed with a Phoibos 150 analyser (SPECS GmbH, Berlin, Germany) in ultra-high vacuum conditions (base pressure  $5 \cdot 10^{-10}$  mbar) with a monochromatic aluminium K $\alpha$  X-ray source (1486.74 eV). The energy resolution measured by the FWHM (full width at half maximum) of the Ag 3d $_{5/2}$  peak for a sputtered silver foil was 0.6 eV. The spot size was 3.5 mm by 0.5 mm.

**Time-of-flight secondary ions mass spectrometry (ToF-SIMS)** was used to determine the chemical compositional profile of the OSC:PS blended thin films in Chapter 2. Surface sputter etching of the surface was accomplished with Cs $^+$  beam, over a 300  $\mu\text{m} \times 300 \mu\text{m}$  area using 1 keV energy settings raster. A pulsed beam of 25 keV Bi $_1^+$  ions scanned over a 50  $\mu\text{m} \times 50 \mu\text{m}$  region centred within the sputtered area was used. Analysis cycle time was 100  $\mu\text{s}$  and sputtering cycle was 1.6 s and 500 ms flood gun compensation. A high current beam of low energy (< 20 eV) electrons was employed for charge compensation, and negative ions were analysed.

## 7.4 ELECTRICAL CHARACTERISATION

---

### Instrumentation

**OFET electrical characterisation** in this work was carried out in ambient conditions with four different measurement systems:

- An Agilent B1500A semiconductor device analyser connected to the samples with a Karl SÜSS probe station was used to perform all OFET measurements of freshly prepared devices and for time stability measurements of doped devices (Chapter 4).
- A Keithley 2636 SourceMeter, controlled by a custom made Matlab software, was employed to acquire electrical measurement during bending tests (Chapter 5).
- A Keithley 2614 SourceMeter, controlled by a custom made Labview software, was used for measurements during X-ray irradiation tests (Chapter 6) and for aging measurements of the same samples.
- A Keithley 6517A Electrometer was employed to measure the voltage output signal of the Wheatstone bridge architecture (Chapter 6).

**Electrochemical impedance spectroscopy (EIS) measurements** for extracting the dielectric capacitance in EGO-FET configuration (Chapter 2) were carried out with a Novocontrol Alpha-AN impedance analyser equipped with POT/GAL 30 V/2 A electrochemical interface in a frequency range of  $10^5$ - $10^{-1}$  Hz.

### Extraction of OFET parameters

The **field-effect mobility** ( $\mu_{FE}$ ) was extracted in saturation regime from the transfer characteristics using the slope ( $b$ ) of the linear fit of  $|I_{SD}|^{1/2}$  versus  $V_{SG}$ . Afterwards, the following formula was applied:

$$\mu_{FE} = \frac{2 \cdot L}{W \cdot C} \cdot b^2 \quad (7.1)$$

where  $L$  and  $W$  are the channel length and width, respectively, and  $C$  is the dielectric capacitance per unit area.

The **threshold voltage** ( $V_{th}$ ) was calculated using the following equation:

$$V_{th} = -\frac{a}{b} \quad (7.2)$$

where  $a$  stands for the y-intercept of the linear fit of  $|I_{SD}|^{1/2}$  versus  $V_{SG}$ .

It is noteworthy that for all devices the mobility has been extracted by fitting well above the subthreshold regime, in order to exclude mobility overestimation due to effects related to charge injection.<sup>4</sup>

For the extraction of the **subthreshold swing** ( $SS$ ) the following equation was used:

$$SS = \left( \frac{\partial \log |I_{SD}|}{\partial V_{SG}} \right)^{-1} \quad (7.3)$$

The maximum **density of traps** ( $N_T$ ) was estimated using the following approximation:<sup>5</sup>

$$N_T \approx \frac{C}{q^2} \cdot \left[ \frac{q \cdot SS}{k_B \cdot T \cdot \ln(10)} - 1 \right] \quad (7.4)$$

where  $q$  is the electron charge,  $k_B$  is the Boltzmann constant, and  $T$  is the absolute temperature.

## 7.5 CHARACTERISATION UPON PHYSICAL INPUTS

---

### Bending tests

During **bending test** performed on flexible substrates in Chapter 5, the variation of the main OFET parameters (such as mobility and threshold voltage) upon the application of mechanical deformations (either elongation or compression) was investigated. For this purpose, the transfer characteristics were measured both in flat state and during deformation for each of the strain values employed ( $0.19\% \leq |\varepsilon| \leq 1.75\%$ ). Additionally, the mechanical stress of the devices was tested by subjecting them to up to 1000 elongation cycles. In this case, a controlled force ( $\varepsilon = 0.44\%$ ) was applied by an automated system (Imada Digital Force Measurement Gauge) with a mechanical indenter.

### X-ray irradiation tests

**Characterisation under X-rays** (Chapter 6) was performed in darkness and inside a shielded cabinet for X-ray irradiation. The X-ray broad spectrum provided by a tube with molybdenum (Mo) target and accelerating voltage of 35 kV (PANalytical PW2285/20) was employed as radiation source with an X-ray spot of around 10 mm of diameter. The dose rates were in the range 5-55 mGy/s, measured with an error below 5% by means of a BARRACUDA X-ray Analyser from RTI. For the low dose measurements, a system of aluminium filters was built to attenuate the dose rate provided by the X-ray tube and thus work with X-ray doses as low as few  $\mu\text{Gy/s}$ . A mechanical shutter controlled the beam switching, giving cycles of 60 s on and 60 s off.

### Photoconductive gain model and calculation of factor $G$

The real-time response (i.e., the current vs. time variation) of the devices when exposed to X-rays can be described by the photoconductive gain mechanism.<sup>6</sup> As discussed in Chapter 6, in this type of devices the photocurrent signal due to the absorption of high energy photons and the collection of the photogenerated charges is amplified by a factor  $G$ , the photoconductive gain. This process of amplification is activated by the trapping of minority charge carriers (electrons) and, indeed, the factor  $G$  can be expressed as the ratio between the recombination time ( $\tau_r$ ) and the transit time ( $\tau_t$ ):

$$G = \tau_r / \tau_t \quad (7.5)$$

These two characteristic times represent, respectively, the time of recombination of the minority carriers trapped in the organic layer and the transit time of the majority carriers along the OFET channel.

The recombination time is a function of the charge carrier density ( $\rho$ ) in the channel and can be approximated by the phenomenological equation:

$$\tau_r(\rho_x) = \frac{\alpha}{\gamma} \left[ \alpha \ln \left( \frac{\rho_0}{\rho_x} \right) \right]^{\frac{1-\gamma}{\gamma}} \quad (7.6)$$

where  $\alpha$  is the time-scale in which the relaxation after the irradiation takes place,  $\gamma$  represents the width of the distribution of the relaxation time-scale (typically  $\gamma < 1$  in amorphous and polycrystalline materials),  $\rho_0$  is the carrier density in the saturation condition and  $\rho_x$  the carrier density induced by a certain dose of radiation.

In order to determine these material specific parameters, the decay of the carrier density after irradiation (i.e., when X-rays are switched off) was considered. This decay process is related to the slow relaxation of the trapped charge carriers (thus, it is independent from the dose rate previously applied) and can be expressed by a stretched exponential:

$$\rho_x(t) = \rho_0 \cdot e^{-t^\gamma/\alpha} \quad (7.7)$$

Hence, the experimental current curves obtained after irradiating a detector device with different radiation doses were fitted using a single set of parameters ( $\alpha$ ,  $\gamma$ ,  $\rho_0$ ) by using a customised MATLAB code. This allowed to calculate the recombination time for a certain dose of radiation from **Equation 7.6**.

Finally, considering that the transit time is a device specific parameter given by:

$$\tau_t = \frac{L^2}{V \cdot \mu} \quad (7.8)$$

where  $L$  is the channel length,  $\mu$  the mobility, and  $V$  the voltage applied, the photoconductive gain for a certain dose of radiation was calculated from **Equation 7.5**.



7.5 REFERENCES

---

- (1) Crivillers, N.; Oxtoby, N. S.; Mas-Torrent, M.; Veciana, J.; Rovira, C. Improved Synthesis of the High-Mobility Organic Semiconductor Dithiophene-Tetrathiafulvalene. *Synthesis* **2007**, *11*, 1621–1623.
- (2) Lai, S.; Cosseddu, P.; Gazzadi, G. C.; Barbaro, M.; Bonfiglio, A. Towards High Frequency Performances of Ultra-Low Voltage OTFTs: Combining Self-Alignment and Hybrid, Nanosized Dielectrics. *Org. Electron.* **2013**, *14*, 754–761.
- (3) del Pozo, F. G.; Fabiano, S.; Pfattner, R.; Georgakopoulos, S.; Galindo, S.; Liu, X.; Braun, S.; Fahlman, M.; Veciana, J.; Rovira, C.; et al. Single Crystal-Like Performance in Solution-Coated Thin-Film Organic Field-Effect Transistors. *Adv. Funct. Mater.* **2016**, *26*, 2379–2386.
- (4) Bittle, E. G.; Basham, J. I.; Jackson, T. N.; Jurchescu, O. D.; Gundlach, D. J. Mobility Overestimation Due to Gated Contacts in Organic Field-Effect Transistors. *Nat. Commun.* **2015**, *7*, 10908.
- (5) McDowell, M.; Hill, I. G.; McDermott, J. E.; Bernasek, S. L.; Schwartz, J. Improved Organic Thin-Film Transistor Performance Using Novel Self-Assembled Monolayers. *Appl. Phys. Lett.* **2006**, *88*, 073505.
- (6) Basiricò, L.; Ciavatti, A.; Cramer, T.; Cosseddu, P.; Bonfiglio, A.; Fraboni, B. Direct X-Ray Photoconversion in Flexible Organic Thin Film Devices Operated below 1 V. *Nat. Commun.* **2016**, *7*, 13063.

## CHAPTER 8

### Conclusions

---

In this thesis we have studied several aspects related to organic field-effect transistors (OFETs), including their fabrication, their morphological, structural and electrical characterisation, and further applications in the field of physical sensing. We have focused on exploiting bar-assisted meniscus shearing (BAMS) to deposit from solution blends of small molecule organic semiconductors (OSCs) and polystyrene (PS), giving rise to high quality active layers and high performance OFETs. Special attention has been paid to the morphology-performance relationship, and to understand how the final properties of the devices are influenced by the control of different fabrication parameters. The research conducted and presented in this thesis has led to the following conclusions:

- i. The combination of BAMS as solution processing technique with the use of OSC:PS blends as active material has shown to be a promising strategy to obtain thin films exhibiting high homogeneity and crystallinity, enabling the fabrication of OFET devices featuring high and reproducible field-effect mobility values. The versatility and applicability of BAMS were demonstrated by processing four OSCs belonging to different semiconductor families (TIPS-pentacene, diF-TES-ADT, C8-BTBT and DT-TTF) using a unified experimental recipe, and by employing different types of substrates, both rigid and flexible.
- ii. The use of OSC:PS blends typically leads to vertically phase separated thin films. Such stratification was investigated at the nanometre scale for C8-BTBT:PS blends by combining topographic and friction AFM images. From such in detail study it was concluded that the crystalline semiconductor layer is sandwiched between a bottom and a top PS layer, which confer stability by passivating the polar surface of the dielectric and impeding dewetting. In addition, tuning the OSC:PS weight ratio has an important effect on the thickness and continuity of the semiconductor layer, thus determining the electrical performance of the final OFETs.
- iii. Doping has shown to be a powerful tool for achieving high performance OFETs by overcoming the limitations imposed by high contact resistance arising from a high

energetic barrier at the OSC/electrodes interface. Inserting a dopant interlayer at this interface has demonstrated to be the most effective doping route in terms of reduction of power consumption (i.e., operation voltage), while exposure to an iodine water solution resulted in a remarkable fourfold increase of the device mobility. In general, it was concluded that dopant diffusion should be prevented in order to ensure doping stability and to avoid the structural degradation of the active layer.

- iv. The response exhibited by OFET devices subjected to mechanical strain is intimately correlated with the morphology present in the channel area. First, crystal size determines the extent of the response upon bending, which was tuned by changing the shearing direction upon deposition. In particular, devices with small and large crystal domains showed a larger sensitivity under compression and elongation, respectively. In addition, it was observed that recovery is limited by crack formation upon the application of a critical value of strain, especially in the case of films with large crystals, for which deep interconnected cracks are formed. Nevertheless, a remarkable stability and reproducibility was measured over prolonged bending tests.
- v. The direct detection of X-ray radiation can be realised employing OFET devices based on TIPS-pentacene:PS blends, exhibiting sensitivity values that are the highest among organic thin-film X-ray detectors and competitive with the inorganic materials currently used to fabricate large-area detectors. It was found that the morphological and transport properties of the active layer determine the sensing capability of such devices, which can be successfully tuned by controlling the processing parameters. In particular, it was observed that active layers with smaller grain size and higher charge carrier mobility, which were obtained at high coating speeds and by blending PS in the semiconductor ink, gave rise to devices with an improved X-ray sensitivity. In addition, by exploiting the uniformity provided by BAMS deposition technique and a Wheatstone bridge geometry combining 4 OFETs with similar performance, a proof-of-concept X-ray sensor featuring a stable and low dark current was implemented.

## List of publications

---

Temiño, I.; Del Pozo, F. G.; Ajayakumar, M. R.; Galindo, S.; Puigdollers, J.; Mas-Torrent, M. A Rapid, Low-Cost, and Scalable Technique for Printing State-of-the-Art Organic Field-Effect Transistors. *Adv. Mater. Technol.* **2016**, *1*, 1600090.

Zhang, Q.; Leonardi, F.; Casalini, S.; Temiño, I.; Mas-Torrent, M. High Performing Solution-Coated Electrolyte-Gated Organic Field-Effect Transistors for Aqueous Media Operation. *Sci. Rep.* **2016**, *6*, 39623.

Lai, S.; Temiño, I.; Cramer, T.; del Pozo, F. G.; Fraboni, B.; Cosseddu, P.; Bonfiglio, A.; Mas-Torrent, M. Morphology Influence on the Mechanical Stress Response in Bendable Organic Field-Effect Transistors with Solution-Processed Semiconductors. *Adv. Electron. Mater.* **2018**, *4*, 1700271.

Pérez-Rodríguez, A.; Temiño, I.; Ocal, C.; Mas-Torrent, M.; Barrena, E. Decoding the Vertical Phase Separation and Its Impact on C8-BTBT/PS Transistors Properties. *ACS Appl. Mater. Interfaces* **2018**, *10*, 7296–7303.

Temiño, I.; Basiricò, L.; Fratelli I.; Tamayo A.; Ciavatti A.; Mas-Torrent, M.; Fraboni, B. Morphology and Mobility as Tools to Control and Unprecedentedly Enhance X-Ray Sensitivity in Organic Thin-Film Devices. Manuscript submitted.

